



저작자표시-비영리-변경금지 2.0 대한민국

이용자는 아래의 조건을 따르는 경우에 한하여 자유롭게

- 이 저작물을 복제, 배포, 전송, 전시, 공연 및 방송할 수 있습니다.

다음과 같은 조건을 따라야 합니다:



저작자표시. 귀하는 원저작자를 표시하여야 합니다.



비영리. 귀하는 이 저작물을 영리 목적으로 이용할 수 없습니다.



변경금지. 귀하는 이 저작물을 개작, 변형 또는 가공할 수 없습니다.

- 귀하는, 이 저작물의 재이용이나 배포의 경우, 이 저작물에 적용된 이용허락조건을 명확하게 나타내어야 합니다.
- 저작권자로부터 별도의 허가를 받으면 이러한 조건들은 적용되지 않습니다.

저작권법에 따른 이용자의 권리는 위의 내용에 의하여 영향을 받지 않습니다.

이것은 [이용허락규약\(Legal Code\)](#)을 이해하기 쉽게 요약한 것입니다.

[Disclaimer](#)

Doctoral Thesis

**Light Manipulation for High Performance of  
Organic Solar Cells**

Seyeong Song

Department of Energy Engineering  
(Energy Engineering)

Graduate School of UNIST

2019

# Light Manipulation for High Performance of Organic Solar Cells

Seyeong Song

Department of Energy Engineering  
(Energy Engineering)

Graduate School of UNIST

# Light Manipulation for High Performance of Organic Solar Cells

A thesis/dissertation  
submitted to the Graduate School of UNIST  
in partial fulfillment of the  
requirements for the degree of  
Doctor of Philosophy

Seyeong Song

12/12/2018 of submission

Approved by



---

Advisor

Jin Young Kim

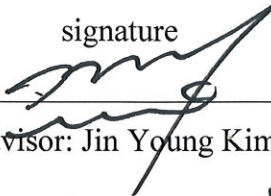
# Light Manipulation for High Performance of Organic Solar Cells

Seyeong Song

This certifies that the thesis/dissertation of Seyeong Song is approved.

12 / 12 / 2018 of submission


signature



---

Advisor: Jin Young Kim

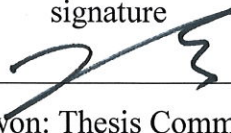
signature



---

Myoung Hoon Song: Thesis Committee Member #1

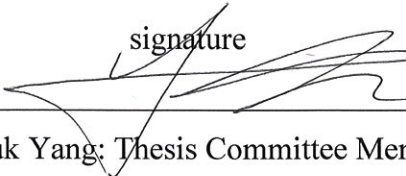
signature



---

Tae-Hyuk Kwon: Thesis Committee Member #2

signature



---

Changduk Yang: Thesis Committee Member #3

signature



---

Han Young Woo: Thesis Committee Member #4;

## Abstract

Organic solar cells (OSCs), a kind of promising photovoltaics in next generation due to lots of advantages such as mechanical flexibility, light weight, easy bandgap tuning, easy fabrication and so on, is direct conversion system from sunlight to electricity through the absorption of photons in active materials. Since light consist of radiant particles (photons) and electromagnetic field (waves) is necessary to work solar cells, there is promising route to enhance the performance of OSCs via combination of the inherent potential in organic solar cells and optical engineering. Furthermore, the studies using light manipulation are expected not only to lead to commercialization of OSCs, but also to use in other optoelectronics engineering as strategies. The main research is as follows.

Firstly, the localized surface plasmon resonance (LSPR) phenomenon generated by light is used in organic solar cells, which arise from two different electron transport layers (ETLs) incorporated with silver (Ag) nanoparticles. According to Mie theory for spherical particles, the LSPR frequency changes depending on the refractive index of surroundings, which shows the different influence and improvement of performance on organic solar cells. In addition, for this study, we used block copolymer micellar lithography (BCML) for Ag dot arrays, optical calculation considering quantum size effect, nonlocal response and plasmon coupling effects.

Secondly, to broaden photon absorption without the light waste, hetero organic tandem solar cells (HOTSCs) were fabricated by accounting into limited factors of tandem structure system as well as requirements of each layers. In this study, two new polymers of wide band gap were used in bottom solar sub-cells, while relatively narrower bandgap polymer was used in top solar sub-cells. Thus, the tandem solar cells in series shows high performance with increased open-circuit voltage ( $V_{oc}$ s).

Thirdly, semitransparent organic solar cells were studied with transparent electrodes based on multilayers of metal and metal oxide. Since organic photoactive layers are so colorful that OSCs are suitable for building-integrated photovoltaics (BIPV), transparent top electrodes were key for semitransparent device. Using  $Sb_2O_3$  layers in dielectric-metal-dielectric (DMD) structure, not only colorful semitransparent solar cells with over around 30% of average visible transmittance (AVT: 380 nm – 780 nm) were fabricated, but also roles of each layers of DMD electrode were studied.

Further, as forth topic, colorant-based electrodes are also interesting approach for colorful semitransparent OSCs. The structure of color filter is reverse to DMD transparent electrode, which has configuration of metal-metal oxide-metal. Incorporating DMD electrode and color filter electrode, high performance and selective clear-colorful semitransparent OSCs were implemented. These optic engineering of metal and metal oxide layers and light manipulation will provide breakthroughs for innovative OSCs.

In addition, as sub-research (Chapter 6-10), I also studied controlling morphologies and molecular packing structures of photoactive films with various conjugated donor polymers, which were modified

side chains on the backbones, and processing method including thermal-, additives-, solvent treatment and so on. Finally, I suggest the potential of flexible OSCs fabricated by a roll-to-roll (R2R) process without performance loss through dual thermal treatment of slot die coating for optimal film morphology and molecular orientation.

These strategic approaches from light manipulation and trying film optimization of various polymers and processing methodology may draw realization of aesthetic OSCs commercial market.

Keywords: Organic solar cells, localized surface plasmon resonance, tandem structure, semitransparent electrode, color filter, optic engineering, morphology control.





## Table of contents

<b>Abstract.....</b>	<b>i</b>
<b>Table of contents .....</b>	<b>iii</b>
<b>List of Figures.....</b>	<b>v</b>
<b>List of Tables .....</b>	<b>xii</b>
<b>List of Abbreviations .....</b>	<b>xiv</b>
<b>Chapter 1. Introduction .....</b>	<b>1</b>
1.1 Organic solar cells .....	1
1.2 Light and Photonics .....	12
<b>Chapter 2. Optically Tunable Plasmonic 2-Dimensional Ag Quantum Dot Arrays for Optimal Light Absorption in Polymer Solar Cells.....</b>	<b>19</b>
2.1 Research background .....	19
2.2 Experimental .....	20
2.3 Results and Discussion.....	23
2.4 Conclusions .....	35
<b>Chapter 3. Efficiency Exceeding 11% in Tandem Polymer Solar Cells Employing High Open-Circuit Voltage Wide-Bandgap <math>\pi</math>-Conjugated Polymers .....</b>	<b>36</b>
3.1 Research background .....	36
3.2 Experimental .....	38
3.3 Results and Discussion.....	39
3.4 Conclusion .....	49
<b>Chapter 4. Effect of Each Layers in <math>Sb_2O_3/Ag/Sb_2O_3</math> sSemitransparent Electrode on Organic Solar Cells .....</b>	<b>50</b>
4.1 Research background .....	50
4.2 Experimental .....	51
4.3 Results and Discussion.....	51
4. Conclusion .....	65
<b>Chapter 5. Colorful Semitransparent Organic Solar Cells by Adjusting Color Saturation of Fabry-Perot Etalon .....</b>	<b>66</b>
5.1 Research background .....	66
5.2 Experimental .....	67
5.3 Results and Discussion.....	67
5.4 conclusion .....	72

<b>Chapter 6. Control of Charge Dynamics via Use of Nonionic Phosphonate Chains and Their Effectiveness for Inverted Structure Solar Cells .....</b>	<b>73</b>
6.1 Research background .....	73
6.2 Experimental .....	74
6.3 Result and Discussion .....	75
6.4 Conclusions .....	85
<b>Chapter 7. Benzodithiophene-Thiophene-Based Photovoltaic Polymers with Different Side-Chains .....</b>	<b>86</b>
7.1 Research background .....	86
7.2 Experimental .....	87
7.3 Results and Discussion.....	87
7.4 Conclusions .....	94
<b>Chapter 8. A Roundabout Approach to Control Morphological Orientation and Solar Cells Performance by Modulating Side-Chain Branching Position in Benzodithiophene-Based Polymers.....</b>	<b>95</b>
8.1 Research background .....	95
8.2 Experimental .....	96
8.3 Results and Discussion.....	97
8.4 Conclusions .....	108
<b>Chapter 9. Semi-Crystalline Photovoltaic Polymers with Siloxane-Terminated Hybrid Side-Chains .....</b>	<b>109</b>
9.1 Research background .....	109
9.2 Experimental .....	110
9.3 Results and Discussion.....	111
9.4 Conclusions .....	122
<b>Chapter 10. Hot Slot Die Coating for Additive-Free Fabrication of High-performance Roll-to-Roll Processed Polymer Solar Cells.....</b>	<b>123</b>
10.1 Research background .....	123
10.2 Experimental .....	124
10.3 Results and Discussion.....	125
10.4 Conclusions .....	141
<b>Chapter 11. Summary .....</b>	<b>142</b>
<b>Reference .....</b>	<b>144</b>
<b>Acknowledgements.....</b>	<b>157</b>

## List of Figures

<b>Figure 1. 1</b> Types of solar cells.....	1
<b>Figure 1. 2</b> Flexible organic solar cells .....	1
<b>Figure 1. 3</b> $\pi$ -conjugated system in semiconducting polymer.....	2
<b>Figure 1. 4</b> Energy band diagram of conjugated polymer.....	2
<b>Figure 1. 5</b> The working mechanism in D:A-based OSCs.....	3
<b>Figure 1. 6</b> $J$ - $V$ curve measurement system.....	4
<b>Figure 1. 7</b> Solar power on earth surface depending on the angle of incident light.....	5
<b>Figure 1. 8</b> Equivalent circuit diagram of solar cell.....	5
<b>Figure 1. 9</b> $J$ - $V$ curve of solar cells .....	6
<b>Figure 1. 10</b> Configurations of conventional structure OSCs and inverted structure OSCs .....	8
<b>Figure 1. 11</b> Transparent electrodes for OSCs.....	8
<b>Figure 1. 12</b> Four device structure of conjugated polymer-based solar cells: (a) single-layer OSCs, (b) bilayer OSCs, (c) ordered BHJ OSCs, (d) disordered bulk heterojunction (BHJ) OSCs <sup>[20]</sup> .....	10
<b>Figure 1. 13</b> Device structure of series organic solar cells and simplified band diagram .....	10
<b>Figure 1. 14</b> Solar irradiance spectrum .....	12
<b>Figure 1. 15</b> Electromagnetic radiation and light spectrum .....	12
<b>Figure 1. 16</b> (a) Plasmon resonance of metallic nanoparticle (b) plasmon peaks depending on metal kinds, shape and size.....	13
<b>Figure 1. 17</b> (a) Light trapping by (a) scattering for presence of metal nanoparticles, (b) by the excited particles near-field and (c) by SPP at metal/semiconductor interface.....	14
<b>Figure 1. 18</b> Illustrated light manipulation: diffraction, reflection, and refraction .....	15
<b>Figure 1. 19</b> Admittance plots for (a) dielectric case, (b) metal case and (c) combination case .....	16
<b>Figure 1. 20</b> (a) Schematic MOM structure and color filter depending on (b) thickness and (c) different refractive indices .....	17
<b>Figure 2. 1</b> Model systems used in the DDA calculation. (a) Model system for calculating the extinction spectra in ZnO or TiO <sub>2</sub> layer systems, which consisted of a total of 104,284 or 137,924 dipoles, respectively. (b) Model system used for calculating the near-field enhancement (i.e. electric field contour plot). An active layer (i.e. PTB7:PC <sub>71</sub> BM) was added to the model system in (a), which consisted of 407,044 dipoles for the ZnO layer system and 440,684 dipoles for the TiO <sub>2</sub> layer system, respectively. (c) Model system for calculating the far-field scattering of 2-dimensional Ag quantum dot arrays, which consisted of 552	

dipoles in an infinite ZnO or TiO<sub>2</sub> medium. *E* (red arrows) and *k* (orange arrows) indicate the directions of electric field and incident light, respectively. Periodic boundary conditions (PBCs) in *x*- and *y*-axis directions were applied in all systems. .... 22

**Figure 2. 2** (a) Chemical Structure of the Polystyrene (Blue) and Poly-2-vinylpyridine (Red) Block Copolymer Molecule; (b) Schematic View of the Fabrication of 2D Ag QAs via BCML; (c) SEM Image of 2D Ag QAs Using PS (172000)-b-P2VP (42000) Block Copolymer on an ITO Substrate. The scale bar is 200 nm..... 24

**Figure 2. 3** Comparison of 2-dimensional Ag quantum dot arrays using block copolymer micellar lithography (BCML): (a)-(e) SEM images of Ag quantum dot patterns on ITO substrates prepared using different block copolymers. The measured interval distances and quantum dot diameters are noted as *I* and *D*, respectively, below each image. .... 24

**Figure 2. 4** (a) Schematic diagram of Ag quantum dots embedded in ZnO and TiO<sub>2</sub> electron transport layers (ETLs). The thicknesses of the ETLs were 20 nm for ZnO and 30 nm for TiO<sub>2</sub> layers, respectively. (b) Normalized experimental absorbance and (c) normalized extinction spectra of 2D Ag QAs in ETLs obtained via DDA calculation. Each extinction spectrum of the ZnO and TiO<sub>2</sub> systems was obtained from the difference of each film with and without 2D Ag QAs..... 27

**Figure 2. 5** Calculated extinction spectra of 2-dimensional Ag quantum dot array in each ETL (i.e. ZnO and TiO<sub>2</sub> layers) without applying quantum effects..... 27

**Figure 2. 6** Calculated extinction spectra of (a) isolated Ag quantum dot from Figure 2.3 (a), where the PBCs were not applied, and (b) 2-dimensionally arrayed Ag quantum dots extended from Figure S2a with PBCs..... 28

**Figure 2. 7** (a) Device structure, (b) *J-V* characteristics under AM 1.5 illumination (100 mW cm<sup>-2</sup>) and (c) EQE of OPVs. Black traces correspond to OPVs without ETLs, while red and blue traces correspond to ZnO and TiO<sub>2</sub> ETLs, respectively. Empty circles correspond to devices without Ag NAs while filled circles are with Ag NAs embedded ZnO or TiO<sub>2</sub> layers ..... 29

**Figure 2. 8** AFM images (4 μm×1 μm) of ETLs with and without embedded 2-dimensional Ag quantum dot arrays..... 31

**Figure 2. 9** EQE and EQE enhancement. (a), (c) EQE with and without 2D Ag QAs embedded in ZnO and TiO<sub>2</sub> ETLs, respectively. (b), (d) Measured absorption enhancement due to 2D Ag QAs embedded in ZnO and TiO<sub>2</sub> ETLs (difference in absorption with and without 2D Ag QAs), respectively. Insets depict the configuration of optical reflectance measurements ..... 33

**Figure 2. 10** (a) Absolute transmittance of ZnO and TiO<sub>2</sub> layers with and without Ag nanodots. (b) Enhanced transmittance of ETL layers with Ag nanodot arrays and (c) Scattering cross-

	section difference between ETL+Ag nanodot arrays and ETLs only .....	33
<b>Figure 2. 11</b>	Reflectance spectra of PSCs based on PTB7:PC <sub>71</sub> BM with Ag nanodots embedded in (a) ZnO and (b) TiO <sub>2</sub> layers.....	34
<b>Figure 2. 12</b>	Calculated near-field electric field enhancement and far-field scattering. (a) Spatial distribution of the electric field of the device with ZnO and TiO <sub>2</sub> layers. $E(\omega)$ is the induced electric field and $E_0$ is the external electric field. (b) Angular plot of the far-field scattering of 2D Ag QAs in each ETL. The results were obtained at a wavelength of 500 nm for ZnO and 530 nm for TiO <sub>2</sub> , which were the peak wavelengths in the extinction spectra (as shown in Figure 2.3 (c))......	35
<b>Figure 3. 1</b>	(a) Polymer structures. (b) UV-vis absorption spectra. (c) Energy level diagram of polymers .....	40
<b>Figure 3. 2</b>	(a) Thermo gravimetric analysis (TGA) and (b) differential scanning calorimetry (DSC) plots of P1, P2. (c) Cyclicvoltammograms of P1, P2.....	40
<b>Figure 3. 3</b>	AFM images of (a) P1:PC <sub>71</sub> BM and (b) P2:PC <sub>71</sub> BM films .....	41
<b>Figure 3. 4</b>	GIXS images of (a) P1:PC <sub>71</sub> BM and (b) P2:PC <sub>71</sub> BM based active layers and with xy-and z-axis cross sections corresponding to each polymer, respectively.....	41
<b>Figure 3. 5</b>	$J$ - $V$ characteristics of (a) P1 and (b) P2 BHJ single junction cells with various post-solvent treatments.....	43
<b>Figure 3. 6</b>	(a) TPSCs device structure, (b) $J$ - $V$ curves of P1 and P2 single-junction PSCs and TPSCs, (c) EQE curves of P1, P2, and PTB7-Th single-junction PSCs, (d) EQE curves of tandem devices.....	44
<b>Figure 3. 7</b>	(a) Double-logarithmic plot of dark $J$ - $V$ characteristics from (a) hole-only diodes (b) Electron-only device (c) Schematic image of charge transport in TPSC and FF-determination .....	46
<b>Figure 3. 8</b>	Optical constants (n, k) of polymers P1, P2 and PTB7-Th. (b), (c) Simulated $J_{sc}$ as a function of thicknesses of front and back cells, showing optimal front and back cell thicknesses for TPSCs based on P1 and P2, respectively. (d), (e) Photon absorption rate of TPSCs based on P1 and P2, respectively .....	48
<b>Figure 4. 1</b>	(a) structure of Sb <sub>2</sub> O <sub>3</sub> /Ag/ Sb <sub>2</sub> O <sub>3</sub> multilayer for top electrode (b) obtained optical properties such as refractive index (n) and absorption coefficient (k), (C) sheet resistance depending on increasing thickness of top Sb <sub>2</sub> O <sub>3</sub> film, (d)-(F) calculated and experimental transmittance of SAS multilayers depending on thickness of upper Sb <sub>2</sub> O <sub>3</sub> for 10nm, 15 nm and 20 nm of Ag film .....	52
<b>Figure 4. 2</b>	Photo of Sb <sub>2</sub> O <sub>3</sub> /Ag/ Sb <sub>2</sub> O <sub>3</sub> multilayer based Ag thin films of (a) 10, (b) 15 and (c) 20 nm,	

respectively .....	52
<b>Figure 4. 3</b> (a) OSCs structure (b) SEM image of Ag thin film (20nm) with and without Sb <sub>2</sub> O <sub>3</sub> thin layer (c) <i>J-V</i> characteristics with and without Sb <sub>2</sub> O <sub>3</sub> thin layers, (d) EQE spectra according the photovoltaic performance.....	53
<b>Figure 4. 4</b> (a) Fabricated OSCs structure (b) <i>J-V</i> characteristics of Sb <sub>2</sub> O <sub>3</sub> ETLs and (c) EQE spectra according the photovoltaic performance .....	54
<b>Figure 4. 5</b> SEM images of Ag thin film with and without 2 nm Sb <sub>2</sub> O <sub>3</sub> thin films on ZnO NPs layer	54
<b>Figure 4. 6</b> AFM images of 10 nm, 15 nm and 20 nm Ag thin films with and without 2nm Sb <sub>2</sub> O <sub>3</sub> thin films on ZnO NPs layers.....	54
<b>Figure 4. 7</b> (a) Illustration of transparent device with both light side (b) <i>J-V</i> characteristics depending on Ag thickness (ITO side illumination) (C) <i>J-V</i> characteristics of SAS side-illumination (d) corresponding transmittance from ITO to SAS electrode (e) FF versus light intensity (f) dark current of the devices.....	57
<b>Figure 4. 8</b> Light intensity dependence of (a) $J_{sc}$ , (b) $V_{oc}$ , and (c) FF of OSCs based on SAS electrode with different Ag thickness .....	57
<b>Figure 4. 9</b> <i>J-V</i> characteristics of (a) ITO side and (b) SAS side illumination for semitransparent OSCs based on thickness of Sb <sub>2</sub> O <sub>3</sub> top layers with 20 nm Ag thin film, and corresponding transmittance of whole device.....	59
<b>Figure 4. 10</b> <i>J-V</i> characteristics of ITO side and SAS side illumination for semitransparent OSCs depending on various Ag thickness.....	60
<b>Figure 4. 11</b> Device transmittance (ITO to SAS) of various Ag thickness and top Sb <sub>2</sub> O <sub>3</sub> layer .....	60
<b>Figure 4. 12</b> (a) Chemical structures for colorful semitransparent OSCs (b) photo of devices (c) <i>J-V</i> characteristics of colorful devices.....	63
<b>Figure 4. 13</b> Semitransparent OSCs based on PBDBT:ITIC-m blend and J52:IEICO-4F blend with various thickness of top Sb <sub>2</sub> O <sub>3</sub> layer.....	63
<b>Figure 5. 1</b> Transmittance of color filter based on 20 nm, 25 nm and 30 nm of Ag thin films .....	68
<b>Figure 5. 2</b> (a) Color filter structure and (b) calculated and experimental transmittance and (c) photo of color filters.....	68
<b>Figure 5. 3</b> (a) OSCs with color filter and 50nm thick Ag electrode for comparison, (b) <i>J-V</i> characteristics, (c) EQE results and (d) corresponded transmittance.....	70
<b>Figure 5. 4</b> Electric field of OSCs fabricated with ITO bottom electrode and MOM or Ag 50 nm top electrode.....	70
<b>Figure 5. 5</b> Two type of OSCs structure and <i>J-V</i> characteristics.....	71
<b>Figure 6. 1</b> Chemical structure of IIGDT-based polymers with varying phosphonate content.....	74

<b>Figure 6. 2</b> (a) XPS spectra of the polymers showing the P 2p region and (b) water contact angle of PIIGDT-Pn films .....	75
<b>Figure 6. 3</b> Normalized UV-Vis absorption spectra in (a) chloroform solution and (b) thin films, (c) cyclic voltammograms and (d) HOMO and LUMO energy diagrams (vs. vacuum) of PIIGDT-P0, PIIGDT-P5, PIIGDT-P15 and PIIGDT-P30.....	76
<b>Figure 6. 4</b> (a,c) $J-V$ characteristics of optimized i-PSCs without and with DPE additive, respectively and (b,d) corresponding external quantum efficiency (EQE) spectra .....	79
<b>Figure 6. 5</b> (a) hole-only devices (ITO/PEDOT:PSS/polymer:PC <sub>71</sub> BM added DPE/Au) (b) Double-logarithmic plot of dark $J-V$ characteristics from electron-only devices (FTO/polymer:PC <sub>71</sub> BM added DPE/Al). Sky blue lines are fits of the curves using the Mott-gurney relationship.....	80
<b>Figure 6. 6</b> (a) Double-logarithmic scale of the short circuit current density as a function of light intensity and (b) photocurrent versus effective voltage of optimal PSCs with DPE: PIIGDT-P0 (blue), P5 (red), P15 (green) and P30 (magenta).....	81
<b>Figure 6. 7</b> Grazing incidence wide angle X-ray scattering (GIWAXS) images of IIGDT-based polymer neat films: (a) PIIGDT-P0, (b) PIIGDT-P5, (c) PIIGDT-P15, (d) PIIGDT-P30. The corresponding GIWAXS diffractogram profiles: (e) in-plane and (f) out-of-plane GIWAXS patterns .....	83
<b>Figure 6. 8</b> GIWAXS images of blended polymer films (a) without and (b) with DPE additive Corresponding GIWAXS diffractogram profiles of (c) in-plane and (d) out-of-plane GIWAXS patterns Solid lines represent polymer:PC <sub>71</sub> BM blends while dotted lines represent polymer:PC <sub>71</sub> BM blends processed with DPE. ....	83
<b>Figure 6. 9</b> AFM images (3×3 μm) of blended polymer:PC <sub>71</sub> BM films (a–d) without and (e-f) with DPE additive films. RMS values: (a) 5.21, (e) 2.72 nm of PIIGDT-P0; (b) 2.55, (f) 2.34 nm of PIIGDT-P5; (c) 8.18, (g) 2.26 nm of PIIGDT-P15; and (d) 11.14, (h) 2.43 nm of PIIGDT-P30 .....	85
<b>Figure 7. 1</b> Chemical structure of donor polymers based BDTT backbone.....	87
<b>Figure 7. 2</b> (a) UV–vis absorption spectra in toluene (open) and in film (solid). (b) Emission spectra of polymers in toluene (open) and in tetrahydrofuran (solid) .....	89
<b>Figure 7. 3</b> (a) Cyclic voltammogram and (b) energy band diagram of polymers.....	89
<b>Figure 7. 4</b> (a) Torsional profiles and (b) energy minimum conformations (red: oxygen, yellow: sulfur) .....	90
<b>Figure 7. 5</b> (a) $J-V$ characteristics and (b) EQE spectra of polymer:PC <sub>71</sub> BM photovoltaic devices....	92
<b>Figure 7. 6</b> (a) 2D-GIWAXS images of pristine and blend films and (b) plotting lines corresponding GIWAXS result. ....	92

<b>Figure 7. 7</b> AFM topography images for blend films ( $1.5 \mu\text{m} \times 1.5 \mu\text{m}$ ).....	93
<b>Figure 8. 1.</b> Chemical structure of PBDTTPD-Cn donor polymers.....	97
<b>Figure 8. 2</b> UV-vis absorption spectra of PBDTTPD-Cn in chloroform solution (a) and as a thin solid films spin-cast from chloroform (b) Cyclic voltammograms of PBDTTPD-Cn thin films (c) Energy level diagrams for PBDTTPD-Cn and PC <sub>71</sub> BM (d).....	98
<b>Figure 8. 3</b> (a) DFT-optimized geometries and charge-density isosurfaces for BDT-TPD-BDT (B3LYP/6-31G*) and (b) their dihedral angles.....	99
<b>Figure 8. 4</b> <i>J-V</i> Characteristics (a) and external quantum efficiency (EQE) spectra of PBDTTPD-C1 (black), C3 (blue) and C4 (red) (b) .....	101
<b>Figure 8. 5</b> Grazing incident wide angle X-ray scattering (GIWAXS) results for neat PBDTTPD-Cn in-plane and out-of-plane line cuts of the corresponding above patterns.....	103
<b>Figure 8. 6</b> GIWAXS images for blends of PBDTTPD-Cn:PC <sub>71</sub> BM and with additive (a). In-plane and out-of-plane line cuts of the corresponding above patterns for PBDTTPD-Cn:PC <sub>71</sub> BM (solid line) and with additive (symbol line) films .....	103
<b>Figure 8. 7</b> Atomic force microscopy (AFM) images ( $2 \times 2 \mu\text{m}^2$ ) of polymer:PC <sub>71</sub> BM on ITO substrate: root-mean-square (RMS) as (a) 3.32 nm (top), 2.13 nm (bottom) of PBDTTPD-C1 (b) 5.22 nm (top), 4.02 nm of PBDTTPD-C3 (c) 7.68 nm (top), 2.64 nm (bottom) of PBDTTPD-C4, respectively.....	104
<b>Figure 8. 8</b> Double-logarithmic plot from dark <i>J-V</i> characteristics of (a) hole-only devices (ITO/PEDOT:PSS/polymer:PC <sub>71</sub> BM/Au) and (b) electron only devices (FTO/polymer:PC <sub>71</sub> BM/Al).....	106
<b>Figure 8. 9</b> The performance of OFETs used OTS treatment as a passive layer (a) The output characteristics, (b) the transfer characteristics and plots of the square root the drain current as a function of the gate voltage for PBDTTPD-C1(black), C3(blue) and C4(red). ( $I_D$ : Drain current. $V_G$ : Voltage of gate in an OFET. $V_{DS}$ : Voltage between drain and source in an OFET) .....	107
<b>Figure 9. 1</b> (a) Synthetic scheme for new designed polymers; normalized UV-Vis absorption spectra of polymers (b) in chloroform and (c) in film; (d) cyclic voltammograms of thin films of three polymers (color online).....	112
<b>Figure 9. 2</b> (a) <i>J-V</i> characteristics and (b) EQE spectra of PSC devices with and without DPE as a processing additive (color online).....	115
<b>Figure 9. 3</b> Topographic morphology images ( $2.5 \mu\text{m} \times 2.5 \mu\text{m}$ ) of polymer:PC <sub>71</sub> BM blends (a–c) without and (d–f) with 3 vol% DPE. (a, d) PPSiDTBT, (b, e) PPSiDTFBT, (c, f) PPSiDT2FBT BHJ films deposited on ITO/PEDOT:PSS under the same condition for the	



optimized devices. RMS roughness values are at the left-bottom corner of each figure (color online).....	117
<b>Figure 9. 4</b> GIWAXS images of (a) neat polymer films and (b) blends of polymer:PC <sub>71</sub> BMwith DPE; (c) in-plane and out-of-plane line cuts of the above patterns (color online).....	119
<b>Figure 9. 5</b> Double-logarithmic plot from dark <i>J-V</i> characteristics of (a) hole-only devices and (b) electron-only devices. ....	120
<b>Figure 9. 6</b> Light intensity dependence of (a) $J_{sc}$ and (b) $V_{oc}$ ; (c) photocurrent versus effective voltage (color online).....	122
<b>Figure 10. 1</b> <i>J-V</i> characteristics and EQE spectra of PPDT2FBT:PC <sub>71</sub> BM-based inverted PSCs with different solvents at Head:25 °C-Substrate: 80 °C (H25-S80) condition.....	127
<b>Figure 10. 2</b> (a) long-term stabilities in air atmosphere (b) thermal stabilities at 120 °C in N <sub>2</sub> filled glove box and (c) photo stabilities under AM 1.5G illumination in air condition. photoactive layer of PSCs spin-coated with and without additives, and slot die coated for comparisons of devices durability. The devices used for stability testing in air were encapsulated in glass. ....	128
<b>Figure 10. 3</b> (a) Slot-die process using with 3D printer for PSCs fabrication and (b) The performance of inverted PP2FBT:PC <sub>71</sub> BM-based PSCs depending on both temperature, changes of photovoltaic parameters (c) on substrate (or/and stage) temperature in case of fixed head T at 80 °C and (d) on slot- die head temperature in fixed substrate T at 80 °C .....	129
<b>Figure 10. 4</b> Dark <i>J-V</i> characteristics of devices processed at various temperature combination conditions. ....	132
<b>Figure 10. 5</b> . (a–d) FE-TEM and (e–h) AFM topography images of active layers processed with the dual temperature treatment (H25–S25, H25–S80, H80–S25 and H80–S80). The RMS scale is 40 nm. (i and j) GIWAXS line-cut profiles of the $q_{xy}$ and the $q_z$ axis for the four films. ....	133
<b>Figure 10. 6</b> Two-dimensional GIWAXS data for films processed at (a) H25-S25, (b) H25-S80, (c) H80-S25 and (d) H80-S80 conditions, respectively .....	135
<b>Figure 10. 7</b> (a) <i>J-V</i> curve of fast and slowly dried PSCs and AFM topography (b-e) and corresponding phase images (f-i) for comparison of film morphologies dried by fast and slow cooling after slot die coating at H80-S60 and H80-S80 .....	136
<b>Figure 10. 8</b> (a) Light intensity dependence of $V_{oc}$ and (b) photocurrent versus effective voltage....	137
<b>Figure 10. 9</b> (a) Pictures of 3D printer-based R2R equipment and (b) <i>J-V</i> characteristics of slot die processed polymer solar cells on ITO coated glass and flexible PET substrates.....	139
<b>Figure 10. 10</b> <i>J-V</i> characteristics and EQE results of PSCs fabricated by slot die-based all solution	140

## List of Tables

<b>Table 2. 1</b>	Number-average molecular weights and polydispersities of block copolymers compared to sizes, interval distances and PSCs performance of 2-dimensional Ag quantum dot arrays with various geometric conditions .....	25
<b>Table 2. 2</b>	Device characteristics of PTB7:PC <sub>71</sub> BM based OPVs with or without 2D Ag QAs in different ETLs.....	29
<b>Table 2. 3</b>	PSCs parameters of devices using various 2-dimensional Ag quantum dot arrays .....	30
<b>Table 2. 4</b>	Device characteristics with variable ETL thicknesses.....	30
<b>Table 3. 1</b>	Crystallographic parameters of WBG polymer films .....	42
<b>Table 3. 2</b>	Photovoltaic parameters of BHJ single junction cells with various post-solvent treatments .....	43
<b>Table 3. 3</b>	Optimized photovoltaic properties of single junction and tandem solar cells .....	45
<b>Table 3. 4</b>	PCE of TPSCs (until 2017.06).....	45
<b>Table 3. 5</b>	Hole mobilities and electron mobilities of polymer blend films using SCLC method.....	47
<b>Table 4. 1</b>	Photovoltaic parameters of OSCs fabricated with Sb <sub>2</sub> O <sub>3</sub> layer as an ETL.....	55
<b>Table 4. 2</b>	Photovoltaic parameters of device with and without ETLs.....	55
<b>Table 4. 3</b>	Photovoltaic parameters of devices depending on Ag thickness of SAS top electrode.....	58
<b>Table 4. 4</b>	Photovoltaic parameters of devices depending on thickness of top Sb <sub>2</sub> O <sub>3</sub> layer in 20 nm Ag-based SAS electrode.....	59
<b>Table 4. 5</b>	Photovoltaic parameters of devices depending on thickness of top Sb <sub>2</sub> O <sub>3</sub> layer in SAS electrode.....	61
<b>Table 4. 6</b>	Photovoltaic parameters of colorful OSCs fabricated with 20 nm Ag and 10 nm top Sb <sub>2</sub> O <sub>3</sub> layer-based SAS electrode.....	62
<b>Table 4. 7</b>	OSCs performance of Blue active blends (PBDB-T:ITIC-m) and red active blends (J52:IEICO-4F). .....	64
<b>Table 5. 1</b>	Photovoltaic parameters of PTB7-Th:PC <sub>71</sub> BM-based OSCs with color filters .....	69
<b>Table 5. 2</b>	Photovoltaic parameters of OSCs based on OMO and color filter electrode .....	72
<b>Table 6. 1</b>	Optical and electrochemical properties of the polymers .....	76
<b>Table 6. 2</b>	All data of photovoltaic performance of the IIGDT-based polymers <sup>a</sup> .....	78
<b>Table 6. 3</b>	Photovoltaic performance of the IIGDT-based polymers.....	79
<b>Table 6. 4</b>	Hole and electron mobilities of blend films of IIGDT-based polymers derived using the	

SCLC method.....	81
<b>Table 6. 5</b> Crystallographic parameters calculated from GIWAXS profiles of IIGDT-based polymers .....	84
<b>Table 7. 1</b> Summary of photophysical-, electrochemical- and thermal properties of polymers .....	88
<b>Table 7. 2</b> Summary of device characteristics .....	91
<b>Table 7. 3</b> Summary of photovoltaic parameters.....	91
<b>Table 7. 4</b> Crystallographic parameters of blend films.....	93
<b>Table 8. 1</b> Photophysical and electrochemical properties of PBDTTPD-Cn.....	98
<b>Table 8. 2</b> Parameters of performance for PBDTTPD-Cn devices with structure of ITO/PEDOT:PSS/polymer:PC <sub>71</sub> BM/Al measured under AM 1.5G illumination at 100 mWcm <sup>-2</sup> .....	100
<b>Table 8. 3</b> Summary of GIWAXS analysis on PBDTTPD-Cn as neat and blend films.....	102
<b>Table 8. 4</b> Calculated electron and hole mobility of PBDTTPD-based polymers by space charge limited current (SCLC) devices and their thickness layers .....	106
<b>Table 8. 5</b> Summarized the performance values of <i>o</i> -FET device with hole mobility, threshold voltage and on-off ratio for PBDTTPD-C1, C3 and C4 .....	107
<b>Table 9. 1</b> Optical and electrochemical properties of polymers .....	112
<b>Table 9. 2</b> Summary of tested and fabricated solar cells .....	114
<b>Table 9. 3</b> Summary of photovoltaic characteristics of polymers .....	115
<b>Table 9. 4</b> Crystallographic parameters calculated from GIWAXS profiles of three polymers .....	118
<b>Table 9. 5</b> Charge mobilities calculated from SCLC modeling devices.....	120
<b>Table 10. 1</b> Detailed photovoltaic parameters at variable processing temperatures.....	127
<b>Table 10. 2</b> Summary of optimal photovoltaic parameters of PSCs processed using various processing temperatures.....	130
<b>Table 10. 3</b> Photovoltaic parameters of representative PSCs .....	131
<b>Table 10. 4</b> PSCs performance with various thickness in H80-S80 process .....	131
<b>Table 10. 5</b> Crystallographic parameters from GIWAXS data .....	135
<b>Table 10. 6</b> PSC performances for comparison of fast cooling and slow cooling after slot die coating .....	136
<b>Table 10. 7</b> Photovoltaic parameters of devices fabricated by slot die-based all solution process including ETL, active layer and HTL .....	140

## List of Abbreviations

Abbreviation	Explanation
OSC	Organic solar cell
PSC	Polymer solar cell
AFM	Atomic force microscopy
AM	Air mass
AVT	Average visible transmittance
BCML	Block copolymer micelle lithography
BHJ	Bulk heterojunction
BIPV	Building integrated photovoltaics
CB	Chlorobenzene
CIGS	Copper indium gallium selenide
CN	Chloronaphthalene
CNT	Carbon nano-tubes
CV	Cyclicvoltammogram
DDA	Discrete Dipole Approximation
DFT	Density functional theory
DIO	Diiodooctane
DPE	Diphenylether
DSC	Differential scanning calorimetry
$E_g^{opt}$	Optical band gap
EM	Electromagnetic
EQE	External quantum efficiency
ETL	Electron transport layer
FF	Fill factor
FTO	Fluorine tin oxide
GIWAXS	Grazing-incidence wide-angle X-ray scattering
HOMO	Highest occupied molecular orbital
HTL	Hole transport layer
ICT	Intramolecular charge transfer
IIG	Isoindigo
IPA	Isopropyl alcohol
IPCE	Incident photon-to-current conversion efficiency

---

IQE	Internal quantum efficiency
ITO	Indium tin oxide
$J_{ph}$	Photocurrent density
$J_{sc}$	Short circuit current density
LBG	Low-bandgap
LSPR	Localized surface plasmon resonance
LUMO	Lowest unoccupied molecular orbital
MOM	Metal-metal oxide-metal
NIR	Near-infrared
NP	Nanoparticle
<i>o</i> -DCB	<i>o</i> -dichlorobenzene
OFET	Organic field effect transistors
OMO/DMD	Metal oxide-metal-metal oxide/Dielectric-metal-dielectric
OTS	Octyltrichlorosilane
PCE	Power conversion efficiency
PL	Photoluminescence
PV	Photovoltaic
R2R	Roll-to-roll
RMS	Root-mean square
$R_s$	Series resistance
$R_{sh}$	Shunt resistance
SCLC	Space charge limited current
SPP	Surface plasmon polaritons
TCO	Transparent conductive oxide
TGA	Thermal gravimetric analysis
TPSC	Tandem polymer solar cells
UPS	Ultraviolet photoelectron spectroscopy
$V_{eff}$	Effective applied voltage
$V_{oc}$	Open-circuit voltage
WBG	Wide-bandgap
XPS	X-ray photoelectron spectroscopy

---

## Chapter 1. Introduction

### 1.1 Organic Solar Cells

A solar cell is one kinds of optoelectronic device that generates electricity from the light of the sun through photovoltaic (PV) effect. The PV effect is the process of materials that directly absorbs the photons of the sunlight to generates either excitons or positive and negative charge carriers for electrical energy. To provide enough electrical power for us, number of solar cells is connected like module panels. There are many kinds of solar cells such as silicon solar cells, copper indium gallium selenide (CI(G)S) solar cells, dye sensitive solar cells, quantum dot solar cells, perovskite solar cells and so on.

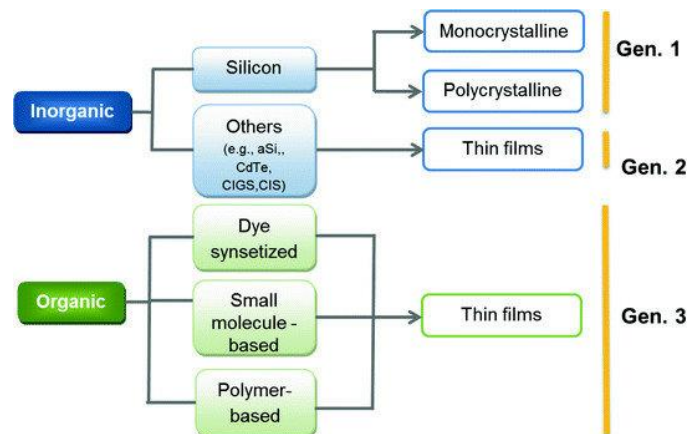


**Figure 1. 1** Types of solar cells

Among them, small molecule and polymer-based organic solar cells, PVs of 3<sup>rd</sup> generation, have their unique advantages<sup>[1]</sup>. First, thin films of organic solar cells (OSCs) has promise for fabricating lightweight and flexible devices, since either polymer and small molecule as photoactive materials has not only high absorption coefficient to enough absorbing light in thin films, but also inherent lightweight of polymer materials compared to inorganic solar cells <sup>[2, 3]</sup>. Second, product costs can be reduced, because the active materials are synthesized with low cost of monomer unit and have high-throughput roll-to-roll production processes in terms of module manufacturing <sup>[4-6]</sup>. Thirdly, due to the inherent semitransparency and feasible color tuning by bandgap engineering of active materials, OSCs have promise for aesthetic application like building integrated photovoltaics (BIPVs) <sup>[7, 8]</sup>. In addition to the above-mentioned advantages, there are benefits like easy fabrication and low light condition of indoor PVs and so on.



**Figure 1. 2** Flexible organic solar cells

### 1.1.1 Basics Principle

An organic solar cell is consisted of thin film of organic semiconducting materials as photoactive layer, this is the reason why it is called “organic solar cells”. Generally, the blends of organic semiconducting materials of donor and acceptor together were used as heterojunction. OSC devices have mainly configuration of two electrode (cathode and anode) and photoactive layer.

- Organic Semiconducting  $\pi$ -conjugated materials

It is substantially important to acquire superior electronic properties from  $\pi$ -conjugated polymer for OSCs. The  $\pi$ -conjugated polymer is formed from  $sp^2$ -hybridization, which is overlapping  $P_z$ -orbitals in aromatic polymers and generating chemical bridge of the interjacent single bonds. Hence the  $\pi$ -bond (above) and  $\sigma$ -bond (below) are formed in polymer as shown in **Figure 1.3**. These delocalized  $\pi$ -electron can transport along the bridge formed from the conjugated bond via both intra- and inter-transfer processes. The semiconducting chemical structure have bandgap and intrinsic electronic conductivity without any doping, the bandgap ( $E_g$ ) between the highest occupied molecular orbital (HOMO) and lowest unoccupied molecular orbital (LUMO) is tuned by polymer synthesis (**Figure 1.4**).

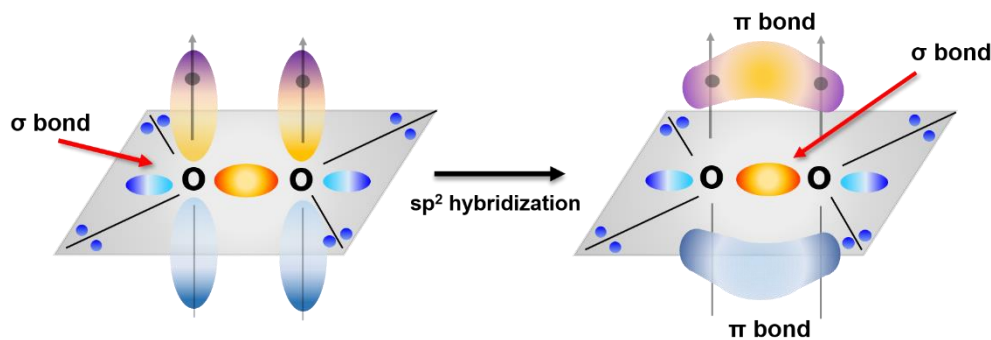


**Figure 1. 3**  $\pi$ -conjugated system in semiconducting polymer

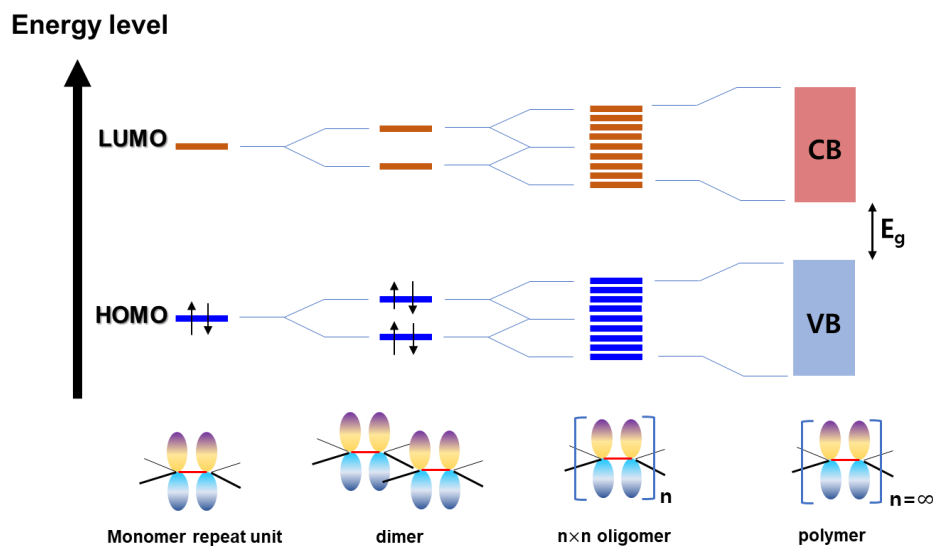


**Figure 1. 4** Energy band diagram of conjugated polymer

• Working Principle of Organic Solar Cells

Excitons (tightly bounded electron-hole pair) are generated when photons of sunlight were absorbed by photoactive layer of OSC. Through applied potential, these excitons are useful to separate from the excitons to hole and electron charge carriers. And the charge carriers flow to two electrodes (cathode and anode) of different work function. This working principle of OSCs, which is donor:acceptor (D:A, conjugated polymers) blend system, can be divided into main four steps.<sup>[9]</sup>

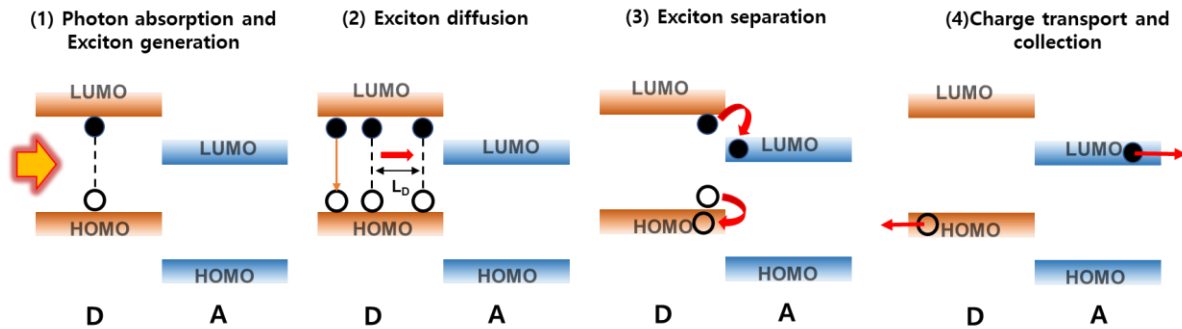


Figure 1. 5 The working mechanism in D:A-based OSCs

i) Absorption of photons into photoactive material

Absorption of photons from sunlight into photoactive layer is affected by spectral bandgap, absorption coefficient of conjugated polymers, thickness of active layer and device internal effects. Although conjugated polymer has high absorption coefficient enough to absorb sunlight, over 100 nm of active layer might occur insufficient photon absorption and charge transport loss. Hence, it needs to consider the balance between absorption and transport following.

ii) Exciton diffusion

The generated excitons randomly move to interface of donor and acceptor materials. Its exciton diffusion length ( $L_D$ ) and distance ( $L_i$ ) were considered in exciton dissociation.

$$L_D = (D\tau)^{1/2} \quad (\text{Eq. 1.1})$$

where  $D$  is diffusion coefficient and  $\tau$  is exciton lifetime.  $L_D$  has commonly been reported 4-20 nm for conjugated polymer, because of it, geminate recombination can be reduced at  $L_i \leq L_D$  condition.<sup>[10]</sup>

iii) Exciton dissociation

Excitons are separated at D:A interface to holes and electrons. By internal electric field for enough to overcome exciton binding energy,<sup>[11] [12]</sup> in other words, the excitons predominantly generated from donor polymer are dissociated in such a way that none bounded electron were located at LUMO energy level of acceptor semiconductor.

iv) Charge transport and collection

The holes and electrons transport to cathode and anode, respectively. Here, well-ordered polymers with high semicrystalline typically provide efficient pathway for carriers.



### 1.1.2 Characterization

Power conversion solar cells of OSCs can be carried out from the current-voltage ( $J$ - $V$ ) characteristic curve: the short circuit current density ( $J_{sc}$ ), the open-circuit voltage ( $V_{oc}$ ), and the fill factor (FF). The energy conversion efficiency can be calculated by **Equation 1.2**.

$$\eta = \frac{J_{sc} \times V_{oc} \times FF}{P_{in}} \times 100 \quad (\text{Eq. 1.2})$$

where  $P_{in}$  is the incident light,  $V_{oc}$  is the voltage at that the current is zero,  $J_{sc}$  is the device current density when no reverse bias is applied. FF is defined as the ratio of the maximum output power to the  $J_{sc} \times V_{oc}$ , which can demonstrate the ratio of two shaded region (**Figure 1.6**)

$$FF = \frac{(J \times V)_{max}}{J_{sc} \times V_{oc}} \quad (\text{Eq. 1.3})$$

For standard test for solar cells, the Air Mass 1.5 global (AM 1.5G) with an incident power density of  $100 \text{ mW/cm}^2$  is used, which is also called 1 sun. In addition, the Air Mass is a measure of the atmospheric absorption of the spectral content and intensity of the solar radiation reaching the Earth's surface. The AM 1.5 is the spectrum at sea level, defining as the spectrum where the length of the actual light direction from the sun to the observer is 1.5 times the length of the shortest possible path (AM1) when the sun is exactly at the zenith ( $\Theta$ ).

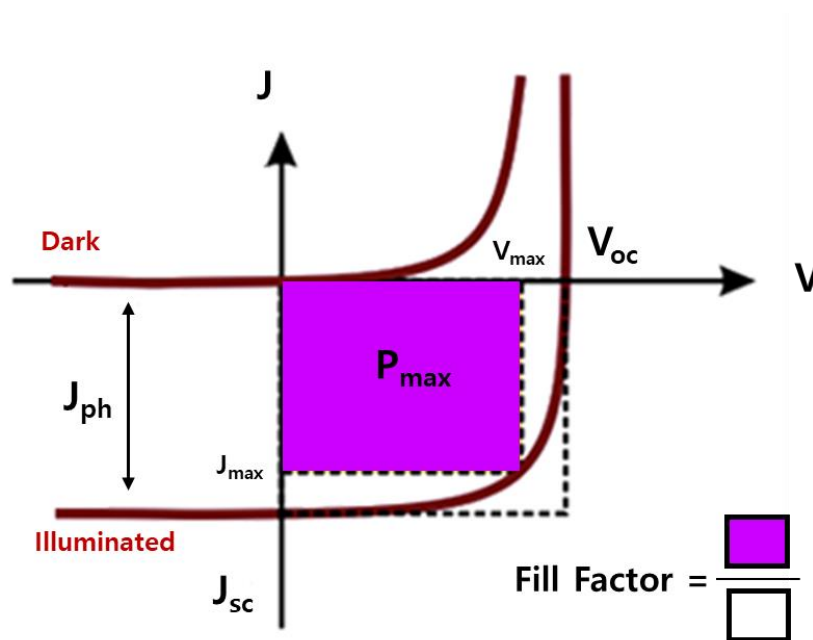


**Figure 1.6**  $J$ - $V$  curve measurement system

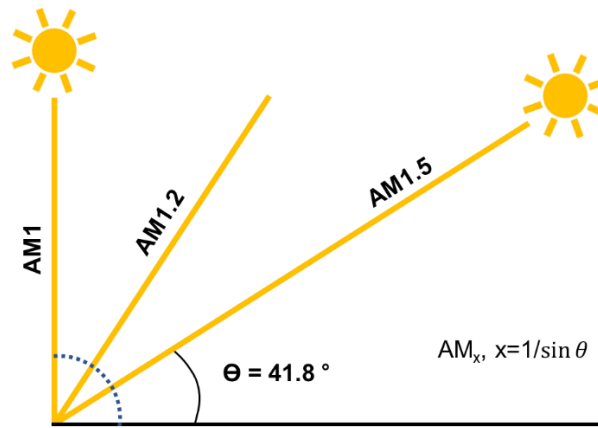


**Figure 1. 7** Solar power on earth surface depending on the angle of incident light

Equivalent circuit of solar cells is shown in **Figure 1.8**.

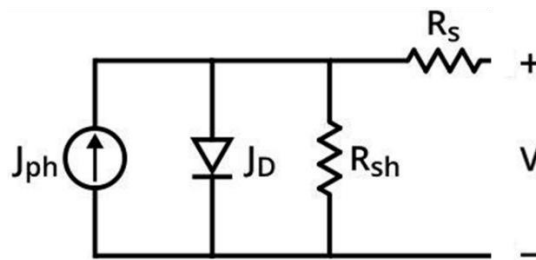


**Figure 1. 8** Equivalent circuit diagram of solar cell

The  $J$ - $V$  curves and photovoltaic parameters is related to other factors, which can be described as following **Equation 1.4**<sup>[13]</sup>.

$$J = J_0 \left\{ \exp \left[ \frac{q(V - J R_s A)}{n k T} \right] - 1 \right\} + \frac{V - J R_s A}{R_{sh} A} - J_{ph} \quad (\text{Eq. 1.4})$$

$k$  is Boltzmann's constant,  $T$  is temperature,  $q$  is elementary charge,  $A$  is device area,  $n$  is ideality factor of the diode,  $J_0$  is reverse saturation current density,  $J_{ph}$  is photocurrent,  $R_s$  is series resistance and  $R_{sh}$  is shunt resistance<sup>[14]</sup>.

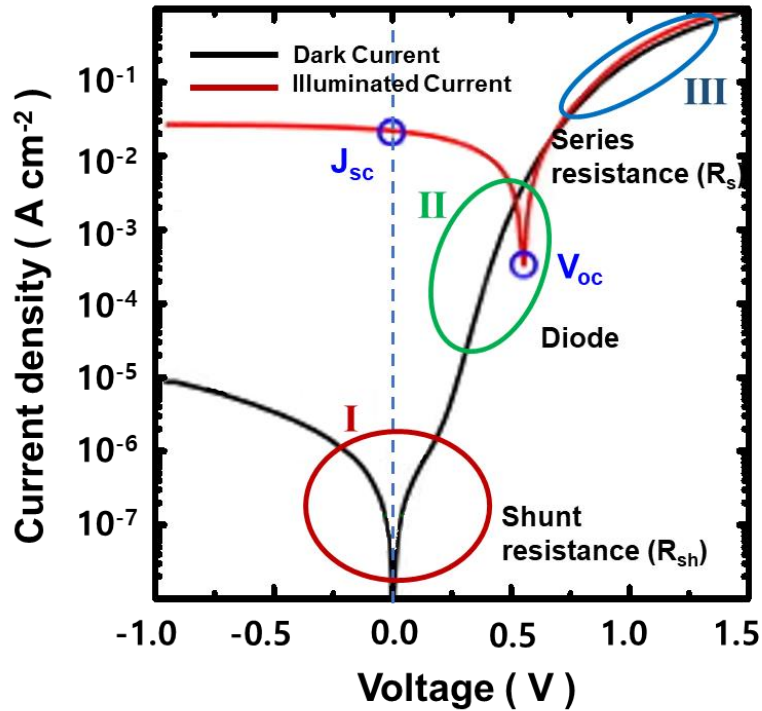


**Figure 1.9**  $J$ - $V$  curve of solar cells

As shown in **Figure 1.9**, dark  $J$ - $V$  curve can be distinct 3 regions. The first **(I)** is the linear region in negative potentials and low forward bias, the current density in this region is dominated by the shunt resistance ( $R_{sh}$ ). The shunt resistance is related to the device structure and film morphology, for instance, increased leakage current in reverse bias region is from the pinholes and recombination of charge carriers in the devices. Further, The  $R_{sh}$  needs to be maximized to reduce the energy loss caused by the current through the solar cells. The  $R_{sh}$  can be simply calculated by the slope of the  $J$ - $V$  curves in the regime near by the  $J_{sc}$ . The second **(II)** region shows an exponential behavior corresponding to the diode. The third **(III)** is another linear part in high forward bias correlating to the series resistance ( $R_s$ ). the  $R_s$  is from limited conductivity of each layers, contact resistance from photoactive layer to electrodes as well as some issues of external circuit. Higher  $R_s$  can decrease FF and  $J_{sc}$ . Typically, the  $R_s$  has no effect on  $V_{oc}$  because the entire current flows through the diode at the  $V_{oc}$  condition, but there is no current flow without  $R_s$ , the  $R_s$  can be easily calculated by slope of the  $J$ - $V$  curve in close to the  $V_{oc}$ .<sup>[14]</sup>

The ideality factor ( $n$ ) is a degree that represents how closely a diode behaves like an ideal diode and it is generally deviated from the ideal by recombination in the junction. The ideality factor ( $n$ ) can be effected by D:A morphology, phase separation and interfacial area and so on.

The reverse saturated current density ( $J_0$ ) is also a parameter to affect the  $J$ - $V$  curves in the exponential regions and corresponding device performance. The  $J_0$  is defined as how many charge carriers can pass

through the barrier in the reverse direction. These charges are considered as minority charges at the D:A interface. In a typical p-n junction,  $J_0$  can be described as following **Equation 1.5**.

$$J_0 = J_i \exp \left[ \frac{-q\Phi}{nkT} \right] \quad (\text{Eq. 1.5})$$

$J_i$  depends on material purity.  $\Phi$  is energetic barrier voltage, which was derived from good consistence with energy difference of the LUMO level of acceptor- and the HOMO level of donor polymer. The  $J_0$  depends on temperature, but it is decreasing as the increasing materials quality and energy barrier.

Through the above-mentioned  $n$ ,  $J_0$ ,  $R_s$  and  $R_{sh}$  affecting the photovoltaic parameters,  $V_{oc}$  is defined as the voltage across the device under illumination of zero current condition at which the dark current and short circuit photocurrent was exactly cancelled out.<sup>[15]</sup>

$$V_{oc} = \frac{nkT}{q} \ln \left( \frac{J_{ph}}{J_0} + 1 - \frac{V_{oc}}{J_0 R_{sh}} \right) \quad (\text{Eq. 1.6})$$

In addition, assuming  $R_{sh}$  is as high as infinity, above equation of  $V_{oc}$  can be modified to like below.

$$V_{oc} = \frac{nkT}{q} \ln \left( \frac{J_{ph}}{J_0} + 1 \right) \quad (\text{Eq.1.7})$$

The FF is highly affected by the  $R_{sh}$  and  $R_s$ . High FF can be achieved in low  $R_s$  and high  $R_{sh}$  (ideally  $R_s = 0$ ,  $R_{sh} = \infty$ ). The equation of FF is described as follows.

$$FF(R_s, R_{sh}) = FF(0, \infty) \left[ \left( 1 - \frac{J_{sc} R_s}{V_{oc}} \right) - \left( \frac{V_{oc}}{J_{sc} R_{sh}} \right) \right] \quad (\text{Eq. 1.8})$$

Incident photon-to-current conversion efficiency (IPCE), which is also called external quantum efficiency (EQE), is significantly useful to examine photocurrent in monochromatic radiation. The IPCE value is the ratio between number of electrons through the external circuit and incident photon flux.

$$IPCE = \frac{[1240 (eV \text{ nm})][\text{photocurrent density } (\mu A \text{ cm}^{-2})]}{[\text{wavelength (nm)}][\text{irradiation (mW cm}^{-2})]} \quad (\text{Eq. 1.9})$$

### 1.1.3 Device Structure and Materials

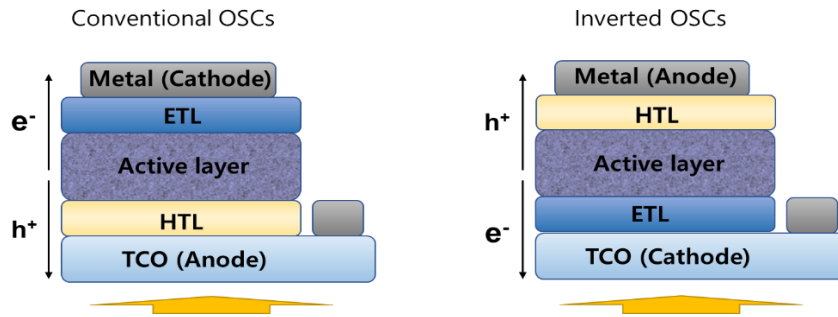


**Figure 1.10** Configurations of conventional structure OSCs and inverted structure OSCs

Two possible device architectures of OSCs are shown in **Figure 1.10**. The first structure (a) of OSCs employed transparent conductive (TCO) oxide as anode, and low work function of metal for cathode. This OSCs architecture is largely used. In another structure, the cathode and anode are exchanged in the position, which represents placement of the high work function anode at the rear of the device. OSCs include buffer layer located between photoactive layer and electrodes, primarily to obtain high charge collection and extraction resulting from appropriate positioning of energy levels. Which subsequently improves the OSCs performance and optimizing the output. Therefore, buffer layers are importance for achieving high performance of OSCs. Electron transport layers (ETLs) are used to transfer of electrons from acceptor layer and hole transport layers (HTLs) are used for hole extraction from donor layer.

#### • Transparent conductive oxide (TCO)

Optically transparent and electorally conductive oxide are typically binary or ternary compounds, including 1-2 metallic elements. Their resistivity could be lower as  $10^{-4} \Omega \text{ cm}$  and lower than 0.0001 of extinction coefficient ( $k$ ) in visible range with greater than 3 eV of optical band gap. For OSCs, Indium tin oxide (ITO) and fluorine tin oxide (FTO) are usually used. Furthermore, potential alternatives to ITO and FTO have been researched with focusing on carbon-based materials such as graphene, carbon nano-tubes (CNT), metal thin films, metal-based multilayers and so on. [16]

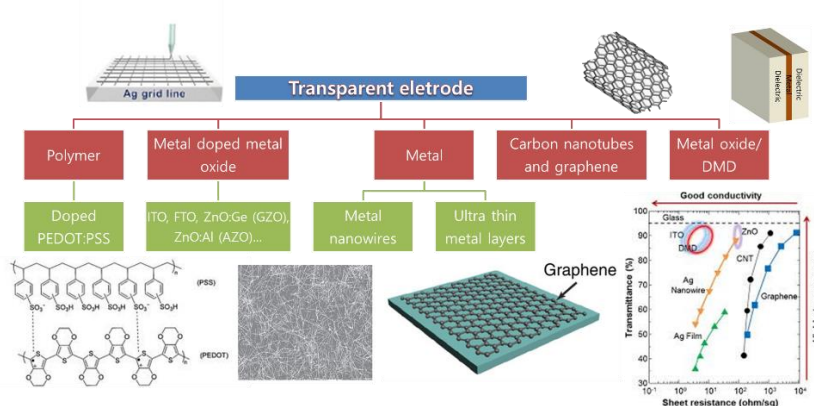


**Figure 1.11** Transparent electrodes for OSCs

• **Buffer layer: Hole transport layer (HTL) and electron transport layer (ETL)**

Buffer layers are predominantly selected on consideration of their energy levels and charge transport properties. It is used to not only engineering interface of active layer/electrodes by providing steps to reduce energy barrier, but also protection against the roughness of bottom layer as well as oxygen and water scavengers. Furthermore, buffer layer is used to be light absorption as a role of optical spacer. Typically, metal oxide-based layers are useful: ETLs ( $\text{TiO}_x$ ,  $\text{TiO}_2$ ,  $\text{ZnO}$ ,  $\text{Cs}_2\text{CO}_3$ ,  $\text{SnO}_2$  etc.), HTLs ( $\text{MoO}_3$ ,  $\text{V}_2\text{O}_3$ ,  $\text{WO}_3$ ,  $\text{NiO}$ ,  $\text{ReO}_3$  etc.). Among various buffer layers, there are special materials mainly used for OSCs fabrication as shown below. <sup>[17]</sup>

i) Poly (3,4-ethylenedioxythiophene):poly(styrene sulfonic acid) (PEDOT:PSS) is usually used as an HTL for conventional OSCs, due to lots of advantage including high transparency in the visible range, efficient hole extracting property, providing smooth surface on rough ITO surface, and aqueous processing due to PSS moiety etc. In addition, PEDOT:PSS of high work function (5.0-5.2 eV) allows to form an ohmic contact with electrons of donor polymers <sup>[18]</sup>.

ii) Molybdenum oxide ( $\text{MoO}_3$ ) is mostly used to inverted OSCs by thermal evaporated deposition as an HTL. Hole transport mechanism of  $\text{MoO}_3$  is different to that of general HTLs. Since the fermi level is quite deep, which is lower than HOMO level of donor polymers, it leads to fermi level pinning of ohmic contact at the photoactive layer/ $\text{MoO}_3$  interface.

• **Metals**

For conventional OSCs, metals of low work function (Al, Ag, Ca, Ca/Al, Ba etc.) are used for cathode to form an ohmic contact at cathode side, which requires that the work function is typically located lower than LUMO of the acceptor polymer. In contrast, metals of high work function (Pt, Au, Ag etc.) is for inverted OSCs.

• **Photoactive layer**

**Figure 1.12** shows schematic cross-section of photoactive types.

**Figure 1.12 (a)** shows that OSCs with only one conjugated polymer. Although using one conjugated polymer by combined donor unit and withdrawing unit of chemical moiety has been studied, this OSC type shows insufficient working and low performance, since exciton (bounded electron and hole) left in the LUMO band and drift is not occur in an electric field and hardly reach electrode. As a result, the geminated recombination is mainly derived instead of collection at electrodes. To avoid this problem, second semiconducting polymer with electron accepting property (acceptor, A) are incorporated. When the exciton in donor polymer is formed near the interface, the electron can move to the acceptor (**Figure 1.11 (b)**). In this case, the polymer film generally needs to be at least 100 nm thick for enough light absorption. This bilayer requires longer charge lifetime and high crystalline to overcome thick active layer for collection at electrodes. As shown in **Figure 1.12 (c)**, highly ordered donor and acceptor

domains in vertical phase will contribute to excellent charge transport, if a domain has twice width of the exciton diffusion length and efficient charge generation together. Although this type is ideal phase for OSCs, the nano-patterning technology to control film phase is challenging. A real bulk-heterojunction (BHJ) phase is shown as **Figure 1.12 (d)**, which is an useful strategy for more extensive interfaces of D:A. BHJ phase is formed by dissolving both donor and acceptor in the same solvent and casting a blend. The semi-crystalline preferential BHJ morphology by thermal annealing, additive treatment, etc. has influence on OSCs performance.<sup>[19]</sup>

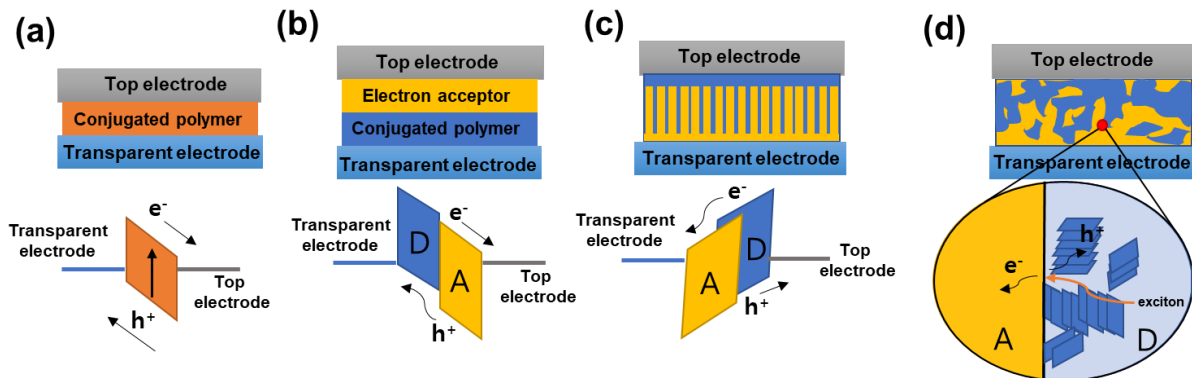


**Figure 1.12** Four device structure of conjugated polymer-based solar cells: (a) single-layer OSCs, (b) bilayer OSCs, (c) ordered BHJ OSCs, (d) disordered bulk heterojunction (BHJ) OSCs <sup>[20]</sup>

### • Tandem OSCs

One way to improve OSCs performance is through device-architectural approach. **Figure 1.11 (a)** shows general organic tandem cells.<sup>[21, 22]</sup> which is comprised of two distinct BHJ devices stacked to reduce light loss. The light can be absorbed broadly by hetero organic tandem solar cells of different bandgap of subcells. Organic tandem solar cells have two types of structure; connecting either in series or in parallel relying on property of intermediate layer and the connecting way between intermediate layer and electrodes. The series connected tandem cells is used predominantly. The energy diagram of the tandem cells is shown as **Figure 1.11 (b)**.

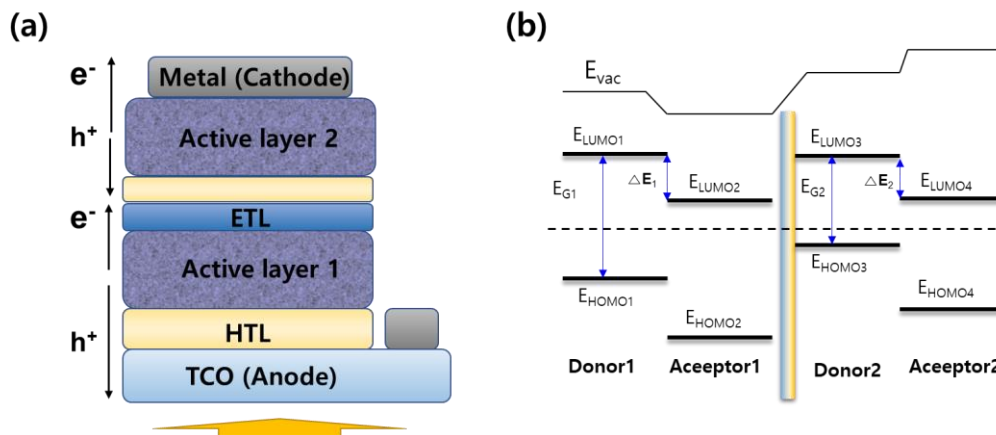


**Figure 1.13** Device structure of series organic solar cells and simplified band diagram

The intermediate layer is required the alignment of the quasi-Fermi level of the acceptor of the bottom cell and the donor of the top cell to allow the recombination of electrons and holes generated from each subcell. Therefore, the intermediate layer is also called recombination layer. According to Kirchhoff's law, this series type implies that the total voltage for whole device is equal to the sum of the voltage of each subcell:  $V_{oc\ 1} + V_{oc\ 2} + V_{oc\ 3} \dots = V_{oc\ tandem}$ , while the current is mainly determined by the smallest short circuit current of the sub-cells:  $J_{sc} = \text{Min}(J_{sc\ 1}, J_{sc\ 2} \dots)$  [23].



## 1.2 Light and Photonics

### 1.2.1 Light

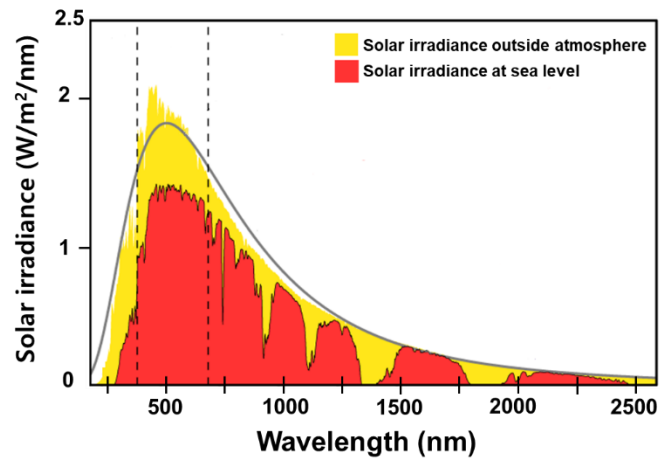


**Figure 1.14** Solar irradiance spectrum

The sun is involved in most of the energy on the earth such as hydropower by evaporation transpiration of solar radiant heat, wind power originated from rough heating of the atmosphere by the sun, fossil fuel sources from nourished organism by the sun. Notably, the sun is also responsible for photovoltaic electricity produced by sunlight. As shown in **Figure 1.13**, not all of the incident light on atmosphere arrives at the surface of earth. The atmosphere is a great absorber and block the sun energy more than 50%. The peak intensity of sunlight reaching on earth surface is about  $1000 \text{ W/m}^2$ . Which can be changed, because the sun intensity depends on weather, season and location.

Since the light is electromagnetic radiation (EM) which is combination of electric wave and magnetic wave, it propagates like waves (**Figure 1.14**). The energy arise from the waves is also absorbed like particles, which is called a photon. Nanophotonics mainly focused on the light behavior of light propagating in free space and application to either device or nanoscience technology. In this sub-chapter, the field of plasmonic with OSCs applications and Fabry-Perot interferometer of multilayer, which are the core of nanophotonics, will be introduced briefly.

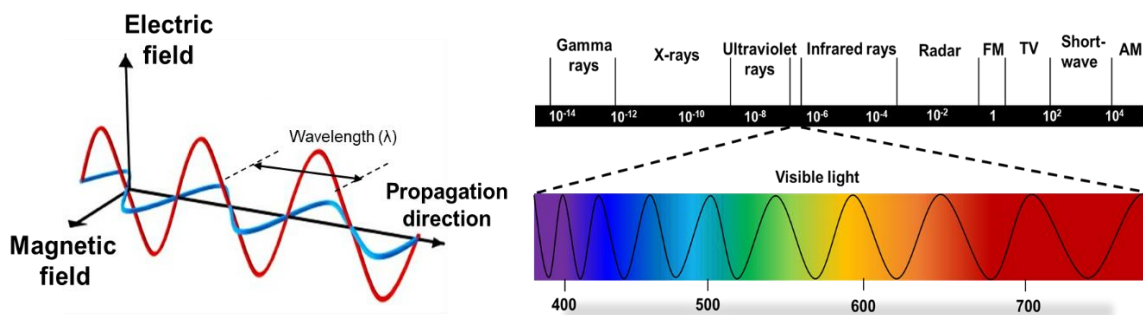


**Figure 1.15** Electromagnetic radiation and light spectrum

### 1.2.2 Localized Surface Plasmon Resonance (LSPR)

The field of plasmon can be divided into two parts: surface plasmon polaritons (SPPs) and localized surface plasmon resonances (LSPRs). SPPs is a propagation derived by coupling of electrons of conductor metals and dispersive electromagnetic waves, its propagation length is confined to the losses in the metal and usually in range of from less than a micrometer to a few micrometers. SPP is generated in metallic nanoparticles (NPs), but has limited free propagation [24, 25]. In contrast, LSPRs, the resonant photon-induced collective oscillations of electrons of metal nanoparticles (NPs) and the radiation into the surrounding dielectric, are confined to not only the NP geometry including metal kinds, sizes and shapes but also surrounding media (Figure 1.15).

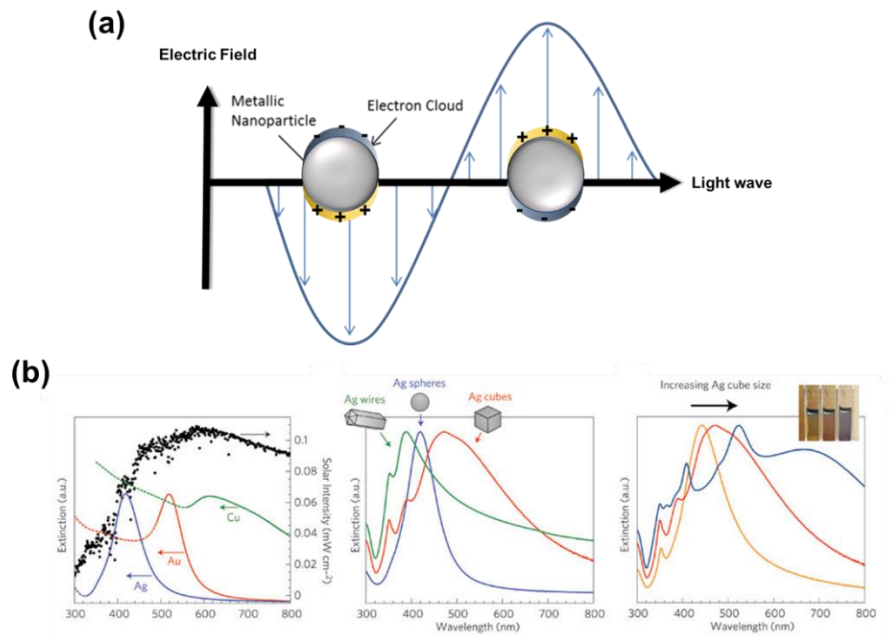


**Figure 1. 16** (a) Plasmon resonance of metallic nanoparticle (b) plasmon peaks depending on metal kinds, shape and size.

- Theoretical description: Mie theory

Rigorously, LSPRs requires a multipole expansion of the metallic NPs in the electric field resulting superposition of plasmon modes generated at a given certain frequency. However, it is simplified with assuming that the multipole expansion originated from the only excited mode. Mie theory is one of numerical methods about model the LSPRs of metallic NPs.

The Mie modeling is for particles of spheroidal shape and the Mie formalism shows extension from NPs smaller than the light wavelength ( $\lambda$ ) to aggregates of particles with involving the Rayleigh approximation which is called dipole or quasi-static. This Mie modeling is useful into LSPR study by providing relatively simple formulae and reasonable parameters. The modeling equation is like below

$$\alpha(\lambda) = 4\pi\epsilon_0 R^3 \left| \frac{\epsilon(\lambda) - \epsilon_m(\lambda)}{\epsilon(\lambda) + 2\epsilon_m(\lambda)} \right| \quad (\text{Eq. 1.10})$$

where  $\epsilon_0$  is the vacuum permittivity,  $R$  is the particle radius,  $\epsilon_m$  is surrounding medium permittivity. From  $\epsilon = \epsilon' + i\epsilon''$  of the complex relative permittivity of NP, LSPR absorbance can be arranged like **Equation 1.11**.

$$\alpha(\lambda) \propto \frac{\epsilon_m^{3/2} R^3}{\lambda} \frac{\epsilon''}{(\epsilon' + 2\epsilon_m)^2 + \epsilon''^2} \quad (\text{Eq. 1.11})$$

The LSPR absorbance is expressed that first term is scattering related  $1/\lambda$  dependence and the second term is independent on the dielectric constants of metal and medium.

The efficiency of the absorption /scattering (cross-section) are given by:

$$\sigma_{sca} = \frac{k^4}{6\pi\epsilon_0^2} |\alpha(\lambda)|^2, \quad \sigma_{abs} = \frac{k}{\epsilon_0} \text{Im}[\alpha(\lambda)] \quad (\text{Eq. 1.12})$$

The resonance condition in zero of second term denominator is that  $\epsilon' = -2\epsilon_m$ , which shows dramatically generated resonance at the peak in plasmon absorbance.

#### • Plasmon resonance in OSCs

Plasmonic can be derive typically three ways to organic solar cells to keep the physical thickness of thin photoactive layer. Firstly, metallic nanoparticle (NPs) can offer subwavelength scattering and trapping the freely propagating waves from the light into thin film, which enhances OSCs performance by providing effective optical path length in the device (**Figure 1.16 (a)**). Second, LSPR of metallic nanoparticle can be used by light trapping of the excited particles near-field, like subwavelength antennas (**Figure 1.16 (b)**). This way increases the substantial cross-section absorption of the photoactive layer at certain wavelength. Thirdly, surface of grating patterned metallic films behind the photoactive layer is feasible to generate SPP modes at the metal/semiconductor interface and guided modes of converting to photocarriers of photons (**Figure 1.16 (c)**). To enhance the OSCs performance by increasing absorption in range of longer wavelength, metallic nanoparticles with various shape and size, alloy two metal composites have been applied to OSCs. Furthermore, to prevent quenching site of metal surface occurring charge recombination in photoactive layer, core-shell types of metal nanoparticle also have been reported <sup>[26] [24]</sup>.

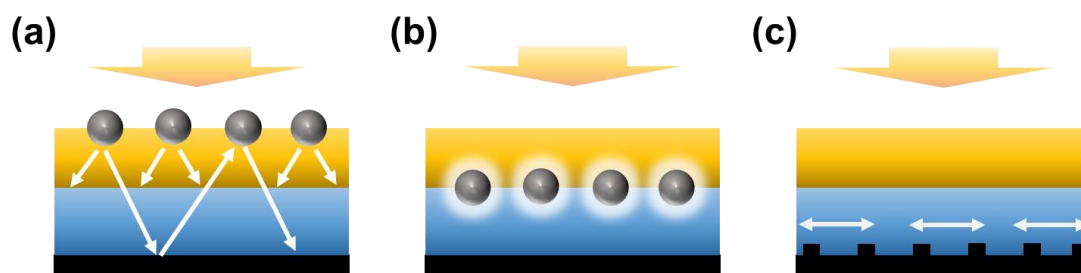


**Figure 1.17** (a) Light trapping by (a) scattering for presence of metal nanoparticles, (b) by the excited particles near-field and (c) by SPP at metal/semiconductor interface

### 1.2.3 Optical Interference in Multi-Films

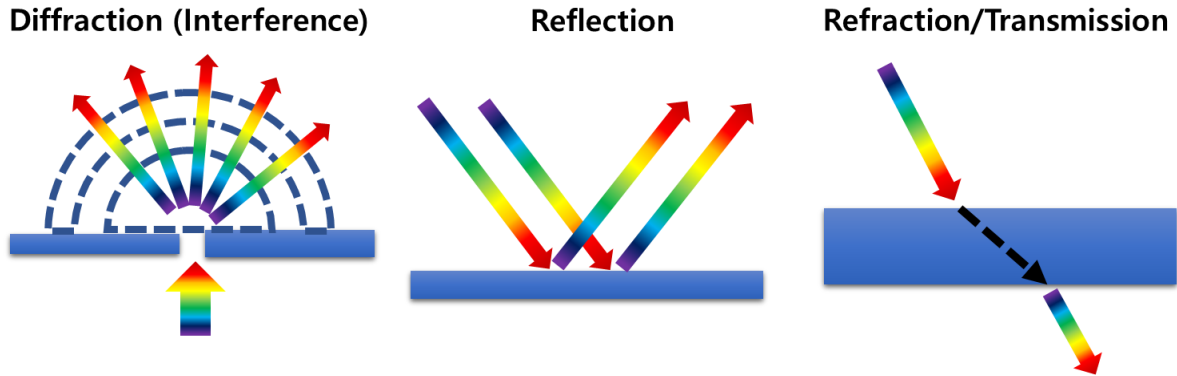


**Figure 1. 18** Illustrated light manipulation: diffraction, reflection, and refraction

Application of multilayers with multiple wave interference is important ways to light manipulation in photonic research including quantum optics and optoelectronic devices. Figure 1.17 shows several basic phenomena of light manipulation. Diffraction is represented as the bending of waves around the edge of an obstacle, also defined as the optical wave interference according to the Huygens-Fresnel principle. The optical interference is defined that two or more light waves matching in the same space at a time form larger or smaller amplitude of wave, which is called constructive interference and destructive interference, respectively. This diffraction with optical interference contributes to other light phenomena. Light reflection is the varying in way of a certain wavefront at an interface between two different media (media have different refractive indices), therefore, the wavefront returns to the original media. Light refraction is an optical passing from one medium to another media. In detail, it means change of wavelength together angle at the interface between two different media arise from different wave phase speed. Where, the refractive index ( $n$ ) is greatly used than the wave phase speed, it is related the light speed in vacuum ( $c$ ).

$$n = c/v \quad (\text{Eq. 1.13})$$

In addition, the law of refraction is like as

$$n_1 \sin \theta_1 = n_2 \sin \theta_2 \quad (\text{Eq. 1.14})$$

- Metal oxide/metal/metal oxide (OMO) multilayer electrodes

One promising optical multilayer as an electrode for OSCs is metal-dielectric multilayer structure. Notably, the transparent multilayer by controlling the light phase by refractive index of materials can be used for electrode of transparent OSCs with building integrated photovoltaics (BIPV). Typically, the refractive indices and the thickness of films can control the optical phase to non-reflection condition. metal oxide/metal/metal oxide structure is also called dielectric/metal/dielectric (DMD) structure. The Admittance diagram is useful to calculate and obtain minimum reflection and maximum transmittance at a certain optical wavelength as shown in **Figure 1.18**. Admittance is the ratio of electric field and

magnetic field of light. Admittance plot begins from the real axis at  $n_s$  of refractive index of the substrate at a wavelength ( $n_s, 0$ ). Depositing dielectric layer like metal oxide, which has thickness  $d$ , refractive index ( $n_d$ ), in without absorption losses, the trace of admittance starts on a circular locus in direction of clockwise until the trace arrives the real axis again ( $n_d/n_s, 0$ ) with intersecting of  $n_d d = \lambda/4$ . When a further transfer of the dielectric layer by increasing thickness is  $n_d d = \lambda/2$ , the trace goes back to starting point ( $n_s, 0$ ) with showing the circle (**Figure 1.18 (a)**). Secondly, at a metal layer of optical constants  $n_m = (n_m, k_m)$  and  $n_m < k_m$  on the substrate, the admittance transfers clockwise from ( $n_s, 0$ ) and arrives the  $\text{Im}(Y)$  axis at  $-k_m$ . Because the metal has an imaginary term in the refractive index (**Figure 1.18 (b)**). Lastly, in combination of two dielectrics and metal as sandwich structure, the thickness of each layers offers tails and have influence on beginning point for each layer's trace. The entire stack is implemented to arrive air admittance condition ( $n_{\text{air}}, 0$ ). The admittance of the air (1.0) has the reflection close to zero and high transmittance. The entire film reflection can be calculated with an admittance formula. [27] [28]

$$Y = \frac{\cos\delta Y_{\text{sub}} + i n_f \sin\delta}{\cos\delta + i \frac{\sin\delta}{n_f} Y_{\text{sub}}}, \quad Y = H/E = N y_0 \quad (\text{Eq. 1.15})$$

Where  $H$  is magnetic field,  $E$  is electric field,  $N$  is complex refractive index of film,  $y_0$  is vacuum admittance ( $= \sqrt{\epsilon_0/\mu_0}$ ), and  $\delta$  is optical phase thickness, respectively.

$$\delta = \frac{2\pi}{\lambda} N d \cos\theta \quad (\text{Eq. 1.16})$$

Where  $d$  is the thickness of film,  $\lambda$  is wavelength,  $\theta$  is angle of incident light, respectively.

$$R = \left| \frac{Y_{\text{air}} - Y}{Y_{\text{air}} + Y} \right|^2 \quad (\text{Eq. 1.17})$$

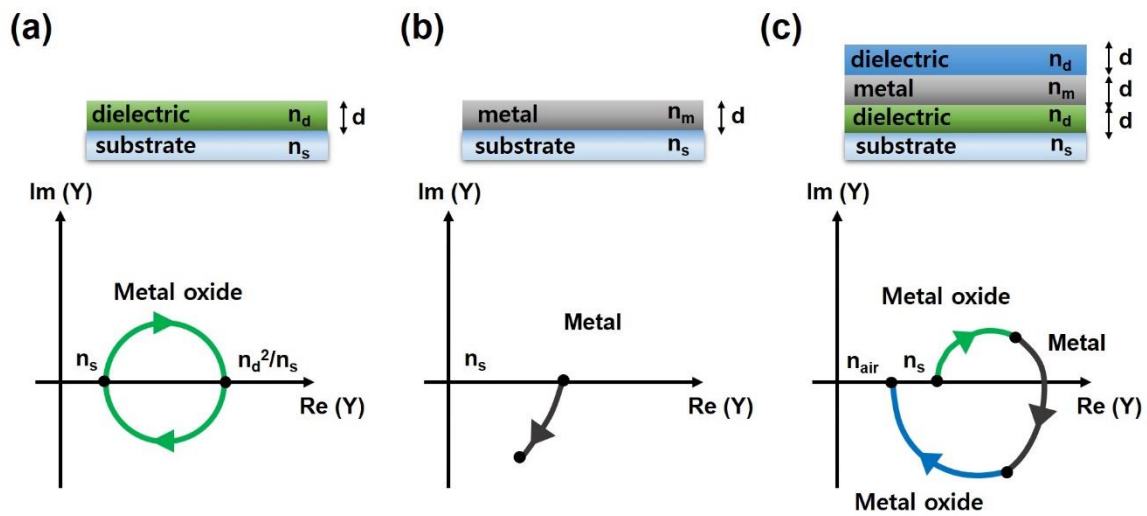


**Figure 1.19** Admittance plots for (a) dielectric case, (b) metal case and (c) combination case

• **Metal /metal oxide/metal (MOM) multilayer-based color filter**

The Metal/metal oxide/metal (MOM) multi-deposited structure for color filter effect is also called metal/dielectric/metal (MDM) layer, Fabry-Perot etalon. This approach of structural colors is based on Fabry-Perot interferometer, which consists of two parallel metallic surface and transparent dielectric as a cavity layer, like sandwich structure. At a certain optical wavelength, constructive interferences are generated in transparent dielectric layer, showing transmission of a certain wavelength through bottom metal layer like monochromatic light and reflection peak on the top metallic surface. The reflected color of yellow, magenta and cyan is corresponds to the transmitted color of blue, green and red, respectively. Hence, this MOM filters have been used to obtain selective transmission or reflection of a certain parts in visible light. The dielectric material of high refractive index can reduce refraction with leading strong interference based on nanocavities and SPP resonances in metallic surface. Generally silver (Ag) has been used as the reflecting mirrors in MOM structure, since Ag film has high reflection in range of visible frequencies. The optical transmission of the MOM structure is described in following equations.

$$T = \frac{(1-R)^2}{[1+R^2-2R\cos\delta]} \quad (\text{Eq. 1.18})$$

Where,  $\delta$  is the total phase in the cavity and R is the reflectivity at interface of metal and dielectric layer.  $\delta$  is given by

$$\delta = \frac{4\pi n_d t_d}{\lambda - 2\phi} \quad (\text{Eq. 1.19})$$

Where,  $\phi$  is the phase shift of the reflection at interface,  $n_d$  is refractive index,  $t_d$  is the the thickness of the cavity. A transmission peak generated at a certain resonance wavelength for  $\phi$  of  $2m\pi$ , where  $m$  an integer is the mode related the order of the resonance. The corresponding wavelength of resonance is defined by

$$\lambda_m = \frac{4\pi n_d t_d}{(m\pi + \phi)} \quad (\text{Eq. 1.20})$$

The optical reflection of the MOM structure arising from  $T+R=1$  is described in following equations.

$$R = \frac{2(1-R)(1-\cos\delta)}{1+R^2-2R\cos\delta} \quad (\text{Eq. 1.21})$$

Color of MOM multilayer can be tuned by either thickness or refractive index of cavity layer.

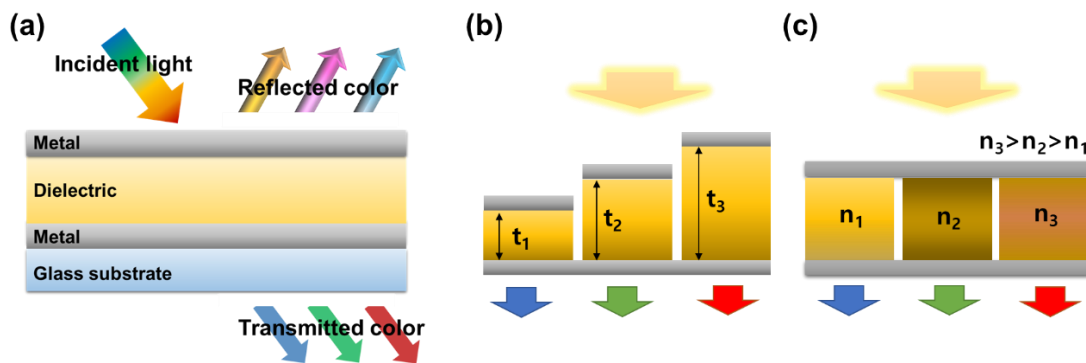


**Figure 1. 20** (a) Schematic MOM structure and color filter depending on (b) thickness and (c) different refractive indices

The nanophotonics such as plasmon resonance, film interference, anti-reflection films and color filter is very useful to optoelectronics. These light manipulations will offer substantial strategies for OSCs development because the light is essential in solar cells, resulting in semitransparent OSCs.

I have highlighted the combination of OSCs and nanophotonic of plasmon resonance based on metallic NPs, film interference and color filtering structure, and tried to use the given incident light to OSCs with reducing light loss.

## Chapter 2. Optically Tunable Plasmonic 2-Dimensional Ag Quantum Dot Arrays for Optimal Light Absorption in Polymer Solar Cells

### 2.1 Research Background

The utilization of localized surface plasmon resonance (LSPR) phenomena has attracted a lot of interest as a feasible approach for the enhancement of optoelectronic device performance [29]. LSPR is attributed to the resonant coupling between incident photons and a collective oscillation of the conduction electrons at a specific plasma frequency in metal nanoparticles. Since this resonance enhances the absorption and scattering of light at a resonant wavelength, LSPR constitutes a useful strategy to improve the performance of polymer solar cells (PSCs) [30]. Although the active layers in PSCs offer unique advantages such as light-weight, mechanical flexibility, solution-processability, and large-area processability with low cost, their thicknesses are typically close to 100 nm thick and rarely more than 300 nm, resulting in limited absorption of photons compared to other next-generation solar cells. Under this constraint, LSPR by metal nanoparticles scatter light at the resonant wavelength within the active layer, increasing the effective optical path length and leading to higher photon absorption efficiency in the device. There have been many reports demonstrating the ability to control the plasma frequency of metal nanoparticles by changing the composition, size, and shape, [31] however, tuning the optical properties of the surrounding medium has not yet been explored as a method to control LSPR properties in solid state.

In 1908, Gustav Mie discovered an exact solution to Maxwell's system of equations for a homogeneous metallic sphere. According to his solution, the plasma frequency of the metallic sphere can be tuned by varying the complex dielectric function of surrounding medium. Complex dielectric functions and the complex index of refraction obey the following relationships

$$\varepsilon = \varepsilon' + i\varepsilon'' = (n + ik)^2 = (n^2 - k^2) + i(2nk) \quad (\text{Eq. 2.1})$$

where  $\varepsilon'$  and  $\varepsilon''$  represents real and imaginary part of the dielectric function, respectively, while  $n$  and  $k$  denote the real and imaginary parts of the complex index of refraction, respectively. Because  $k$  indicates the attenuation of the propagating electromagnetic (EM) wave in a medium, the plasma frequency of metal nanoparticles embedded in a transparent medium depends predominantly on the  $n$  value of the medium. [32]

In this letter, for the first time, we demonstrate that the refractive index of the medium surrounding 2-dimensional Ag quantum dot arrays (2D Ag QAs) can be used to tune the LSPR peak for use in PSCs. 2D Ag QAs were synthesized using block copolymer micelle lithography (BCML) to obtain a clear resonant wavelength and highly uniform arrays. ZnO and TiO<sub>2</sub> were chosen as low and high refractive



index media, respectively, to surround the 2D Ag QAs. ZnO and TiO<sub>2</sub> are both well known as effective ETLs which have very similar effects on the electronic band structure of polymer solar cells. They possess similar band gaps and material properties and differ mainly in their refractive indices, which allows us to isolate how the change in refractive index influences plasmonic and device properties in real devices. In this way, the LSPR peak shift of 2D Ag QAs embedded in ZnO and TiO<sub>2</sub> was analyzed by both experiment and theory, considering the plasmon coupling, size dependent damping constant, and nonlocal response, which also have not been reported so far. In addition, we show that the enhanced  $J_{SC}$  of PCSs arises from the radiation of light via LSPR enhanced EM waves in the far-field region. External quantum efficiency (EQE) spectra of 2D Ag QAs incorporated PSCs in both ZnO and TiO<sub>2</sub> ETLs are in good agreement with the measured and simulated extinction spectra.

## 2.2 Experimental

### 2.2.1 2D Ag QAs Fabrication.

2D Ag QAs were fabricated by block copolymer micelle lithography (BCML). Polystyrene-*block*-poly(2-vinylpyridine) (PS-*b*-P2VP) block copolymers (purchased from Polymer source) with molecular weights of 417 kg/mol ( $M_n^{PS} = 325$  kg/mol,  $M_n^{P2VP} = 92$  kg/mol), 214 kg/mol ( $M_n^{PS} = 172$  kg/mol,  $M_n^{P2VP} = 42$  kg/mol), 265 kg/mol ( $M_n^{PS} = 133$  kg/mol,  $M_n^{P2VP} = 132$  kg/mol), 428 kg/mol ( $M_n^{PS} = 213$  kg/mol,  $M_n^{P2VP} = 215$  kg/mol), 793 kg/mol ( $M_n^{PS} = 440$  kg/mol,  $M_n^{P2VP} = 353$  kg/mol) were used. These copolymers were dissolved in toluene (0.5 wt% solution) as the precursor solutions. Then, silver nitrate (AgNO<sub>3</sub>) was added to the precursor solutions with a molar ratio of 0.5 (Ag<sup>+</sup> ions / vinylpyridine repeat unit) and stirred overnight at room temperature. The precursor solutions were spin-cast on cleaned ITO substrates at 3000 rpm for 40s, then exposed to hydrogen (H<sub>2</sub>) plasma for 3 minutes to etch the polymer template.

### 2.2.2 Polymer Solar Cells Fabrication and Characterization.

Polymer solar cells were fabricated with an inverted configuration of ITO glass/2D Ag QAs/ZnO NPs or TiO<sub>2</sub> NPs/PTB7:PC<sub>71</sub>BM/MoO<sub>3</sub>/Ag, where ZnO NPs and TiO<sub>2</sub> NPs were synthesized following protocols reported elsewhere. The thicknesses of electron transfer layers were measured by profilometry. Patterned indium tin oxide (ITO) coated glass substrates were cleaned by ultrasonication using detergent, distilled water, acetone and isopropanol and dried in an oven overnight at 100 °C. After application of 2D Ag QAs (described above), ZnO NPs or TiO<sub>2</sub> NPs were spin coated at 3000 rpm or 1500 rpm for 40s on top of patterned 2D Ag QAs, and baked at 100 °C for 10 min or 150 °C for 30 min, respectively. Photoactive layers were spin-cast from solutions containing a blend of PTB7:PC<sub>71</sub>BM dissolved in chlorobenzene (CB) solvent at a concentration of 12 mg/ml with additional (3% v/v) diiodooctane (DIO) as a solvent additive. After drying, MoO<sub>3</sub> (5 nm) and Ag (85 nm) anodes were sequentially deposited on top of the active layers by thermal evaporation under high vacuum (< 10<sup>-6</sup> Torr).

### 2.2.3 DDA Method and Quantum Effects

Discrete Dipole Approximation (DDA) is a method to calculate the optical properties of an arbitrarily shaped target material, which is partitioned into a finite array of dipole points. To set appropriate dipole spacing, the criterion of  $|m|kd < 1$  must be satisfied, where  $|m|$  is the modulus of complex refractive index,  $k$  is the reciprocal value of the incident wavelength, and  $d$  is the dipole spacing. For the DDA calculations, we used the DDSCAT program (ver 7.3.0) [33]. The dielectric functions of ITO, ZnO, and TiO<sub>2</sub> were taken from Sopra N&K Database (Sopra Group, Belfast, Ireland), literature, and our own experimental measurements, respectively. The dielectric function of silver was determined as a function of quantum dot radius, since quantum effects became significant as the size of the metal nanoparticles approached the mean free path length of conduction electrons in the bulk metal. Also, intrinsic size and nonlocal effects were considered in this work. In order to apply these two quantum effects, we used the modified dielectric function of bulk metals as follows,

$$\varepsilon(k, \omega, R) = \varepsilon_{bound-electrons}(\omega) + \varepsilon_{free-electrons}(k, \omega, R) \quad (\text{Eq. 2.2})$$

The first term includes the interband transition from  $d$ -band to the conduction  $sp$ -band. However, when the radius of the metal nanoparticle is over 1 nm, this term becomes independent of the size. Hence, the quantum effects were not included in the first term and the bulk dielectric function of bound-electrons, taken from Palik's handbook, was used. But for the second term, the Drude-Sommerfeld model including the intrinsic size and nonlocal effects was used as follows,

$$\varepsilon_{free-electrons}(k, \omega, R) = 1 - \frac{\omega_p^2}{\omega(\omega + i\gamma_{free}(R)) - \beta^2 k^2} \quad (\text{Eq. 2.3})$$

where  $\omega_p$  is the bulk plasma frequency, which was  $1.36 \times 10^{16}$  Hz and  $\gamma_{free}$  is the damping constant for conduction electrons. The intrinsic size effect was implemented by adding the size-dependent term as follows, [34]

$$\gamma_{free}(R) = \gamma_{bulk} + C \frac{v_F}{R} \quad (\text{Eq. 2.4})$$

where  $v_F$  is the Fermi velocity,  $R$  is the radius of the particle, and  $C$  is a constant related to electron scattering. The values of  $\gamma_{bulk}$ ,  $v_F$  [35] and  $C$  were  $1.36 \times 10^{13}$  Hz,  $1.39 \times 10^{15}$  nm/s and 0.75, respectively. The  $\beta^2 k^2$  term represents the nonlocal effect, [36] where  $k$  (i.e. wave vector) is  $2\pi/b$  ( $b$  is the particle size), and  $\beta^2$  is  $Av_F^2 / DAv_F^2 / D$  ( $D$  is the dimension of the target structure and  $A = 1$  for low frequencies and  $A = 3D/(D+2)$  for high frequencies). The values of  $D$  and  $A$  were set to be 3 and 1.8, respectively, in this work.

### 2.2.4 Model Systems

We considered three model systems to investigate key factors, which affected the performance of PSC devices. First, to calculate optical properties (i.e. extinction spectra), model systems were constructed using Ag quantum dots with 10 nm diameter on top of ITO substrates with dimensions of  $58 \text{ nm} \times 58 \text{ nm} \times 11 \text{ nm}$ , and 20 nm (30 nm) thick ZnO (TiO<sub>2</sub>) ETLs (**Figure 2.1 (a)**). Second, to calculate the spatial distribution of the electric field (to observe the near-field effect), a 90 nm thick PTB7:PC<sub>71</sub>BM active layer was added to the previously described model system (**Figure 2.1 (b)**). To calculate the far-field scattering, we assigned Ag quantum dots as the main scattering object and changed the medium according to the corresponding ETL's refractive index (i.e. ZnO and TiO<sub>2</sub>) as shown in **Figure 2.1 (c)**. Periodic boundary conditions were applied to implement an infinite array into all systems. The ambient medium was air for the model systems used to obtain the optical properties and the near-field enhancements. For the far-field scattering calculation, the ambient medium was ZnO or TiO<sub>2</sub>. The dipole spacing ( $d$ ) was set to 1 nm for all systems.

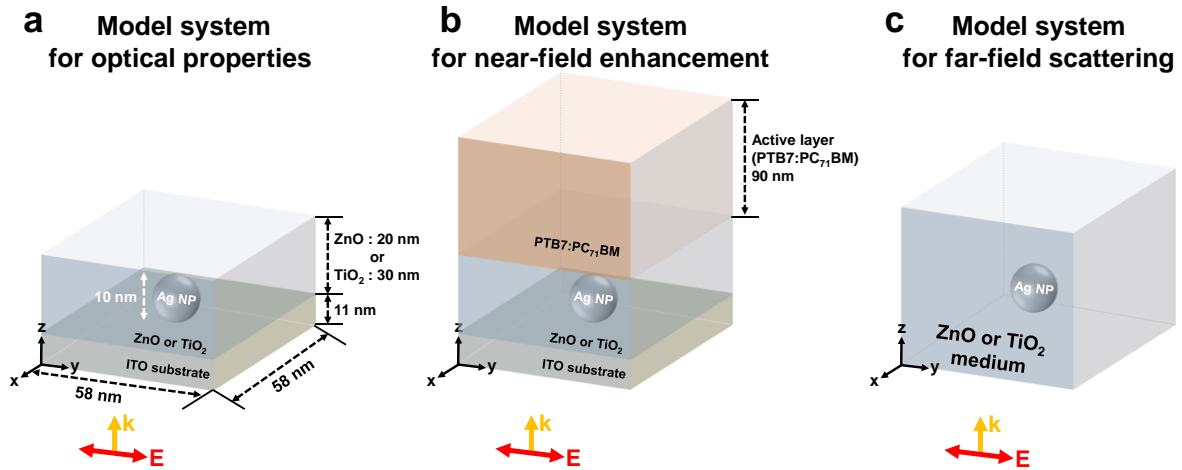


**Figure 2. 1** Model systems used in the DDA calculation. (a) Model system for calculating the extinction spectra in ZnO or TiO<sub>2</sub> layer systems, which consisted of a total of 104,284 or 137,924 dipoles, respectively. (b) Model system used for calculating the near-field enhancement (i.e. electric field contour plot). An active layer (i.e. PTB7:PC<sub>71</sub>BM) was added to the model system in (a), which consisted of 407,044 dipoles for the ZnO layer system and 440,684 dipoles for the TiO<sub>2</sub> layer system, respectively. (c) Model system for calculating the far-field scattering of 2-dimensional Ag quantum dot arrays, which consisted of 552 dipoles in an infinite ZnO or TiO<sub>2</sub> medium.  $E$  (red arrows) and  $k$  (orange arrows) indicate the directions of electric field and incident light, respectively. Periodic boundary conditions (PBCs) in  $x$ - and  $y$ -axis directions were applied in all systems.

## 2.3 Results and Discussion

### 2.3.1 Silver Quantum Arrays through Block Copolymer Micelle Lithography

Prior to the application of 2D Ag QAs into PSCs, it is necessary to optimize both the size of quantum dots and dot-to-dot spacing. Excessively large metal particles ( $> 30$  nm) may, for example, have an influence on the internal quantum efficiency (IQE) of the device arising from direct contact between photogenerated excitons and the metal. Additionally, excessively dense 2D Ag QAs can reduce the transmittance of light through the transparent substrate. For these reasons, BCML was carried out to achieve optimal quantum dot size and spacing. This method allows accurate control of the size of the quantum dots with a narrow distribution of particle diameters, while also allowing control of the density of quantum dots by varying the molecular weight of the block copolymers that are utilized as soft templates. <sup>[37]</sup>

In this work, polystyrene-*block*-poly(2-vinylpyridine) (PS-*b*-P2VP) block copolymers were used for BCML. A 0.5 wt% solution of PS-*b*-P2VP was prepared in toluene, which is a selective solvent for hydrophobic PS blocks, leading to the formation of a micellar structure with P2VP cores and PS coronas. AgNO<sub>3</sub> was added to the polymer solution with a molar ratio of 0.5 Ag<sup>+</sup> ions per vinylpyridine repeat unit. The solution was then stirred thoroughly for selective penetration of Ag<sup>+</sup> ions into the P2VP micellar cores. Ag<sup>+</sup> incorporated polymer micelle solutions were spin-cast onto ITO glass substrates, followed by removal of the polymer templates by hydrogen (H<sub>2</sub>) plasma treatment to yield reduced 2D Ag QAs. We prepared 2D Ag QAs using 214k (PS 172k-P2VP 42k) PS-*b*-P2VP resulting in an average particle diameter of  $10 \pm 2$  nm and a dot-to-dot spacing of  $48 \pm 2$  nm, as shown in scanning electron microscopy (SEM) images (**Figure 2.2**). A summary of intrinsic properties, SEM image statistics and transmittance spectra of 2D Ag QAs as a function of the molecular weight of PS-*b*-P2VP polymers are summarized in **Figure 2.3** and **Table 2.1**.

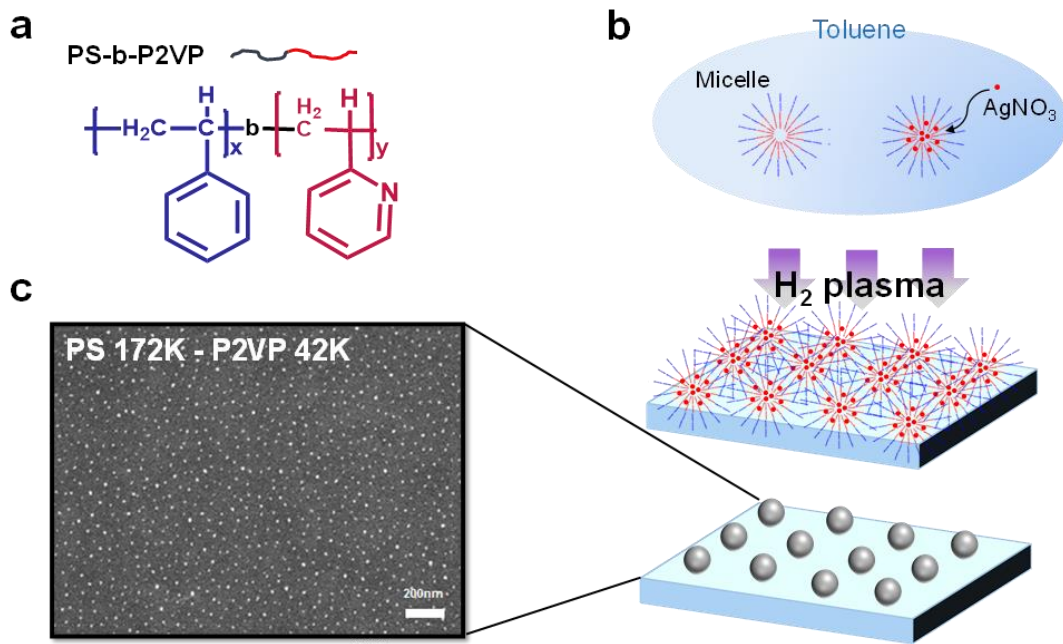


**Figure 2. 2** (a) Chemical Structure of the Polystyrene (Blue) and Poly-2-vinylpyridine (Red) Block Copolymer Molecule; (b) Schematic View of the Fabrication of 2D Ag QAs via BCML; (c) SEM Image of 2D Ag QAs Using PS (172000)-b-P2VP (42000) Block Copolymer on an ITO Substrate. The scale bar is 200 nm.

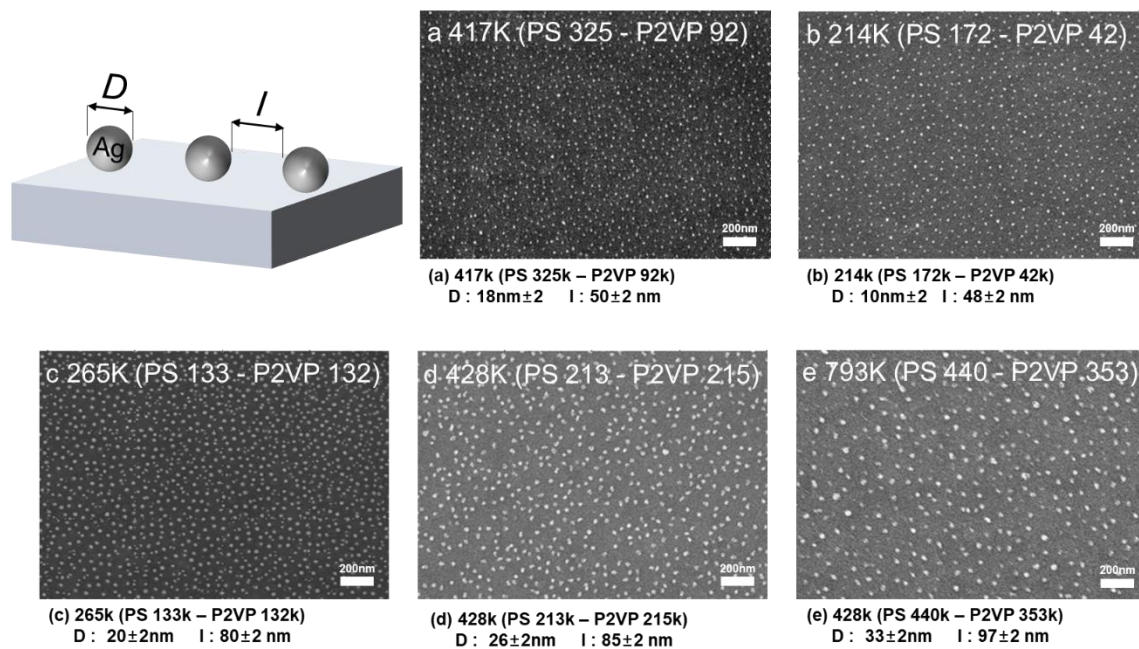


**Figure 2. 3** Comparison of 2-dimensional Ag quantum dot arrays using block copolymer micellar lithography (BCML): (a)-(e) SEM images of Ag quantum dot patterns on ITO substrates prepared using different block copolymers. The measured interval distances and quantum dot diameters are noted as I and D, respectively, below each image.

**Table 2. 1** Number-average molecular weights and polydispersities of block copolymers compared to sizes, interval distances and PSCs performance of 2-dimensional Ag quantum dot arrays with various geometric conditions

<b>BCP</b>	<b>PS (Mn kDa)</b>	<b>P2VP (Mn kDa)</b>	<b>PDI (Mw/Mn)</b>	<b>Average size of Ag-dot (nm)</b>	<b>Average distance between Ag dots (nm)</b>
A	325	92	1.06	18±2	50±2
B	172	42	1.08	10±2	48±2
C	133	132	1.15	20±2	80±2
D	213	215	1.29	26±2	82±2
E	440	353	1.19	33±2	97±2

### 2.3.2 Computational Analysis for Ag QAs

To characterize the optical properties inherent to synthesized 2D Ag QAs, we performed UV-vis absorption measurements. For the UV-vis measurements, 2D Ag QAs on ITO coated glass substrates were covered with ZnO or TiO<sub>2</sub> layers (**Figure 2.3 (a)**). Each metal oxide layer was spin-cast using nanoparticles which were prepared following procedures reported elsewhere <sup>[38]</sup>. **Figure 2.3 (b)** shows the simulated extinction spectra for two 2D Ag QAs samples embedded in ZnO and TiO<sub>2</sub> media. The LSPR extinction peak for ZnO covered 2D Ag QAs occurs at 480 nm wavelength, while the peak for TiO<sub>2</sub> covered 2D Ag QAs exhibits a bathochromic shift of 40 nm. The higher refractive index of the TiO<sub>2</sub> layer relative to the ZnO layer clearly resulted in a bathochromic shift of the LSPR of the nanoparticles, consistent with Mie's theory.

To confirm experimental observations, we performed DDA calculations. Before performing the calculations, one critical issue was considered, which is whether the quantum confinement effects significantly affected the properties of the small-sized metal nanoparticles used in this study. In previous studies, quantum effects have been neglected in the context of polymer solar cells due to the large size of metal nanoparticles (i.e., diameter >20 nm). However, in our system, the size of Ag quantum dots was 10 nm. In general, when the diameter of metal nanoparticles is less than 20 nm, quantum effects appear which affect LSPR properties. Considering quantum effects such as spatially nonlocal response of polarization and size dependent damping effects in our 10 nm Ag quantum dots, we implemented the hydrodynamic Drude model in DDA calculations to calculate the extinction spectra (**Figure 2.3 (c)**). The results were consistent with the measured UV-vis absorbance, as shown in **Figure 2.3 (b)**. Furthermore, when we compared the extinction spectra including the quantum effects (**Figure 2.3 (c)**) to nonquantum effects (**Figure 2.4**), the overestimated extinction spectra of ZnO and TiO<sub>2</sub> layers below 500 nm wavelength were reduced and subpeaks, which appeared over 550 nm wavelength, were smoothed out. These results indicated that quantum effects in 10 nm Ag quantum dots are ineluctable and must be dealt with to accurately model this system. Next, to verify the effect of plasmon coupling between Ag quantum dots in 2D Ag QA systems, we calculated the extinction spectra of isolated Ag quantum dots, which consisted of one Ag quantum dot and compared this to an infinite array as shown in **Figure 2.5**. The isolated Ag quantum dot system showed a sharp extinction peak at its characteristic resonance wavelength, consistent with previously reported results from a number of plasmonic research studies. In contrast, the arrayed Ag quantum dots exhibited a broad resonance peak with a bathochromic shift of  $\sim 30$  nm. Thus, we infer that plasmon coupling between adjacent Ag quantum dots was one of the key mechanisms which led to the improved performance of PSC devices in this work.

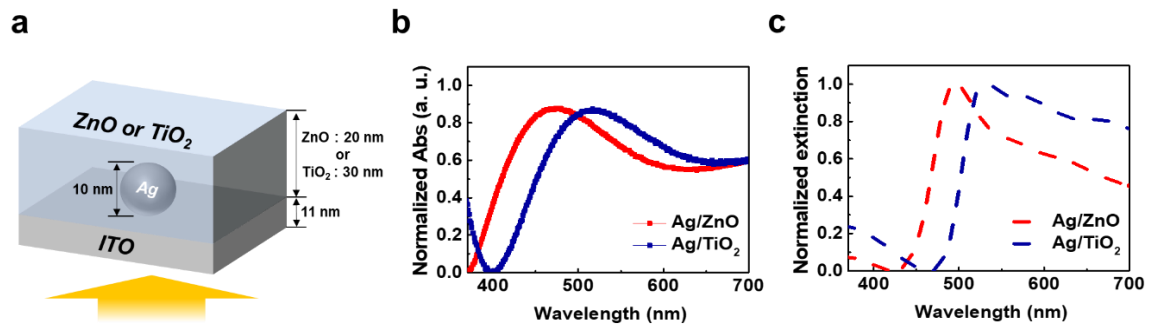


**Figure 2. 4** (a) Schematic diagram of Ag quantum dots embedded in ZnO and TiO<sub>2</sub> electron transport layers (ETLs). The thicknesses of the ETLs were 20 nm for ZnO and 30 nm for TiO<sub>2</sub> layers, respectively. (b) Normalized experimental absorbance and (c) normalized extinction spectra of 2D Ag QAs in ETLs obtained via DDA calculation. Each extinction spectrum of the ZnO and TiO<sub>2</sub> systems was obtained from the difference of each film with and without 2D Ag QAs.

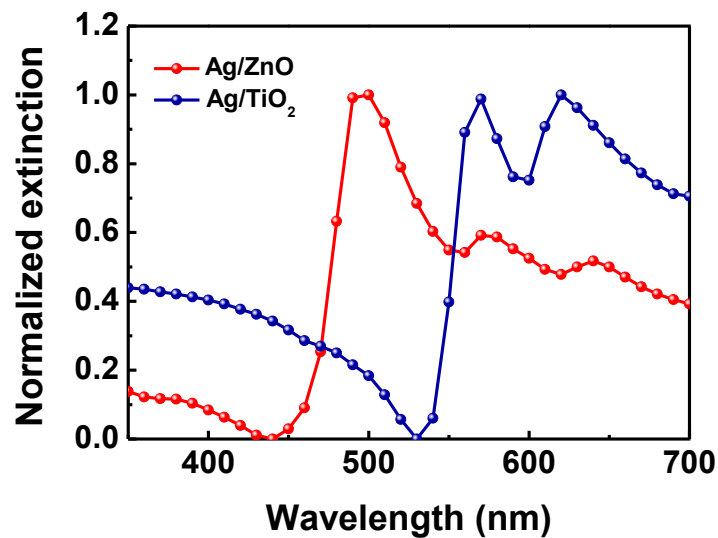


**Figure 2. 5** Calculated extinction spectra of 2-dimensional Ag quantum dot array in each ETL (i.e. ZnO and TiO<sub>2</sub> layers) without applying quantum effects



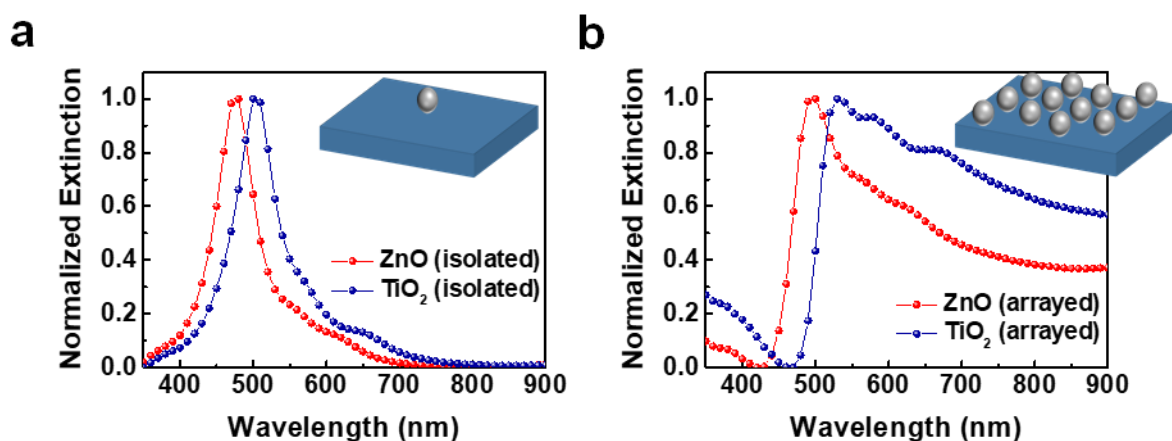


**Figure 2. 6** Calculated extinction spectra of (a) isolated Ag quantum dot from Figure 2.3 (a), where the PBCs were not applied, and (b) 2-dimensionally arrayed Ag quantum dots extended from Figure S2a with PBCs

### 2.3.3 Fabrication and Analysis of PSCs

PSCs were constructed using a blend of [4,8-bis[(2-ethylhexyl)oxy]benzo[1,2-b:4,5-b']dithiophene-2,6-diyl][3-fluoro-2-[(2-ethylhexyl)carbonyl]thieno[3,4-b]-thiophenediyl] (PTB7) and [6,6]-phenyl C71 butyric acid methyl ester (PC<sub>71</sub>BM) as an active layer. The device architecture used was glass/ITO/Ag quantum dots/ZnO or TiO<sub>2</sub>/PTB7:PC<sub>71</sub>BM/MoO<sub>3</sub>/Ag (**Figure 2.6 (a)**). 2D Ag QAs were synthesized by BCML using 214000 (PS 172000–P2VP 42000) block copolymers. This block copolymer exhibited superior transmittance and PSC performance, without a reduction in fill factor (FF) compared to other PSCs incorporating 2D Ag QAs prepared using different molecular weight block copolymers. *J–V* characteristics of PSCs prepared using PS-*b*-P2VP with various molecular weights are summarized in **Table 2.3**. The optimal thicknesses of ZnO and TiO<sub>2</sub> layers for our structures were around 20 and 30 nm, respectively (see **Table 2.4**). **Figure 2.6 (b-c)** shows the current density versus voltage (*J–V*) characteristics and external quantum efficiency (EQE) spectra of PSCs not only with and without 2D Ag QAs embedded in ZnO and TiO<sub>2</sub> but also 2D Ag QAs without ETLs deposited on ITO substrates. PSC parameters are summarized in **Table 2.2**. Devices comprising 2D Ag QAs without electron transport layers (ETLs) showed a low power conversion efficiency (PCE) of 1.87%, because of a low open-circuit voltage ( $V_{oc}$ ) of 0.23 V, and a low fill factor (FF) of 0.46. The performance of devices with ETLs was dramatically improved, with significant increases in  $V_{oc}$  and FF, due to their roles of energy level alignment between the active layer and the electrodes, which facilitated balanced charge extraction as well as preventing charge carrier recombination which is mediated by direct contact between the active layer and metallic nanoparticles. The use of a ZnO layer with 2D Ag QAs increased the PCE substantially, compared to that of the reference device without 2D Ag QAs. Specifically, the  $J_{sc}$  was significantly improved from 14.5 to 15.8 mA cm<sup>-2</sup>, corresponding to a 9.0% increase upon

incorporation of 2D Ag QAs. Likewise, the device using a TiO<sub>2</sub> layer on the 2D Ag QAs reached an optimal PCE of 8.51%. This improvement arose from a remarkable enhancement of  $J_{sc}$  from 14.6 to 16.2 mA cm<sup>-2</sup>, corresponding to a 11.0% increase compared to reference devices without 2D Ag QAs. The open-circuit voltage and fill factor, however, showed no dramatic change in the presence or absence of 2D Ag QAs, implying that the 2D Ag QAs only increased the photocurrent generation via optical effects without greatly affecting the electronic properties of the devices. It is noteworthy that the insertion of 2D Ag QAs into ETLs resulted in negligible morphological changes of the ETL surface (see **Figure 2.8**). Consequently, the best PCEs were obtained in devices incorporating 2D Ag QAs with ETLs deposited atop the NAs, resulting in performance enhancements of 10.5% in the case of ZnO and 12.7% in the case of TiO<sub>2</sub>.

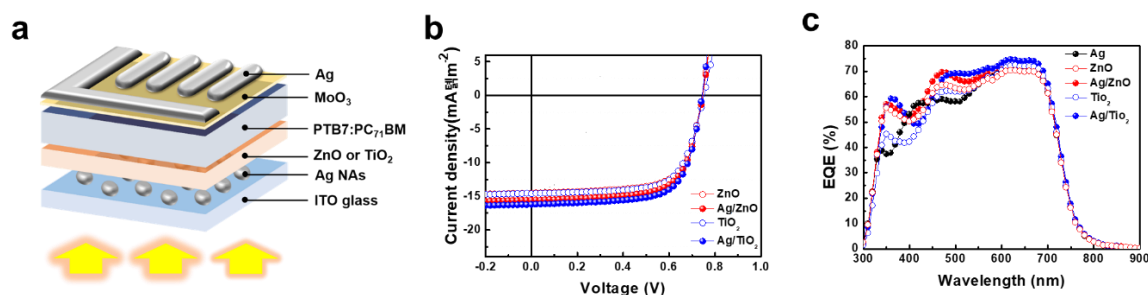


**Figure 2. 7** (a) Device structure, (b)  $J$ - $V$  characteristics under AM 1.5 illumination (100 mW cm<sup>-2</sup>) and (c) EQE of OPVs. Black traces correspond to OPVs without ETLs, while red and blue traces correspond to ZnO and TiO<sub>2</sub> ETLs, respectively. Empty circles correspond to devices without Ag NAs while filled circles are with Ag NAs embedded ZnO or TiO<sub>2</sub> layers

**Table 2. 2** Device characteristics of PTB7:PC<sub>71</sub>BM based OPVs with or without 2D Ag QAs in different ETLs

ETL	$J_{sc}$ (mA/cm <sup>2</sup> )	$V_{oc}$ (V)	FF	Average PCE (%)	best PCE (%)	Cal. $J_{sc}$ (mA/cm <sup>2</sup> )
None	14.4 ± 0.23	0.28 ± 0.02	0.46 ± 0.03	1.87	2.03	14.21
ZnO	14.5 ± 0.17	0.74 ± 0.01	0.69 ± 0.01	7.39	7.40	14.67
Ag/ZnO	15.8 ± 0.19	0.75 ± 0.01	0.69 ± 0.01	7.97	8.18	15.29
TiO <sub>2</sub>	14.6 ± 0.21	0.75 ± 0.01	0.69 ± 0.01	7.49	7.55	14.57
Ag/TiO <sub>2</sub>	16.2 ± 0.15	0.75 ± 0.01	0.70 ± 0.01	8.27	8.51	15.52

**Table 2. 3** PSCs parameters of devices using various 2-dimensional Ag quantum dot arrays

PS (Mn kDa)	P2VP (Mn kDa)	$J_{sc}$ (mA·cm <sup>-2</sup> )	$V_{oc}$ (V)	FF	PCE (%)
-	-	14.8 ±0.88	0.74 ±0.01	0.66 ±0.01	7.30 ±0.12
325	92	15.2 ±1.21	0.74 ±0.01	0.59 ±0.04	6.63 ±0.45
172	42	15.4 ±1.08	0.75 ±0.01	0.67 ±0.02	7.66 ±0.09
133	132	15.6 ±2.63	0.69 ±0.03	0.46 ±0.06	5.00 ±1.21
213	215	13.8 ±3.24	0.55 ±0.10	0.43 ±0.11	3.23 ±2.01
440	353	14.6 ±2.21	0.71 ±0.07	0.49 ±0.06	5.06 ±1.64

**Table 2. 4** Device characteristics with variable ETL thicknesses

Configuration	ETL- spin rate (rpm)	ETL average thickness (nm)	$J_{sc}$ (mA·cm <sup>-2</sup> )	$V_{oc}$ (V)	FF	PCE (%)
ITO/ZnO NPs/PTB7:PC <sub>71</sub> BM/ MoO <sub>3</sub> /Ag	800	35	14.8 ±0.30	0.74 ±0.01	0.67 ±0.01	7.34 ±0.08
	1500	26	15.0 ±0.38	0.74 ±0.01	0.66 ±0.01	7.26 ±0.06
	3000	20	15.1 ±0.22	0.74 ±0.01	0.66 ±0.01	7.61 ±0.11
	5000	14	14.8 ±0.43	0.74 ±0.01	0.63 ±0.01	7.45 ±0.09
ITO/TiO <sub>2</sub> NPs/PTB7:PC <sub>71</sub> BM/ MoO <sub>3</sub> /Ag	800	42	15.1 ±2.18	0.74 ±0.01	0.61 ±0.06	6.82 ±0.98
	1500	30	14.8 ±0.28	0.74 ±0.01	0.68 ±0.01	7.45 ±0.07
	3000	23	14.5 ±0.32	0.74 ±0.01	0.69 ±0.01	7.40 ±0.12
	5000	18	13.8 ±1.21	0.74 ±0.01	0.67 ±0.03	6.84 ±1.05

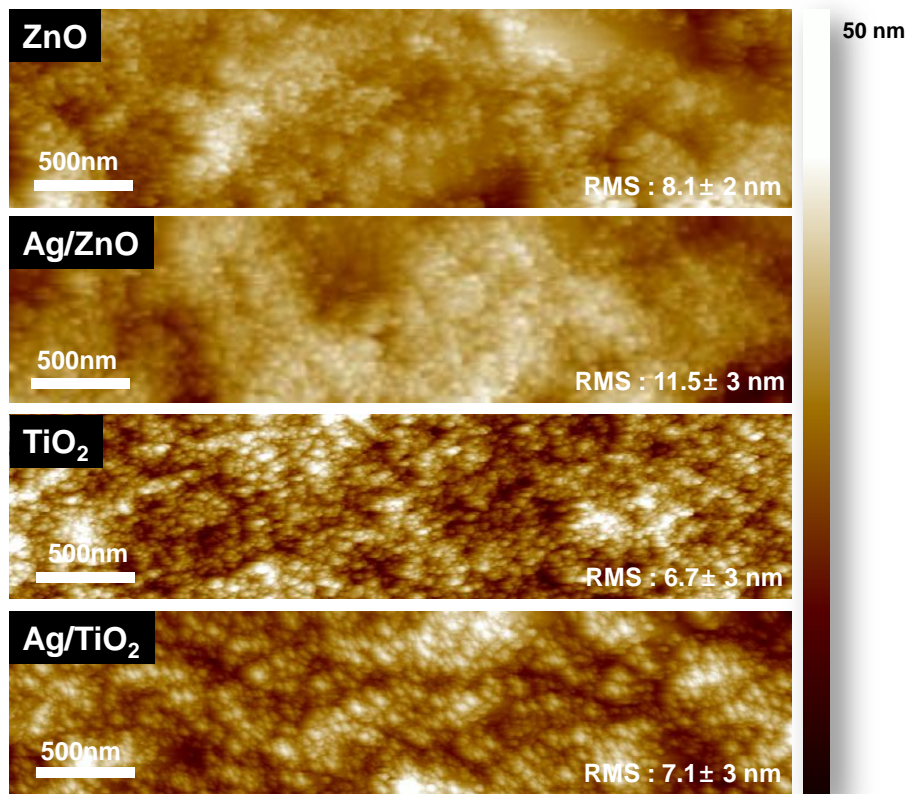


**Figure 2. 8** AFM images ( $4 \mu\text{m} \times 1 \mu\text{m}$ ) of ETLs with and without embedded 2-dimensional Ag quantum dot arrays

To clarify the  $J_{sc}$  enhancement, EQE spectra as well as changes in EQE upon incorporating 2D Ag QAs are shown in **Figures 2.9 (a) and (c)**. The EQE of devices incorporating 2D Ag QAs surrounded by ZnO exhibit enhanced photocurrent generation throughout the visible spectrum from 300 to 700 nm, with a distinct resonant peak at 470 nm, while the EQE spectra of devices with 2D Ag QAs inside TiO<sub>2</sub> also exhibited significantly increased photocurrent generation, with two peaks in improvement around 370 and 510 nm. The EQE enhancement from 350 to 400 nm is due to enhanced transmittance of the TiO<sub>2</sub> matrix after embedding 2D Ag QAs. The transmittance spectra of ETL layers with and without 2D Ag QAs are shown in **Figure 2.10 (a)**. We observed that the transmittance improved at wavelengths less than 400 nm, despite the incorporation of 2D Ag QAs. This change can be attributed to reduced scattering of ETL layers upon 2D Ag QAs insertion (see **Figure 2.10 (b)**), an effect which was confirmed via DDA modeling. The EQE enhancement from 440 to 570 nm can be attributed to the strong LSPR of the 2D Ag QAs. Notably, the Ag QAs embedded in TiO<sub>2</sub> showed two strong enhancements at 370 and 510 nm, whereas Ag QAs embedded in ZnO showed only one peak at 470 nm. To understand this difference and to further investigate the effect of Ag quantum dots on the light absorption in the active layer, the absorption enhancement ( $\Delta\alpha_{abs}$ ) was calculated from the following equation based on the reflectance spectra of each film (see **Figure 2.11**).

$$\Delta\alpha_{abs} = -\ln(R_{Ag/ETLs} - R_{ETLs}) \quad (\text{Eq. 2.1})$$

The  $\Delta\alpha_{abs}$  spectrum strongly correlates with the EQE enhancement as shown in **Figure 2.9 (b-d)**. This indicates that the enhanced photocurrent in devices with 2D Ag QAs can be attributed to additional absorption of the photoactive layer in these devices. The region of EQE enhancement and  $\Delta\alpha_{abs}$  peak of devices with TiO<sub>2</sub> ETLs shifted toward longer wavelengths compared to devices with ZnO ETLs, a consequence of the greater index of refraction of the corresponding medium. This tendency shows excellent agreement with the tendency observed in UV–vis absorption spectra. In addition, it is found that the EQE enhancement and  $\Delta\alpha_{abs}$  in the TiO<sub>2</sub> case is higher than that of ZnO. This can be attributed to the stronger intensity of LSPR-enhanced scattering in the case of TiO<sub>2</sub>. Whereas ZnO showed a small increase in  $\Delta\alpha_{abs}$  below 400 nm, TiO<sub>2</sub> showed a much stronger increase in absorption due to this increased scattering efficiency at short wavelengths, consistent with the increased scattering in TiO<sub>2</sub> predicted by DDA modeling (**Figure 2.10 (c)**). These attributes explain why 2D QAs embedded in TiO<sub>2</sub> showed an additional band of EQE enhancement at 370 nm compared to ZnO.

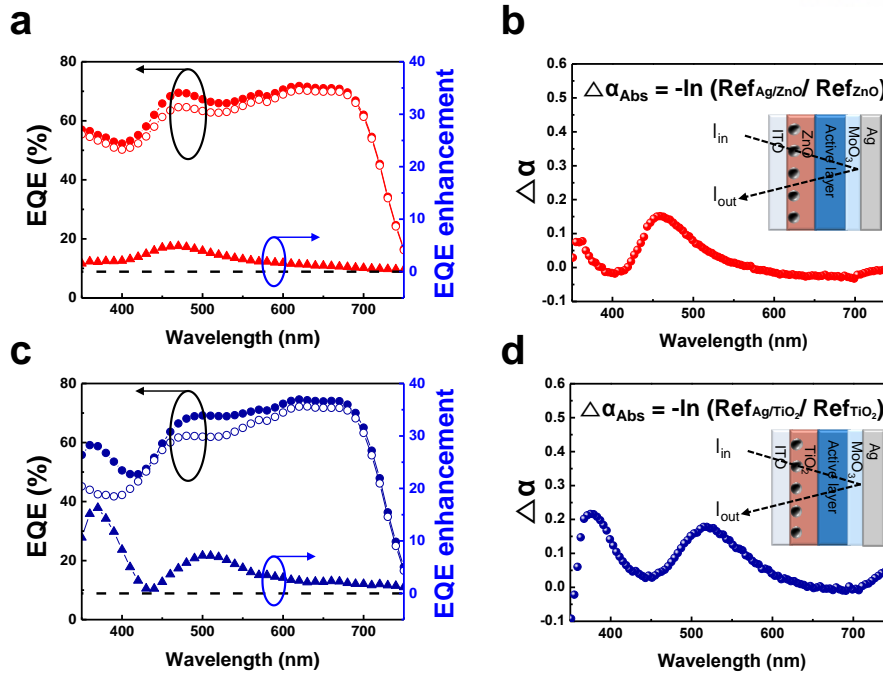


**Figure 2. 9** EQE and EQE enhancement. (a), (c) EQE with and without 2D Ag QAs embedded in ZnO and TiO<sub>2</sub> ETLs, respectively. (b), (d) Measured absorption enhancement due to 2D Ag QAs embedded in ZnO and TiO<sub>2</sub> ETLs (difference in absorption with and without 2D Ag QAs), respectively. Insets depict the configuration of optical reflectance measurements

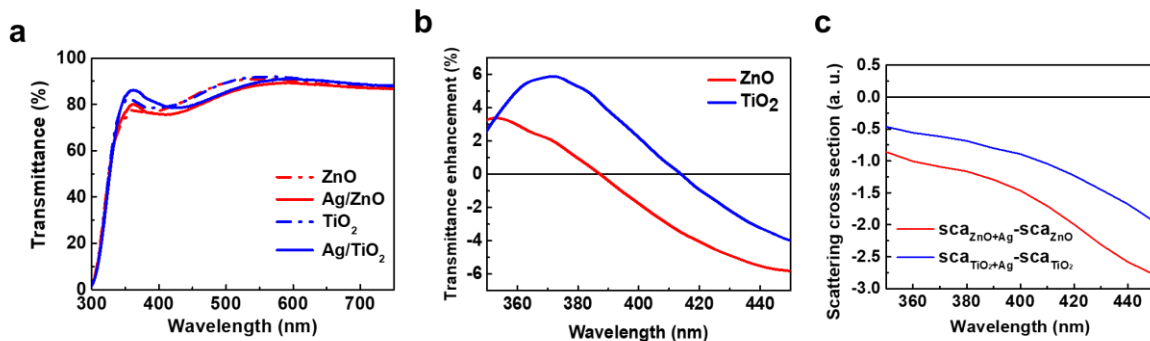


**Figure 2. 10** (a) Absolute transmittance of ZnO and TiO<sub>2</sub> layers with and without Ag nanodots. (b) Enhanced transmittance of ETL layers with Ag nanodot arrays and (c) Scattering cross-section difference between ETL+Ag nanodot arrays and ETLs only

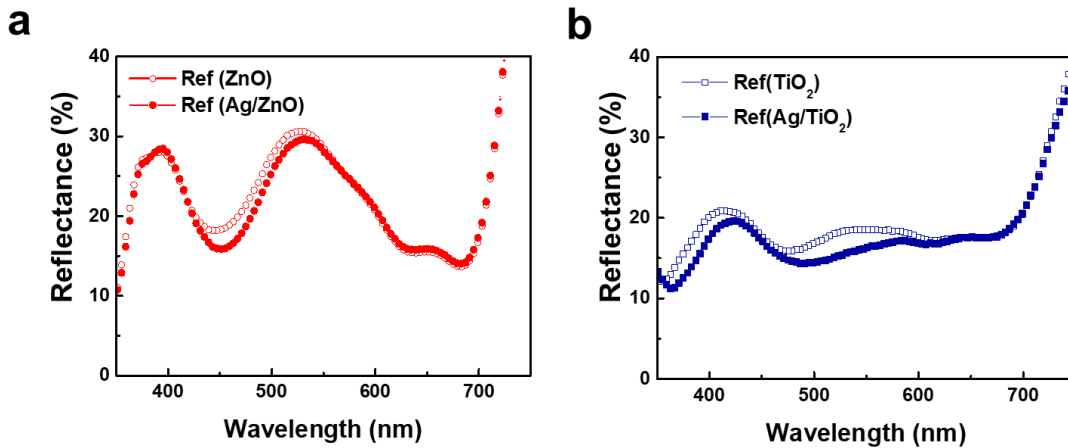


**Figure 2. 11** Reflectance spectra of PSCs based on PTB7:PC<sub>71</sub>BM with Ag nanodots embedded in (a) ZnO and (b) TiO<sub>2</sub> layers

To investigate the effect of 2D Ag QAs on the device performance in different media (i.e., ZnO and TiO<sub>2</sub>), we calculated the near-field enhancement inside the devices through electric field contour plots, which show the spatial distribution of the electric field (**Figure 2.12 (a)**), and the far-field scattering of Ag quantum dots (**Figure 2.12 (b)**) at peak wavelengths, respectively. The intensity of the electric field in the vicinity of the Ag quantum dots was enhanced by about 13–15 times in both ZnO and TiO<sub>2</sub> layers. However, the near-field effect is spatially confined near the surface of Ag quantum dots and cannot propagate to the active layer. Therefore, the active layer could not be significantly affected by the near-field enhancement of 2D Ag QAs, implying that the near-field effect had only a minor influence on the device performance. In contrast, the far-field scattering of Ag quantum dots showed quite different results (**Figure 2.12 (b)**). When the incident light interacted with 2D Ag QAs, both ETL media showed that the forward direction (i.e., from 0° to 90° and from 270° to 360°) of light scattering was dominant in comparison to backward scattering (i.e., from 90° to 270°). This result indicated that LSPR-enhanced EM wave could effectively propagate to the active layer. The induced variation in the angle of the incident light increased the effective optical path length of light in the active layer; this phenomenon is often called light trapping or a wave-guided mode. Similarly, in our system, the light-trapping effect led to increased exciton generation in the active layer. Furthermore, because the far-field scattering shows a large propagation distance, direct contact between excitons and Ag quantum dots is not necessary, confirming that charge recombination by the metallic nanoparticles could be avoided. Overall, we have identified the far-field scattering effect was the main mechanism for enhanced performance in PSC devices. In particular, the higher EQE enhancement in devices using TiO<sub>2</sub> ETLs could be explained largely by the stronger far-field scattering in comparison to ZnO.

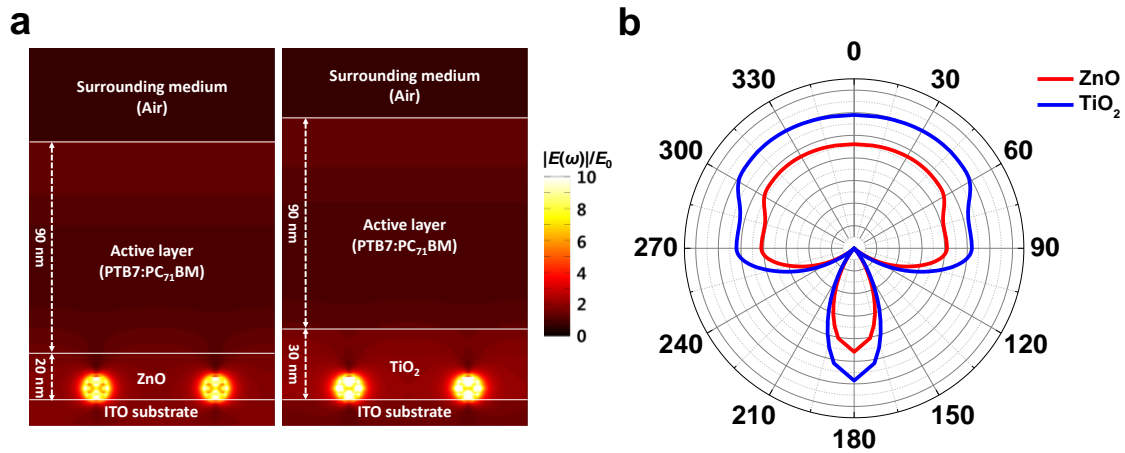


**Figure 2. 12** Calculated near-field electric field enhancement and far-field scattering. (a) Spatial distribution of the electric field of the device with ZnO and TiO<sub>2</sub> layers.  $E(\omega)$  is the induced electric field and  $E_0$  is the external electric field. (b) Angular plot of the far-field scattering of 2D Ag QAs in each ETL. The results were obtained at a wavelength of 500 nm for ZnO and 530 nm for TiO<sub>2</sub>, which were the peak wavelengths in the extinction spectra (as shown in Figure 2.3 (c)).

## 2.4 Conclusion

In conclusion, we have demonstrated highly enhanced performance in polymer solar cells using 2D Ag QAs synthesized by BCML. The LSPR peaks of 2D Ag QAs were tuned by varying the index of refraction of the surrounding medium. Ten-nanometer-sized 2D Ag QAs did not greatly affect the transmittance of ITO films; however, they did exhibit strong LSPR intensity in the visible range. DDA calculations of near-field enhancement and far-field scattering, considering quantum effects (i.e., intrinsic size effect and nonlocal effect) demonstrated that the far-field scattering of incident light led to light trapping in the active layer and was the primary reason for enhancement in device performance. Optimized 2D Ag QAs embedded in a TiO<sub>2</sub> ETL resulted in a champion PCE of 8.51%. We believe that the environment-sensitive tunability of LSPR peaks in plasmonic nanomaterials offers a new and powerful method to tune the properties of plasmonic materials for a broad range of applications in various polymer-based optoelectronic devices.



## Chapter 3. Efficiency Exceeding 11% in Tandem Polymer Solar Cells Employing High Open-Circuit Voltage Wide-Bandgap $\pi$ -Conjugated Polymers

### 3.1 Research Background

The ever-increasing demand for energy is a global issue which has garnered the attention of researchers worldwide in an effort to harvest renewable energy sources such as solar energy.<sup>[3]</sup> In this regard, bulk heterojunction polymer solar cells (BHJ PSCs) based on  $\pi$ -conjugated polymers have emerged as promising alternatives to inorganic silicon solar cells owing to their attractive features such as low-cost, roll-to-roll processability, large-area scalability, and mechanical flexibility<sup>[39]</sup>. To achieve power conversion efficiencies (PCEs) over 10%<sup>[40, 41, 42]</sup> necessary for commercialization, a tremendous research effort has been dedicated toward material design strategies<sup>[43, 44]</sup> and device fabrication techniques<sup>[22]</sup>. Notably, the demonstration of tandem polymer solar cells (TPSCs) with over 6% PCE in 2007 established tandem devices as an important route to overcome the PCE limitations of single-junction BHJ PSCs arising from thermalization losses and narrow absorption bands.<sup>[22]</sup> The strategy of TPSCs typically comprises using two subcells connected in series through a transparent interconnecting layer; the use of two subcells allows a wider range of photons to be harvested while the output voltages of the two subcells are added together, allowing for substantial improvements in device performance.<sup>[21, 45]</sup> For the successful realization of high-performance, solution-processable TPSCs<sup>[22, 46]</sup>, it is necessary to consider the optical and electrical properties of the two photoactive layers in a logical manner. The steps of TPSC fabrication and the overall TPSCs design must be carefully planned in order to realize a successful device. PSCs are usually deposited on top of transparent conducting substrates. Thus, under operation, light enters through the bottom subcell first. There are several important considerations when designing the bottom cell.

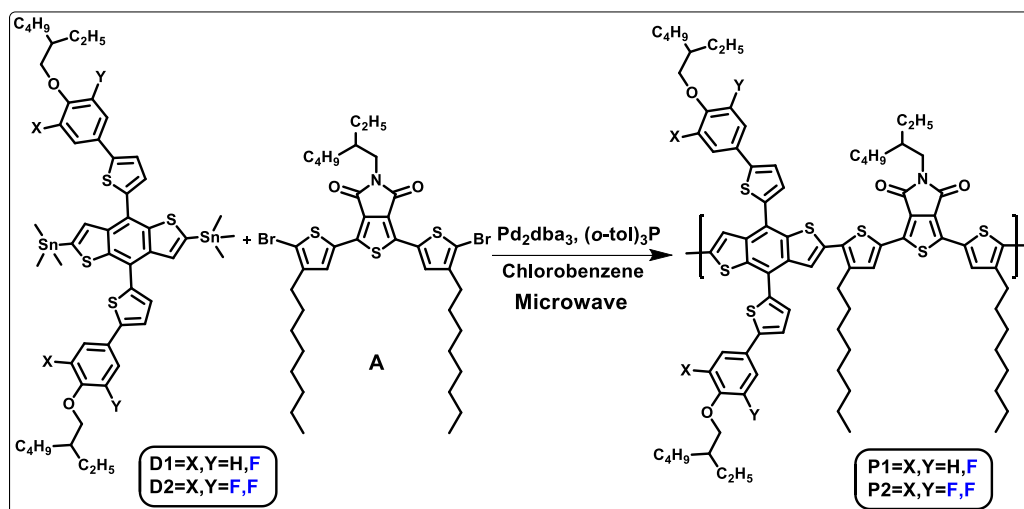
(i) A wide-bandgap (WBG) polymer is ideally employed in the bottom cell, absorbing high-energy photons and allowing low energy photons to pass through to the top subcell ; optimal spectral utilization is achieved when the bottom cell and top cell have complementary, nonoverlapping absorption spectra<sup>[40, 47]</sup>.

(ii) Good thermal stability is necessary during the fabrication procedure. In most of the successful TPSCs demonstrated to date, the top and bottom subcells have been separated by an interconnecting layer of pH neutral PEDOT:PSS, which requires thermal annealing at over 140 °C to remove residual moisture and allow electrical percolation between neighboring PEDOT:PSS grains.<sup>[48]</sup> For this reason, it is preferable for the bottom donor polymer to have strong stability toward thermal annealing.<sup>[49]</sup>

(iii) A high open-circuit voltage ( $V_{oc}$ ) in the bottom cell directly contributes to TPSCs performance,

since the photocurrent is limited by the lowest current between the two subcells and TPSC voltage is from sum of individual subcells voltage ( $V_{oc}(\text{tandem}) \doteq V_{oc}(\text{bottom}) + V_{oc}(\text{top})$ ), the wide bandgap of the bottom cell allows it to produce a high  $V_{oc}$ , which constitutes one of the main benefits of using a tandem architecture.<sup>[49]</sup> On the other hand, the PCE in TPSCs is limited by photocurrent and fill factor (FF) between the two subcells; these parameters must be carefully optimized by adjusting each subcell thickness, understanding of interaction between two cells and modifying interconnecting layers.<sup>[50]</sup> For example, in 1985, it was demonstrated that the FF in tandem silicon solar cells is determined by the  $I_{sc}$  balance ( $I_{sc} \text{ bottom cell}/I_{sc} \text{ top cell}$ ), which indicated the FF could be approximately predicted based on the limiting single cell's current output.<sup>[49]</sup> Immense progress has been achieved, not only the development of new WBG and low-bandgap (LBG) polymers<sup>[44, 51]</sup>, but also in the modification of device structures with new interconnecting layers for efficient charge recombination.<sup>[43, 52]</sup> These advances have increased the current PCEs of TPSCs. Nevertheless, these PCEs have been limited largely by the performance of WBG polymers. Notably, a recent example of a WBG small molecule which was incorporated as a bottom cell in TPSCs showed a remarkable improvement in PCE to over 11%, clearly indicating the potential for improvement in performance by employing appropriate WBG materials. Although a few WBG polymers exist, the highest performing materials (with PCEs of  $\approx 8\%$  and  $V_{oc}$ s over 0.9 V) have not been thoroughly investigated in TPSCs, since it is a highly challenging task to incorporate them in TPSCs while maintaining a high PCE without compromising the  $V_{oc}$ . Herein, we have selected two WBG polymers for bottom cells: poly[4,8-bis(2-(4-(2-ethylhexyloxy)3-fluorophenyl)-5-thienyl) benzo[1,2-*b*:4,5-*b'*] dithiophene-*alt*-1,3-bis(4-octylthien-2-yl)-5-(2-ethylhexyl)thieno[3,4-*c*]pyrrole-4,6 dione] (P1), poly[4,8-bis(2-(4-(2-ethylhexyloxy)3,5-fluorophenyl)-5-thienyl)benzo[1,2-*b*:4,5-*b'*]dithiophene-*alt*-1,3-bis(4-octylthien-2-yl)-5-(2-ethylhexyl)thieno[3,4-*c*]pyrrole-4,6-dione] (P2). We used the high-performance polymer poly[4,8-bis(5-(2-ethylhexyl)thiophen-2-yl) benzo[1,2-*b*:4,5-*b'*]dithiophene-2,6-diyl-*alt*-(4-(2-ethylhexyl)-3-fluorothieno[3,4-*b*]thiophene-)-2-carboxylate-2-6-diyl)] (PTB7-Th) as a LBG polymer for the top subcell. The synthetic procedure for WBG polymers P1, P2 (**Scheme 3.1**) is given in the Experimental Section. P1 and P2 offer impressive photovoltaic parameters; for P1 these include a  $V_{oc}$  of 0.91 V, a  $J_{sc}$  of 12.3 mA cm<sup>-2</sup>, and a FF of 0.68. For P2 these include a  $V_{oc}$  of 1.00 V, a  $J_{sc}$  of 12.3 mA cm<sup>-2</sup>, and a FF of 0.64. The high  $V_{oc}$  values and reduced current loss in TPSCs arise from their deep highest occupied molecular orbitals (HOMOs) and high absorption coefficients. Optimized TPSCs with P1 and PTB7-Th displayed a champion PCE of 11.42% ( $V_{oc} = 1.64$  V;  $J_{sc} = 10.10$  mA cm<sup>-2</sup>; FF = 0.69) and TPSCs based on P2 also delivered a peak PCE of 10.05% ( $V_{oc} = 1.72$  V;  $J_{sc} = 9.28$  mA cm<sup>-2</sup>; FF = 0.63). These high-performance devices were realized by judicious consideration and analysis of critical device parameters such as charge carrier transport behavior, optical and electrical simulations, as well as processing strategies like alcohol treatment,<sup>[53]</sup> which allowed optimal utilization of the photovoltaic

properties of both subcells.



**Scheme 3.1.** Synthesis route for P1 and P2 donor polymer

## 3.2 Experimental

### 3.2.1 Fabrication of Single Junction BHJ PSCs

Indium tin oxide (ITO) coated glass substrates were ultrasonically cleaned with detergent, water, acetone, and IPA. Then, a thin hole injection layer ( $\sim 40$  nm) of PEDOT:PSS (Clevios P VP AI 4083, filtered at  $0.45 \mu\text{m}$ ) was spin-cast on the ITO-coated glass substrates and baked at  $150^\circ\text{C}$  for 15 min under ambient conditions. The thickness of P1:PC<sub>71</sub>BM, P2:PC<sub>71</sub>BM and PTB7-Th:PC<sub>71</sub>BM active layers were found to be 150 nm of P1 and P2 and around 110 nm of PTB7-Th, respectively. P1-P2:PC<sub>71</sub>BM was spin coated using a mixture of polymer:PC<sub>71</sub>BM (1:1) that was dissolved in CB:DPE (97:3). 100 nm thick Al cathodes were deposited via thermal evaporation onto the active layer. The active area of the device was  $3.5 \text{ mm}^2$ . For Fabrication of TPSCs, PEDOT:PSS (Clevios P VP AI 4083, filtered at  $0.45 \mu\text{m}$ ) was spin-cast on glass/ITO substrates and annealed  $150^\circ\text{C}$  for 15 min. Then, P1 or P2 based active solution were coated in the same conditions and procedure described above single junction BHJ PSCs. ZnO nanoparticles dissolved in methanol at a concentration of  $5 \text{ mg ml}^{-1}$  were spin cast onto bottom junction active layers (P1:PC<sub>71</sub>BM or P2:PC<sub>71</sub>BM) under an atmosphere of N<sub>2</sub> to yield  $\sim 5$  nm thick films. The ZnO nanoparticle layer was annealed at  $130^\circ\text{C}$  for 1 minute in glove box. pH neutral PEDOT:PSS was prepared by mixing with distilled water and 2-propanol (1:1:1 v/v%), then spin-coated onto ZnO NP layer with  $\sim 10$  nm under N<sub>2</sub> atmosphere. The ZnO nanoparticle solution and modified pH neutral PEDOT:PSS were filtered with a  $0.45 \mu\text{m}$  syringe filter for well-formed interconnecting layer. Before coating second active layer (PTB7-Th:PC<sub>71</sub>BM), the PEDOT:PSS layer were annealed at  $130^\circ\text{C}$  for 5 minutes. PTB7-Th:PC<sub>71</sub>BM active solution (D:A=1:1.5, dissolved in CB:DPE (97:3)) were spin casted as top subcells, then PTB7-Th:PC<sub>71</sub>BM layers were treated with methanol. 100 nm of Al electrodes were deposited on top subcell by thermal evaporation at  $\sim 5 \times 10^{-7}$

Torr.

### 3.2.3 Characterization

Current density vs voltage ( $J$ - $V$ ) curves were measured under 3~100  $\text{mW}\cdot\text{cm}^{-2}$  illumination with uses of neutral density filters for tuning the light intensity, All device were carried out 3.5  $\text{mm}^2$  of active area. The measurements were performed in a glovebox with filled with  $\text{N}_2$ . To ensure accurate EQE results, a calibrated silicon diode was used as a reference. The chopped monochromatic light were used with white light as well as light bias by 650 nm blue-band pass and 700nm high pass, which excites the bottom and top cells to measure the EQE of the top and bottom subcells, respectively. The bias intensity was  $\sim 10 \text{ mW}\cdot\text{cm}^{-2}$ . The EQE without bias light was quite much lower than that with bias light. Furthermore, we calculated EQE *via* simulation with considering assuming ‘Half is absorbed by front cell and the other half by back cell’ in tandem polymer solar cells.

## 3.3 Results and Discussion

### 3.3.1 Donor Polymers for Appropriate Bottom Cells

Donor materials for bottom cells in TPSCs should possess not only a WBG (to allow a fraction of the light to pass to the top cell), but also good photovoltaic characteristics such as high  $V_{\text{oc}}$ , high  $J_{\text{sc}}$ , and FF, in order to improve the  $V_{\text{oc}}$  sum value and minimize current losses arising from mismatched currents in the two subcells. Furthermore, the top cell must also be considered; it must absorb long-wavelength light efficiently, be amenable to TPSC solution-processing techniques, possess a high absorption coefficient, and also have strong thermal stability. The WBG polymers P1 and P2 were used as bottom photoactive materials in this study, while PTB7-Th (a LBG polymer which is able to absorb light up to  $\approx 800 \text{ nm}$  in wavelength) was deposited as a top cell in each case. The chemical structure, film absorption spectra, and energy levels of the polymers are presented in **Figure 3.1**. The thermal stabilities of the WBG polymers, P1 and P2, were evaluated by thermal gravimetric analysis (TGA) and differential scanning calorimetry (DSC), as shown in **Figure 3.2 (a-b)**. The polymers showed broad absorption profiles in the range of 300–700 nm, with optical bandgaps of 1.82 eV, and deep HOMO levels of  $-5.43$  and  $-5.50 \text{ eV}$  for P1 and P2, respectively (**Figure 3.2 (c)**). These polymers exhibited well-ordered  $\pi$ - $\pi$  packing in photoactive layers and in film morphologies (**Figures 3.3 and 3.4 and Table 3.1**). Therefore, the BHJ single junction cells of P1 and P2 were able to yield high performance with characteristics including a PCE of 7.62%,  $V_{\text{oc}}$  of 0.91 V,  $J_{\text{sc}}$  of  $12.3 \text{ mA cm}^{-2}$ , and FF of 0.68 for P1, and a PCE of 7.83%,  $V_{\text{oc}}$  of 1.00 V,  $J_{\text{sc}}$  of  $12.3 \text{ mA cm}^{-2}$ , and FF of 0.64 for P2 after optimization of processing conditions. These intrinsic properties and photovoltaic characteristics indicated that the polymers were quite well suited for application as bottom solar cells in TPSCs.

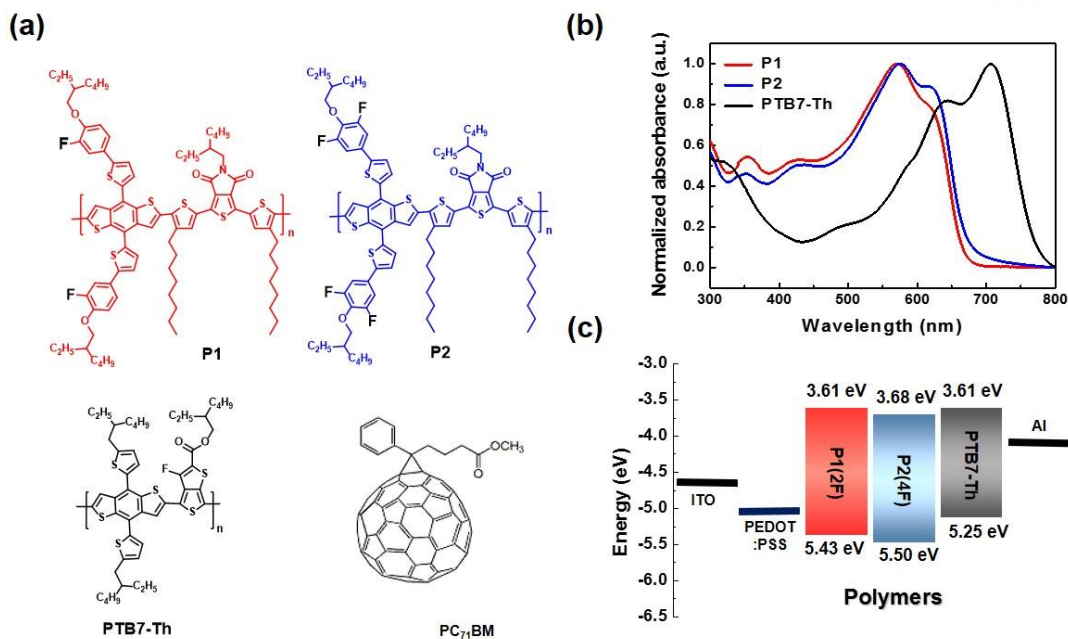


**Figure 3. 1** (a) Polymer structures. (b) UV-vis absorption spectra. (c) Energy level diagram of polymers

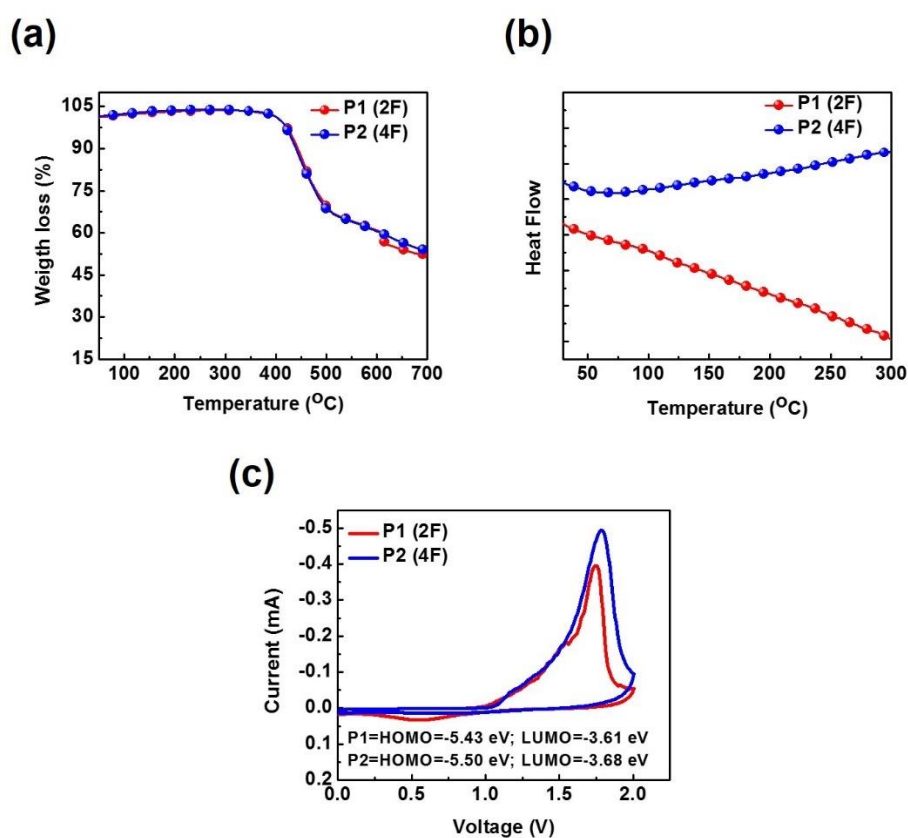


**Figure 3. 2** (a) Thermo gravimetric analysis (TGA) and (b) differential scanning calorimetry (DSC) plots of P1, P2. (c) Cyclicvoltammograms of P1, P2

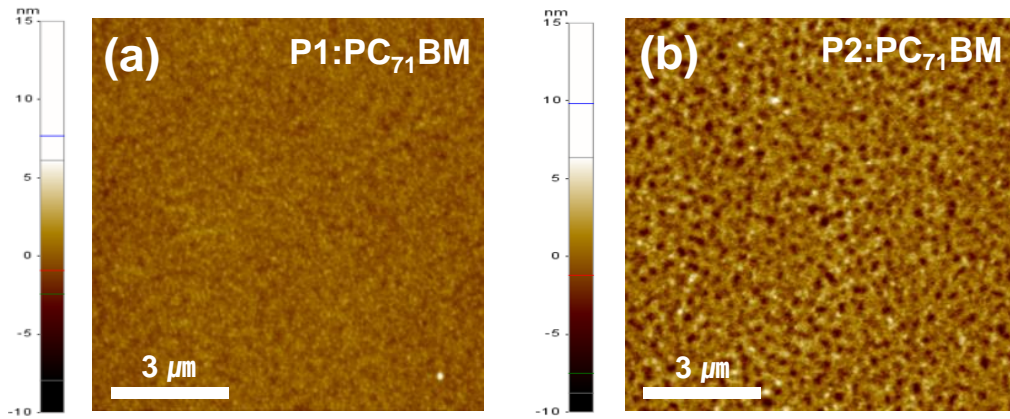


Figure 3. 3 AFM images of (a) P1:PC<sub>71</sub>BM and (b) P2:PC<sub>71</sub>BM films

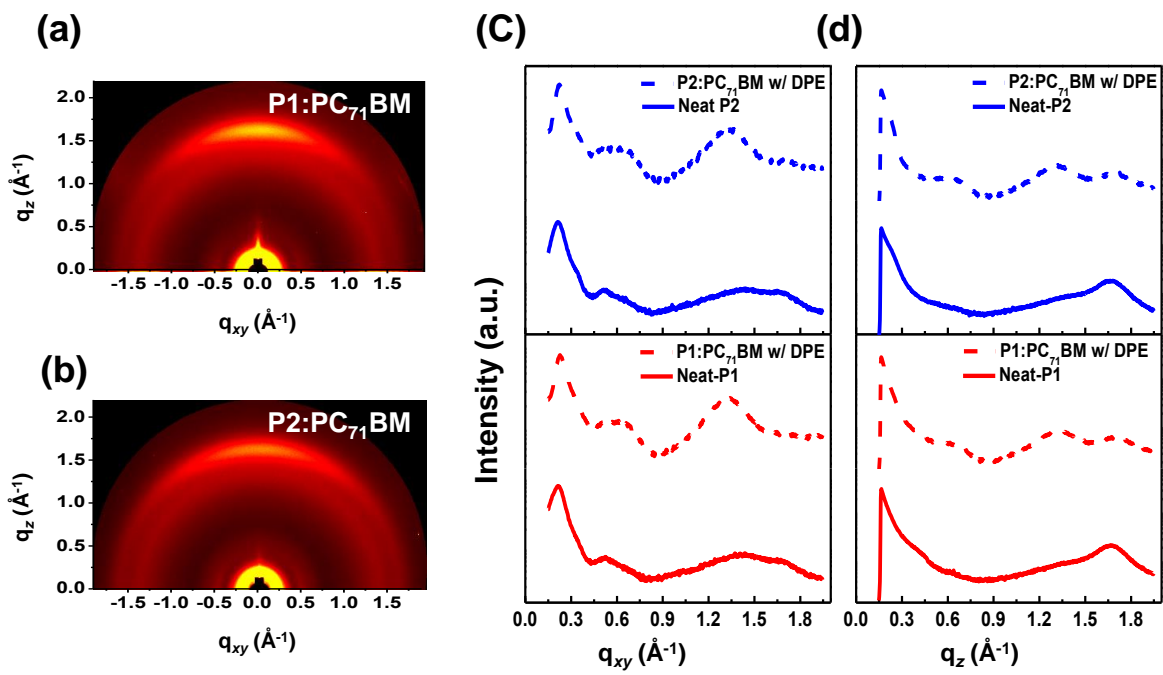


Figure 3. 4 GIXS images of (a) P1:PC<sub>71</sub>BM and (b) P2:PC<sub>71</sub>BM based active layers and with xy-and z-axis cross sections corresponding to each polymer, respectively

**Table 3. 1** Crystallographic parameters of WBG polymer films

Polymer	films	Crystallographic parameters					
		Axis	$\pi$ - $\pi$ stacking [ $\text{\AA}^{-1}$ ]	d-spacing [ $\text{\AA}$ ]	Coherence length [ $\text{\AA}$ ]	Lamellar stacking [ $\text{\AA}^{-1}$ ]	d-spacing [ $\text{\AA}$ ]
P1	Neat	$q_{xy}$	-	-	-	0.22	29.0
		$q_z$	1.675	3.8	31.1	0.17	37.6
	Blend w/ DPE	$q_{xy}$	-	-	-	0.23	27.6
		$q_z$	1.710	3.7	25.4	0.17	37.6
P2	Neat	$q_{xy}$	-	-	-	0.22	29.0
		$q_z$	1.665	3.8	27.2	0.17	37.6
	Blend w/ DPE	$q_{xy}$	-	-	-	0.22	29.0
		$q_z$	1.70	3.7	23.8	0.17	37.6

### 3.3.2 TPSCs Fabrication and Photovoltaic Properties

We fabricated TPSCs via solution processing in the architecture ITO/PEDOT:PSS/P1 or P2:PC<sub>71</sub>BM/ZnO/PEDOT:PSS/PTB7-Th:PC<sub>71</sub>BM/Al. TPSCs comprised a bottom cell with the new WBG polymers (P1 or P2) and a top cell with the LBG polymer PTB7-Th connected via a charge recombination layer to harvest a broad fraction of the solar spectrum and make efficient use of each subcell. We used solution-processed ZnO nanoparticles and pH-neutral PEDOT:PSS as a thin interconnecting layer to enable efficient charge recombination. The use of pH-neutral PEDOT:PSS ensured minimal damage to the underlying ZnO layer. ZnO nanoparticles were dissolved in methanol (MeOH), because MeOH has been shown to have beneficial effects on device characteristics as it is able to rinse out residual diphenyl ether (DPE) additive and draw PC<sub>71</sub>BM up toward the top interface of BHJ films, resulting in improved charge transport. Furthermore, MeOH was also used to treat PTB7-Th top cells for efficient electron extraction in normal TPSC structures. Since the optimal processing conditions of P1 and P2 single junction solar cells included MeOH post solvent treatment (**Figure 3.5** and **Table 3.2**), bottom cells were processed in the same way. In **Figure 3.6 (a-b)**, optimized TPSCs based on P1 and P2 showed maximum performances of 11.42% ( $V_{oc} = 1.64$  V;  $J_{sc} = 10.10$  mA cm<sup>-2</sup>; FF = 0.69) and 10.05% ( $V_{oc} = 1.72$  V;  $J_{sc} = 9.28$  mA cm<sup>-2</sup>; FF = 0.63), respectively. Photovoltaic properties are summarized in **Table 3.3**. These results are among a handful of tandem devices based on polymer:PC<sub>71</sub>BM subcells to exhibit PCEs over 10% (11.42% PCE for P1-based devices; see literature survey, **Table 3.4**). The TPSCs reported in this study constitute the highest  $V_{oc}$  (1.72 V for P2-based devices, see literature survey, **Table S3.4**). In addition, external quantum efficiencies (EQE) of PTB7-Th, P1, and P2-based single-junction devices were measured and demonstrated corresponding to results of  $J$ - $V$  characteristics. To thoroughly characterize TPSC performance, the EQEs of both the bottom subcells (P1:PC<sub>71</sub>BM and P2:PC<sub>71</sub>BM) and the top subcells (PTB7-Th:PC<sub>71</sub>BM) in tandem devices

were measured using bias light. Optical filters including a 715 nm high pass and 300–650 nm blue band pass filter were utilized to isolate the EQE response of each subcell in tandem devices. As shown in **Figure 3.6 (d)**, the bottom subcells showed photocurrent generation in the range of 300–700 nm for either P1 (8.87 mA cm<sup>-2</sup> of integrated  $J_{sc}$ ) or P2 (9.14 mA cm<sup>-2</sup> of integrated  $J_{sc}$ ) and in the 300–800 nm range for PTB7-Th (8.82 and 7.59 mA cm<sup>-2</sup> of integrated  $J_{sc}$  for P1 and P2-based TPSCs, respectively). The top cells based on PTB7-Th showed strong photocurrent generation in the wavelength range of 650–800 nm, which was not significantly absorbed by the bottom cells. Simulated EQE spectra were calculated for photocurrent generation in both the bottom cell and top cell, which allowed total EQE of TPSCs. The calculated active layer absorption indicated that a maximum possible  $J_{sc}$  of 10.16 mA cm<sup>-2</sup> for P1-based TPSCs and 10.23 mA cm<sup>-2</sup> for P2-based TPSCs. The EQE declined somewhat in the region of 650–800 nm, compared to the calculated active layer absorption, an effect which was stronger for P2 than for P1-based devices.

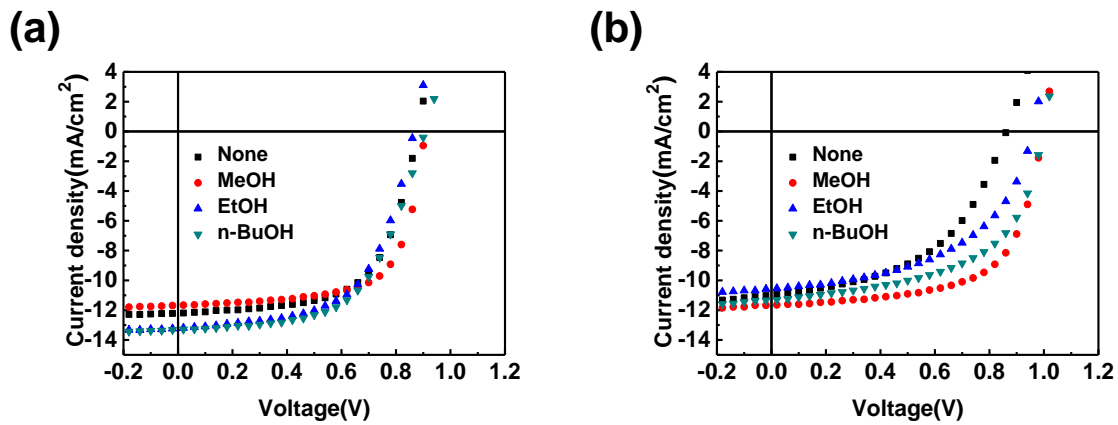


**Figure 3. 5**  $J$ - $V$  characteristics of (a) P1 and (b) P2 BJJ single junction cells with various post-solvent treatments

**Table 3. 2** Photovoltaic parameters of BJJ single junction cells with various post-solvent treatments

BJJ single cell	Solvent treatment	$J_{sc}$ [mA·cm <sup>-2</sup> ]	$V_{oc}$ [V]	FF	PCE [%]
P1:PC <sub>71</sub> BM	None	12.2	0.88	0.62	6.70
	Methanol	11.7	0.90	0.69	7.18
	Ethanol	13.2	0.87	0.60	6.81
	n-Buthanol	13.3	0.90	0.59	7.05
P2:PC <sub>71</sub> BM	None	11.0	0.86	0.50	4.69
	Methanol	11.7	1.00	0.64	7.38
	Ethanol	10.6	0.96	0.52	5.23
	n-Buthanol	11.3	1.00	0.56	6.31



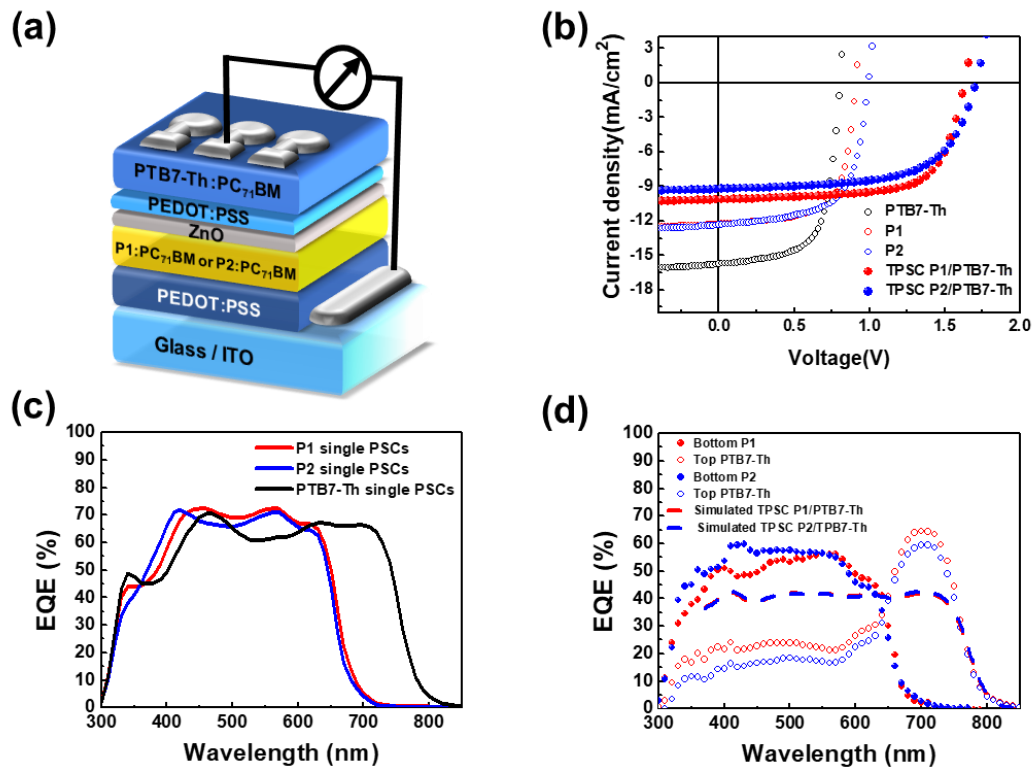


**Figure 3. 6** (a) TPSCs device structure, (b)  $J-V$  curves of P1 and P2 single-junction PSCs and TPSCs, (c) EQE curves of P1, P2, and PTB7-Th single-junction PSCs, (d) EQE curves of tandem devices

**Table 3. 3** Optimized photovoltaic properties of single junction and tandem solar cells

Cell	Blend	Ratio	$V_{oc}$ [V]	$J_{sc}$ [ mA·cm <sup>-2</sup> ]	$Cal.J_{sc}$ [ mA·cm <sup>-2</sup> ]	FF	PCE [%]
Top	PTB7-Th	1:1.5	0.81	15.74	15.49	0.66	8.41
Bottom1	P1-2F	1:1	0.91	12.27	12.10	0.68	7.62
Bottom2	P2-4F	1:1	1.00	12.29	11.61	0.64	7.83
Tandem1	P1:PTB7-Th		1.64	10.10	8.87 <sup>B</sup> /8.82 <sup>T</sup>	0.69	11.42
Tandem2	P2:PTB7-Th		1.72	9.28	9.14 <sup>B</sup> /7.59 <sup>T</sup>	0.63	10.05

B and T Values in parentheses in the calculated  $J_{sc}$  of TPSCs represent integrated  $J_{sc}$  of bottom and top subcells from EQE spectra.

**Table 3. 4** PCE of TPSCs (until 2017.06)

No	$V_{oc}$ (V)	PCE [%] Maximum	PCE [%] Average	Reference
<b>1</b>	<b>1.64</b>	<b>11.42</b>	<b>11.30</b>	<b>P1-based TPSCs (Current work)</b>
<b>2</b>	<b>1.72</b>	<b>10.05</b>	<b>9.87</b>	<b>P2-based TPSCs (Current work)</b>
3	1.68	11.62	11.32	Adv. Mater. 2016, 28, 5133.
4	1.68	11.47	11.21	Adv. Mater., 2016, 28, 7008.
5	1.54	10.39	-	Energy Environ. Sci., 2015, 8, 303.
6	1.54	11.3	-	Adv. Mater. 2015, 27, 1767.
7	1.59	9.40	-	J. Am. Chem. Soc. 2013, 135, 13549.
8	1.47	7.3	6.6	Energy Environ. Sci. 2013, 6, 2714.
9	1.58	9.35	9.28	Energy Environ. Sci. 2014, 7, 4118.
10	1.51	7.40	7.20	Chem. Mater. 2013, 25, 2722.
11	1.57	8.66	8.41	Chem. Mater. 2014, 26, 1234.
12	1.42	8.9	8.7	Adv. Mater. 2015, 27, 4461.
13	1.55	7.15	-	Macromolecules 2014, 47, 1613.
14	1.53	10.6	-	Nat. Commun. 2013, 4, 1446.
16	1.42	10.70	-	Adv. Mater. 2014, 26, 5670.
17	1.53	10.12	-	Macromolecules 2016, 49, 2993.
18	1.59	10.02	-	Adv. Mater. 2015, 27, 1189.
19	1.36	10.2	-	Adv. Mater. 2013, 25, 3973.
20	1.70	11.15	10.63	Nano Energy 2017, 33, 313.
21	1.63	12.50	12.28	Nat. Photonics 2017, 11, 85

### 3.3.3 Analyses for Limiting Factors in TPSCs

Although P1 and P2 polymers have similar optical properties, film crystallography, current output in single-junction PSCs, absorption coefficients ( $5.3 \times 10^4$  and  $4.9 \times 10^4 \text{ cm}^{-1}$ , respectively) and optimal photoactive thickness as bottom cells in TPSCs, we observed that P1-based TPSCs showed significantly higher  $J_{sc}$  values, which approached the theoretically calculated  $J_{sc}$  values, compared to P2-based TPSCs. In addition, P1-based TPSCs exhibited superior FFs. To analyze these phenomena, we investigated the balance of charge transport in the devices by the space charge limited current (SCLC) method. As shown in **Figure 3.7** and **Table 3.5**, hole ( $\mu_h$ ) and electron mobilities ( $\mu_e$ ) for polymer: PC71BM blends were calculated by fitting  $J$ - $V$  curves of hole- and electron-only diodes with the Mott-Gurney law. Hole mobilities were found to be  $3.7 \times 10^{-5}$  (P1),  $1.4 \times 10^{-6}$  (P2), and  $5.2 \times 10^{-4} \text{ cm}^2\text{V}^{-1}\text{s}^{-1}$  (PTB7-Th). Electron mobilities were found to be  $7.5 \times 10^{-5}$  (P1),  $7.2 \times 10^{-5}$  (P2), and  $5.4 \times 10^{-4} \text{ cm}^2\text{V}^{-1}\text{s}^{-1}$  (PTB7-Th). The charge balance ( $\mu_e / \mu_h$ ) between the hole mobility of the bottom cell and electron mobility of the top cell is important for charge extraction and collection at the electrodes in TPSCs. Additionally, the balance of electron mobility (bottom cell) and hole mobility (top cell) is important for charge recombination in the interconnecting layer. P1-based TPSCs showed a better  $\mu_e(\text{P1})/\mu_h(\text{PTB7-Th})$  value of 11.62 with enhancement by an order magnitude compared to that of P2-based TPSCs. On the other hand, FF limitation can be predicted by the ratio of bottom current to top current. Since the ratio ( $J_{sc}(\text{Bottom})/J_{sc}(\text{Top})$ ) was 0.78 (less than one) for tandem devices based on both P1 and P2, the FF of the two TPSCs clearly showed bottom cell dominated trends as shown in **Figure 3.7 (c)**.

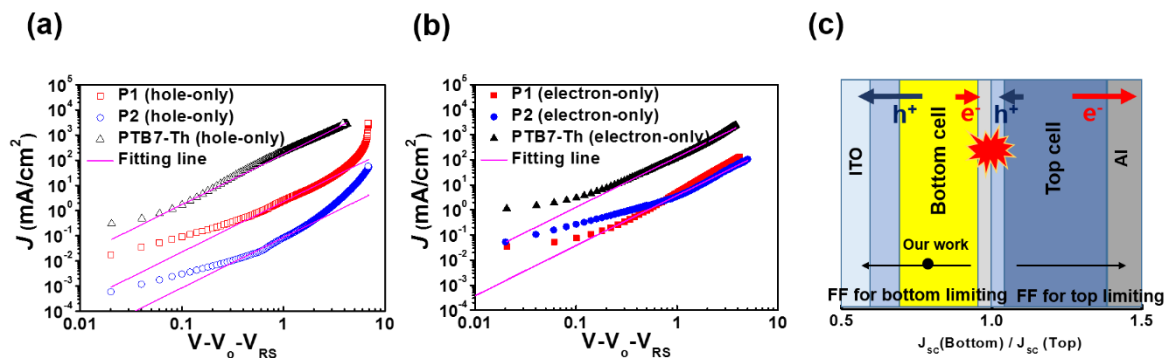


**Figure 3. 7** (a) Double-logarithmic plot of dark  $J$ - $V$  characteristics from (a) hole-only diodes (b) Electron-only device (c) Schematic image of charge transport in TPSC and FF-determination

**Table 3. 5** Hole mobilities and electron mobilities of polymer blend films using SCLC method

Polymer	Hole mobility [cm <sup>2</sup> V <sup>-1</sup> s <sup>-1</sup> ]	Electron mobility [cm <sup>2</sup> V <sup>-1</sup> s <sup>-1</sup> ]	$\mu_e/\mu_{\text{hole}}$
P1	3.68x10 <sup>-5</sup>	7.51x10 <sup>-5</sup>	2.02
P2	1.43x10 <sup>-6</sup>	7.20x10 <sup>-5</sup>	51.43
PTB7-Th	4.23x10 <sup>-4</sup>	4.30x10 <sup>-4</sup>	1.02

### 3.3.4 Optical and Electrical Simulations of TPSCs

Optical and electrical simulations were performed based on the intrinsic optical properties of each material using a transfer matrix protocol. These simulations revealed the light intensity distribution and photon absorption rate within each subcell. Assuming 100% internal quantum efficiency for each subcell allows the maximum  $J_{sc}$  for each subcell to be calculated and optimal top/bottom thicknesses to be identified to achieve optimal photocurrent matching between subcells; this information guided the optimization of processing conditions. Using the optical constants ( $n, k$ ) of P1, P2, and PTB7-Th, the modeling results as function of thickness for each bottom and top cell are shown in **Figure 3.8 (a–c)**. The simulated electric field distributions in the devices are shown in **Figure 3.9**. There are two maximum photocurrent regions in thickness simulation data of P1- and P2-based TPSCs each maximum corresponds to a combination of film thicknesses which results in both constructive optical interference and current matching between subcells. The local maxima corresponding to a thinner top cell matched well with the experimentally observed optimal film thicknesses. In **Figure 3.8 (d–e)**, although top cell has a higher photon absorption rate, over  $8.0 \times 10^{-21} \text{ cm}^{-3}\text{s}^{-1}$ , the calculated  $J_{sc}$  of the bottom cells were most equal to that of the top cell. These results indicated that our TPSCs were fabricated at a nearly optimal combination of subcell thicknesses to maximize light absorption while matching current outputs between the top and bottom subcells. However, the output currents and calculated EQE values of the two TPSCs are apparently limited by the bottom cells due to slightly lower current output than the top cells.

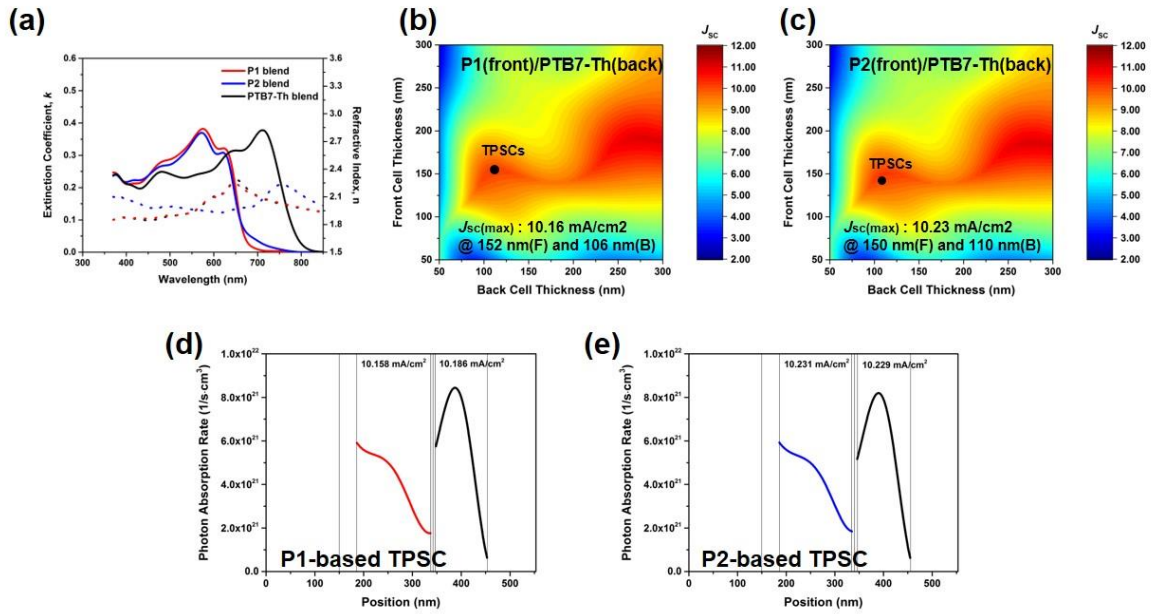


**Figure 3. 8** Optical constants ( $n$ ,  $k$ ) of polymers P1, P2 and PTB7-Th. (b), (c) Simulated  $J_{sc}$  as a function of thicknesses of front and back cells, showing optimal front and back cell thicknesses for TPSCs based on P1 and P2, respectively. (d), (e) Photon absorption rate of TPSCs based on P1 and P2, respectively

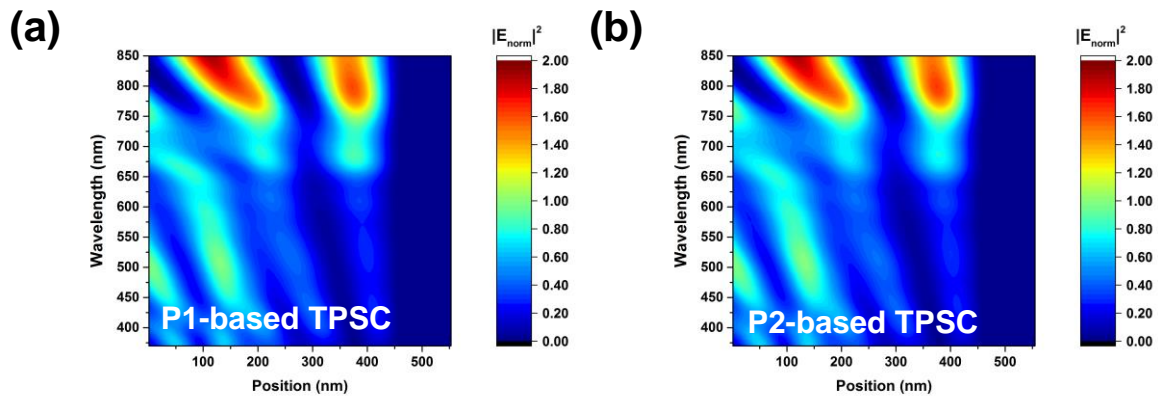


**Figure 3. 9** Electric field distribution for (a) P1- and (b) P2-based TPSCs.

### 3.4 Conclusion

In summary, we have successfully employed two WBG polymers (P1 and P2) in TPSCs as bottom cells. Compared to single-junction devices, we noticed a dramatic enhancement in the overall performance in TPSCs with maximum PCEs of 11.42 and 10.05% for P1 and P2, respectively. The substantial increase in PCE in these TPSCs stems from the WBG polymers having outstanding characteristics for application as bottom cells in TPSC devices. The deep HOMO energy levels, outstanding photovoltaic parameters in single-junction cells, high absorption coefficients, and good thermal stability all contribute to their efficacy as WBG tandem subcells. The correlation between bottom and top cells was analyzed by charge transport modeling and optical simulations which provided detailed information about each material's contribution to high TPSC performance. The observed PCE of 11.42% and high  $V_{oc}$  of 1.64 V TPSCs effectively demonstrated that the synthetic approach of side chain fluorination in conjugated polymers (P1 and P2) constitutes a highly effective strategy to design bottom cells materials for TPSCs. Overall, our results constitute an excellent example for new materials design approaches to advance the field of TPSCs. In addition, we anticipate that the judicious exchange of the current LBG in the study for one with a lower bandgap may lead to additional improvements in device characteristics and set new milestones in the field of TPSCs.

## Chapter 4. Effect of Each Layers in $\text{Sb}_2\text{O}_3/\text{Ag}/\text{Sb}_2\text{O}_3$ Semitransparent Electrode on Organic Solar Cells

### 4.1 Research Background

Semitransparent solar cells are a type of attractive technology to suggest great capability of integration for windows in building as an aesthetically designed energy source. Since organic solar cells (OSCs) based conjugated semiconductor has advantage of inherent transparency corresponding to much higher absorption coefficient than inorganic photovoltaics as well as light weight, color tuning of active material by bandgap engineering, notably, the colorful and semitransparent organic solar cells is suitable for exterior building integrated photovoltaics (BIPV). [7], [54], [55] By introducing effective non-fullerene acceptors, state-of-the-art OSCs have been reported achieving over 14 % [56] and 17.35 % [57] of power conversion efficiency (PCE) for single solar cells and tandem solar cells, respectively. In this regard, since non-fullerene absorbs to the near IR region, OSCs becomes more transparent in a way that the device color depends on donor materials. With the dramatic development of OSCs performance, the research for commercial marketing of OSCs becomes a newly derived direction of OSCs technology to be actively studied.

Dielectric-metal-dielectric (DMD) (it is also called metal oxide-metal-metal oxide (OMO)) multilayer structure, derived from optical interference at interface of dielectric layer and metal layer, is feasible to be use transparent electrode as an alternative indium tin oxide (ITO) electrode. [27, 58] In terms of application to OSCs of DMD electrode, since buffer layers both of electron transport layer (ETL) such as  $\text{ZnO}$ ,  $\text{TiO}_x$ , [59]  $\text{TiO}_2$ ,  $\text{SnO}_2$ , etc. and hole transport layer (HTL) such as  $\text{NiO}$ ,  $\text{MoO}_3$ ,  $\text{V}_2\text{O}_3$ , etc. are generally semiconducting metal oxides, the combination of OSCs and DMD structure can be easily implemented considering the OSCs structure type. The DMD transparent electrode have been introduced as  $\text{ZnS}/\text{Ag}/\text{ZnS}$ , [60]  $\text{MoO}_3/\text{Ag}/\text{MoO}_3$ , [61]  $\text{GZO}/\text{Ag}/\text{GZO}$  [62] and so on for OSCs application with high transmittance and low sheet resistance, and the DMD multilayer electrode have been commonly used bottom electrode instead of ITO electrode.

In this work, DMD transparent electrode-composed of thin  $\text{Ag}$  and  $\text{Sb}_2\text{O}_3$  layers, fabricated by thermal evaporation method for easy deposition, were applied to organic solar cells as a top electrode. We investigated the roles of each layers in the DMD electrode with controlling film thickness, including effect of bottom  $\text{Sb}_2\text{O}_3$  layer on thin  $\text{Ag}$  film, of  $\text{Ag}$  thickness on entire OSCs, and of top  $\text{Sb}_2\text{O}_3$  layer on transmittance and OSCs performance. In addition, it also demonstrated the possibility of the aesthetic OSCs by fabricating entirely colorful and semitransparent OSCs with active blends of red, green and blue.

## 4.2 Experimental

### 4.2.1. OSCs Fabrication with OMO Electrode

Polymer solar cells were fabricated with a configuration of indium tin oxide (ITO)/poly(3,4-ethylenedioxythiophene): poly(styrenesulfonate) (PEDOT:PSS)/Donor:Acceptor/ZnO NPs/Ag or SAS. The cleaned ITO substrates were ultraviolet- ozone treated for 20 min and PEDOT:PSS (Baytron P clevios™ AI 4083, Germany) was spin-coated (ca. 45 nm thick), dried at 140 °C for 10 min and transferred into a nitrogen filled glove box. The used active blends were J52:IEICO-4F, PTB7-Th:IEICO-4F and PBDB-T:ITIC-m for red, green, blue, respectively. These active blends were spin-cast on top of the PEDOT: PSS film. The devices were pumped down in vacuum ( $<10^{-6}$  Torr) and SAS multi-layers were deposited on top of the active layer by thermal evaporation using a shadow mask (3.51 mm<sup>2</sup>). The current density-voltage ( $J$ - $V$ ) characteristics were measured using a Keithley 2635 (USA) source measurement unit under AM 1.5G illumination at 10-100 mW cm<sup>-2</sup>. External quantum efficiency (EQE) measurement was conducted in ambient air using an EQE system (Model QEX7) from PV measurements Inc. Sb<sub>2</sub>O<sub>3</sub> layers were deposited by 1.2-1.6 Ås<sup>-1</sup> and Ag thin films were deposited by 1.4-2.0 Ås<sup>-1</sup>.

## 4.3 Results and Discussion

### 4.3.1 Fabrication of Dielectric-Metal-Dielectric (DMD) Multilayer

To fabricate semitransparent organic solar cells, transparent electrode based on DMD multilayer were firstly studied. Sb<sub>2</sub>O<sub>3</sub> (antimony trioxide) were selected as dielectric portion of DMD electrode as shown in **Figure 4.1(a)**. The Sb<sub>2</sub>O<sub>3</sub> has distinct optical property of high refractive index ( $n$ ) and low absorption coefficient ( $a$ ) (**Figure 4.1(b)**), which is suitable to be dielectric layer to obtain high transmittance and reduced reflection in even thick layer. Silver (Ag) was also chosen for thin metallic film due to high conductivity and lowest absorptivity in the visible range of 400-800 nm wavelength among other metals such as gold, copper, aluminum. As regard to application to OSCs, ZnO semiconducting layer can also be served as a dielectric layer. However, since the optimal thickness of ZnO nanoparticles (NPs) layer as an ETL has been fixed, the influence of ZnO NPs thin film has been excluded in this work. The sandwich structure of Sb<sub>2</sub>O<sub>3</sub>-Ag-Sb<sub>2</sub>O<sub>3</sub> (SAS) multilayer exploits reasonable low sheet resistance of around 10 Ω/sq, 4 Ω/sq and 3 Ω/sq for case in 10 nm, 15 nm and 20 nm of thin Ag film, respectively. As shown in **Figure 4.1 (c)**, the measured sheet resistances of SAS films are independent on top Sb<sub>2</sub>O<sub>3</sub> layer which is even upto 60 nm, indicating the sheet resistance is determined by only Ag films thickness. The SAS multilayer by dielectric-metal interference carries out high transmittance. **Figure 4.1** resents the transmittance of SAS structure depending on thickness of Ag thin film of **(d)** 10 nm, **(e)** 15 nm and **(f)** 20 nm, respectively and thickness of top Sb<sub>2</sub>O<sub>3</sub> layer. The dash lines are transmittance spectrum calculated by transfer matrix using the measured Sb<sub>2</sub>O<sub>3</sub> optical values ( $n$ ,  $k$ ), and solid lines are



experimental transmittance peaks, and the two transmittances are shown to be consistent for each condition. Thinner Ag film-based SAS multilayer exhibited higher transmittance and more red-shifted maxima peak of transmittance at fixed a thickness of  $\text{Sb}_2\text{O}_3$  top layer as well as more broaden width of the peaks. In addition, at a fixed Ag thin films, increasing thickness of top  $\text{Sb}_2\text{O}_3$  layer showed more red-shift and lower transmittance, and the decreasing transmittance is shown more severely depending on increasing Ag film thickness. The photos corresponding the SAS multilayer were in **Figure 4.2**.

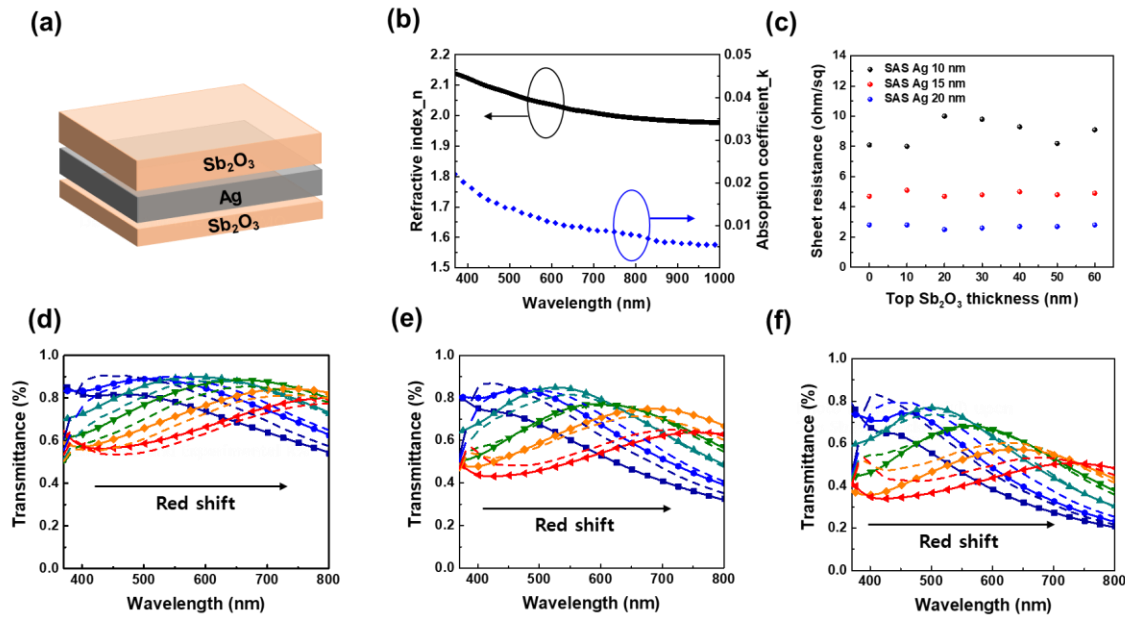


**Figure 4. 1** (a) structure of  $\text{Sb}_2\text{O}_3/\text{Ag}/\text{Sb}_2\text{O}_3$  multilayer for top electrode (b) obtained optical properties such as refractive index ( $n$ ) and absorption coefficient ( $k$ ), (C) sheet resistance depending on increasing thickness of top  $\text{Sb}_2\text{O}_3$  film, (d)-(F) calculated and experimental transmittance of SAS multilayers depending on thickness of upper  $\text{Sb}_2\text{O}_3$  for 10nm, 15 nm and 20 nm of Ag film

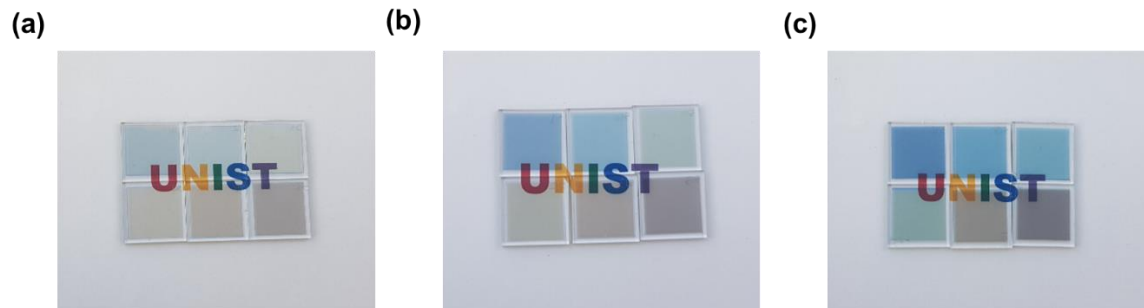


**Figure 4. 2** Photo of  $\text{Sb}_2\text{O}_3/\text{Ag}/\text{Sb}_2\text{O}_3$  multilayer based Ag thin films of (a) 10, (b) 15 and (c) 20 nm, respectively

### 4.3.2 The Role of Bottom $\text{Sb}_2\text{O}_3$ Thin Layer

To investigate role of thin  $\text{Sb}_2\text{O}_3$  films on ZnO NPs in entire OSCs prior to application intact SAS multilayer as top electrode, OSCs were fabricated in configuration of ITO/ poly(3,4-ethylenedioxythiophene) polystyrene sulfonate (PEDOT:PSS)/PTB7-Th:IEICO-4F/either ZnO NPs or  $\text{Sb}_2\text{O}_3$ /20 nm Ag/ 30 nm  $\text{Sb}_2\text{O}_3$  for conventional structure as shown in **Figure 4.3 (a)**. The optimized ZnO NPs layer was 20 nm. We fabricated OSCs with various thickness of  $\text{Sb}_2\text{O}_3$  layer as an ETL to confirm the electrical property, as a result, 2 nm  $\text{Sb}_2\text{O}_3$  layer showed higher performance arising from FF improvement and  $J_{sc}$  increase (**Figure 4.4** and **Table 4.1**). However, since  $\text{Sb}_2\text{O}_3$  has higher band gap ( $E_g$ ) of 4.3 eV and lower conductivity compared to ZnO NPs, it showed that it does not implement well as an ETL. **Figure 4.3 (b)**, exploited SEM image of 20 nm thin Ag films with or without thin  $\text{Sb}_2\text{O}_3$  layer on ZnO NPs layer, interestingly, just 2 nm  $\text{Sb}_2\text{O}_3$  layer led to uniform Ag thin films compared to Ag film deposited without  $\text{Sb}_2\text{O}_3$  on ZnO NPs layer, indicating that  $\text{Sb}_2\text{O}_3$  film was sufficient as an oxide support to enhance the wetting of Ag film. <sup>[63]</sup> In this regard, AFM and additional SEM for various Ag thin films were also measured as shown in **Figure 4.5** and **Figure 4.6**, films with presence of  $\text{Sb}_2\text{O}_3$  showed smoother and all coverage appearance.

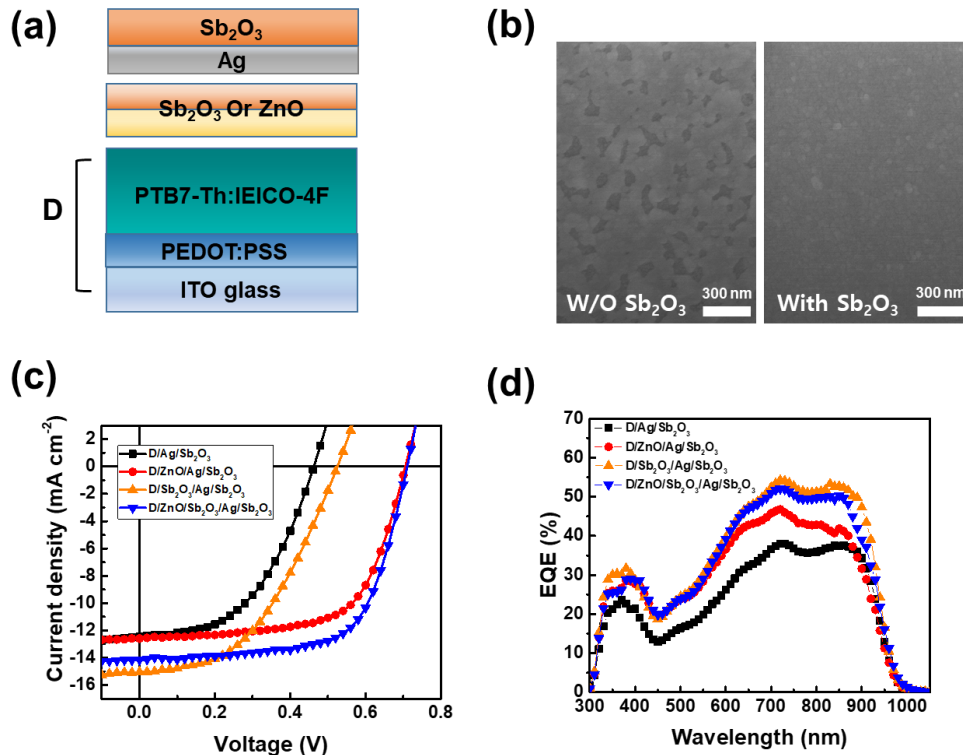


**Figure 4. 3** (a) OSCs structure (b) SEM image of Ag thin film (20nm) with and without  $\text{Sb}_2\text{O}_3$  thin layer (c)  $J$ - $V$  characteristics with and without  $\text{Sb}_2\text{O}_3$  thin layers, (d) EQE spectra according the photovoltaic performance

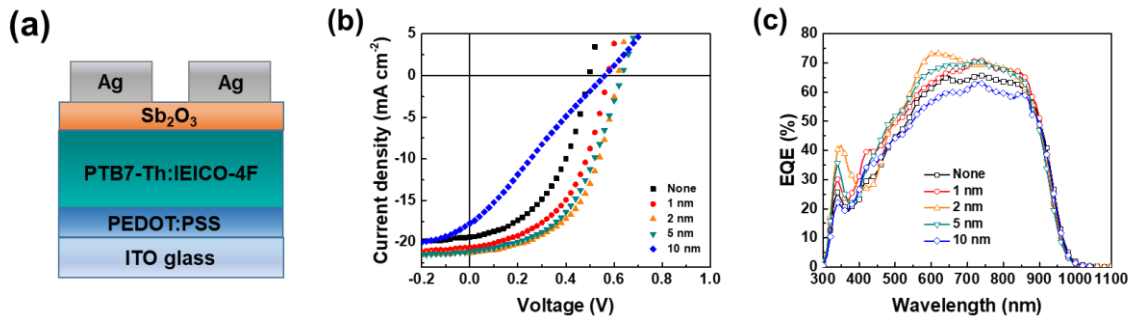


**Figure 4.** (a) Fabricated OSCs structure (b)  $J$ - $V$  characteristics of  $\text{Sb}_2\text{O}_3$  ETLs and (c) EQE spectra according the photovoltaic performance

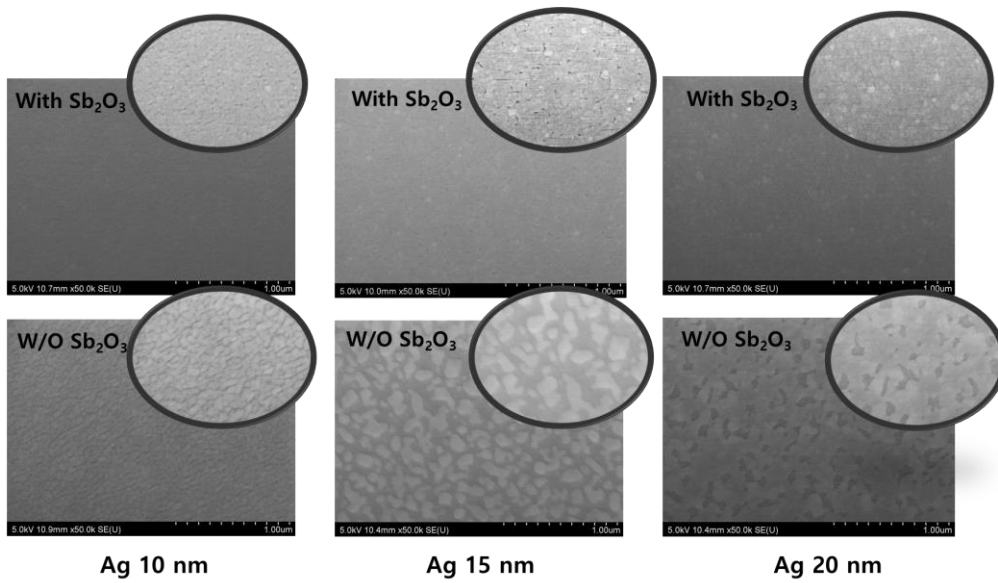


**Figure 4. 5** SEM images of Ag thin film with and without 2 nm  $\text{Sb}_2\text{O}_3$  thin films on ZnO NPs layer

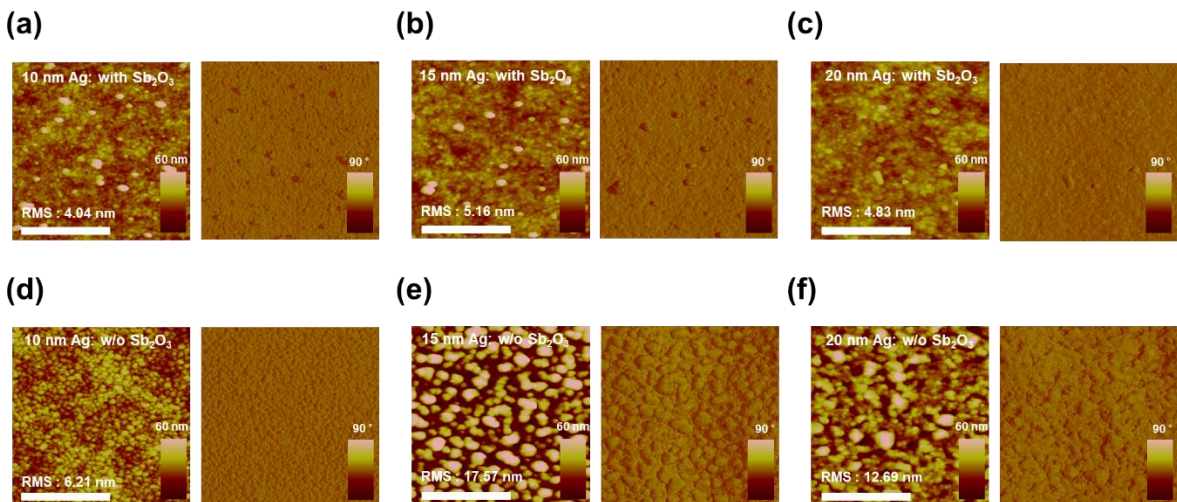


**Figure 4. 6** AFM images of 10 nm, 15 nm and 20 nm Ag thin films with and without 2nm  $\text{Sb}_2\text{O}_3$  thin films on ZnO NPs layers

**Table 4. 1** Photovoltaic parameters of OSCs fabricated with Sb<sub>2</sub>O<sub>3</sub> layer as an ETL

<b>Sb<sub>2</sub>O<sub>3</sub> Thickness (nm)</b>	<b><i>J</i><sub>sc</sub> (mA cm<sup>-2</sup>)</b>	<b><i>Cal. J</i><sub>sc</sub> (mA cm<sup>-2</sup>)</b>	<b><i>V</i><sub>oc</sub> (V)</b>	<b>FF</b>	<b>PCE (%)</b>
None	19.38	19.41	0.50	0.47	4.52
1	20.62	20.65	0.57	0.50	5.96
2	21.29	21.14	0.62	0.54	7.04
5	21.12	20.80	0.63	0.49	6.57
10	17.74	18.50	0.56	0.25	2.54

As shown in **Figure 4.3 (c-d)** and **Table 4.2**, absence of ETL showed low performance of 2.83 % PCE resulted from poor photovoltaic parameters. Although introduction of ZnO NPs layer derived increase of FF and *V*<sub>oc</sub>, *J*<sub>sc</sub> was still low. In contrast, uses of Sb<sub>2</sub>O<sub>3</sub> layer as an ETL showed significantly higher *J*<sub>sc</sub> (15.05 mA cm<sup>-2</sup>) and poor FF and *V*<sub>oc</sub> values. By depositing collaborated ZnO- Sb<sub>2</sub>O<sub>3</sub> layer stack, the higher performance with the improved *J*<sub>sc</sub>, *V*<sub>oc</sub> and FF were obtained corresponding combination both positive influence for photovoltaic parameters. This double oxide layers showed 6.71 % of PCE, 14.32 mA cm<sup>-2</sup> of *J*<sub>sc</sub>, 0.71 V of *V*<sub>oc</sub> and 0.66 of FF. In brief, ZnO NPs layer worked for effective electron transfer in OSCs, and Sb<sub>2</sub>O<sub>3</sub> worked for preferential coverage of thin Ag films in OMO multilayer system as well as for transparent electrode via optical interference.

**Table 4. 2** Photovoltaic parameters of device with and without ETLs

<b>Top electrode (nm)</b>	<b>Device condition</b>	<b><i>J</i><sub>sc</sub> (mA cm<sup>-2</sup>)</b>	<b><i>Cal. J</i><sub>sc</sub> (mA cm<sup>-2</sup>)</b>	<b><i>V</i><sub>oc</sub> (V)</b>	<b>FF</b>	<b>PCE (%)</b>
Ag 20nm/Sb <sub>2</sub> O <sub>3</sub> 30 nm	D/Ag	12.45	10.16	0.46	0.49	2.83
	D/ZnO/Ag	12.59	12.50	0.71	0.65	5.71
	D/Sb <sub>2</sub> O <sub>3</sub> /Ag	15.05	14.61	0.53	0.46	3.64
	D/ZnO/Sb <sub>2</sub> O <sub>3</sub> /Ag	14.32	13.96	0.71	0.66	6.71

### 4.3.3 Effect of Ag Thin Film in SAS Electrode

To examine the effect of thin Ag film in SAS electrode on entire OSCs, 10 nm, 15 nm and 20 nm thickness of Ag film sandwiched between dielectrics were prepared and applied to the device. These three kinds of Ag films were deposited by thermal evaporation on 2 nm of bottom  $\text{Sb}_2\text{O}_3$  dielectric layer and 30 nm of top  $\text{Sb}_2\text{O}_3$  dielectric layers were deposited after Ag films for complete transparent SAS electrode. Additionally, controlled basic OSCs had a fixed configuration of ITO/PEDOT:PSS/PTB7-Th:IEICO-4F/ZnO NPs as shown in **Figure 4.7 (a)**. semitransparent OSCs were tested under 1 sun ( $100 \text{ mW cm}^{-2}$ ) irradiation. As a result, the OSCs showed 7.34 %, 5.73 % and 3.37% of PCE in case of 20 nm, 15 nm and 10 nm thickness of Ag films with 25.81%, 30.98 % and 31.83 % of average visible transmittance (AVT, 380-780 nm) for whole device, respectively, at ITO side of 1sun illumination (**Figure 4.7 (b) and (d)**). Which indicated that OSCs with thicker Ag films are able to reabsorb the reflected photon from top metallic film leading to significant  $J_{sc}$  enhancement and increasing the thickness of the metal layer contributes to reduction of OSCs transmittance due to their high reflection and absorption. As shown in **Table 4.3** summarized photovoltaic parameters of performance both side of illumination, increasing Ag thickness also carried out increases of FF parameter correlating to sheet resistance of Ag thin films, furthermore, the resistance has effect on  $J_{sc}$  parameters. For the top illumination (SAS side), the 10 nm Ag film-based OSCs showed 2.42 % of PCE resulted from  $5.51 \text{ mA cm}^{-2}$  of  $J_{sc}$ , 0.69 V of  $V_{oc}$  and 0.64 of FF, the case of 15 nm Ag film showed 3.26 % of PCE with  $7.04 \text{ mA cm}^{-2}$  of  $J_{sc}$ , 0.69 V of  $V_{oc}$  and 0.67 of FF. The enhanced current density is from the highly improved sheet resistance of Ag film, which corresponds to significantly reduced series resistance ( $R_s$ ) from  $33.37$  to  $6.22 \Omega \text{ cm}^2$ . In contrast, In the SAS side illumination, the OSCs of 20 nm thick Ag film showed a decreased in  $J_{sc}$  compared to case of 15 nm thick due to the dramatically reduced photons at lower transmittance of the SAS electrode than relatively reduced series resistance. On the other hand, in comparison between illumination direction at same thickness of Ag films, the increased FF and decreased  $V_{oc}$ s were obviously manifested. Notably, OSCs of 10 nm thick Ag films more clearly showed the FF increase, these appearances relate to shunt resistance ( $R_{sh}$ ) and series resistance of SAS electrode. In this regard, OSCs with three kinds thickness of Ag films in SAS were measured under various light intensity (**Figure 4.8**) in order to investigate the relationship both resistance and OSCs performance and indirectly explain the increased FF and decreased  $V_{oc}$  in SAS side illumination. **Figure 4.7 (e)** shows a graph of FF depending on light intensity for SAS electrodes measured in ITO side illumination. Thinner Ag films in SAS electrode showed the larger slopes (slope:  $10 \text{ nm} > 15 \text{ nm} > 20 \text{ nm}$ ). The 10 nm thick Ag films showed highly improved FF at less photons of lower light intensity than the other case, because it has higher shunt resistance, which is consistent that the large slope on the FF dependence on the light intensity is only affected by large  $R_{sh}$ , not by  $R_s$ . Hence, the reduced light through lower transmittance of SAS electrode compared to ITO side might cause decrease of  $V_{oc}$  and  $J_{sc}$  and FF increase.

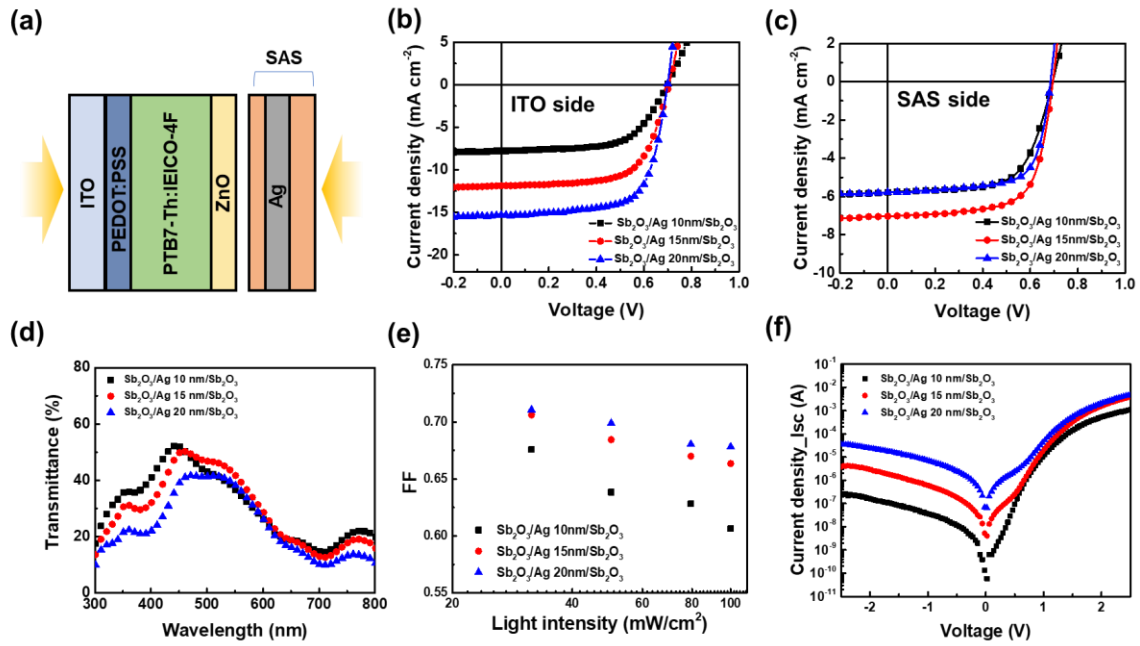


**Figure 4. 7** (a) Illustration of transparent device with both light side (b)  $J$ - $V$  characteristics depending on Ag thickness (ITO side illumination) (C)  $J$ - $V$  characteristics of SAS side-illumination (d) corresponding transmittance from ITO to SAS electrode (e) FF versus light intensity (f) dark current of the devices.

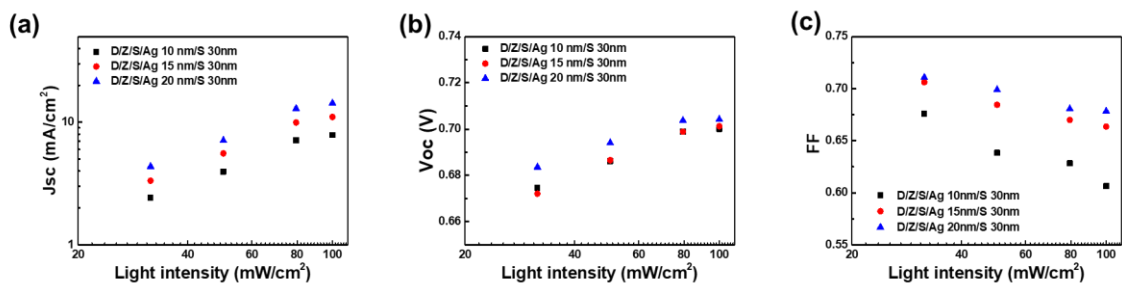


**Figure 4. 8** Light intensity dependence of (a)  $J_{sc}$  , (b)  $V_{oc}$ , and (c) FF of OSCs based on SAS electrode with different Ag thickness

**Table 4. 3** Photovoltaic parameters of devices depending on Ag thickness of SAS top electrode

Top Ag electrode (nm)	Illumination direction	$J_{sc}$ (mA cm <sup>-2</sup> )	$V_{oc}$ (V)	FF	PCE (%)	AVT	Rsh (k $\Omega$ cm <sup>2</sup> )	Rs ( $\Omega$ cm <sup>2</sup> )
10	ITO	7.79	0.70	0.62	3.37	31.83	2657.07	33.37
	SAS	5.51	0.69	0.64	2.42			
15	ITO	12.36	0.70	0.66	5.73	30.98	169.18	7.07
	SAS	7.04	0.69	0.67	3.26			
20	ITO	15.34	0.70	0.68	7.34	25.81	9.86	6.22
	SAS	5.78	0.69	0.69	2.76			

#### 4.3.4 Effect of Thickness of Top Sb<sub>2</sub>O<sub>3</sub> Dielectric Layer on OSCs

The last optical interference at interface of dielectric/metal layer in DMD multilayer generally has effect on overall transmittance of the corresponding DMD electrode by maximizing the transmission of the light of interest. As mentioned before (**Figure 4.1 (d)-(f)**), increasing thickness of top Sb<sub>2</sub>O<sub>3</sub> layer showed red shifted transmittance with decreasing maximum transmittance peak, typically it is clearly observed in the thicker Ag films. This appearance naturally affected the application of DMD electrode to OSCs. The control OSCs structure was composed of ITO/PEDOT:PSS/PTB7-Th:IEICO-4F/ZnO NPs/2nm thick Sb<sub>2</sub>O<sub>3</sub> and Ag electrode of 20 nm, and top Sb<sub>2</sub>O<sub>3</sub> layers were deposited from 10 nm to 60 nm thickness. **Figure 4.9** represents 20 nm Ag film-based OSCs performances both side of light illumination and transmittance for entire device configured ITO to DMD electrode. The photovoltaic parameters were listed in **Table 4.4**. For OSCs performance tested through light of ITO side, 10 nm and 60 nm of top Sb<sub>2</sub>O<sub>3</sub> layer showed relatively higher  $J_{sc}$ s, relating to optical transmittance of SAS electrode and optical property of active blends. Since the active blend is able to absorb until near IR region (from 300 nm to 1050 nm of wavelength), for 10 nm thick Sb<sub>2</sub>O<sub>3</sub>, active layer reabsorbs the reflected photons in larger wavelength region with reduced photon loss. While, 60 nm thick Sb<sub>2</sub>O<sub>3</sub>-based DMD showed maxima peak of transmittance at 720-750 nm, the wavelength is consistent with the highest absorption region of active blend, indicating that the photons are enough absorbed to generate high current density regardless of photon loss. Furthermore, it is observed that for OSCs tested on the SAS electrode side of the illumination, the increase in the  $J_{sc}$  value is dependent on the increased thickness of the upper Sb<sub>2</sub>O<sub>3</sub> layer of the SAS electrode. The transmittance of overall device has similar tendency with transmittance of SAS multilayers, the highest AVT is 29.30 % at OSCs with SAS electrode based on Ag thin films of 20 nm and upper Sb<sub>2</sub>O<sub>3</sub> layer of 20 nm. The performance depending

on thickness of Ag thin films and upper  $\text{Sb}_2\text{O}_3$  layers are shown in **Figure S3** and **Table S2**, in addition, corresponding the transmittance for whole device are shown in **Figure S4**. The highest transmittance was at 34.35% in the OSCs based on a 15nm Ag film and a 40 nm top  $\text{Sb}_2\text{O}_3$  film, with 5.65 % of PCE.

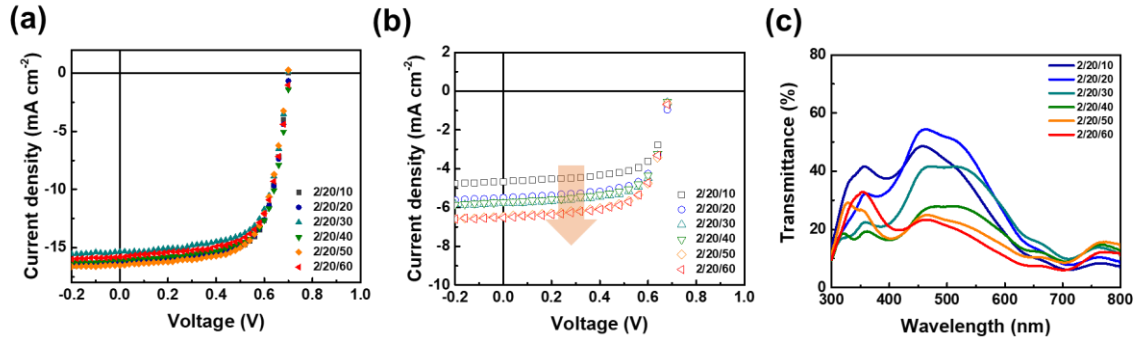


**Figure 4. 9**  $J$ - $V$  characteristics of (a) ITO side and (b) SAS side illumination for semitransparent OSCs based on thickness of  $\text{Sb}_2\text{O}_3$  top layers with 20 nm Ag thin film, and corresponding transmittance of whole device

**Table 4. 4** Photovoltaic parameters of devices depending on thickness of top  $\text{Sb}_2\text{O}_3$  layer in 20 nm Ag-based SAS electrode

Top $\text{Sb}_2\text{O}_3$ Thickness (nm)	Illumination direction	$J_{sc}$ ( $\text{mA cm}^{-2}$ )	$V_{oc}$ (V)	FF	PCE (%)	AVT
10	ITO	16.36	0.70	0.69	7.88	25.23
	SAS	4.66	0.69	0.69	2.21	
20	ITO	16.27	0.70	0.68	7.81	29.30
	SAS	5.49	0.69	0.69	2.62	
30	ITO	15.34	0.70	0.68	7.34	25.81
	SAS	5.78	0.69	0.69	2.76	
40	ITO	16.09	0.70	0.69	7.75	18.44
	SAS	5.72	0.69	0.69	2.70	
50	ITO	15.82	0.71	0.66	7.38	16.33
	SAS	6.46	0.69	0.68	3.00	
60	ITO	16.52	0.70	0.67	7.77	14.44
	SAS	6.53	0.69	0.67	3.00	



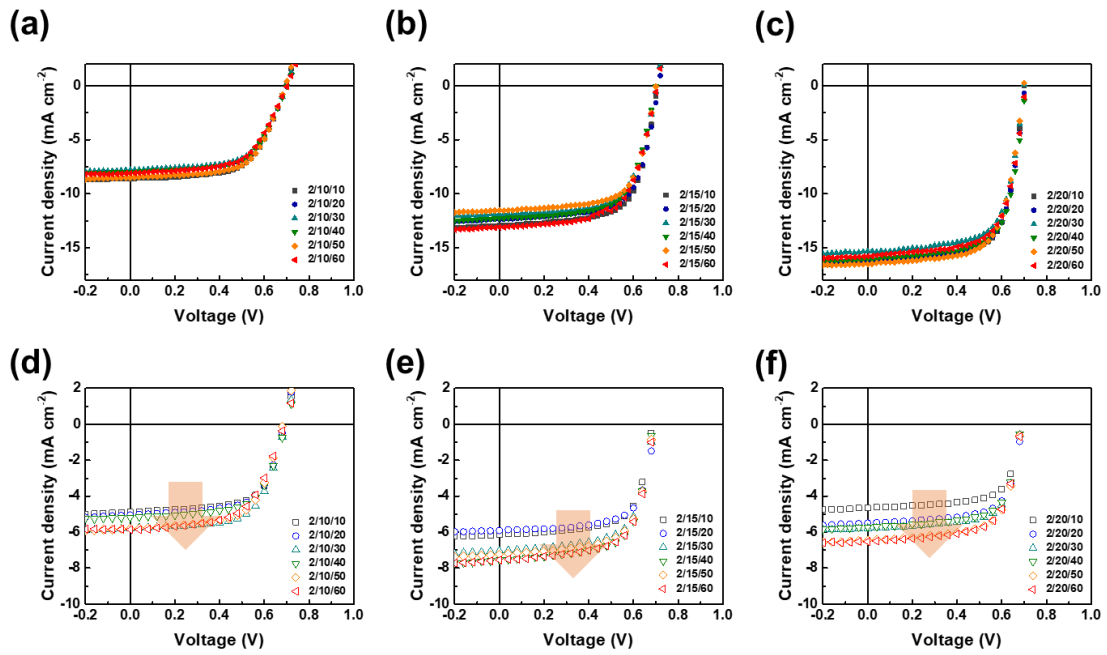


**Figure 4. 10**  $J$ - $V$  characteristics of ITO side and SAS side illumination for semitransparent OSCs depending on various Ag thickness

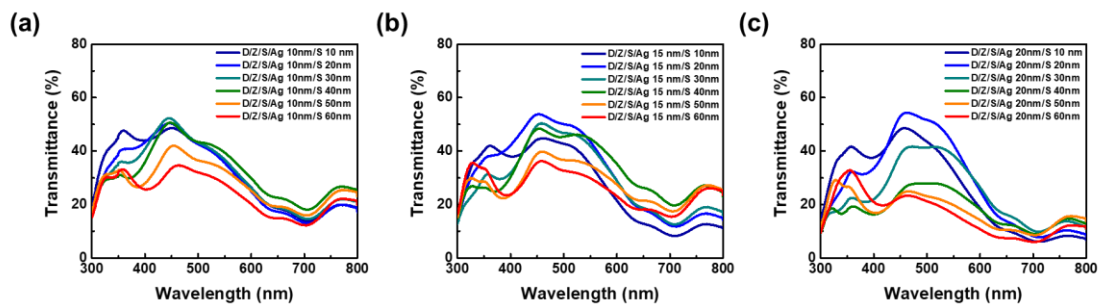


**Figure 4. 11** Device transmittance (ITO to SAS) of various Ag thickness and top  $\text{Sb}_2\text{O}_3$  layer

**Table 4. 5** Photovoltaic parameters of devices depending on thickness of top  $\text{Sb}_2\text{O}_3$  layer in SAS electrode

Top Ag electrode (nm)	Top $\text{Sb}_2\text{O}_3$ Thickness (nm)	Illumination direction	$J_{\text{SC}}$ ( $\text{mA cm}^{-2}$ )	$V_{\text{OC}}$ (V)	FF	PCE (%)	AVT
10	10	ITO	8.58	0.70	0.62	3.71	30.86
		SAS	4.88	0.69	0.65	2.21	
	20	ITO	7.93	0.70	0.62	3.42	30.34
		SAS	5.05	0.69	0.65	2.27	
	30	ITO	7.79	0.70	0.62	3.37	31.83
		SAS	5.61	0.69	0.64	2.42	
	40	ITO	7.97	0.70	0.62	3.47	32.94
		SAS	5.18	0.70	0.64	2.31	
	50	ITO	8.50	0.69	0.63	3.69	27.76
		SAS	5.81	0.68	0.63	2.48	
	60	ITO	8.10	0.70	0.60	3.41	23.22
		SAS	5.86	0.69	0.59	2.40	
15	10	ITO	12.95	0.71	0.67	6.13	26.44
		SAS	6.15	0.68	0.68	2.86	
	20	ITO	12.36	0.71	0.66	5.86	32.64
		SAS	5.91	0.70	0.69	2.84	
	30	ITO	12.36	0.70	0.66	5.73	30.98
		SAS	7.04	0.69	0.67	3.26	
	40	ITO	12.27	0.70	0.66	5.65	34.35
		SAS	7.55	0.69	0.67	3.48	
	50	ITO	11.54	0.70	0.67	5.43	28.14
		SAS	7.24	0.69	0.67	3.33	
	60	ITO	12.61	0.70	0.67	5.90	25.26
		SAS	7.55	0.69	0.67	3.46	

### 4.3.5 Colorful Semitransparent OSCs

We finally demonstrated the colorful semitransparent organic solar cells by using colorful active blends and application SAS multilayer. To implement red (R), green (G), blue (B) colored device, J52:IEICO-4F, PTB7-Th:IEICO-4F (this blend was used as base OSCs in this work.), PBDB-T:ITIC-m blends were used as shown in **Figure 4.12 (a)**. **Figure 4.12 (b)** and **(c)** show  $J-V$  characteristics and corresponding photos of the colorful semitransparent OSCs. In the photo, the transparent 'L' shape in each device is due to SAS electrode, shapes of circle and long rods is overall device. When OSCs were fabricated with 20 nm Ag film and 10 nm top  $\text{Sb}_2\text{O}_3$  layer and measured on ITO side of illumination, the J52:IEICO-4F-based red OSCs showed 23.02 % of AVT and 6.51 % of PCE resulted from 13.96  $\text{mA cm}^{-2}$  of  $J_{sc}$ , 0.72 V of  $V_{oc}$  and 0.65 of FF, the blue OSCs showed 6.33 % of PCE with 10.58  $\text{mA cm}^{-2}$  of  $J_{sc}$ , 0.91 V of  $V_{oc}$ , 0.65 of FF and 22.98 % of AVT respectively. In addition, Blue OSCs based on PBDB-T:ITIC-m blend showed relatively higher performance showing 3.00 % of PCE at irradiation through SAS electrode compared to green OSCs (2.21 %) and red OSCs (1.81 %). According to the relationship between the optical absorption of the photoactive layers and the transmittance of the SAS electrodes, the OSCs performance can be expected to have higher performance of red, green, blue in this order under assuming that colorful active blends have same absorption range and OSCs performance. The performance for colorful OSCs fabricated with control of upper  $\text{Sb}_2\text{O}_3$  layer were shown in **Figure 4.13** and **Table 4.7**, in addition, corresponded transmittances of device were also shown. We believe that these colorful semitransparent OSCs can be applied to commercial applications such as BIPV and aesthetic exterior items.

**Table 4. 6** Photovoltaic parameters of colorful OSCs fabricated with 20 nm Ag and 10 nm top  $\text{Sb}_2\text{O}_3$  laye-based SAS electrode

D:A	Top $\text{Sb}_2\text{O}_3$ Thickness (nm)	Illumination direction	$J_{sc}$ ( $\text{mA cm}^{-2}$ )	$V_{oc}$ (V)	FF	PCE (%)	AVT of device (%)
J52 :IEICO-4F	10	ITO	13.96	0.72	0.65	6.51	23.02
		SAS	4.17	0.69	0.67	1.81	
PTB7-Th :IEICO-4F	10	ITO	16.36	0.70	0.69	7.88	25.23
		SAS	4.66	0.69	0.69	2.21	
PBDB-T :ITIC-m	10	ITO	10.58	0.91	0.65	6.33	22.98
		SAS	4.93	0.89	0.68	3.00	

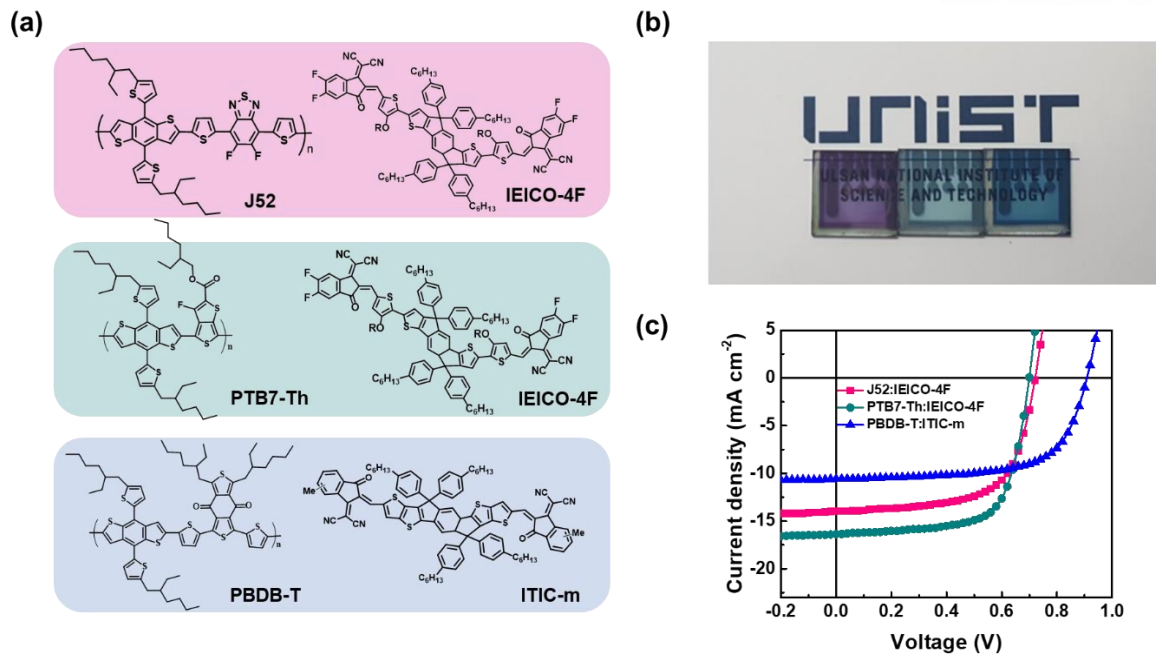


**Figure 4. 12** (a) Chemical structures for colorful semitransparent OSCs (b) photo of devices (c) J-V characteristics of colorful devices.

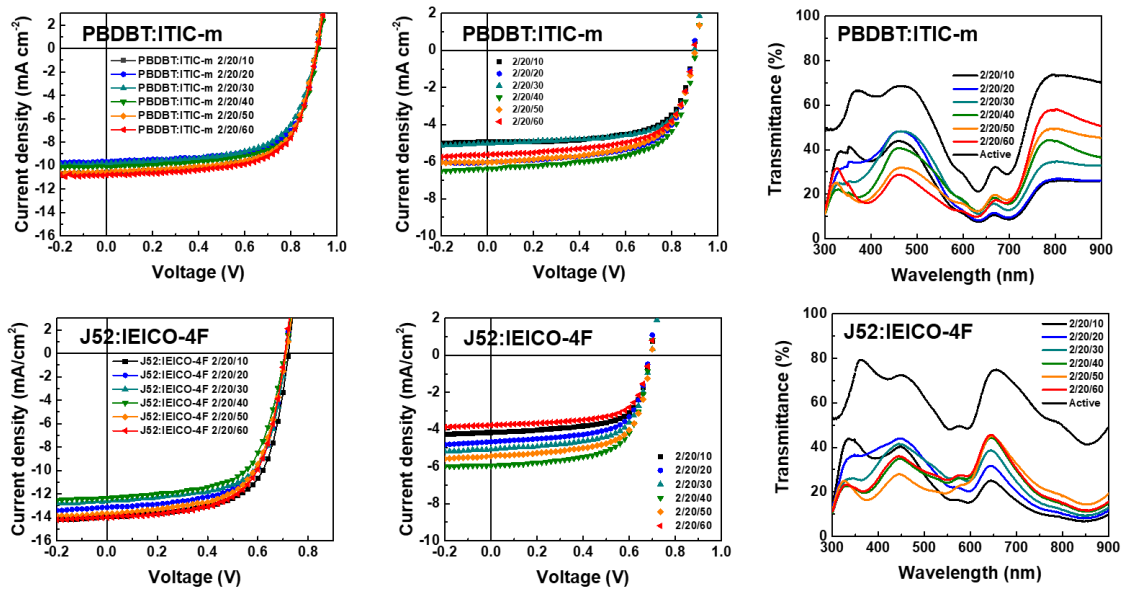


**Figure 4. 13** Semitransparent OSCs based on PBDBT:ITIC-m blend and J52:IEICO-4F blend with various thickness of top Sb<sub>2</sub>O<sub>3</sub> layer

**Table 4. 7** OSCs performance of Blue active blends (PBDB-T:ITIC-m) and red active blends (J52:IEICO-4F).

D:A	Top Ag electrode (nm)	Top Sb <sub>2</sub> O <sub>3</sub> Thickness (nm)	Illumination direction	$J_{sc}$ (mA cm <sup>-2</sup> )	$V_{oc}$ (V)	FF	PCE (%)	AVT		
PBDB-T :ITIC-m	20	10	ITO	10.58	0.91	0.65	6.33	22.98		
			SAS	4.93	0.89	0.68	3.00			
		20	ITO	9.66	0.91	0.67	5.89	25.22		
			SAS	6.04	0.89	0.65	3.52			
		30	ITO	9.82	0.91	0.64	5.71	27.82		
			SAS	5.02	0.89	0.68	3.07			
		40	ITO	10.12	0.91	0.66	6.13	26.36		
			SAS	6.04	0.90	0.65	3.52			
		50	ITO	10.56	0.91	0.66	6.33	22.88		
			SAS	5.78	0.90	0.66	3.42			
		60	ITO	10.82	0.91	0.66	6.49	21.95		
			SAS	5.63	0.90	0.65	3.27			
			100	-	ITO	14.97(14.40)	0.92	0.66	9.10	-
		J52 :IEICO-4F	20	10	ITO	13.96	0.72	0.65	6.51	23.02
SAS	4.17				0.69	0.67	1.81			
20	ITO			13.16	0.71	0.65	6.06	27.85		
	SAS			4.67	0.69	0.66	2.10			
30	ITO			12.62	0.71	0.66	5.89	29.61		
	SAS			5.08	0.69	0.65	2.29			
40	ITO			12.35	0.71	0.63	5.51	28.77		
	SAS			5.96	0.69	0.65	2.67			
50	ITO			13.68	0.71	0.62	6.08	26.73		
	SAS			5.44	0.70	0.66	2.50			
60	ITO			14.02	0.71	0.63	6.30	23.73		
	SAS			3.77	0.69	0.67	1.73			
	100			-	ITO	19.64(19.10)	0.73	0.62	8.95	-

#### 4. Conclusion

DMD multilayer composed of two  $\text{Sb}_2\text{O}_3$  layer and a silver (Ag) layer was used a top electrode for semitransparent OSCs, which called SAS electrode. In this work, the OSCs were fabricated a configuration of ITO/PEDOT:PSS/active layer/ZnO NPs/SAS electrode. The roles of each layers and effects depending thickness of each layers on OSCs had been investigated with introduction of optical and electrical property of  $\text{Sb}_2\text{O}_3$  dielectric.  $\text{Sb}_2\text{O}_3$  is rarely used in DMD multilayer, and it is first time to be successfully applied to organic solar cells. Bottom  $\text{Sb}_2\text{O}_3$  layer had effect on well-coverage of Ag thin films and top  $\text{Sb}_2\text{O}_3$  affected the determination of the maximum transmittance peak of the SAS electrode. The thickness of Ag thin film was related to not only sheet resistance but also series resistance and  $J_{sc}$  enhancement in OSCs. Finally, by implement SAS electrode to colorful active blend, we demonstrated the semitransparent organic solar cells colored red, green and blue with 6.33-7.88 % of PCE and 23-25 % of transmittance. This work suggests ways to approach the DMD multilayer as well as considerations for OSCs applications.

## Chapter 5. Colorful Semitransparent Organic Solar Cells by Adjusting Color Saturation of Fabry-Perot Etalon

### 5.1 Research Background

Growing development of organic solar cells (OSCs) achieving over 14 % power conversion efficiency (PCE) of single bulk heterojunction (BHJ) solar cells recently provides ability for OSCs commercialization such as building integrated photovoltaics, photovoltaic roofs, house windows and so on. The main concept of OSCs market will be alternative energy source of next generation including benefits of flexible, lightweight, colorful and semitransparent properties. State-of-the-art, the smart windows have been reported exhibiting vivid color selection, as developed as organic solar cells have been studied for colorful semitransparent solar cells. There is two ways to easy fabrication for colorful semitransparent solar cells. One is using two transparency electrodes and inherently colorful photoactive blends implying color dominance on donor:acceptor blending, the other one is using color filter on OSCs uniformed absorbing visible range of 300-800 nm, indicating that device color is determined by color filter. The formal strategy for colorful semitransparent OSC can be easily limited by performance of active materials and light loss arising from transparent top electrode and result in lower performance of entire OSCs. Reversely, the latter, color filter based on microcavity of Fabry-Perot etalon, is feasible to choose the wavelength of transmittances and reflections, resulting in higher performance and high transmittance of a selected wavelength. [64, 65]

The Fabry-Perot resonance have been well known for a thin film structure composing two metal mirrors such as silver, gold, copper, aluminum, and transparent dielectric medium such as metal oxides. The generated constructive interferences at interface of metal-dielectric were located cavity layer with a specific light wavelength. The certain wavelength can be selected by thickness of cavity medium. [65, 66]

In this work, we demonstrated the color filter based on  $\text{Sb}_2\text{O}_3$  cavity medium and silver (Ag) metallic mirrors. The effects of each layers were analyzed and the variety color of color filter were implemented. Furthermore, we applied the color filter to organic solar cells based on PTB7-Th:PC<sub>71</sub>BM, where Indium Tin Oxide (ITO) and oxide-metal-oxide (OMO) were used as transparent electrodes.

## 5.2 Experimental

### 5.2.1 OSCs Fabrication with OMO Electrode

Polymer solar cells were fabricated with a configuration of indium tin oxide (ITO)/poly(3,4-ethylenedioxythiophene): poly(styrenesulfonate) (PEDOT:PSS)/PTB7-Th:PC<sub>71</sub>BM/ZnO NPs/Ag or color filter. The cleaned ITO substrates were ultraviolet- ozone treated for 20 min and PEDOT:PSS (Baytron P clevis™ AI 4083, Germany) was spin-coated (ca. 45 nm thick), dried at 140 °C for 1 min and transferred into a nitrogen filled glove box. OMO transparent electrode were deposited by thermal evaporation composing 30 nm Sb<sub>2</sub>O<sub>3</sub> and 15 nm Ag and 2 nm Sb<sub>2</sub>O<sub>3</sub>. The used active blend was PTB7-Th:PC<sub>71</sub>BM, the active blend was spin-cast on top of the PEDOT: PSS film. The devices were pumped down in vacuum ( $<10^{-6}$  Torr) and color filter were deposited on top of the active layer by thermal evaporation using a shadow mask (3.51 mm<sup>2</sup>). The current density-voltage (*J-V*) characteristics were measured using a Keithley 2635 (USA) source measurement unit under AM 1.5G illumination at 100 mW cm<sup>-2</sup>. External quantum efficiency (EQE) measurement was conducted in ambient air using an EQE system (Model QEX7) from PV measurements Inc. Sb<sub>2</sub>O<sub>3</sub> layers were deposited by 1.2-1.6 Ås<sup>-1</sup> and Ag thin films were deposited by 1.4-2.0 Ås<sup>-1</sup> evaporating speed, respectively.

## 5.3 Results and Discussion

### 5.3.1 Color Filters Based on Sb<sub>2</sub>O<sub>3</sub> Cavity Medium and Silver Metallic Mirrors

Sb<sub>2</sub>O<sub>3</sub> dielectric was used as cavity material and Ag was used for metallic mirrors. To investigate the effect of thickness of Ag films and Sb<sub>2</sub>O<sub>3</sub> dielectric film, metal-dielectric-metal structure were fabricated. As shown in **Figure 5.1**, increase of Ag film thickness showed obviously reduced transmittance and decreased peak widths. Furthermore, at same thickness of dielectric medium, the transmittance peaks were blue-shifted with increment of Ag thickness. The green color filter (520-570 nm of wavelength) showed higher transmittance, while blue color filter (around 450 nm wavelength) exhibited lower transmittance due to the overlapping with Ag absorption range.

For applying to OSCs, it is considered the transmittance at a certain wavelength and reflection for reabsorption of photoactive film. As a result, the 25 nm thickness of Ag film was selected as an appropriate thickness of metallic mirror. Color filter structure is shown **Figure 5.2 (a)**. The calculated transmittances were exhibited in **Figure 5.2 (b)**, increasing thickness of Sb<sub>2</sub>O<sub>3</sub> layer showed red shifted transmittance and decreasing maximum transmittance peaks as well as peak widths. The transmittance presented symbols are measured transmittance of color filter which fabricated by 45 nm, 65 nm and 95 nm of Sb<sub>2</sub>O<sub>3</sub> layers for blue, green and red colored selective wavelength according to simulated results. Therefore, we successfully demonstrated vivid three colors for transmission mode and yellow, magenta and cyan colors for reflection mode corresponding to blue, green and red color filters. Figure 5.2 (c) is photos of the color filters.



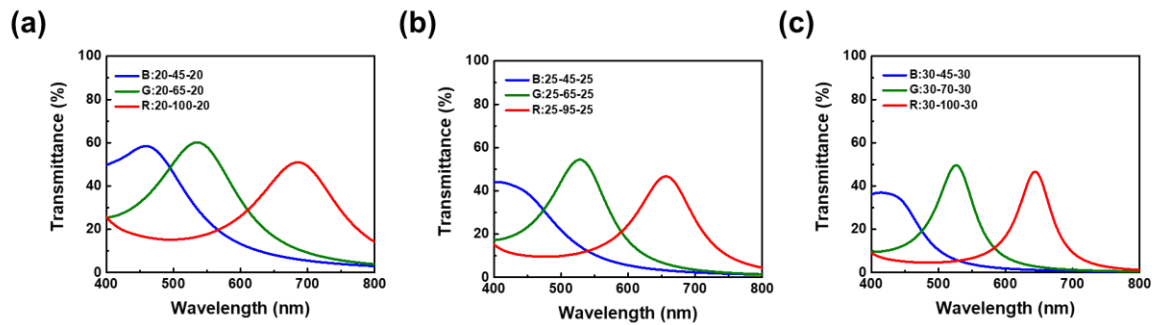


**Figure 5. 1** Transmittance of color filter based on 20 nm, 25 nm and 30 nm of Ag thin films

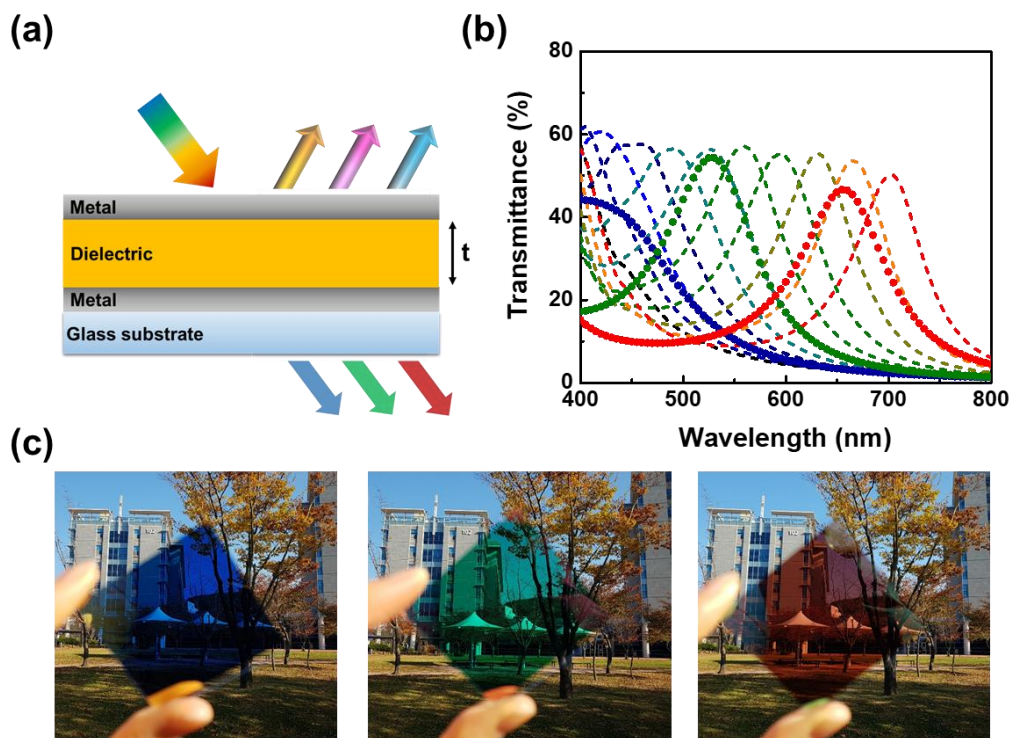


**Figure 5. 2** (a) Color filter structure and (b) calculated and experimental transmittance and (c) photo of color filters

### 5.3.2 Application Color Filter to OSCs

We fabricated the colorful OSCs in configuration of ITO/PEDOT:PSS/PTB7-Th:PC<sub>71</sub>BM/ZnO/color filter or Ag 50nm (**Figure 5.3 (a)**). All OSCs were measured under 100 mWcm<sup>-2</sup>. Figure 5.3 and Table 5.1 showed the performance of OSCs fabricated with color filters. The PCE of the OSCs introducing a 50 nm of Ag films was 8.52 % resulting from 14.79 mA cm<sup>-2</sup> of  $J_{sc}$ , 0.82 V of  $V_{oc}$  and 0.71 of FF. The device has almost dark gray colors, indicating that PTB7-Th:PC<sub>71</sub>BM blends almost fairly absorbed visible light. Since both donor and acceptor has high absorption coefficient and inherent transparency, it was suitable to applying color filter. The current density of the devices with color filter showed 12.37 mA cm<sup>-2</sup>, 12.36 mA cm<sup>-2</sup> and 11.36 mA cm<sup>-2</sup> for blue, green and red, respectively. These appearances indicated that the device performance have been dependent on transmission of top electrode. Since OSCs have been obtained high current density from as longer as wavelength and blue color filter was able to provide the reflection of the longer wavelength irradiation to reabsorption of photoactive layer, blue colored OSCs showed higher current density and performance at same photovoltaic values such as  $V_{oc}$  and FF. **Figure 5.3 (c)** is EQE spectra of corresponding the devices and **Figure 5.3 (d)** is transmittance of entire device (from ITO to color filter), the EQE valley characteristic for the devices is well consistent with the top transmittance. At selected wavelength of color filters, the transmittances were 22.59 % at 450 nm wavelength (blue), 31.76 % at 520 nm wavelength (green) and 30.50 % at 635 nm wavelength (red), respectively. **Figure 5.4** showed electric field of OSCs fabricated with color filter. 200 -300 nm of device position presented photoactive layer. According to selected wavelength of color filter, the electric field intensity showed the consistently reduced intensity.

**Table 5. 1** Photovoltaic parameters of PTB7-Th:PC<sub>71</sub>BM-based OSCs with color filters

Top electrode	$J_{sc}$ (mA cm <sup>-2</sup> )	Cal. $J_{sc}$ (mA cm <sup>-2</sup> )	$V_{oc}$ (V)	FF	PCE (%)
Color filter (Blue)	12.37	12.75	0.81	0.70	7.03
Color filter (Green)	12.36	11.51	0.81	0.71	7.07
Color filter (Red)	11.36	11.86	0.80	0.71	6.43
Ag 50 nm	14.79	14.69	0.82	0.71	8.52

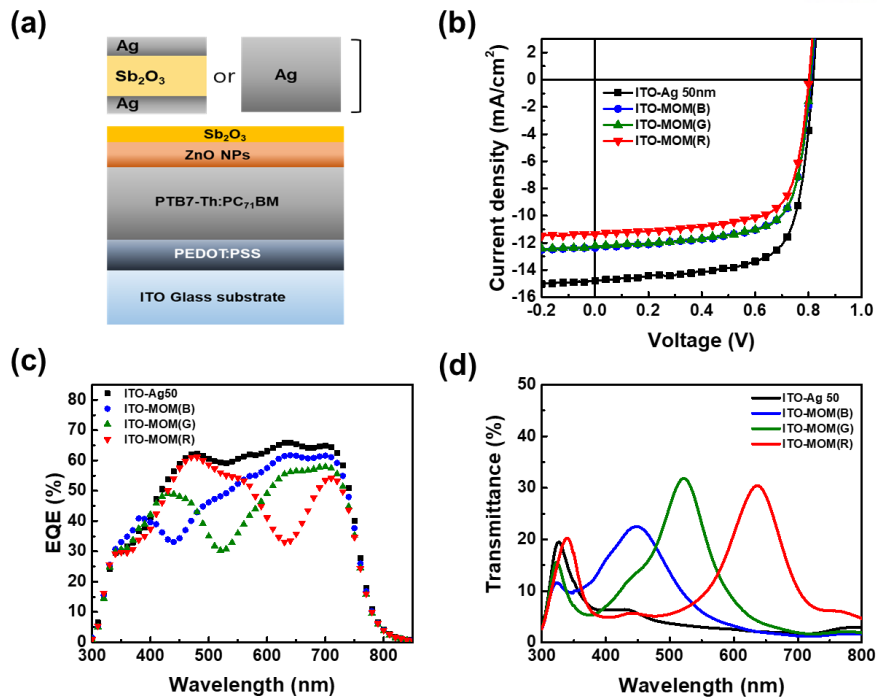


Figure 5. 3 (a) OSCs with color filter and 50nm thick Ag electrode for comparison, (b)  $J$ - $V$  characteristics, (c) EQE results and (d) corresponded transmittance

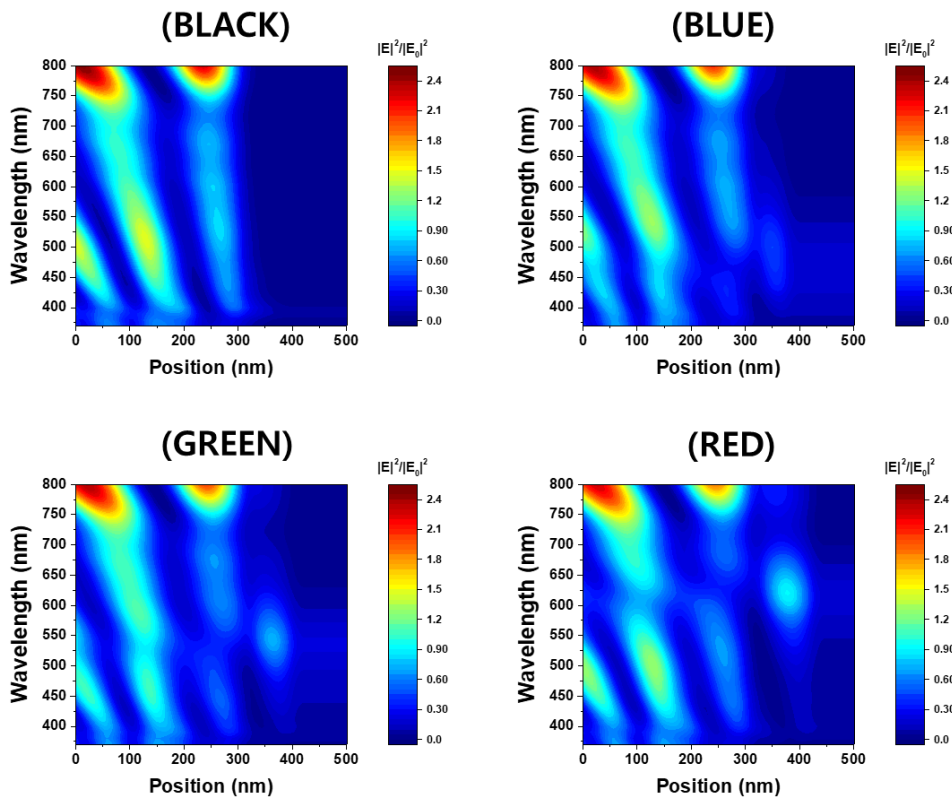
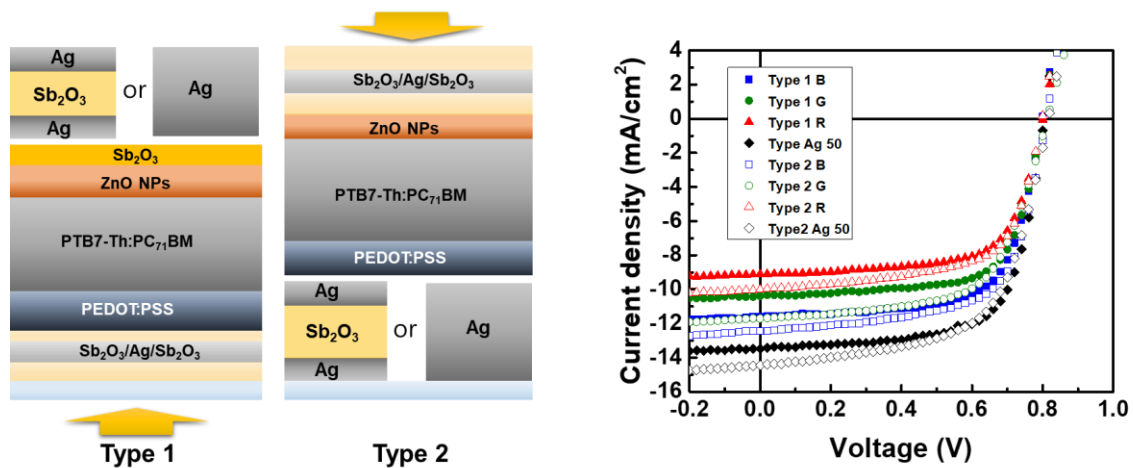


Figure 5. 4 Electric field of OSCs fabricated with ITO bottom electrode and MOM or Ag 50 nm top electrode

Furthermore, we used OMO electrode as an alternative to ITO electrode. OMO multilayer was fabricated with 2 nm  $\text{Sb}_2\text{O}_3$ /15 nm Ag/30nm  $\text{Sb}_2\text{O}_3$ . OSCs were fabricated in two ways, one is using bottom ITO substrate and color filter for top electrode (type 1), the other one is composed with color filter for bottom electrode and OMO top electrode (type 2). Since OMO electrode based on 2 nm  $\text{Sb}_2\text{O}_3$ /15 nm Ag/30nm  $\text{Sb}_2\text{O}_3$  had lower transmittance than ITO substrate, comparing **Figure 5.4**, the performance of Type1 showed lower performance. OSCs with Ag 50nm top electrode exhibited 7.4 % of PCE resulting from  $13.51 \text{ mA cm}^{-2}$  of  $J_{\text{sc}}$ , 0.81 V of  $V_{\text{oc}}$  and 0.68 of FF. The OSCs with color filters showed higher  $J_{\text{sc}}$ : blue > green > red in this order, as same tendency to abovementioned trend. Type 2 OSCs were measured via top illumination. This structure of devices showed higher performance compared to Type 1, notably, enhanced  $J_{\text{sc}}$  values were observed due to larger photon without light loss from glass substrates.



**Figure 5. 5** Two type of OSCs structure and  $J$ - $V$  characteristics

**Table 5. 2** Photovoltaic parameters of OSCs based on OMO and color filter electrode

Device	Top Electrode	$J_{sc}$ (mA cm <sup>-2</sup> )	$V_{oc}$ (V)	FF	PCE (%)
Type 1	Color filter (Blue)	11.59	0.80	0.69	6.29
	Color filter (Green)	10.39	0.80	0.69	5.74
	Color filter (Red)	9.11	0.80	0.68	4.94
	Ag 50 nm	13.51	0.81	0.68	7.40
Type 2	Color filter (Blue)	12.45	0.81	0.65	6.58
	Color filter (Green)	11.70	0.81	0.63	5.99
	Color filter (Red)	10.01	0.80	0.64	5.15
	Ag 50 nm	14.44	0.82	0.61	7.23

## 5.4 Conclusion

We have fabricated color filter based on Sb<sub>2</sub>O<sub>3</sub> cavity medium and Ag metallic mirrors. The calculated entire wave optics interference of Fabry-Perot etalon structure, and we successfully demonstrated selected color filters by controlling cavity thickness, according to the simulated transmittance. The effect of Ag thickness as mirrors were confirmed, we choose the 25 nm Ag films for color filter. Furthermore, we applied the color filter to OSCs which were fabricated using ITO or oxide-metal-oxide transparent electrode. consequently, the vivid colored devices were obtained, higher PCEs were observed in OSC device incorporating blue color filter due to reflection of longer wavelength of penetrated light to inside the device.

## Chapter 6. Control of Charge Dynamics via Use of Nonionic Phosphonate Chains and Their Effectiveness for Inverted Structure Solar Cells

### 6.1 Research Background

Inverted structure of OSCs (i-OSCs) has superior long-term stability, comparing to conventional OSCs. Because not only corrosive and hygroscopic properties of poly(3,4-ethylenedioxythiophene):poly(styrene-sulfonate) (PEDOT:PSS) as a common hole transporting layer, but also low-work function of metal cathodes, both of which leads device degradation, are avoided. [67] In addition, i-OSCs has extra advantage of vertical phase separation and donor-acceptor component gradients in the photoactive layer. Recently, appropriate metal oxides are one of promising issues of interlayer materials with relatively high mobility, environmental stability, and high transparency, for efficient transporting charge carriers. Lots of metal oxide has been reported for hole transporting layers such as MoO<sub>3</sub>, V<sub>2</sub>O<sub>5</sub>, NiO, Sb<sub>2</sub>O<sub>3</sub> and WO<sub>3</sub> [68] as well as for electron transporting layer such as Cs<sub>2</sub>CO<sub>3</sub>, TiO<sub>x</sub>, and zinc oxide (ZnO) and so on, [69], which are effective for charge extraction with enhancing power conversion efficiencies (PCEs) in OSCs. Nevertheless, there is phase inhibition issue of electron transporting arising from poor interfacial contact between polar surfaces of metal oxide layers and hydrophobic organic active layers.

Here, we investigated a various amount of phosphonate-terminated side chain into an isoindigo (IIG)-based polymer to overcome the phase compatibility problems at the interfaces of organic/inorganic films. considerations for new designed polymers include: (1) the phosphonate groups may offer improve interfacial contact of organic/inorganic layer with dipole formation, because of their intrinsic hydrophilic and polar properties. (2) the phosphonate side chain increases the dielectric constant of donor polymer leading reduction of nongeminate recombination losses and improved short-circuit current ( $J_{scs}$ ). [70] (3) phosphonates, nonionic character, doesn't generate electrical field-induced redistribution at ions/electrode interfaces. [71] To confirm the effects, we demonstrated and studied charge collection efficiency, recombination, analysis of device performance and film morphology.

## 6.2 Experimental

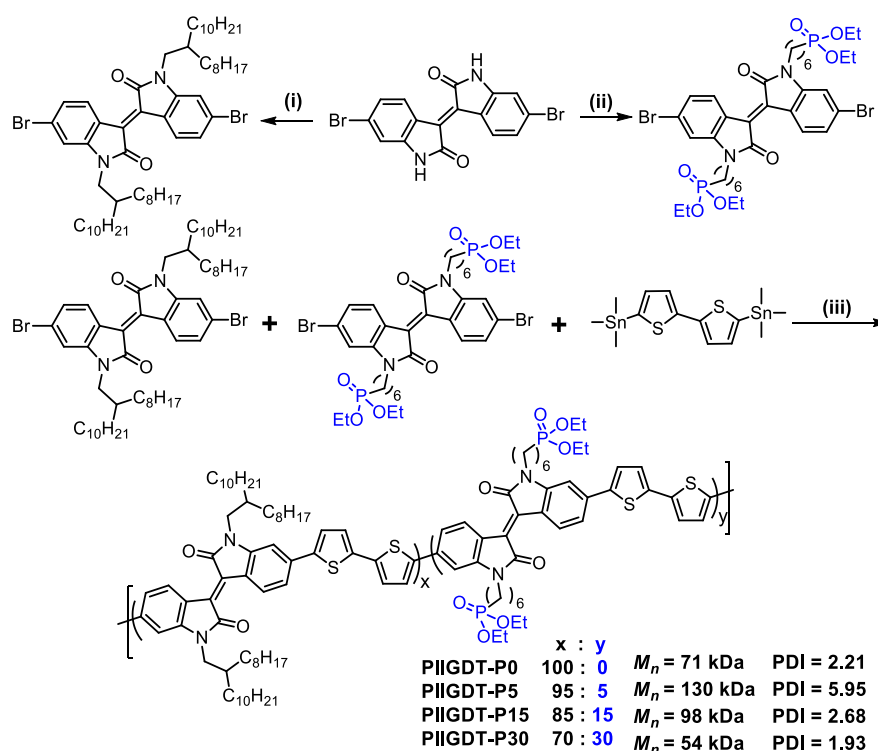


**Figure 6. 1** Chemical structure of IIGDT-based polymers with varying phosphonate content

### 6.2.1 Fabrication of Inverted OSCs

Polymer solar cells were fabricated with an inverted configuration of ITO/ZnO/polymer:PC<sub>71</sub>BM/MoO<sub>3</sub>/Ag. Patterned ITO glass substrates were cleaned by rubbing with detergent, rinsing with distilled water, acetone, and isopropyl alcohol. Then the substrates were dried in an oven at 100 °C and treated with UV ozone for 20 min to remove residues and surface treatment. ZnO layer was deposited by spin coating, where ZnO solution is made of diethylzinc (5 wt%) dissolved in a 1:2 mixture of toluene:Tetrahydrofuran (THF), at 3000 rpm for 30 s onto cleaned ITO substrates, then dried for 10 min at 110 °C. Subsequently, active solutions of polymers : PC<sub>71</sub>BM (1 wt% (w/w) in chlorobenzene (CB)) containing 0%–3% (v/v) diphenylether were spin casted on ZnO film in a nitrogen (N<sub>2</sub>) filled glove box. 5 nm MoO<sub>3</sub> ( $\approx 0.1 \text{ \AA s}^{-1}$ ) layer and 80 nm Ag ( $\approx 0.6 \text{ \AA s}^{-1}$ ) electrodes were thermally evaporated at  $<1.0 \times 10^{-6}$  Torr. Active area is 13 mm<sup>2</sup>. The current density–voltage ( $J$ – $V$ ) characteristics of the devices were measured using a Keithley 2635A source Measure unit under AM 1.5G solar irradiation at 100 mW cm<sup>-2</sup>. EQE measurements were conducted in ambient air using an EQE system (Model QEX7) by PV measurements Inc. (Boulder, CO). Spectral mismatch factors were found to be 10% or less. Optimal active layer thicknesses were found to be 110, 120, 105, and 115 nm for active layers based on IIGDT-P0, P5, P15, and P30, respectively (**Figure 6.1**).

## 6.3 Result and Discussion

### 6.3.1 Polymer Characterization

PIIGDT-Pn polymers have broadened resonances in  $^1\text{H}$  NMR at  $\delta = 4.0\text{--}4.4$  ppm related to the  $\alpha$  hydrogens of phosphonate units ( $\text{O}=\text{PO}_2\text{C}_2\text{H}_4$ ) and their intensities agreed with the ratio of the phosphonate terminated units. Although integrated area of peak is commonly used to confirm quantify ratio of aliphatic/aromatic proton, it does not qualitatively identify the presence of targeting phosphonate protons because of overlap with nonmodified alkyl protons. Therefore, X-ray photoelectron spectroscopy (XPS) was used to confirm presence of phosphonate groups at interface between organic layer and electrode. As shown in **Figure 6.2 (a)**, P2p peaks existed phosphonate side chain were characterized at 132–135 eV region of the photoelectron spectrum. The reference polymer (PIIGDT-P0) shows any P2p signal, in contrast, the phosphonate unit-substituted polymers display peaks. The P2p signals were increased depending on phosphonate monomer feed ratio. Furthermore, contact angle of PIIGDT-Pn-coated films were measured to investigate interfacial effect of the phosphonate groups. The wettability was changed as difference in the surface energy of the films, which indicated the increase in polarity of the polymer surface and suggested improved compatibility with ionic metal oxides. The contact angles of films were decreased as increasing phosphonate content, showing PIIGDTP0 ( $100.6^\circ$ ) > P5 ( $96.6^\circ$ ) > P15 ( $93.5^\circ$ ) > P30 ( $87.5^\circ$ ), as shown in **Figure 6.2 (b)**.

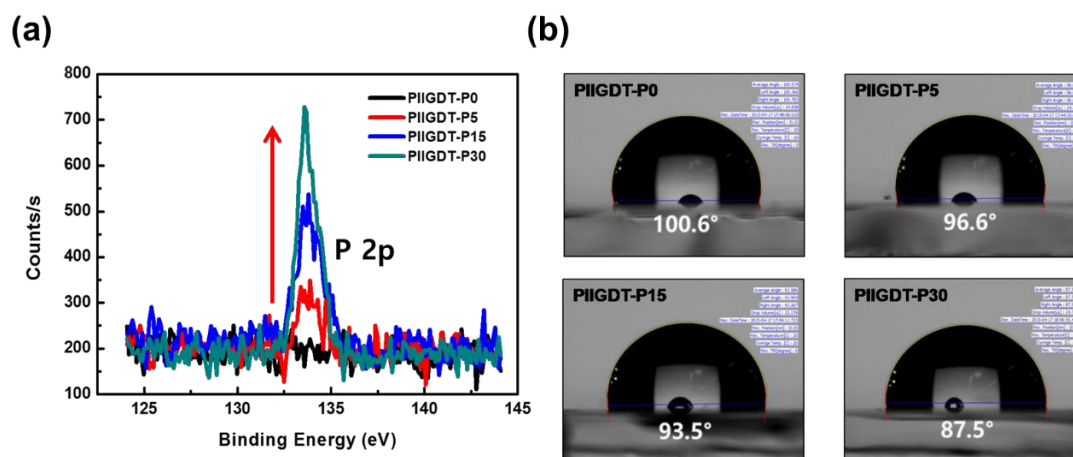


**Figure 6.2** (a) XPS spectra of the polymers showing the P 2p region and (b) water contact angle of PIIGDT-Pn films

### 6.3.2 Optical and Electrochemical Properties

**Figure 6.3 (a-b)** showed absorption spectra of the four polymers dissolved in chloroform solution and as spin-casted films. the spectra. All polymers in both solution and thin films show absorption in range of 400–770 nm with a maximum peak at  $\sim 700$  nm. Where, regardless the introducing phosphonate substituent unit, the optical properties of all polymers were identical. Additionally, there are no redshift



in absorption spectra between solution and film case, which indicate that molecular packing had been formed in the solution.

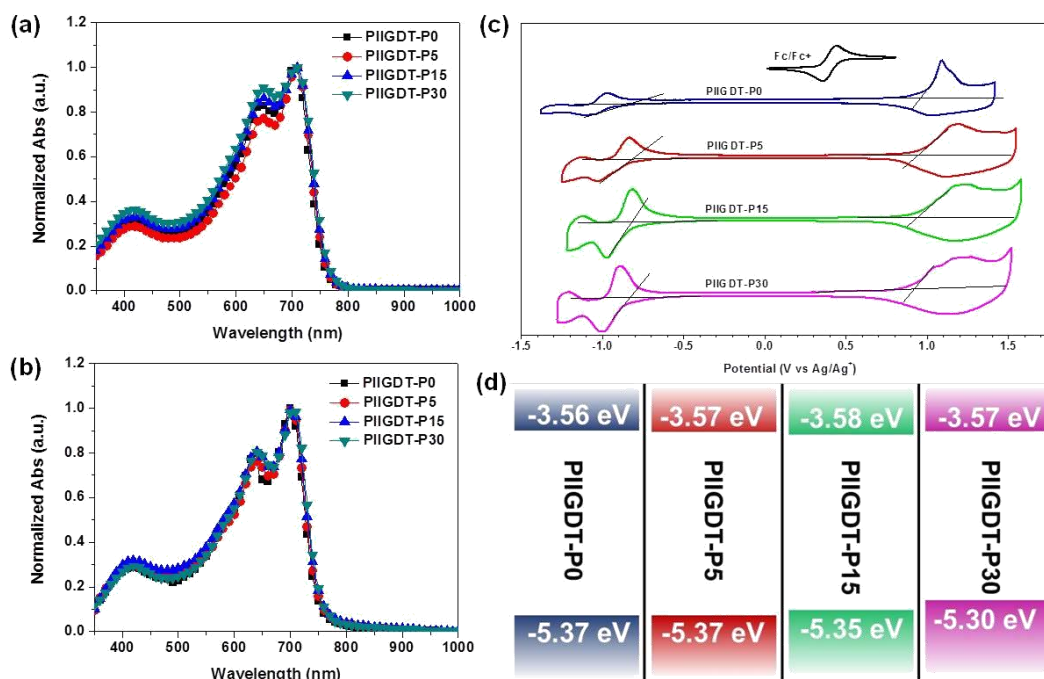


**Figure 6.3** Normalized UV-Vis absorption spectra in (a) chloroform solution and (b) thin films, (c) cyclic voltammograms and (d) HOMO and LUMO energy diagrams (vs. vacuum) of PIIGDT-P0, PIIGDT-P5, PIIGDT-P15 and PIIGDT-P30.

The molecular electrochemical properties (orbital energy;  $E_{\text{HOMO}}$  and  $E_{\text{LUMO}}$ ) were shown in **Figure 6.3 (c)**. The energy level of four polymers were listed in **Table 6.1** together with spectroscopic values. It shows that the phosphonate side chain substitution has slightly effect on the  $E_{\text{HOMO}}$  levels, leading increase of calculated  $E_{\text{HOMO}}$  levels (**Figure 6.3 (d)**).

**Table 6.1** Optical and electrochemical properties of the polymers

	$\lambda_{\text{max,sol}}$ (nm)	$\lambda_{\text{max,film}}$ (nm)	$E_{\text{HOMO}}^{\text{a)}$ (eV)	$E_{\text{LUMO}}$ (eV)	$E_{\text{g}}^{\text{elec}}$ (eV)	IP
PIIGDT-P0	705	700	-5.37	-3.56	1.81	5.54
PIIGDT-P5	708	702	-5.37	-3.57	1.80	5.52
PIIGDT-P15	707	704	-5.35	-3.58	1.77	5.51
PIIGDT-P30	708	706	-5.30	-3.57	1.73	5.50

To confirm this trend, the ionization potential (IP, |HOMO|) of the PIIGDT-Pn polymers was measured by ultraviolet photoelectron spectroscopy (UPS). Slight shift in IP from 5.54 to 5.50 eV for PIIGDT-P0 to PIIGDT-P30 were observed, which is agreed with trend of the CV data. These increased  $E_{\text{HOMO}}$  energy levels is also consistent with reduced open circuit voltages ( $V_{\text{oc}}$ s) of OSCs. These subtle changes for energy level can result from different molecular packing in the films.

### 6.3.3 Photovoltaic Performance

Bulk heterojunction (BHJ) i-OSCs were fabrication with PIIGDT-P0, PIIGDT-P5, PIIGDT-P15, or PIIGDT-P30 donor active materials. And the devices were measured under 1 sun (AM 1.5G, 100  $\text{mWcm}^{-2}$ ) illumination. The OSCs were optimized through the various fabrication condition controlling solvents, additives, concentration and thickness, as shown in **Table 6.2**. Additive processing of diphenylether (DPE) obviously showed to help optimize the photoactive morphologies in PIIGDT-Pn polymers:PC<sub>71</sub>BM-based BHJ OSCs. **Figure 6.4** shows the current density-voltage ( $J$ - $V$ ) characteristic and external quantum efficiency (EQE) of the OSCs with and without processing DPE additive. Their photovoltaic parameter such as  $V_{\text{oc}}$ s, short-circuit currents ( $J_{\text{sc}}$ s), fill factor (FF), and PCEs are summarized in **Table 6.3**. The control device, OSCs without additives, showed a PCE of 4.06%, 4.17%, 3.87%, and 1.96% for PIIGDT-P0, PIIGDT-P5, PIIGDT-P15, and PIIGDT-P30, respectively. Increasing content of phosphonate side chain on polymer backbone, OSCs performances have been limited by marginal solubility and poor films formation during the active films casting process from organic solvents such as chlorobenzene and *o*-dichlorobenzene (*o*-DCB). The performance of OSCs added 3% (v/v) of DPE additive were significantly improved with mainly increased  $J_{\text{sc}}$ s. Notably, a PCE of 5.95% was achieved using PIIGDT-P5, which is nearly 20% higher than the PIIGDT-P5 based control device. Further, we confirmed the improved photocurrent generation efficiency of devices by measuring EQE and calculating integrated  $J_{\text{sc}}$ s, all  $J_{\text{sc}}$  values of EQE spectra agreed within less than 10% of the  $J_{\text{sc}}$ s from the  $J$ - $V$  curve. Even although small content of phosphonate terminated group enhances  $J_{\text{sc}}$ s, higher amount of hydrophilic phosphonate incorporation deteriorates both the  $V_{\text{oc}}$ s and FFs of the devices. Polar interfacial layers such as conjugated polyelectrolytes or polythylenimines typically have influence on improvement of  $V_{\text{oc}}$ s and FFs due to the formation of interfacial dipoles. we expect that phosphonate group are also appended to the photovoltaic polymer increasing  $V_{\text{oc}}$ s and FF, however, it shows that there is negligible to interfacial dipole effect when phosphonate group are distributed all over the active amount of polar phosphonate groups on the conjugated polymer also have a positive effect on the interface between active layer and metal oxide layer. The polymers with high phosphonate content (PIIGDT-P15 and PIIGDT-P30) exhibited less improvement in photovoltaic performance even when the solvent additive DPE was used, which could be attributed to the relatively lower solubility. To understand comprehensive analysis of property-device performance relationships in the PIIGDT-

**Table 6. 2** All data of photovoltaic performance of the IIGDT-based polymers<sup>a</sup>

Polymer	Solvent (v/v)	J <sub>sc</sub> (mA/cm <sup>2</sup> )	V <sub>oc</sub> (V)	FF	PCE (%)
<b>PIIGDT- P0:PC<sub>71</sub>BM</b>	<b>DCB</b>	9.17±0.53 (9.58)	0.84±0.10 (0.88)	0.51±0.03 (0.52)	3.94±0.53 (4.36)
	<b>97%DCB+3%DIO</b>	7.15±0.30 (6.95)	0.78±0.14 (0.82)	0.50±0.03 (0.54)	2.47±0.60 (3.03)
	<b>97%DCB+3%DPE</b>	7.74±0.19 (7.60)	0.77±0.12 (0.84)	0.53±0.03 (0.54)	3.14±0.47 (3.47)
	<b>CB</b>	8.07±0.11 (8.15)	0.86±0.05 (0.91)	0.52±0.01 (0.55)	3.75±0.06 (4.06)
	<b>97%CB+3%DIO</b>	9.20±0.24 (9.00)	0.81±0.02 (0.87)	0.48±0.04 (0.49)	3.57±0.48 (3.83)
	<b>97%CB+3%DPE</b>	8.72±0.14 (9.01)	0.90±0.01 (0.91)	0.59±0.02 (0.61)	4.63±0.06 (5.00)
<b>PIIGDT- P5:PC<sub>71</sub>BM</b>	<b>DCB</b>	8.40±0.32 (8.62)	0.81±0.01 (0.81)	0.49±0.01 (0.49)	3.33±0.14 (3.42)
	<b>97%DCB+3%DIO</b>	6.33±0.79 (6.70)	0.82±0.01 (0.87)	0.50±0.02 (0.57)	2.72±0.29 (3.36)
	<b>97%DCB+3%DPE</b>	7.76±0.55 (8.24)	0.86±0.01 (0.87)	0.57±0.02 (0.58)	3.80±0.36 (4.11)
	<b>CB</b>	8.06±0.27 (7.00)	0.83±0.02 (0.89)	0.61±0.04 (0.67)	3.49±0.34 (4.17)
	<b>97%CB+3%DIO</b>	-	-	-	-
	<b>97%CB+3%DPE</b>	11.87±0.10 (12.26)	0.78±0.06 (0.84)	0.56±0.01 (0.58)	5.62±0.43 (5.95)
<b>PIIGDT- P15:PC<sub>71</sub>BM</b>	<b>DCB</b>	5.27±0.51 (5.77)	0.85±0.04 (0.87)	0.58±0.02 (0.59)	2.81±0.18 (2.94)
	<b>97%DCB+3%DIO</b>	5.82±0.54 (6.27)	0.84±0.03 (0.83)	0.51±0.04 (0.51)	2.48±0.18 (2.63)
	<b>97%DCB+3%DPE</b>	8.08±0.24 (8.23)	0.81±0.03 (0.83)	0.50±0.01 (0.50)	3.25±0.16 (3.43)
	<b>CB</b>	7.41±0.36 (7.72)	0.81±0.03 (0.85)	0.52±0.05 (0.60)	3.44±0.21 (3.87)
	<b>97%CB+3%DIO</b>	7.32±0.24 (7.60)	0.76±0.01 (0.77)	0.53±0.01 (0.55)	2.92±0.19 (3.19)
	<b>97%CB+3%DPE</b>	8.91±0.33 (9.24)	0.83±0.02 (0.85)	0.53±0.02 (0.55)	4.07±0.37 (4.30)
<b>PIIGDT- P30:PC<sub>71</sub>BM</b>	<b>DCB</b>	3.81±0.30 (4.17)	0.81±0.01 (0.82)	0.45±0.02 (0.47)	1.23±0.32 (1.59)
	<b>97%DCB+3%DIO</b>	6.48±0.21 (6.23)	0.71±0.09 (0.77)	0.37±0.03 (0.41)	1.63±0.31 (1.96)
	<b>97%DCB+3%DPE</b>	7.30±0.04 (7.27)	0.77±0.02 (0.78)	0.38±0.01 (0.38)	2.12±0.03 (2.14)
	<b>CB</b>	6.68±0.36 (6.77)	0.72±0.02 (0.72)	0.39±0.01 (0.40)	1.87±0.15 (1.96)
	<b>97%CB+3%DIO</b>	6.39±0.34 (6.72)	0.73±0.01 (0.73)	0.50±0.02 (0.51)	2.34±0.22 (2.48)
	<b>97%CB+3%DPE</b>	7.58±0.29 (7.60)	0.71±0.09 (0.78)	0.46±0.02 (0.47)	2.48±0.35 (2.81)

<sup>a</sup> i-PSCs (ITO/ZnO/polymer:PC<sub>71</sub>BM(1:1) without and/or with DPE/MoO<sub>3</sub> (5 nm)/Ag (80 nm)) were measured under irradiation of AM 1.5G at 100 mWcm<sup>-2</sup>.

layer. Since PIIGDT-Pn polymers have the similar structural features and show increased  $J_{sc}$  corresponding to improved charge transport at organic/inorganic interface, we presume that a certain Pn:PC<sub>71</sub>BM blend films, we have characterized the morphology, molecule structural orientation and charge carrier dynamics including recombination and charge extraction.

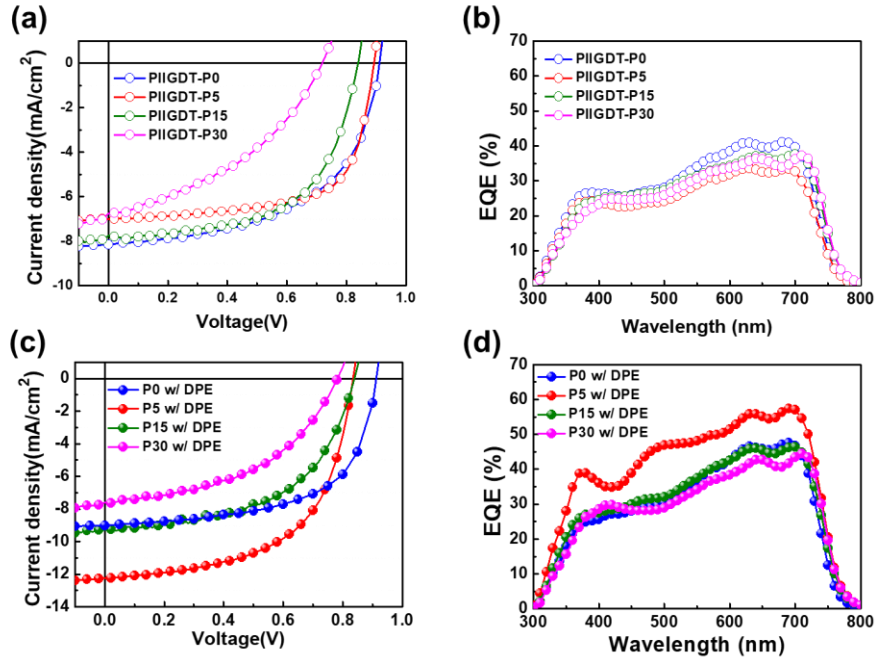


**Figure 6. 4** (a,c)  $J$ - $V$  characteristics of optimized i-PSCs without and with DPE additive, respectively and (b,d) corresponding external quantum efficiency (EQE) spectra

**Table 6. 3** Photovoltaic performance of the IIGDT-based polymers

Polymer	Additive	$J_{sc}$ ( $\text{mA cm}^{-2}$ )	$V_{oc}$ (V)	$FF$	$PCE_{best}(avg)^a$ (%)	$Cal. J_{sc}$ ( $\text{mA cm}^{-2}$ )
<b>PIIGDT-ref</b>	None	8.15	0.91	0.55	4.06 (3.82)	7.86
	DPE	9.01	0.91	0.61	5.00 (4.78)	8.71
<b>PIIGDT-P5</b>	None	7.00	0.89	0.67	4.17 (4.10)	6.60
	DPE	12.26	0.84	0.58	5.95 (5.85)	11.45
<b>PIIGDT-P15</b>	None	7.72	0.85	0.60	3.87 (3.56)	7.47
	DPE	9.24	0.85	0.55	4.30 (4.19)	9.04
<b>PIIGDT-P30</b>	None	6.77	0.72	0.40	1.96 (1.76)	7.20
	DPE	7.60	0.78	0.47	2.81 (2.72)	8.42

a) Values in parentheses represent the average of 10 devices.

### 6.3.4 Charge Transport and Extraction

The space-charge limited current (SCLC) model was used to investigate the vertical carrier transport properties of the device. We fabricated hole-only diodes (ITO/PEDOT:PSS/polymer:PC<sub>71</sub>BM/Au) and electron-only diodes (FTO/polymer:PC<sub>71</sub>BM/Al) with each optimal condition introducing DPE additive for quantifying hole and electron mobilities. As shown in **Figure 6.5** and **Table 6.4**, the electron mobilities shows increase ( $7.5 \times 10^{-4}$  to  $9.9 \times 10^{-4} \text{ cm}^2\text{V}^{-1}\text{s}^{-1}$ ), while hole mobilities decreased from  $8.9 \times 10^{-5}$  to  $5.7 \times 10^{-5} \text{ cm}^2\text{V}^{-1}\text{s}^{-1}$  depending on increment of phosphonate group. Although phosphonate group facilitated efficient electron transport, balancing values of  $\mu_{\text{electron}}/\mu_{\text{hole}}$  ratio for high phosphonate content (PIIGDT-P15 and P30) were poor, which resulted in decrease in FF of OSCs.

Furthermore, we analyzed the  $J$ - $V$  characteristics depending on the light intensity to understand recombination and charge extraction within OSCs. i-OSCs based on PIIGDT-Pn:PC<sub>71</sub>BM blend were measured under various illumination intensities in range of 0.1 sun to 1 sun ( $10$ – $100 \text{ mWcm}^{-2}$ ). By using the dependence of  $J_{\text{sc}}$  on light intensity, the limited  $J_{\text{sc}}$ s arising from bimolecular recombination and/or trap-assisted recombination can be analyzed. Fitting photocurrent plots with **equation (6.1)**,

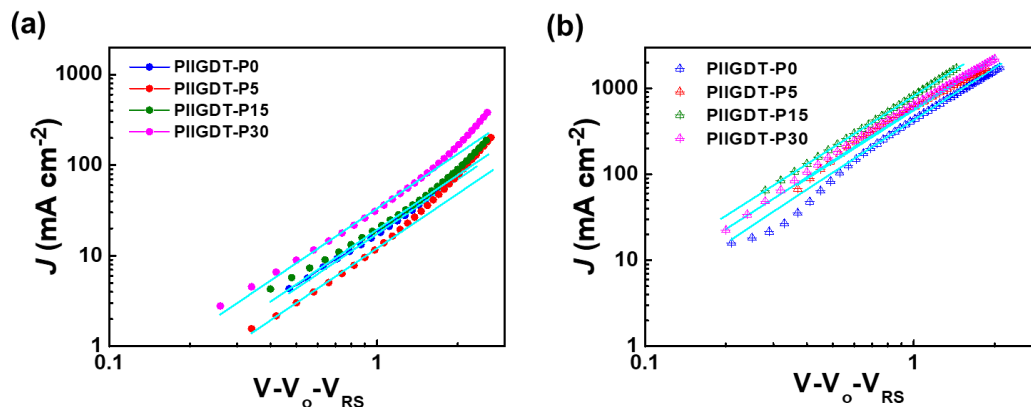


**Figure 6. 5** (a) hole-only devices (ITO/PEDOT:PSS/polymer:PC<sub>71</sub>BM added DPE/Au) (b) Double-logarithmic plot of dark  $J$ - $V$  characteristics from electron-only devices (FTO/polymer:PC<sub>71</sub>BM added DPE/Al). Sky blue lines are fits of the curves using the Mott-gurney relationship.

**Table 6. 4** Hole and electron mobilities of blend films of IIGDT-based polymers derived using the SCLC method

Polymer	Electron mobility ( $\text{cm}^2\text{V}^{-1}\text{s}^{-1}$ )	Hole mobility ( $\text{cm}^2\text{V}^{-1}\text{s}^{-1}$ )	$\mu_e/\mu_{\text{hole}}$
PIIGDT-P0	$7.5 \times 10^{-4}$	$8.9 \times 10^{-5}$	8.43
PIIGDT-P5	$9.5 \times 10^{-4}$	$6.9 \times 10^{-5}$	13.77
PIIGDT-P15	$9.5 \times 10^{-4}$	$6.5 \times 10^{-5}$	14.62
PIIGDT-P30	$9.9 \times 10^{-4}$	$5.7 \times 10^{-5}$	17.37

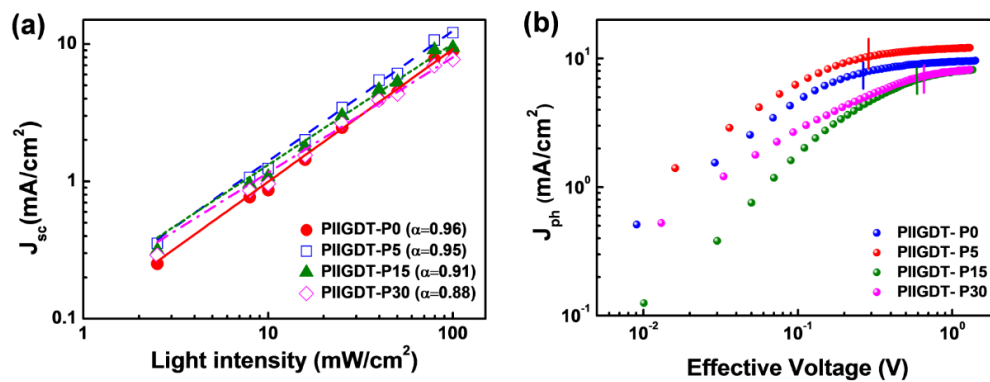


**Figure 6. 6** (a) Double-logarithmic scale of the short circuit current density as a function of light intensity and (b) photocurrent versus effective voltage of optimal PSCs with DPE: PIIGDT-P0 (blue), P5 (red), P15 (green) and P30 (magenta)

where  $I$  is the light intensity,  $\alpha$  indicates degree of bimolecular recombination and space charge accumulation.

$$J_{sc} \propto I^\alpha \quad (\text{Eq. 6.1})$$

As shown in **Figure 6.6 (a)**,  $J_{sc}$ s on logarithmic light intensity dependence,  $\alpha$  values for PIIGDT-P0 and PIIGDT-P5 are close to unity ( $\alpha = 1$ ). this shows that PIIGDT-P0 and P5-based OCSs has the weak bimolecular recombination at short circuit and thus carriers are completely swept out, while PIIGDT-P15 and P30 appeared higher bimolecular recombination resulting from poor phase separation and morphologies. In addition, we investigated the net photocurrent ( $J_{ph}$ ) on the effective applied voltage ( $V_{\text{eff}}$ ) to clarify the effect of the phosphonate nonionic side chains on the interface of active/metal oxide layers.  $J_{ph}$  indicates the difference between the current density under illumination and dark conditions ( $J_{ph} = J_L - J_D$ ) and effective applied voltage is difference of  $V_o$  and  $V_a$ ;  $V_{\text{eff}} = V_o - V_a$  ( $V_o$  is voltage at  $J_{ph} = 0$  and  $V_a$  is applied bias voltage). The results provide influence of compatibility at the interface active/metal oxide layers corresponding effect of polar and hydrophilic properties on device performance. As shown in **Figure 6.6 (b)**,  $J_{ph}$ s are saturated at high  $V_{\text{eff}}$ , indicating complete collection

of all photogenerated charges at both electrodes. The saturation voltages of PSCs on the  $J_{\text{ph}} - V_{\text{eff}}$  curve, beginning voltage of bimolecular recombination and the build-up of space charges, with increasing phosphonate content are extended to higher effective voltages; 0.26 V (PIIGDT-P0) < 0.28 V (PIIGDT-P5) < 0.59 V (PIIGDT-P15) < 0.65 V (PIIGDT-P30). These appearances are due to increasing difference of electron and hole mobilities and consistent with results of SCLC modeling. Under the short-circuit condition, PIIGDT-P0 and P5 represent  $J_{\text{ph}}/J_{\text{sat}}$  ratios of 98% and 99%, respectively, assuming  $J_{\text{sat}}$  at 1.2  $V_{\text{eff}}$ , respectively, where the ratio of  $J_{\text{ph}}/J_{\text{sat}}$  ratio is exciton dissociation probability. Even the ratio at short-circuit condition exhibited minor difference of PIIGDT-P0 and P5-based OSCs, under the maximum power output condition, PIIGDT-P5 OSCs shows higher charge extraction and collection of 82% than that of 76% for PIIGDT-P0 case. This higher value of  $J_{\text{ph}}/J_{\text{sat}}$  ratio for PIIGDT-P5 OSCs is due to the improved organic/inorganic interface, whereas PIIGDT-P15 and P30 showed inferior values due to stronger bimolecular recombination.

### 6.3.5 Microstructure Analyses of Thin Films

By collecting grazing-incidence wide-angle X-ray scattering (GIWAXS) patterns for pure polymer films and PIIGDT-Pn:PC<sub>71</sub>BM blend films with and without DPE additive, the microstructural orientation was analyzed and correlated with OSCs performance. 2D GIWAXS images and plotting lines corresponding the results are shown in **Figure 6.7** and **Figure 6.8**, and detailed crystallographic parameters are summarized in **Table 6.5**. Multi-diffraction (h00) up to the fourth order along the out-of-plane ( $q_z$ ) axis were exhibited both all neat polymer films and all blend films, indicating well-ordered lamellar structure packing and  $\pi$ - $\pi$  stacking of the polymer backbones on in-plane ( $q_{xy}$ ) axis; edge-on orientation. For GIWAXS patterns of neat polymer, interestingly, a (010) peak along the  $q_z$  plane for PIIGDT-P0 was only observed, suggesting the combination of face-on ( $\pi$ - $\pi$  stacking of backbones along  $q_z$  axis) and edge-on orientations. In addition, (010) peaks on  $q_{xy}$  shows stronger scattering intensity depending on high content of phosphonate group. For GIWAXS result based PIIGDT-Pn:PC<sub>71</sub>BM blend films, it shows broad peaks around 1.24 – 1.30  $\text{\AA}^{-1}$  assigned to PC<sub>71</sub>BM. The (010) peaks along the  $q_{xy}$  plane are also clearly observed with increasing intensities according to the increment of the phosphonate side chain on PIIGDT polymers. The diffraction peaks in the PIIGDT-Pn:PC<sub>71</sub>BM films processed 3% DPE additive shows almost same trend with pristine polymer:PC<sub>71</sub>BM blends. Exceptionally, the (010) peak in films of PIIGDT-P5 processed with DPE is displayed in the out-of-plane with some lamellar packing along the  $q_{xy}$  axis, which indicates that the polymer has coexistence of packing orientations.

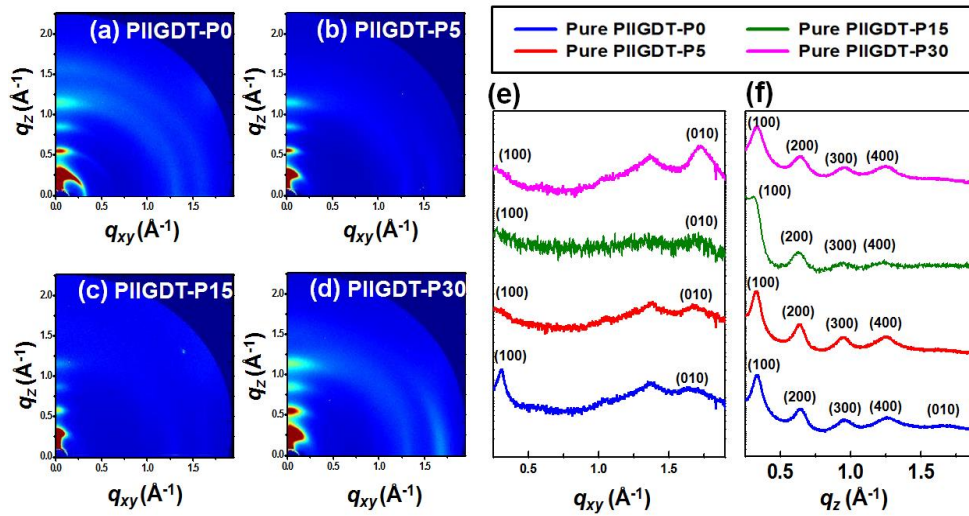


**Figure 6. 7** Grazing incidence wide angle X-ray scattering (GIWAXS) images of IIGDT-based polymer neat films: (a) PIIGDT-P0, (b) PIIGDT-P5, (c) PIIGDT-P15, (d) PIIGDT-P30. The corresponding GIWAXS diffractogram profiles: (e) in-plane and (f) out-of-plane GIWAXS patterns

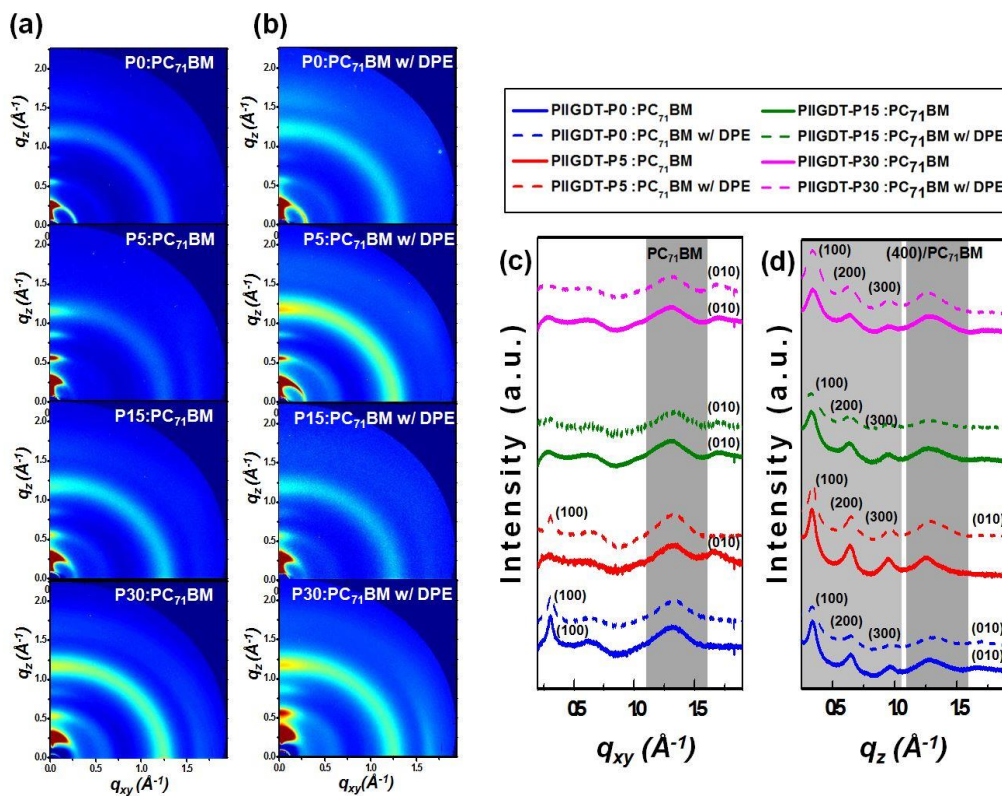


**Figure 6. 8** GIWAXS images of blended polymer films (a) without and (b) with DPE additive Corresponding GIWAXS diffractogram profiles of (c) in-plane and (d) out-of-plane GIWAXS patterns Solid lines represent polymer:PC<sub>71</sub>BM blends while dotted lines represent polymer:PC<sub>71</sub>BM blends processed with DPE.



**Table 6. 5** Crystallographic parameters calculated from GIWAXS profiles of IIGDT-based polymers

Polymer	Crystallographic parameters				
	Axis	$\pi$ - $\pi$ stack [ $\text{\AA}^{-1}$ ]	d-spacing [ $\text{\AA}$ ]	Lamella stack [ $\text{\AA}^{-1}$ ]	d-spacing [ $\text{\AA}$ ]
Neat PIIGDT-P0	$q_{xy}$	1.63	3.85	0.31	20.33
	$q_z$	1.69	3.72	0.33	19.04
PIIGDT-P0:PC <sub>71</sub> BM	$q_{xy}$	-	-	0.30	20.81
	$q_z$	1.70	3.70	0.34	18.48
PIIGDT-P0:PC <sub>71</sub> BM w/ DPE	$q_{xy}$	-	-	0.31	20.27
	$q_z$	1.70	3.70	0.34	18.48
Neat PIIGDT-P5	$q_{xy}$	1.67	3.76	0.28	22.44
	$q_z$	-	-	0.32	19.63
PIIGDT-P5:PC <sub>71</sub> BM	$q_{xy}$	1.67	3.76	0.30	20.94
	$q_z$	-	-	0.33	19.04
PIIGDT-P5:PC <sub>71</sub> BM w/ DPE	$q_{xy}$	-	-	0.31	20.53
	$q_z$	1.77	3.55	0.34	18.48
Neat PIIGDT-P15	$q_{xy}$	1.70	3.70	0.28	22.77
	$q_z$	-	-	0.31	20.27
PIIGDT-P15:PC <sub>71</sub> BM	$q_{xy}$	1.71	3.67	0.29	21.67
	$q_z$	1.75	3.59	0.33	19.04
PIIGDT-P15:PC <sub>71</sub> BM w/ DPE	$q_{xy}$	1.71	3.57	0.34	18.48
	$q_z$	-	-	0.33	19.04
Neat PIIGDT-P30	$q_{xy}$	1.72	3.65	0.27	23.53
	$q_z$	-	-	0.33	19.04
PIIGDT-P30:PC <sub>71</sub> BM	$q_{xy}$	1.71	3.67	0.29	21.67
	$q_z$	-	-	0.34	18.48
PIIGDT-P30:PC <sub>71</sub> BM w/ DPE	$q_{xy}$	1.70	3.70	0.29	21.67
	$q_z$	-	-	0.34	18.48

We measured tapping mode atomic force microscopy (AFM) to investigate surface morphologies of the PIIGDT-Pn:PC<sub>71</sub>BM blends with and without DPE additive. As shown in **Figure 6.9**, there are huge agglomerates were observed for PIIGDT-P15 and P30-based blend films without processing DPE additive, these appearances could be related to the increased hydrophilic nature of high phosphonate content. Interestingly, multilength-scale phase-separated morphology were observed for all active films by processing 3% DPE additive. Although root-mean square (RMS) roughness values of these four polymers were different, the smooth and homogeneous films are beneficial for forming large BHJ interface areas, which is also consistent with enhanced  $J_{sc}$ s.

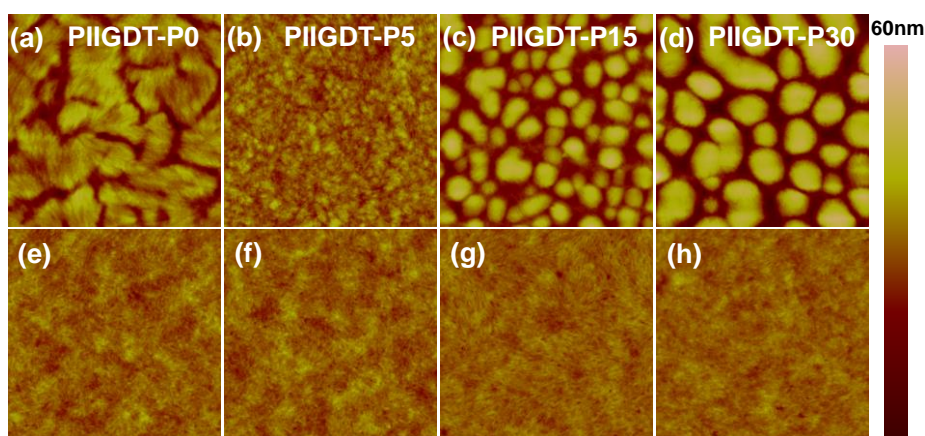


**Figure 6.9** AFM images ( $3 \times 3 \mu\text{m}$ ) of blended polymer:PC<sub>71</sub>BM films (a–d) without and (e–f) with DPE additive films. RMS values: (a) 5.21, (e) 2.72 nm of PIIGDT-P0; (b) 2.55, (f) 2.34 nm of PIIGDT-P5; (c) 8.18, (g) 2.26 nm of PIIGDT-P15; and (d) 11.14, (h) 2.43 nm of PIIGDT-P30

## 6.4 Conclusion

In summary, we studied new designed conjugated polymer introducing nonionic phosphonate side chain on IIG-based polymer and their OSCs to investigate compatibility at the organic/inorganic interfaces. Furthermore, we analyzed by using the SCLC model, light intensity dependence, net photocurrent ( $J_{ph}$ ), and film characterization (GIWAXS and AFM). The synthesized polymer has various phosphonate content of 0%, 5%, 15% and 30%, i-OSCs based on PIIGDT-P5 showed improvement in PCE about  $\approx 20\%$ , comparing to i-OSCs using the nonmodified control polymer without DPE additive treatment. This study was able to elucidate that introduction of phosphonate group enhances the OSCs performance due to improved compatibility at hybrid interfaces and charge-transport/collection. Furthermore, we suggest new molecular design strategy for high performance of i-OSCs without compromising the benefits provided by reference polymer structure.

## Chapter 7. Benzodithiophene-Thiophene-Based Photovoltaic Polymers with Different Side-Chains

### 7.1 Research Background

Since organic solar cells (OSCs) have been demonstrated widely for portable and flexible photovoltaic device with many advantages, over the past decade, it has been remarkably developed ideal conjugated polymers and of device architectures.<sup>[72]</sup> For the molecular design, it was considered to low bandgap, highest occupied molecular orbital (HOMO) energy level, interchain interactions and molecular planarity with a polymer packing.<sup>[73]</sup> These obviously contributes to the OSCs performance of  $V_{ocS}$ ,  $J_{scS}$  and fill factors. Notably, low bandgap polymers including strong crystalline and deep HOMO levels may be expected as a promising candidate for improvement of thermal and oxidative stability of OSCs. The low bandgap polymers, which have absorption from visible to near-infrared (NIR) wavelength of incident light spectrum<sup>[74]</sup> and flatly tight  $\pi$ - $\pi$  stacking, generate lots of carriers and improve exciton delocalization together with charge transfer in thin films. Generally, composition of conjugated polymers is conjugated backbone, side chains and substituents. The conjugated backbone mainly affects optical, electrochemical, electrical characterization, while the side chains improve the molecular weight, solubility and processability of designed polymer. Lastly, substituents have influence on fine-tune the properties such as energy levels, bandgap, mobility etc. The selection of side-chains should be considered in various respects.<sup>[75]</sup> Although alky substituents on the backbone generally improve the solubility, for example, it increases the HOMO energy level and disturbs intermolecular orientation with molecular coplanarity.<sup>[76]</sup> A strategic approach to planar molecular structures with well-ordered packing without compromising solution processability is to form intra-and/or interchain noncovalent coulomb interactions through inherent hydrogen bonds and dipole-dipole interactions. Noncovalent coulomb interactions such as S-O, S-F, and CH-N) have often been reported to control chain conformation and intermolecular packing.<sup>[77]</sup> Here, a series of benzodithiophene (BDT) - thiophene (T)-based donor polymers substituted with hydrogen (BDTT), n-octyl (BDTOT), and octylcarbonyl groups (BDTCOT) were synthesized. Furthermore, this article discusses the relationships between properties of new designed polymers including chain conformation, frontier orbital levels, film morphology, degree of crystalline and their OSCs performance.

## 7.2 Experimental

### 7.2.1 OSCs Fabrication and Characterization

ITO patterned glasses were cleaned by detergent and by rinsing with distilled water, ultra-sonicated in acetone and isopropyl alcohol. and the substrates subsequently were dried in oven at 100 °C. After UV/ozone treatment for 20 min, poly(3,4-ethylenedioxythiophene):polystyrene sulfonic acid (PEDOT:PSS, Clevios P VP.AI4083, Germany) solution was spin cast at 5000 rpm for 40 s. the PEDOT:PSS films were dried for 10 min at 140 °C. Active solutions, mixture of polymers:[6,6]-phenyl-C71butyric acid methyl ester (PC<sub>71</sub>BM) in *o*-dichlorobenzene (*o*-DCB, 12 mg/mL), were spin cast on PEDOT:PSS layer. The devices were pumped down in vacuum (<10<sup>-6</sup> Torr) and a 100 nm thick Al layer was deposited by thermal evaporation (active area: 13 mm<sup>2</sup>). Current density–voltage (*J*–*V* curve) characteristics were measured, using a Keithley 2635A source measurement, under an AM 1.5G illumination at 100 mWcm<sup>-2</sup>. External quantum efficiency (EQE) applying monochromatic light from a xenon lamp under ambient was also measured.

## 7.3 Results and Discussion

### 7.3.1 Characterization of Synthesized Polymers

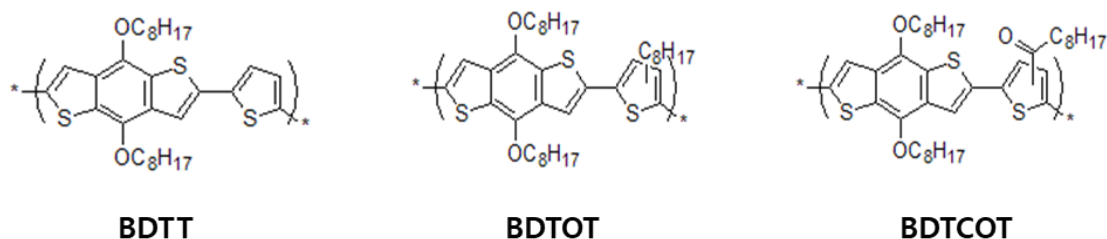


**Figure 7. 1** Chemical structure of donor polymers based BDTT backbone

Designed polymers have the number average molecular weight ( $M_n$ ) of 8.2 (polydispersity index, PDI 2.5), 34 (1.5) and 32 kDa (1.9) for BDTT, BDTOT and BDTCOT, respectively (**Figure 7.1**). The lower  $M_n$  of BDTT is resulted from poor solubility and none solubilizing side chains on the backbone structure. Excepting for BDTT polymer, the other polymers showed well solubility in general organic solvent as well as reasonable high molecular weight. There are the UV-vis absorption spectra of polymer dissolved in toluene and film cases in **Figure 7.2 (a)**. Maximum absorption peaks were observed at  $\lambda_{\text{abs}} = 498$ , 494 and 535 nm for BDTT, BDTOT and BDTCOT, respectively. Introducing carbonyl side chain (BDTCOT) exhibited substantial red shift in absorption spectra of solution, comparing to that of BDTOT. This appearance can be resulted from the increased conjugation originating due to electron withdrawing ability of the octylcarbonyl side chain. Red shifted maximum peak of BDTT, BDTOT and

BDTCOT films were observed, which can be explained by pronounced interchain packing and p-conjugation. The optical bandgaps were 2.08, 2.07 and 1.97 eV. **Figure 7.2 (b)** shows the emission spectra of the polymers in toluene and tetrahydrofuran (THF). BDTCOT case exhibited red shifted spectrum comparing to the other polymer case, which indicate that BDTCOT has stronger intramolecular charge transfer (ICT). Furthermore, BDTCOT in THF shows more shifted emission peak relating to polar character of BDTCOT with carbonyl moiety. Depending on alkyl substituents on the same backbone, electrochemical properties were determined. The HOMO energy level of polymers were obtained from cyclic voltage (CV) measurement (**Figure 7.3 (a)**) and the lowest unoccupied molecular orbital (LUMO) were calculated from the HOMO level and optical bandgap ( $E_{\text{LUMO}} = E_{\text{HOMO}} + E_g$ ). The calculated HOMO and LUMO values were shown in **Figure 7.3 (b)**. The optical and electrochemical properties of the polymers are listed in **Table 7.1**.

**Table 7. 1** Summary of photophysical-, electrochemical- and thermal properties of polymers

Polymer	$M_n$ (kDa) <sup>a</sup>	PDI ( $M_w/M_n$ )	$\lambda_{\text{abs}}$ [sol.] (nm)	$\lambda_{\text{onset}}$ [film] (nm)	$E_{\text{g}}^{\text{opt}}$ (eV) <sup>b</sup>	HOMO [eV] <sup>c</sup>	LUMO [eV] <sup>d</sup>
BDDT	8.2	2.5	498	595	2.08	-5.31	-3.23
BDTOT	34	1.5	494	600	2.07	-5.28	-3.21
BDTCOT	32	1.9	535	630	1.97	-5.40	-3.43

<sup>a</sup>Number-average molecular weight ( $M_n$ ) determined by GPC in chloroform. <sup>b</sup>Optical bandgap in film.

<sup>c</sup>HOMO level was measured from the onset of oxidation by cyclic voltammetry. <sup>d</sup>LUMO level was estimated from the HOMO value and optical bandgap in film.

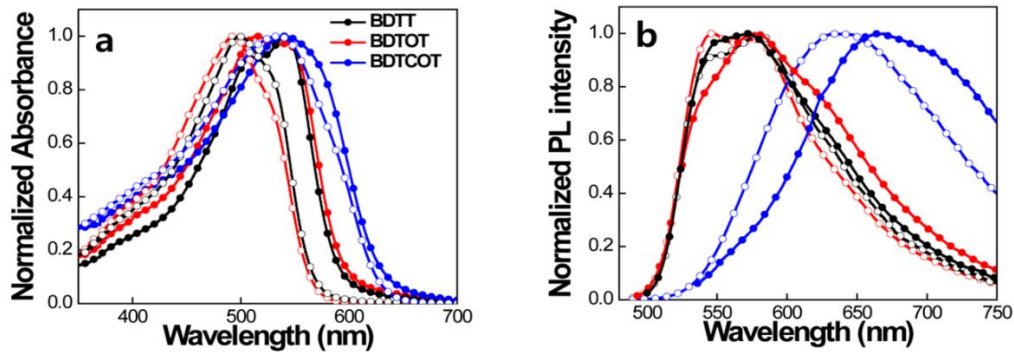


**Figure 7. 2** (a) UV-vis absorption spectra in toluene (open) and in film (solid). (b) Emission spectra of polymers in toluene (open) and in tetrahydrofuran (solid)

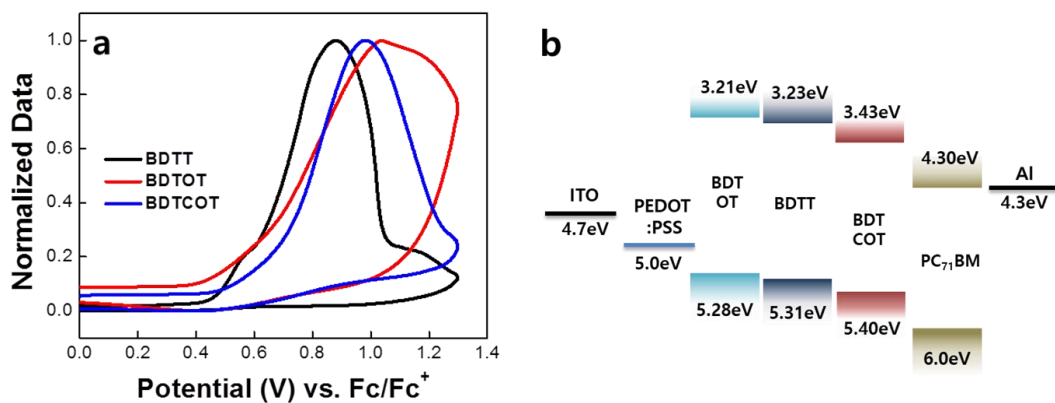


**Figure 7. 3** (a) Cyclic voltammogram and (b) energy band diagram of polymers

Through density functional theory (DFT, B3LYP/6-31G\*\* level) simulation, polymer conformation for BDTT, BDTOT and BDTCOT chemical structure were calculated. **Figure 7.4** shows the torsional profiles and energy minimal conformational structures, respectively, where, the ethyl moiety was used instead of octyl and ethylhexyl side chains for a simple calculation. Introduction of side chain displayed increased torsional angle between the BDT and T, comparing to BDTT polymer without any side chain, due to the steric hindrance. BDTCOT shows smaller torsion angle of 30° than dihedral angle (40°) of BDTOT polymer due to a non-covalent hydrogen bonding interaction of the carbonyl oxygen and hydrogen in the BDT group. In additional evidence, BDTCOT shows a minimum energy indicating that O-H hydrogen bonding contribute to fixing the conformation. These structural characters may increase the interchain organization with semicrystalline.

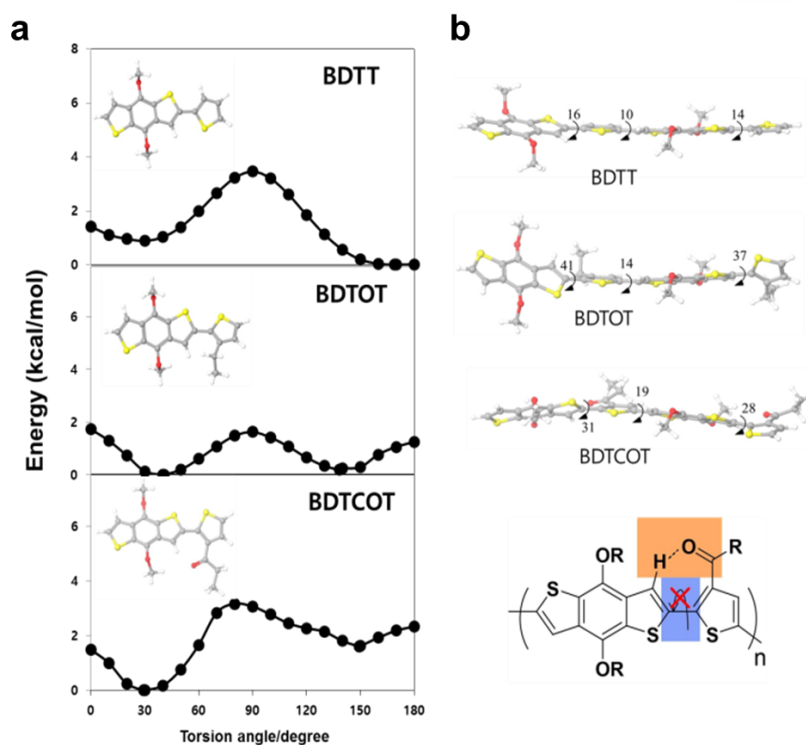


**Figure 7. 4** (a) Torsional profiles and (b) energy minimum conformations (red: oxygen, yellow: sulfur)

### 7.3.2 OSC Fabrication and Photovoltaic Performance

Conventional single OSCs with BDTT series polymer:PC<sub>71</sub>BM blend were fabricated as a structure of ITO/PEDOT:PSS/Polymers:PC<sub>71</sub>BM/Al to investigate the photovoltaic properties. The active blends were dissolved in *o*-dichlorobenzene (*o*-DCB). The OSCs tested under various conditions, such as the blend ratio, thermal treatment, and processing additives, were listed **Table 7.2**. The best OSCs performance are shown in **Figure 7.5** and **Table 7.3**. The BDTT-based OSCs showed a  $V_{oc}$  of 0.75 V,  $J_{sc}$  of 5.95 mAcm<sup>-2</sup> and Fill factor (FF) of 0.56 with 2.52 % of power conversion efficiency (PCE). BDTOT showed a slightly increased PCE of 2.68 % due to improved  $J_{sc}$  and  $V_{oc}$  values. The best photovoltaic performance was obtained for BDTCOT:PC<sub>71</sub>BM, which showed 4.66 % of PCE from  $V_{oc}$  of 0.81 V,  $J_{sc}$  of 9.22 mAcm<sup>-2</sup>, FF of 0.62. The significantly enhanced  $V_{oc}$  was related to clearly deeper HOMO energy level of octylcarbonyl substituent unit. In addition, photoluminescence (PL) spectra of neat and blended polymer films were measured to examine the quenching of photogenerated exciton and their separation in active layer. The PL quenching presents an effective charge transfer between a donor and acceptor blended system. By exciting at 470 nm, the PL maximum peak were observed 630, 630 and 690 nm for BDTT, BDTOT and OBDTCOT, respectively, resulting in quenching efficiency of 87.5, 94 and 95.9 % for BDTT-, BDTOT- and BDTCOT-based blend films, respectively. The smaller PL quenching for BDTT:PC<sub>71</sub>BM blend film is consistent with agglomerated morphology.

**Table 7. 2** Summary of device characteristics

	Polymer:PC <sub>71</sub> BM ( w/w )	Solvent (v/v)	$J_{sc}$ ( mA/cm <sup>2</sup> )	$V_{oc}$ ( V )	$FF$	$PCE$ ( % )
BDTT	1:1	DCB	5.95	0.75	0.56	2.52
	1:2	DCB	5.50	0.76	0.52	2.17
	1:3	DCB	5.49	0.68	0.48	1.79
	1:1	98% DCB+2% DIO	5.71	0.72	0.49	2.00
	1:1	98% DCB+2% ODT	6.20	0.69	0.54	2.30
	1:1	98% DCB+2% CN	6.10	0.71	0.56	2.30
	1:1	98% DCB+2% DPE	6.91	0.68	0.46	2.15
BDTOT	1:1	DCB	6.84	0.68	0.57	2.68
	1:2	DCB	6.30	0.65	0.57	2.33
	1:3	DCB	7.14	0.64	0.44	1.98
	1:1	98% DCB+2% DIO	6.72	0.65	0.58	2.54
	1:1	98% DCB+2% ODT	5.14	0.63	0.43	1.39
	1:1	98% DCB+2% CN	6.62	0.67	0.54	2.38
	1:1	98% DCB+2% DPE	7.01	0.60	0.51	2.16
BDTCOT	1:1	DCB	9.22	0.81	0.62	4.66
	1:2	DCB	7.56	0.76	0.61	3.54
	1:3	DCB	4.96	0.74	0.54	1.97
	1:1	98% DCB+2% DIO	8.90	0.79	0.63	4.45
	1:1	98% DCB+2% ODT	8.84	0.81	0.60	4.27
	1:1	98% DCB+2% CN	8.19	0.73	0.66	3.91
	1:1	98% DCB+2% DPE	7.90	0.72	0.65	3.74

**Table 7. 3** Summary of photovoltaic parameters

polymer	$J_{sc}$ (mA/cm <sup>2</sup> )	$V_{oc}$ (V)	$FF$	$PCE$ (%)	$J_{sc}$ [cal.] (mA/cm <sup>2</sup> ) <sup>a</sup>
BDTT	5.95	0.75	0.56	2.52	5.56
BDTOT	6.84	0.68	0.57	2.68	6.20
BDTCOT	9.22	0.81	0.62	4.66	9.53

<sup>a</sup> $J_{sc}$  [cal.], calculated  $J_{sc}$  from a EQE curve.



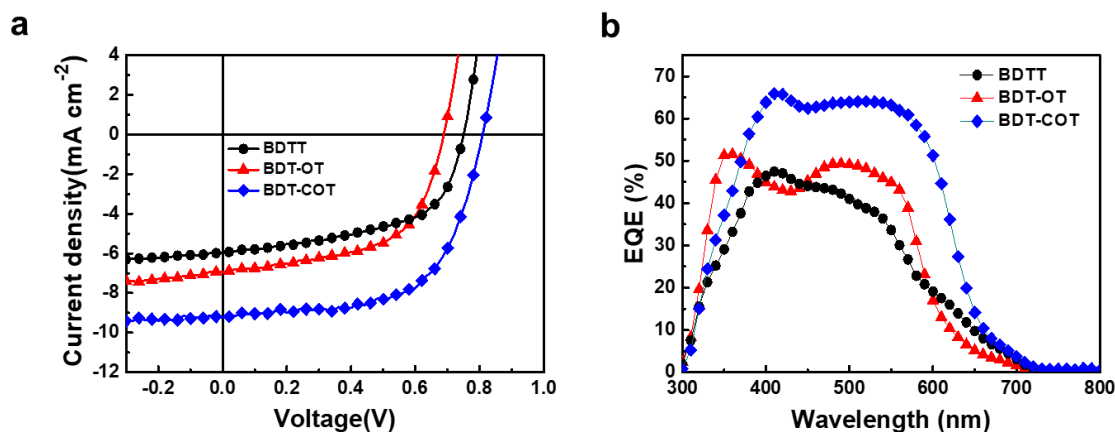


Figure 7. 5 (a)  $J$ - $V$  characteristics and (b) EQE spectra of polymer:PC<sub>71</sub>BM photovoltaic devices

### 7.3.3 Microstructure Analyses and Morphology of Thin Films

The microstructural orientation obtained from measurement of wide-angle X-ray scattering (GIWAXS) patterns for pristine polymer films and BDTT series polymers:PC<sub>71</sub>BM blend films were analyzed to understand correlation with OSCs performance. 2D GIWAXS images and plotting lines corresponding the results are shown in **Figure 7.6**, and detailed crystallographic parameters of blended films are summarized in **Table 7.4**. Interestingly, the interlamellar d-spacing (100) along in-plane direction for BDTT, BDTOT and BDTCOT showed 17 Å, 24.2 Å and 26.2 Å, respectively, indicating that the presence of side chains on the thiophene group disturbs tight lamellar packing. All polymers exhibited (010) patterns of  $\pi$ - $\pi$  stacking on out-of-plane direction, which suggests favorable face-on orientation. The d-spacing of  $\pi$ - $\pi$  stacking calculated 3.93 Å, 3.81 Å and 3.74 Å for BDTT, BDTOT and BDTCOT, respectively. The interchain hydrogen bonding interactions of BDTCOT contribute to well-ordered molecular packing. The blended films with PC<sub>71</sub>BM showed a similar tendency to pristine films, all the

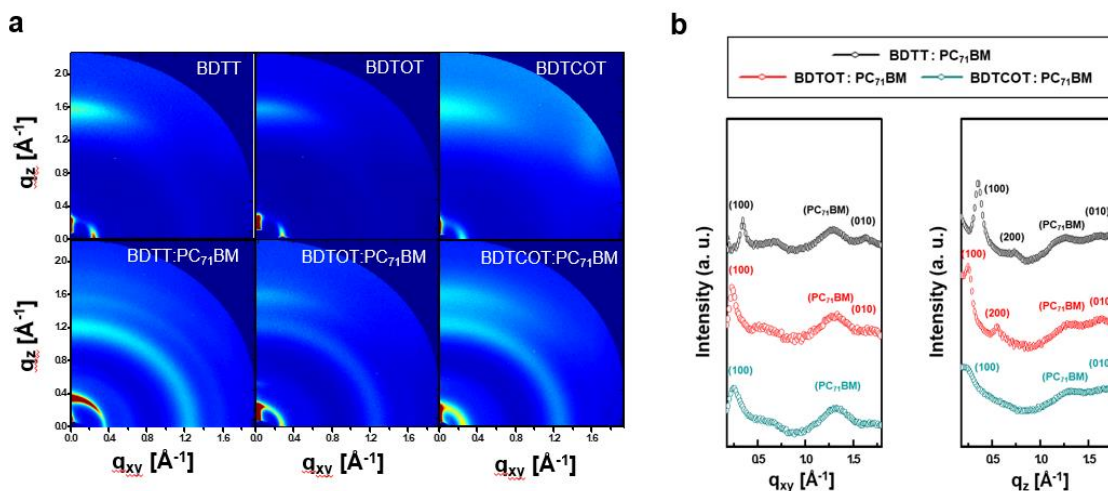
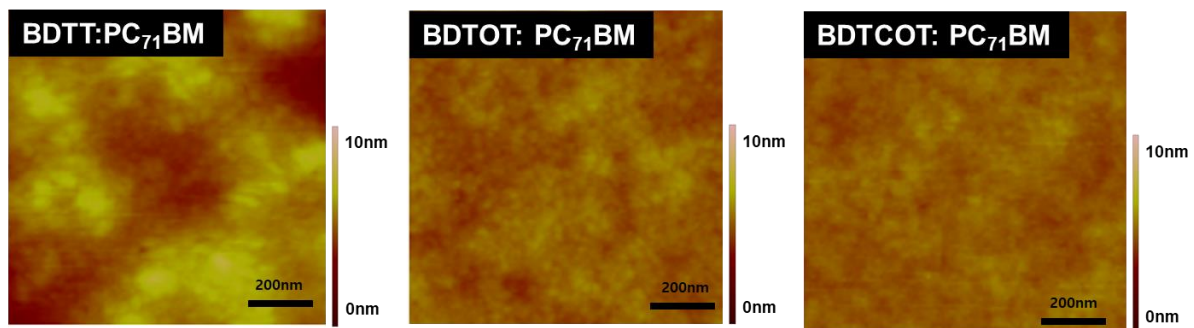


Figure 7. 6 (a) 2D-GIWAXS images of pristine and blend films and (b) plotting lines corresponding GIWAXS result.

**Table 7. 4** Crystallographic parameters of blend films

Polymer:PC <sub>71</sub> BM	Direction	Scattering vector (q) of $\pi$ - $\pi$ stacking [ $\text{\AA}^{-1}$ ]	d-spacing [ $\text{\AA}$ ]	Scattering vector of Lamella peak [ $\text{\AA}^{-1}$ ]	lamella interaction distance [ $\text{\AA}$ ]
BDTOT:PC <sub>71</sub> BM	In-plane ( $q_{xy}$ )	1.70	3.70	0.26	24.17
	Out-of- plane ( $q_z$ )	1.67	3.76	0.25	25.13
BDTT:PC <sub>71</sub> BM	In-plane ( $q_{xy}$ )	1.64	3.83	0.37	16.98
	Out-of- plane ( $q_z$ )	1.62	3.88	0.36	17.45
BDTCOT :PC <sub>71</sub> BM	In-plane ( $q_{xy}$ )	-	-	0.25	25.13
	Out-of- plane ( $q_z$ )	1.69	3.72	0.23	27.32

blend films also showed the (010) peak along the out-of-plane and clear lamellar patterns along the in-plane direction. The film morphology was measured by tapping mode atomic force microscope (AFM). **Figure 7.7** exhibited AFM topography images of the BDTT series polymers:PC<sub>71</sub>BM blended films. BDTT-based blend films showed larger domain size with high root mean square (RMS) roughness of around 4.1 nm due to poor solubility, which agglomerated morphology resulted in reduced  $J_{sc}$ s. while the other films based on BDTOT and BDTCOT showed less than 1 nm of RMS roughness.



**Figure 7. 7** AFM topography images for blend films ( $1.5 \mu\text{m} \times 1.5 \mu\text{m}$ )

## 7.4 Conclusion

A series of BDT and T-based donor polymers were synthesized with varying solubilizing side-chains, resulting in different optical, electrochemical, morphological and conformational characterization. The influence of substituents on backbone contributes to photovoltaic performance. Non alkyl side chain on thiophene moiety shows lower OSCs performance arising from poor solubility and huge aggregated morphology. In contrast, introduction of side chain presents deeper HOMO level and smooth surface morphology of photoactive films with good solution processability. Notably, BDTCOT polymer-based OSCs shows higher performance of 4.66% with tighter  $\pi$ - $\pi$  stacking of 3.72 Å of d-spacing, due to intrachain hydrogen bonding. Furthermore, since alkylcarbonyl side chain has stronger electron withdrawing properties, deeper HOMO energy level was obtained together with larger  $V_{oc}$  value.

## Chapter 8. A Roundabout Approach to Control Morphological Orientation and Solar Cells Performance by Modulating Side-Chain Branching Position in Benzodithiophene-Based Polymers

### 8.1 Research Background

Developing polymer-based bulk-heterojunction (BHJ) solar cells consisting of electron-donating polymers and electron-accepting fullerene derivatives continues to garner research interests because of several distinct benefits in terms of compatibility with flexible and light-weight substrates, architectural tunability over multiple length scales, and high-throughput yet low-cost processing.<sup>[78, 79]</sup> To achieve such high performances, one of the most critical contributions is the materials development, along with innovations and optimizations in the device structure and processing.<sup>[80]</sup> Therefore, relying on universal donor-acceptor (D-A) strategies, vast numbers of new D-A copolymeric donor materials have been developed in which most of the efforts have been focused on the structural modification of the conjugated backbones for precisely tuning the frontier energy levels, in order to harvest as much of the solar energy as possible while at the same time maintaining a sufficient energetic driving force for charge separation.<sup>[81]</sup> Taking into account the above-mentioned prerequisites, D-A copolymers based on benzo[1,2-*b*:4,5-*b'*]dithiophene (BDT) units—relatively simple, compact, symmetric, and planar structure—have been subject to increasing of particular interest for use in high-performance solar cells, since their inception on BHJ solar cells. Thereafter, many D-A copolymers based on BDT with different conjugated units have been successfully demonstrated with high PCE in BHJ devices. Besides manipulating their backbone structures, structural modifications brought about by means of alkyl side chain variations. For example, the BDT-containing 2-D polymers by replacing alkoxy groups with alkylthienyl side chains were synthesized.<sup>[79, 82]</sup> Recently, Beaujuge et al. reported the synthesis of BDT-based copolymers bearing linear alkoxy side chains in the BDT motifs, instead of the branched ones. Progress of these classes of polymer materials has been impressive, with PCE as high as 9.2%,<sup>[83]</sup> but it is also believed that superior performance is possible through implementation of the newly fine-tuned molecular structures of BDT building core to copolymerize with suitable co-units.

Therefore, an afresh design and synthesis of BDT-containing polymers are still worthy of investigation in polymer BHJ solar cell fields, which will be made in in-depth understanding the materials science and the associated improvement in PCEs.

As an work on the side chains' engineering, in this context, we chose the copolymer of BDT and TPD referred to as PBDTTPD-C<sub>n</sub> and tried to shed light on the structure-property device performance relationship associated with structural dynamics of the side chains by moving the branching position away from BDT core (see the three PBDTTPD-C<sub>n</sub> polymers in **Figure 8.1**, where n is the number of carbon atoms between alkoxyated oxygen and the branching point).

## 8.2 Experimental

### 8.2.1 Fabrication of Organic Devices

Organic solar cells (OSCs) were fabricated with a configuration of ITO/PEDOT:PSS/ PBDTTPD-Cn:PC<sub>71</sub>BM/Al. The patterned indium tin oxide (ITO) on glass was pre-cleaned with detergent, and ultrasonic bath of distilled water, acetone and isopropanol. And substrates are treated in an ultraviolet-ozone chamber for 20 min after dried in an oven overnight at 100 °C. Poly(3,4-ethylenedioxythiophene):poly(styrene sulfonate) (PEDOT:PSS, Baytron P clevis™ AI 4083, Germany) was spin-coated onto the ITO glass as 45 nm thin layer and dried at 140 °C for 10 min, transferred into a nitrogen filled glove box. Solutions containing mixture of PBDTTPD-Cn:PC<sub>71</sub>BM in *o*-dichlorobenzene (*o*-DCB) solvent with concentration of 2 wt% for PBDTTPD-C1 and PBDTTPD-C3, 1wt% for PBDTTPD-C4 were spin-cast on the PEDOT:PSS layer. The mixed solutions of PBDTTPD-Cn:PC<sub>71</sub>BM were with and without additive. Then, Al cathode (100 nm) was deposited on the active layer by thermal evaporation in pumped down in vacuum (<10<sup>-6</sup> Torr) condition. The thickness of the photoactive layer was measured using a surface profiler (KLA\_tencor (USA)). The active area of the device was 13 mm<sup>2</sup>. *J-V* characteristics were measured by a computer-controlled Keithley 2635A Source Measurement under an AM 1.5G illumination at 100 mWcm<sup>-2</sup> coupled with a xenon lamp. EQE (PV measurements Inc.) spectra were obtained by applied monochromatic light from a xenon lamp. The *J<sub>sc</sub>* value of monochromatic power was calibrated using a silicon photodiode for ambient conditions.

All organic field-effect transistors (OFETs) were fabricated on heavily n-type doped silicon wafer coated thick SiO<sub>2</sub> layer as gate electrode and gate dielectric. The device structure was top contact bottom gate architecture. The semiconducting PBDTTPD-Cn were spin-cast from solution at 1700 rpm after cleaned wafers were pretreated with a solution of 1.0 mM octyltrichlorosilane (OTS) in toluene under N<sub>2</sub> filled condition to refine apolar and smooth surface. Source and drain electrodes were deposited by thermal evaporation. The thickness of top electrode (source and drain) was 80 nm. The channel's width to length ratio (W/L) of the devices was 59/1. Electrical characterization was tested using a keithley semiconductor parametric equipment (keithley 4200) under N<sub>2</sub> atmosphere.

Hole only devices for measuring hole mobility were fabricated as diode configuration of ITO/PEDOT:PSS/polymer:PC<sub>71</sub>BM/Au. While electron only devices were fabricated with diode configuration of FTO/polymer:PC<sub>71</sub>BM/Al. The blend solutions were each optimized condition of PBDTTPD-Cn, which equate to polymer solar cells. The solutions were spin coated on ITO and FTO substrates at each optimal spin-rate. The thickness of devices was measured by using surface profiler (KLA\_tencor (USA)). The gold and aluminium were deposited by thermal evaporation as electrode (thickness ≈ 100 nm) under high vacuum condition. The devices were measured under dark condition taking in the range of ~ 3 V.

## 8.3 Results and Discussion

### 8.3.1 Characterization of Synthesized Polymers

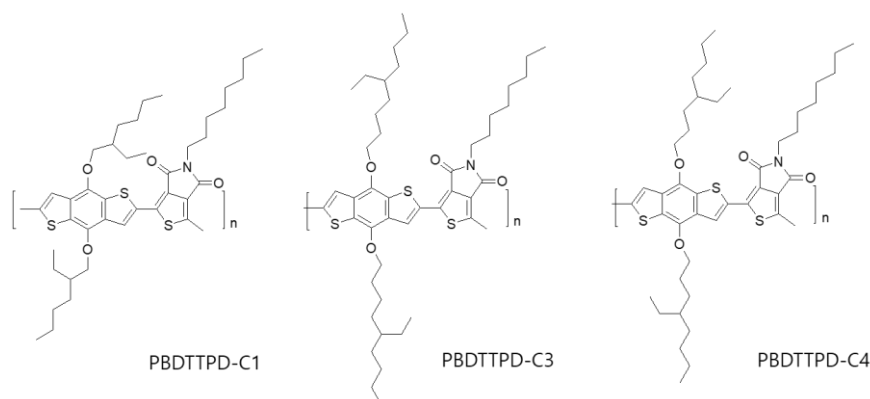


**Figure 8. 1.** Chemical structure of PBDTTPD-Cn donor polymers

As shown in **Figure 8.2 (a-b)**, the normalized UV-vis absorption spectra for PBDTTPD-Cn both solution in chloroform and thin films were measured. All polymers showed quite similar absorption band both cases showing shoulder peaks around the maximum absorption. The appearance can indicate the intramolecular charge transfer (ICT) between electron-donating BDT and withdrawing TPD units. For absorption spectra of thin films, shoulder peaks at maximum absorption were clearly observed with broadening in range of 400–670 nm of wavelength. The optical band gap ( $E_g^{\text{opt}}$ ) from thin films absorption for PBDTTPD-Cn polymers were obtained.

Cyclic voltammetry (CV) was used to examine the frontier orbital energy levels of all polymers. (see **Figure 8.2(c)**) The highest occupied molecular orbital (HOMO) levels were -5.44, -5.35, and -5.44 eV for PBDTTPD-C1, C3 and C4, respectively. Also, all polymers showed lowest unoccupied molecular orbital (LUMO) values of -3.55, -3.51, -3.53 eV for PBDTTPD-Cn. **Figure 8.2 (d)** shows the band diagram of materials for OSCs. Detailed optical and electrochemical properties are listed in **Table 8.1**.

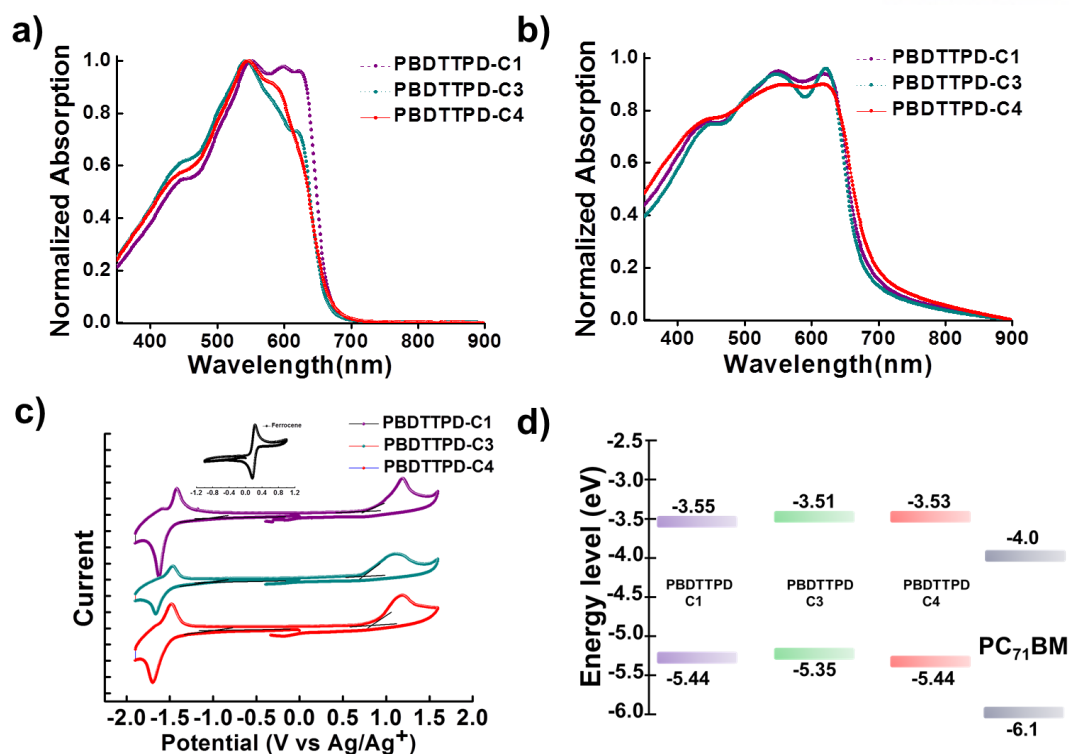


**Figure 8.** 2 UV-vis absorption spectra of PBDTTPD-Cn in chloroform solution (a) and as a thin solid films spin-cast from chloroform (b) Cyclic voltammograms of PBDTTPD-Cn thin films (c) Energy level diagrams for PBDTTPD-Cn and PC<sub>71</sub>BM (d)

**Table 8. 1** Photophysical and electrochemical properties of PBDTTPD-Cn

Polymer	$M_n$ (kDa)	PDI	$\lambda_{\max}^{\text{sol}}$ (nm)	$\lambda_{\max}^{\text{film}}$ (nm)	$E_g^{\text{opt}}$ (eV)	$E_{\text{HOMO}}$ (eV)	$E_{\text{LUMO}}$ (eV)	$E_g^{\text{CV}}$ (eV)
PBDTTPD-C1	13.0	2.10	550	620	1.78	-5.44	-3.55	1.89
PBDTTPD-C3	23.0	1.92	543	622	1.81	-5.35	-3.51	1.84
PBDTTPD-C4	16.0	2.32	547	620	1.77	-5.44	-3.53	1.91

### 8.3.2. Polymer Conformation

The aim is to provide insight into one of the branched side groups that exhibit the effect of the selective fine-tuning of LUMO levels. By investigating the possible subtle change of the molecular architecture arising from moving the branching point on the BDT unit, we conducted density functional theory (DFT) calculations of the model molecules using Gaussian 09 at the B3LYP/6-31G\* level. To simplify the calculations, the octyl chains on the TPD acceptor unit were replaced with methyl groups, and the backbones were simplified to a BDT-TPD-BDT structure. Interestingly, the dihedral angle of 0.6° between BDT and TPD in the optimized structure of BDT-TPD-BDT-C1 is reduced to 0.2–0.3° in BDT-TPD-BDT-C3 and -C4, implying that a strengthened coplanar conformation can be achieved by tuning the branching point further from the backbone. In addition, in all cases, the HOMOs are mostly distributed along the BDT donor unit, whereas the LUMOs are localized on the TPD acceptor moiety,

implying that the distance of the branching position from BDT has a negligible effect on the electron state density distributions of the polymers.

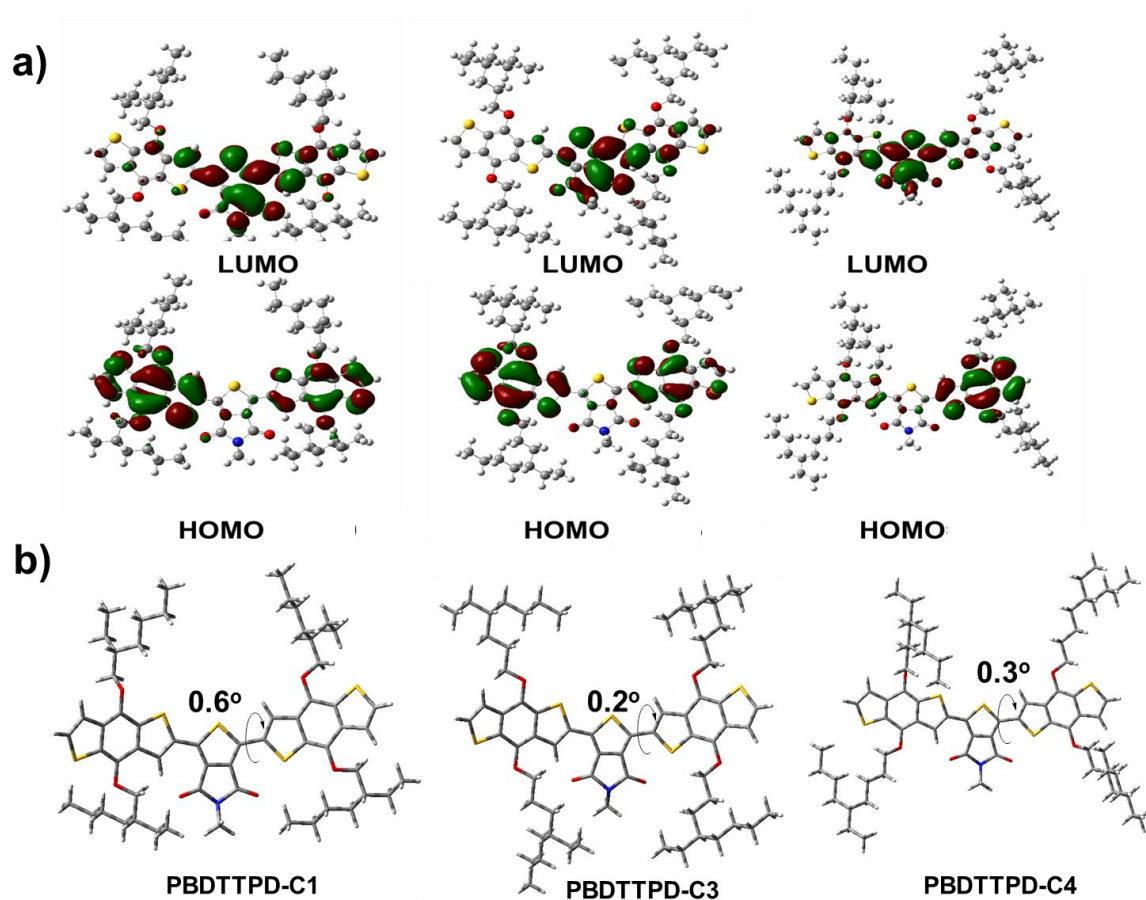


**Figure 8. 3** (a) DFT-optimized geometries and charge-density isosurfaces for BDT-TPD-BDT (B3LYP/6-31G\*) and (b) their dihedral angles



### 8.3.3 OSCs Performance and Film Morphology

To examine the effect of the alkyl chain branching point on both performance and blend morphology in polymer-based BHJ solar cells with a PC<sub>71</sub>BM acceptor, we fabricated with standard structure of indium tin oxide (ITO)/poly(3,4-ethylenedioxythiophene):poly(styrenesulfonate) (PEDOT:PSS)/BDT-based polymer:PC<sub>71</sub>BM/Al. The detailed parameters of the optimized devices for each polymer are summarized in **Table 8.2**, with the corresponding current density–voltage ( $J$ – $V$ ) curves and external quantum efficiency (EQE) spectra shown in **Figures 8.4**. The best device performance was achieved based on PBDTTPD-C1:PC<sub>71</sub>BM (1:2 w/w) devices processed with 3 vol% DIO, which showed a high current density ( $J_{sc}$ ) of 11.6 mAcm<sup>-2</sup>, open-circuit voltage ( $V_{oc}$ ) of 0.84 V, a fill factor (FF) of 0.47, and an impressive PCE of 4.56 %. In both PBDTTPD-C3 and PBDTTPD-C4, even though FF values were comparable to that of PBDTTPD-C1, and even higher  $V_{oc}$  values were obtained without processing additives, significantly reduced  $J_{sc}$  values led to greatly lowered PCEs. We found that after employing 3 vol% CN, the  $J_{sc}$  values of the devices were dramatically improved, from 1.74–2.83 to 6.55–7.09 mAcm<sup>-2</sup>, and thus PCEs were increased to 2.37–2.80 %, however, it was still lower than of that of the optimized BHJ solar cells cast from PBDTTPD-C1:PC<sub>71</sub>BM. The EQE curves of the solar cells were fabricated under the same optimized conditions as those used for the  $J$ – $V$  measurements. The  $J_{sc}$  values calculated by integrating the EQE curve with an AM1.5G reference spectrum have an average 6.1% error compared to the corresponding  $J_{sc}$  obtained from the  $J$ – $V$  curves. This indicates that our photovoltaic measurement is both accurate and reliable. Obviously, the EQE values for PBDTTPD-C1 are all higher than those of PBDTTPD-C3- and PBDTTPD-C4-based cells, which are consistent with the higher  $J_{sc}$  values of the devices derived from PBDTTPD-C1.

**Table 8. 2** Parameters of performance for PBDTTPD-C<sub>n</sub> devices with structure of ITO/PEDOT:PSS/polymer:PC<sub>71</sub>BM/Al measured under AM 1.5G illumination at 100 mWcm<sup>-2</sup>

Polymer	Polymer: PC <sub>71</sub> BM (w/w)	Solvent (v/v)	$J_{sc}$ (mAcm <sup>-2</sup> )	$V_{oc}$ (V)	FF	PCE (%)	Cal. $J_{sc}$ (mAcm <sup>-2</sup> )
<b>C1</b>	1:2	CB	9.54	0.81	0.53	4.07	8.72
		97%CB +3%DIO	11.60	0.84	0.47	4.56	11.92
<b>C3</b>	1:1	CB	1.74	0.91	0.49	0.78	2.10
		97%CB+ 3%CN	7.09	0.76	0.52	2.80	6.90
<b>C4</b>	1:2	CB	2.83	0.86	0.51	1.24	2.73
		97%CB+ 3%CN	6.55	0.70	0.52	2.37	6.64

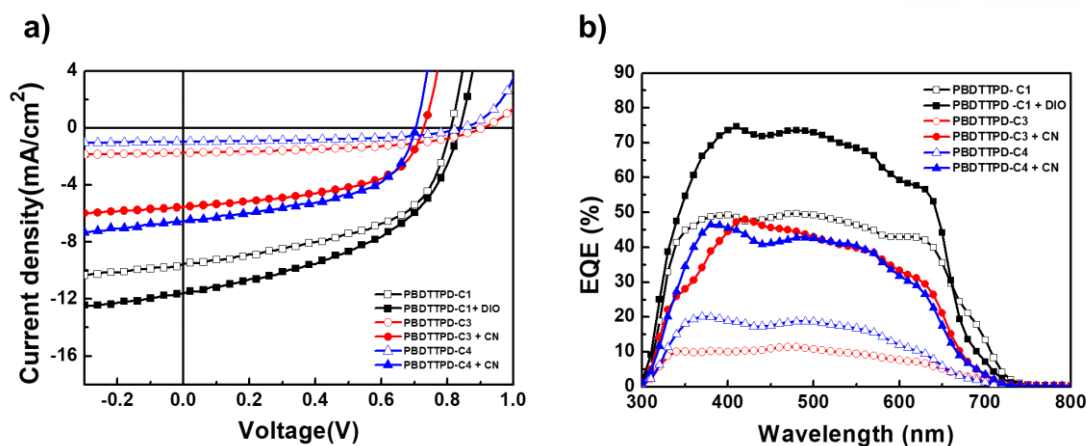


**Figure 8. 4** *J-V* Characteristics (a) and external quantum efficiency (EQE) spectra of PBDTTPD-C1 (black), C3 (blue) and C4 (red) (b)

To correlate the polymer side-chain patterns effectively, the microstructural order in thin films, and device performance, we employed a grazing-incidence wide-angle X-ray scattering (GIWAXS), and examined the films of the pure polymers and optimized polymer:PC<sub>71</sub>BM blends. As shown in **Figure 8.5**, all neat polymer films exhibited (h00) diffraction patterns along the  $q_z$  (out-of-plane) axis, corresponding to a lamellar structure, together with (010) peaks along the  $q_{xy}$  (in-plane) axis arising from the  $\pi$ - $\pi$  stacking of polymer backbones; the detailed crystallographic parameters are presented in **Table 8.3**. Notably, the neat films of both PBDTTPD-C3 and PBDTTPD-C4 not only revealed more intense and sharper (100) peaks and multi-peak diffraction up to the third order, but also the (100) peaks shifted towards a slightly smaller  $q$  as the branching point length was increased. Thus, the lamellar d-spacing distances follow the sequence PBDTTPD-C1 (16.98 Å) < PBDTTPD-C3 (19.04 Å) < PBDTTPD-C4 (19.63 Å) from GIWAXS. A face-on orientation was found for all pure polymer films, with evident (010)  $\pi$ - $\pi$  stacking reflection in the out-of-plane direction ( $q_{xy} \approx 0$ ) and the (100) lamellar d-spacing reflection in the in-plane direction ( $q_z \approx 0$ ). In parallel, it should be noted that the relative intensity of the  $\pi$ - $\pi$  spacing peak in the in-plane direction became stronger as the branching point was shifted away from the backbone, which seems to slightly encourage the edge-on character population in PBDTTPD-C3 and PBDTTPD-C4. A similar effect of the position of the chain branching point on the thin-film morphology has previously been noticed in our and other groups. In addition to a diffraction halo patterned at 1.34-1.37 Å<sup>-1</sup> associated with PC<sub>71</sub>BM (as shown in **Figure 8.6**), a similar trend was observed for the polymer:PC<sub>71</sub>BM blend films. Moving the branching point further from the backbone resulted in higher-order diffraction peaks in the out-of-plane direction, and slightly more pronounced  $\pi$ - $\pi$  peaks in the in-plane direction. Additionally, once the processing additive was used, the intensities of the out-of-plane (010) and in-plane (100) peaks in the blending systems became more obvious and increased slightly, indicating that the crystallinity and the face-on orientation population

were both enhanced. Consequently, GIWAXS data indicated the fractions of PBDTTPD-C1 crystallinity. In both cases, the pure polymers and blends decreased not only the lamellar ordering, but also relatively favourable face-on characteristic. Therefore, we assume that the intrinsic differences in preferential polymer orientation and the overall degree of structural order correlates with the variations in material performance observed in BHJ solar cells with PC<sub>71</sub>BM.

**Table 8. 3** Summary of GIWAXS analysis on PBDTTPD-Cn as neat and blend films

Polymer	Direction	Angle of $\pi$ - $\pi$ interaction [ $\theta$ ]	Scattering vector (q) of $\pi$ - $\pi$ stacking [ $\text{\AA}^{-1}$ ]	d-spacing [ $\text{\AA}$ ]	Lamella interaction (h00)	Angle of Lamella peak [ $\theta$ ]	Scattering vector of Lamella peak [ $\text{\AA}^{-1}$ ]	lamella interaction distance [ $\text{\AA}$ ]
Neat-C1	In-plane	-	-	-	(100)	1.75	0.31	20.27
	Out-of-plane	10.06	1.77	3.55	(100)	2.09	0.37	16.98
Neat-C3	In-plane	9.94	1.75	3.59	(100)	1.58	0.28	22.44
	Out-of-plane	10.06	1.77	3.55	(100)	1.87	0.33	19.04
Neat-C4	In-plane	9.94	1.75	3.59	(100)	1.55	0.275	22.84
	Out-of-plane	10.06	1.77	3.55	(100)	1.81	0.32	19.63
Blend-C1	In-plane	9.94	1.75	3.59	(100)	1.75	0.31	20.27
	Out-of-plane	10.11	1.78	3.53	(100)	2.09	0.37	16.98
Blend-C3	In-plane	9.94	1.75	3.59	(100)	1.58	0.28	22.44
	Out-of-plane	10.11	1.78	3.53	(100)	1.92	0.34	18.48
Blend-C4	In-plane	9.94	1.75	3.59	(100)	1.55	0.275	22.84
	Out-of-plane	10.11	1.78	3.53	(100)	1.87	0.33	19.04

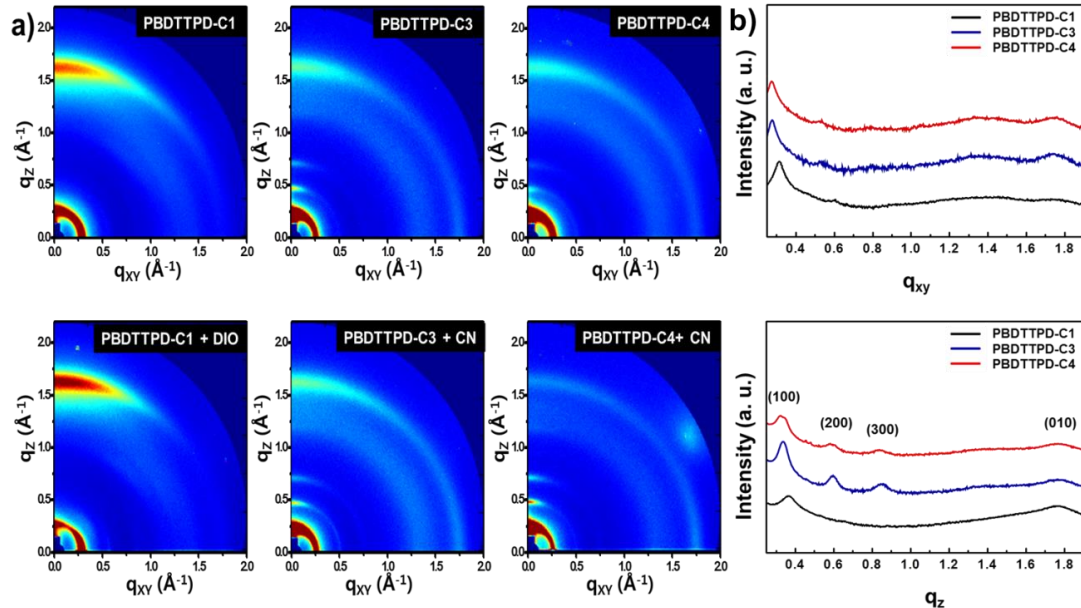


**Figure 8. 5** Grazing incident wide angle X-ray scattering (GIWAXS) results for neat PBDTTPD-Cn in-plane and out-of-plane line cuts of the corresponding above patterns

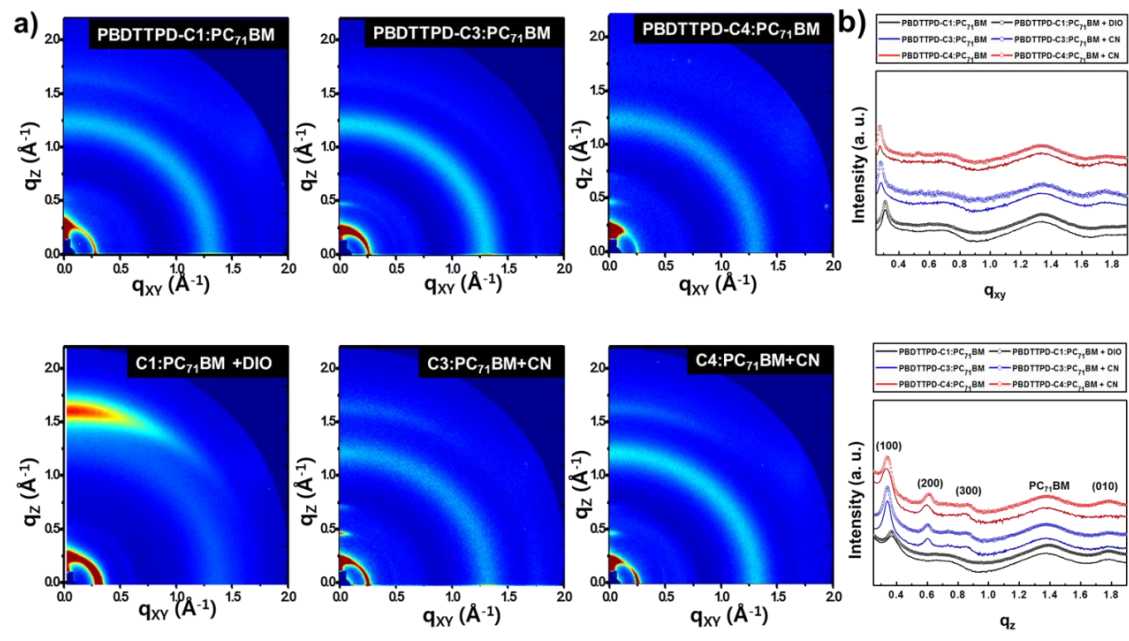


**Figure 8. 6** GIWAXS images for blends of PBDTTPD-Cn:PC<sub>71</sub>BM and with additive (a). In-plane and out-of-plane line cuts of the corresponding above patterns for PBDTTPD-Cn:PC<sub>71</sub>BM (solid line) and with additive (symbol line) films

The surface morphologies of polymer:PC<sub>71</sub>BM blends cast without and with the corresponding optimal additives were explored using tapping-mode atomic force microscopy (AFM), as shown in **Figure 8.7**. Thin films processed without additives contained a smooth and featureless texture with RMS roughness of 2.35 nm for PBDTTPD-C1. In contrast, the large agglomerated clusters with RMSs of 5.22–7.68 nm were observed for PBDTTPD-C3 and PBDTTPD-C4, which is consistent with the high crystallinity revealed by GIWAXS. This nonhomogeneity on the macroscopic level is most likely responsible for the inferior device performance for PBDTTPD-C3 and PBDTTPD-C4. In addition, the additives were regulating the domain size of the morphology by selectively solubilizing the PC<sub>71</sub>BM, facilitating the integration of the PC<sub>71</sub>BM molecules into the polymer aggregates, which is in good agreement with similar reports. According to the GIWAXS and AFM results, it can be concluded that the intrinsic differences in preferential polymer orientation and overall degree of structural order correlate with the variations in BDT-based polymer performances observed in the BHJ solar cells with PC<sub>71</sub>BM.

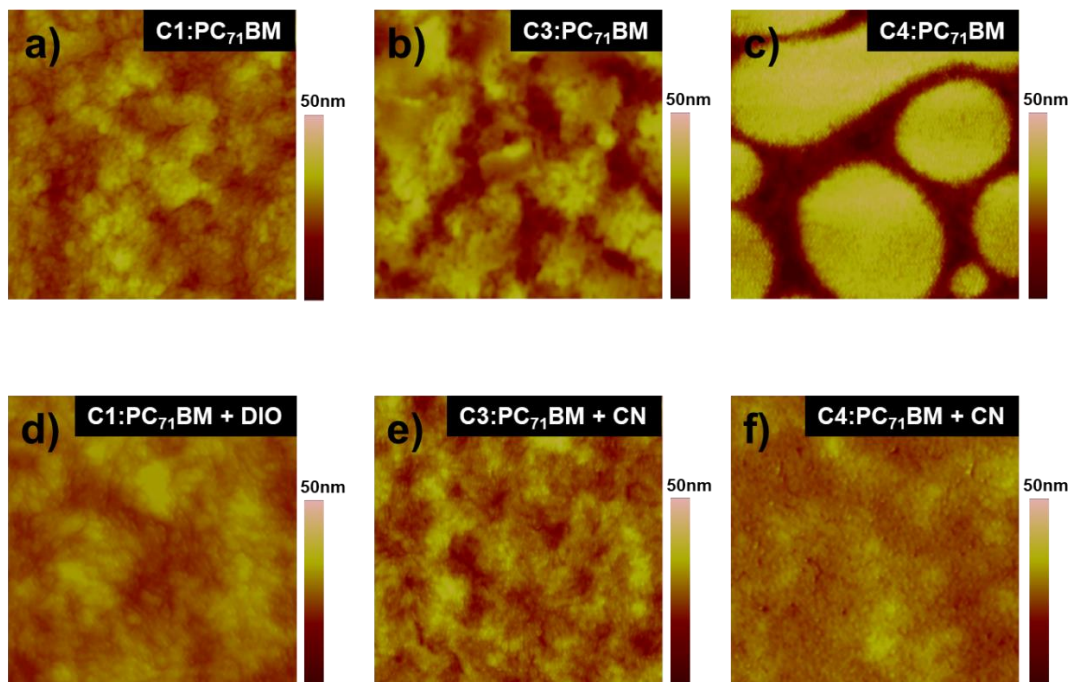


**Figure 8. 7** Atomic force microscopy (AFM) images ( $2 \times 2 \mu\text{m}^2$ ) of polymer:PC<sub>71</sub>BM on ITO substrate: root-mean-square (RMS) as (a) 3.32 nm (top), 2.13 nm (bottom) of PBDTTPD-C1 (b) 5.22 nm (top), 4.02 nm of PBDTTPD-C3 (c) 7.68 nm (top), 2.64 nm (bottom) of PBDTTPD-C4, respectively

To find the origin of the difference in the solar cells' performances, the charge–transport properties were investigated by examining the charge–carrier mobility of the polymer:PC<sub>71</sub>BM under the each optimized condition, using the space-charge limited current (SCLC) model (hole only (ITO/PEDOT:PSS/polymer:PC<sub>71</sub>BM/Au) and electron only (FTO/polymers:PC<sub>71</sub>BM/Al) devices, respectively). Hole and electron mobilities are calculated by Mott-Gurney equation (**Equation 8.1**).

$$J_{SCLC} = \frac{9}{8} \epsilon_r \epsilon_0 \mu \left( \frac{V^2}{L^3} \right) \quad (\text{Eq. 8.1})$$

Where  $\epsilon_r$  is the dielectric constant of the material,  $\epsilon_0$  is the permittivity of free space,  $L$  is the thickness of film between the cathode and anode electrodes, and  $V$  is the applied voltage (The details can be found in the Experimental Section). The  $J$ – $V$  characteristics are plotted in **Figure 8.8**, and the calculated hole and electron mobilities are listed in **Table 8.4**. Together with the electron mobilities being nearly identical for all polymer:PC<sub>71</sub>BM ( $\sim 1.0 \times 10^{-4} \text{ cm}^2/\text{V}\cdot\text{s}$ ), small variations in their hole mobilities are also revealed in the range of  $1.13 \times 10^{-5} - 8.18 \times 10^{-5} \text{ cm}^2/\text{V}\cdot\text{s}$ , consequently leading to similar balanced charge transport ( $\mu_{\text{electron}}/\mu_{\text{hole}}$ ) ratios. This would account for the quite similar FF values in the current series of BHJ solar cells. We also measured the top-contact, organic field-effect transistors (OFETs) with the architecture of Si/SiO<sub>2</sub>/octyltrichlorosilane (OTS)/polymer/Au (the characteristic output and transfer curves as well as the detailed results shown in **Figure 8.9** and **Table 8.5**. It is recognized that the mobilities of all polymers do not vary significantly.

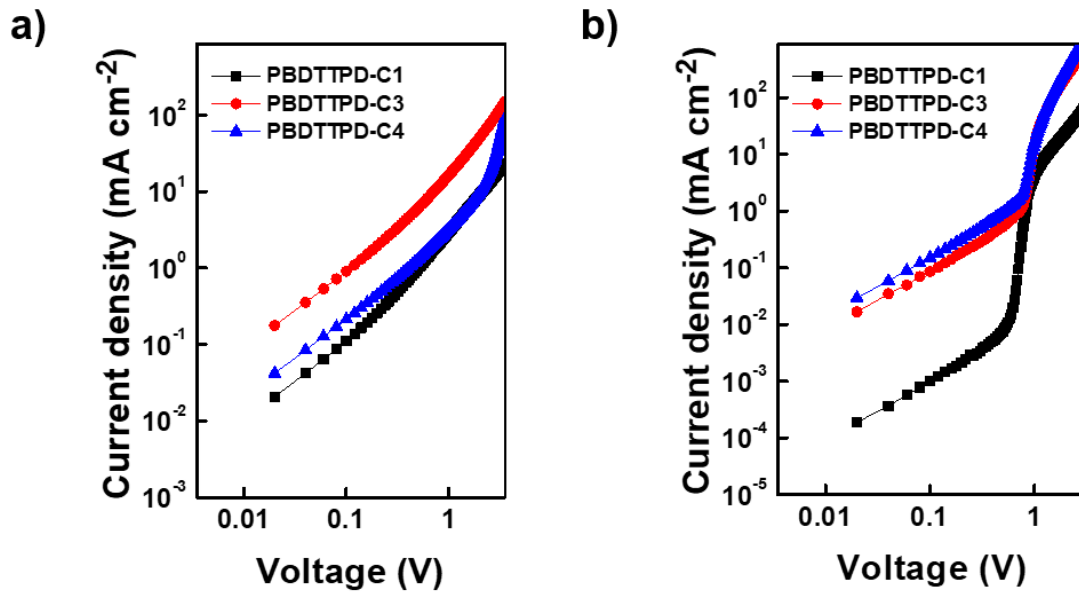


**Figure 8. 8** Double-logarithmic plot from dark  $J$ - $V$  characteristics of (a) hole-only devices (ITO/PEDOT:PSS/polymer:PC<sub>71</sub>BM/Au) and (b) electron only devices (FTO/polymer:PC<sub>71</sub>BM/Al)

**Table 8. 4** Calculated electron and hole mobility of PBDTTPD-based polymers by space charge limited current (SCLC) devices and their thickness layers

Polymer	Active layer (nm)	$\mu_{\text{ele}}$ ( $\text{cm}^2 \text{V}^{-1} \cdot \text{s}^{-1}$ )	Active layer (nm)	$\mu_{\text{hole}}$ ( $\text{cm}^2 \text{V}^{-1} \cdot \text{s}^{-1}$ )	$\mu_{\text{ele}}/\mu_{\text{hole}}$
PBDTTPD-C1	180	$1.08 \times 10^{-4}$	140	$2.35 \times 10^{-5}$	4.59
PBDTTPD-C3	80	$1.23 \times 10^{-4}$	125	$8.18 \times 10^{-5}$	1.50
PBDTTPD-C4	80	$1.10 \times 10^{-4}$	110	$1.13 \times 10^{-5}$	9.73

**Table 8. 5** Summarized the performance values of *o*-FET device with hole mobility, threshold voltage and on-off ratio for PBDTTPD-C1, C3 and C4

Polymer	Thermal Annealing (°C)	Mobility (cm <sup>2</sup> s <sup>-1</sup> V <sup>-1</sup> )	I <sub>off</sub> (A)	I <sub>on</sub> (A)	I <sub>on</sub> /I <sub>off</sub>	V <sub>T</sub> (V)
PBDTTPD-C1	200	4.64E-05	2.91E-11	2.60E-08	8.90E+02	-12.73
PBDTTPD-C3	300	3.83E-05	2.76E-11	3.32E-08	1.20E+03	-15.22
PBDTTPD-C4	200	1.27E-05	9.74E-12	9.81E-09	1.01E+03	-20.81

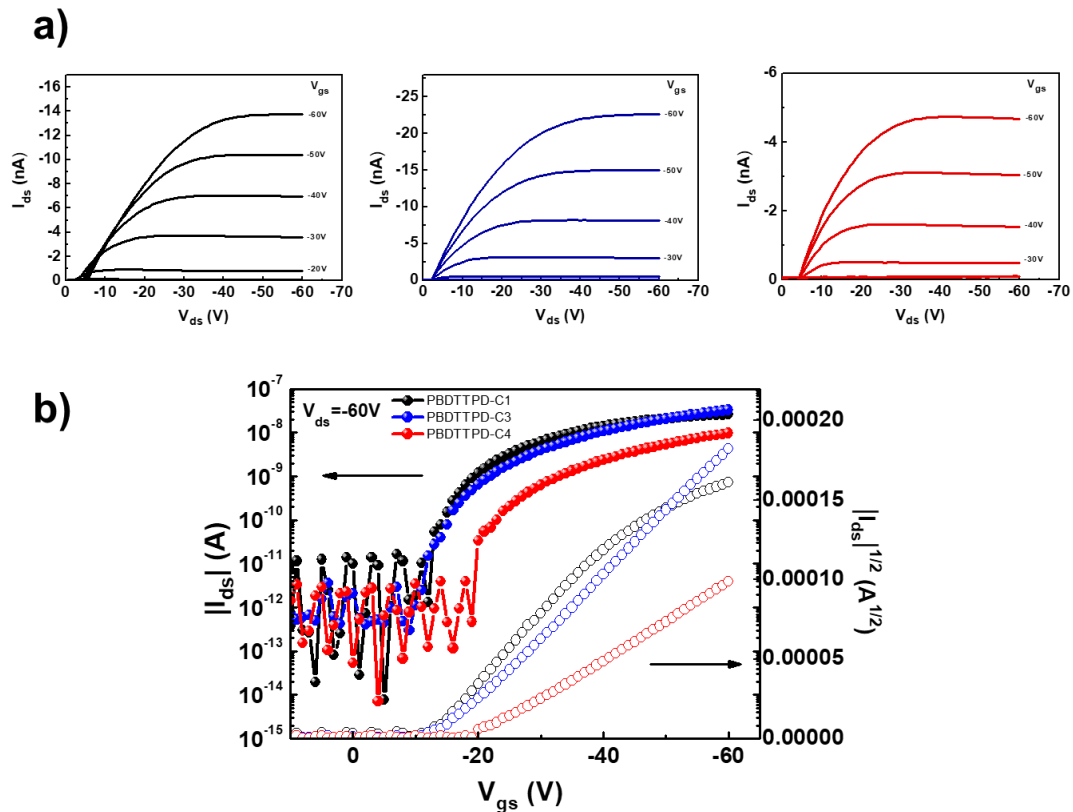


**Figure 8. 9** The performance of OFETs used OTS treatment as a passive layer (a) The output characteristics, (b) the transfer characteristics and plots of the square root the drain current as a function of the gate voltage for PBDTTPD-C1(black), C3(blue) and C4(red). ( $I_D$ : Drain current.  $V_G$ : Voltage of gate in an OFET.  $V_{DS}$ : Voltage between drain and source in an OFET)



## 8.4 Conclusion

2-Ethylhexyl side chains have primarily been utilized as solubilizing groups in many conjugated polymers. In this work, not only do we introduce a 2-ethylhexyl group and two novel-designed branched alkyl chains (4-ethyloctyl and 5-ethylnonyl) into BDT-based conjugated polymers (PBDTTPD-C<sub>n</sub>), but also thoroughly investigate how the branching location of alkyl chains can impact their energetics, morphologies, molecular packing, and solar cell performance. The fine modulation of the branching position on the BDT motif does not significantly affect the polymer energy levels and charge carrier mobilities, yet this strategy triggers a change of preferential polymer orientation in thin films. In other words, PBDTTPD-C1 exhibits a pronounced face-on character, while PBDTTPD-C3 and PBDTTPD-C4 are slightly encouraged to form an edge-on lamellar packing in both neat polymer and blended films. Therefore, PBDTTPD-C1 is found to reach a PCE of 4.56 % in standard BHJ devices with PC<sub>71</sub>BM, which represents a significant improvement over the other polymers, for which PCEs of 2.37–2.80 % were achieved. Our findings exhort the value of expanding the role of a polymer's side chains during the development of high performance polymers for organic solar cells and OFETs.

## Chapter 9. Semi-Crystalline Photovoltaic Polymers with Siloxane-Terminated Hybrid Side-Chains

### 9.1 Research Background

In recent years, outstanding achievements have been demonstrated in developing solution-processable organic photovoltaic materials, interfacial materials, as well as device fabrication for organic photovoltaic cells (OPVs).<sup>[84],[85]</sup> Systematic investigation on the correlation of molecular structure, solubility, molecular packing and self-organized morphology,<sup>[86]</sup> and solution processing condition have resulted in the development of highly efficient photovoltaic materials showing over 10% power conversion efficiency (PCE). To optimize the molecular structure of semiconducting conjugated materials, as well as the conjugated main-chain, alkyl solubilizing side-chains should be considered carefully. Tremendous efforts have been devoted to design and investigate solubilizing chains by considering of length,<sup>[87]</sup> shape,<sup>[88]</sup> bulkiness, chirality, even-odd effect<sup>[89]</sup> and branch point,<sup>[90]</sup> which significantly affect the film morphology and the resulting electrical properties. However, the role and/or effects of side-chains in organic semiconducting materials is quite flexible, hard to expect and highly dependent on the conjugated backbones. As an insulating segment, not only the solubility, surface energy, related molecular packing and thin film morphology from solution to a solid state but also the charge carrier transport in the blend system are necessary to be considered together, which is still a great challenge.

Recently, the siloxane-hybrid side chain has been come in sight as one of popular alkyl chains for semiconducting materials, a block of linear alkyl chain and a flexible trisiloxane terminal unit; shows Si-O bond length shorter than C-C bond one with larger bond angle of Si-O-Si<sup>[91]</sup>. Effectiveness of siloxane-terminated side chain in conjugated backbone were investigated for thin-Film Transistors by Bao et.al, where expected solubility and closer stacking of backbone have been demonstrated, thus the unprecedentedly high carrier mobility was obtained due to well-fined nano-scale thin film morphology and developed favorable molecular packing. Also, Yang and Oh et al. reported the DPP based polymer with the siloxane-terminated side chains and obtained high hole mobilities up to  $8.84 \text{ cm}^2 \text{ V}^{-1} \text{ s}^{-1}$  and electron mobilities up to  $2.20 \text{ cm}^2 \text{ V}^{-1} \text{ s}^{-1}$ .<sup>[92]</sup> Such a subtle change in the terminal of alkyl chain could greatly modulate the molecular packing and charge carriers transport in organic field effect transistors (OFETs). The closer  $\pi$ - $\pi$  stacking (edge-on orientation) between adjacent backbones is pointed out as main reason of favorable hole/electron mobility due to the good molecular alignment in solid state and decreased vibrational motion of side chain. Intensive studies have been devoted to elucidating the effects of the siloxide-terminated hybrid chain on the closer  $\pi$ - $\pi$  stacking; however, little knowledge has been accumulated in the PSCs so far. It is worth delving into the effects of siloxide chain on the molecular packing and morphological behavior on organic photovoltaics (OPVs) for the further

clarified and rational molecular design.

In this work, we reported three semi-crystalline copolymers terminated by siloxane hybrid side chain on dialkoxybenzene moiety with gradually functionalized fluorine atom onto the benzothiadiazole unit (BT), as named PPSiDTBT, PPSiDTFBT and PPSiDT2FBT. The resulting band gap, molecular orbital energy level, molecular packing pattern and self-organized morphology of three copolymers are systemically measured and characterized. The synergistic effects of siloxane terminated side chain and fluorine substitution are presented and directly toward clearly understanding of the impact of siloxane-hybrid terminated side chain for OPVs application. Compare to previous well-known PPDT2FBT with normal hexyldecyl chain, the presented siloxane-terminated polymers with same backbone develop an agglomerated polymer clusters with higher roughness and large domains from AFM investigation; a preferential edge-on molecular packing are also observed from GIWAXS measurement. The small change of side chain significantly influences on two-dimensional molecular packing in bulk active layer, which play an important role for vertical or parallel charge transport. Quantified charge carrier dynamics in existing three copolymers reveal bimolecular recombination as a Langevin recombination was considered negligible and trap-assisted recombination was dominant loss mechanism for charge transport, which resulting in the inefficient photocurrent transition.

## 9.2 Experimental

### 9.2.1 Fabrication of Polymer Solar Cells

Polymer solar cells were fabricated with a configuration of indium tin oxide (ITO)/poly(3,4-ethylenedioxythiophene): poly(styrenesulfonate) (PEDOT:PSS)/polymers: PC<sub>71</sub>BM/Al. The cleaned ITO substrates were ultraviolet- ozone treated for 20 min and PEDOT:PSS (Baytron P clevios<sup>TM</sup> AI 4083, Germany) was spin-coated (ca. 45 nm thick), dried at 140 °C for 10 min and transferred into a nitrogen filled glove box. Subsequently, the polymer:PC<sub>71</sub>BM (0.6 wt% in chlorobenzene) blend solutions containing 3 vol% diphenylether (DPE) were spin-cast on top of the PEDOT: PSS film. The devices were pumped down in vacuum (<10<sup>-6</sup> Torr) and a 100 nm thick Al layer was deposited on top of the active layer by thermal evaporation using a shadow mask (13 mm<sup>2</sup>). The current density-voltage (*J-V*) characteristics were measured using a Keithley 2635 (USA) source measurement unit under AM 1.5G illumination at 100 mW cm<sup>-2</sup>. External quantum efficiency (EQE) measurement was conducted in ambient air using an EQE system (Model QEX7) from PV measurements Inc.

## 9.3 Results and Discussion

### 9.3.1 Synthesis and Characterizations

The number-average molecular weight ( $M_n$ ) and polydispersity index (PDI) of the polymers were measured to be 42.7 kDa and 1.7 for PPSiDTBT; 38.6 kDa and 2.8 for PPSiDTFBT; 40.1 kDa and 2.0 for PPSiDT2FBT, respectively, by GPC using *o*-DCB as an eluent at 80 °C (**Table 9.1**). Absorption spectra of three polymers in chloroform and in film were measured by UV-Vis spectrophotometer (**Figure 9.1 (b, c)**). In solution, three polymers show the absorption maximum ( $\lambda_{\max}$ ) at 643 nm for PPSiDTBT, 657 nm for PPSiDTFBT and 656 nm for PPSiDT2FBT, respectively. The clear shoulder peaks indicate strong interchain aggregation even in dilute solution, which is more intensified with increasing fluorine substitution onto BT. The strong aggregation stems from the chain planarity via intrachain non-covalent Coulombic interactions and siloxane-containing side chains which have a branching point far away from the polymer main chain. Upon solidification, all polymers show a spectral broadening with 10–20 nm red-shift in  $\lambda_{\max}$  and the sharper shoulder peak was observed compared to that in solution. Optical band gaps were estimated to be 1.68–1.73 eV for three polymers from the onset of absorption in film, and the resulting spectra showed broad absorption covering the range of 350 to 740 nm. The electrochemical characteristics of the polymers were measured by CV and the resulting voltammograms are depicted in **Figure 9.1 (d)**. The highest occupied molecular orbital (HOMO) energy level of PPSiDTBT, PPSiDTFBT and PPSiDT2FBT were determined to be  $-5.11$ ,  $-5.18$  and  $-5.25$  eV, respectively. The fluorine substitution decreases the HOMO level, which increases the  $V_{oc}$  of PSCs and improves the oxidational stability under ambient condition. Based on the HOMO value and optical band gap in film, the lowest unoccupied molecular orbital (LUMO) levels were calculated for PPSiDTBT ( $-3.41$  eV), PPSiDTFBT ( $-3.50$  eV) and PPSiDT2FBT ( $-3.52$  eV), which afford enough driving force for exciton dissociation and electron transfer to PC<sub>71</sub>BM.

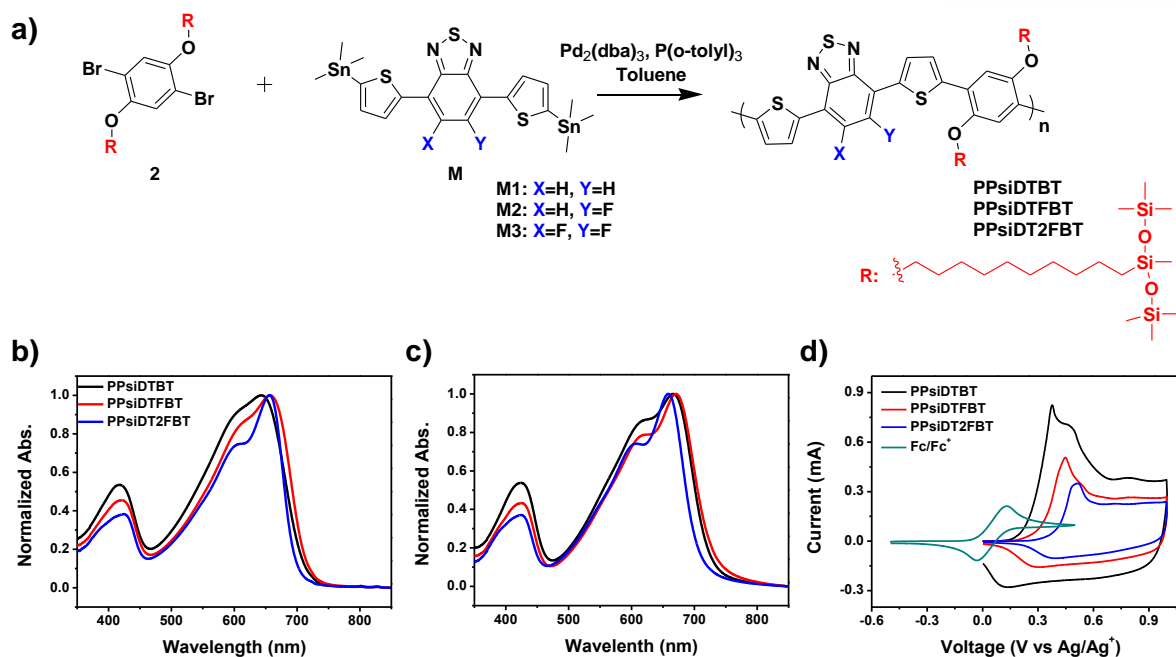


**Figure 9. 1** (a) Synthetic scheme for new designed polymers; normalized UV-Vis absorption spectra of polymers (b) in chloroform and (c) in film; (d) cyclic voltammograms of thin films of three polymers (color online)

**Table 9. 1** Optical and electrochemical properties of polymers

Polymers	$M_n$ (kDa) <sup>a</sup>	PDI <sup>a</sup>	$\lambda_{\text{onset}}$ (film) (nm) <sup>b</sup>	$E_g^{\text{opt}}$ (eV) <sup>b</sup>	HOMO (eV) <sup>c</sup>	LUMO (eV) <sup>d</sup>
PPsiDTBT	43	1.7	730	1.70	-5.11	-3.41
PPsiDTFBT	39	2.8	739	1.68	-5.18	-3.50
PPsiDT2FBT	40	2.0	717	1.73	-5.25	-3.52

a) Number-average molecular weight and PDI determined by GPC in *o*-dichlorobenzene at 80 °C; b) optical band gap was estimated from the optical absorption onset in film; c) HOMO level was estimated from the tangential onset of oxidation ( $E_{\text{ox}}^{\text{onset}}$ ) by cyclic voltammetry using equation  $\text{HOMO}(\text{eV}) = -(E_{\text{ox}}^{\text{onset}} - E_{1/2}^{\text{ferrocene}} + 4.8)$ ; d) LUMO level was estimated from the HOMO value and optical band gap in film.

### 9.3.2 Photovoltaic Fabrication and Performance

Bulk heterojunction (BHJ) photovoltaic devices with a standard structure of ITO/PEDOT:PSS/PPsiDTBT-based polymer:PC<sub>71</sub>BM/Al were fabricated. To optimize the device performance, the blend ratio of polymer:PC<sub>71</sub>BM was modulated from 1:1 to 1:3 (by weight) in chlorobenzene and various processing additives such as 1,8-diiodooctane (DIO), diphenylether (DPE) and 1-chloronaphthalene (CN) were tested (**Table 9.2**). The photovoltaic characteristics were evaluated under simulated AM 1.5G illumination (100 mW cm<sup>-2</sup>). The PSC devices were optimized at a polymer:PC<sub>71</sub>BM blend ratio of 1:3 for PPsiDTBT and PPsiDTFBT, and 1:2 for PPsiDT2FBT with addition of 3 vol% DPE in chlorobenzene. The PCE of PPsiDTBT device was determined to be 1.78 %, with a  $V_{oc}$  of 0.55 V, a  $J_{sc}$  of 5.13 mA cm<sup>-2</sup>, and a fill factor (FF) of 0.63. The PCE (3.52%) of PPsiDTFBT:PC<sub>71</sub>BM was measured with a  $V_{oc}$  of 0.55 V, a  $J_{sc}$  of 9.68 mA cm<sup>-2</sup> and a FF of 0.65. PPsiDT2FBT:PC<sub>71</sub>BM showed a PCE of 3.85 % with a  $V_{oc}$  of 0.62 V, a  $J_{sc}$  of 10.2 mA cm<sup>-2</sup> and a FF of 0.61. Interestingly, all photovoltaic parameters were enhanced with increment of number of fluorine substituents on the polymer backbone, which is related to the deeper HOMO levels and stronger crystalline interchain interactions (via noncovalent coulombic attraction) with fluorine substituents. Among the various additives, DPE showed the most pronounced effects on the BHJ morphology modulation, resulting in a large enhancement in PCE with significantly improved  $J_{sc}$  (by ca. 20 %) compared to the untreated devices. Therefore, upon treatment with DPE, the substantially enhanced PCEs of 3.16 %, 4.40 % and 5.65 % were achieved for PPsiDTBT, PPsiDTFBT and PPsiDT2FBT devices, respectively. The resulting photovoltaic properties are summarized in **Table 9.3** and the corresponding  $J$ - $V$  characteristic and EQE spectra are shown in **Figure 9.4**.

**Table 9. 2** Summary of tested and fabricated solar cells

Polymer	solvent	ratio	Additive	Spin-rate (rpm)	$J_{sc}$ (mA/cm <sup>2</sup> )	$V_{oc}$ (V)	FF	PCE (%)	
PPSiDTBT	DCB (0.6wt%)	1:3	None	800	8.62	0.56	0.65	3.12	
			CN	1200	9.83	0.60	0.67	4.05	
			DIO	1200	9.49	0.60	0.65	3.73	
			DPE	1600	9.62	0.58	0.63	3.47	
	CB (0.6wt%)	1:3	None	4000	5.13	0.55	0.63	1.78	
			CN	2400	6.54	0.60	0.65	2.54	
			DIO	3200	6.32	0.58	0.64	2.32	
			DPE	3200	8.82	0.56	0.64	3.16	
	CF (0.3wt%)	1:1	None	4000	2.14	0.38	0.50	0.40	
			CN	6000	7.44	0.57	0.67	2.82	
			DIO	5000	6.94	0.55	0.63	2.39	
			DPE	5000	8.39	0.54	0.64	2.92	
PPSiDTFBT	None	1:3	None	2400	9.68	0.55	0.65	3.52	
			CN	3200	8.15	0.56	0.63	2.89	
			DIO	2400	9.28	0.56	0.62	3.20	
			DPE	800	11.6	0.58	0.66	4.40	
	CF (0.3wt%)	1:3	None	4800	3.60	0.57	0.56	1.13	
			CN	5600	8.10	0.58	0.65	3.03	
			DIO	6400	7.05	0.54	0.60	2.29	
			DPE	4800	9.34	0.56	0.65	3.39	
	PPSiDT2FBT	None	1:2	None	4000	10.2	0.62	0.61	3.85
				CN	5500	7.55	0.64	0.64	3.07
				DIO	5500	6.41	0.68	0.55	2.39
				DPE	4000	12.59	0.66	0.68	5.65
CF (0.3wt%)		1:2	None	8000	8.91	0.65	0.64	3.71	
			CN	8000	9.20	0.68	0.63	3.90	
			DIO	8000	8.54	0.68	0.61	3.58	
			DPE	9000	8.56	0.71	0.68	4.20	

<sup>a</sup>. Solution : Additives = 97 : 3 (v/v %)

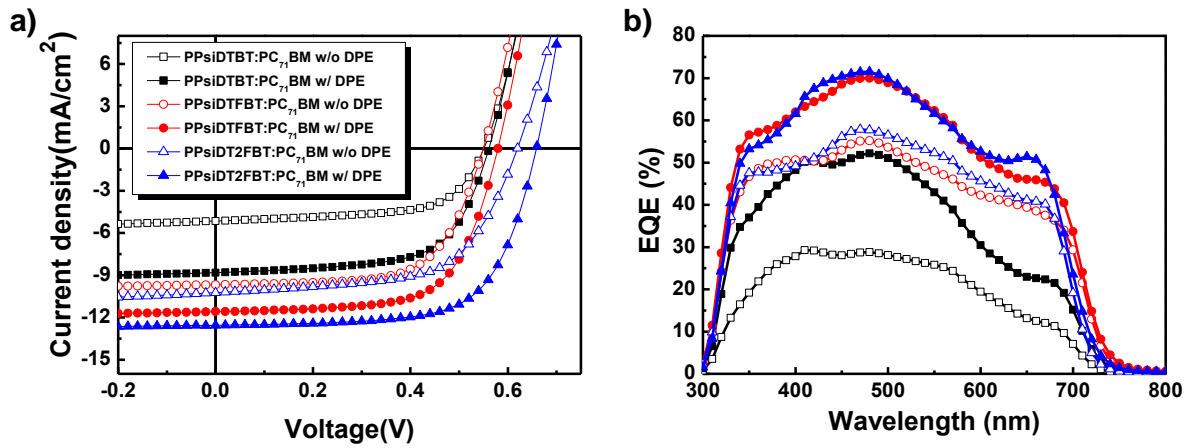


**Figure 9. 2** (a)  $J$ - $V$  characteristics and (b) EQE spectra of PSC devices with and without DPE as a processing additive (color online)

**Table 9. 3** Summary of photovoltaic characteristics of polymers

Polymer	Blend ratio	Additive (3% DPE)	$J_{sc}$ (mA cm <sup>-2</sup> )	cal. $J_{sc}$ (mA/cm <sup>2</sup> )	$V_{oc}$ (V)	FF	PCE (%) <sup>*</sup>
PPSiDTBT	1:3	X	5.13	4.51	0.55	0.63	1.78 (1.54 ± 0.25)
		O	8.82	8.82	0.56	0.64	3.16 (2.97 ± 0.18)
PPSiDTFBT	1:3	X	9.68	9.76	0.55	0.65	3.52 (3.29 ± 0.23)
		O	11.6	12.12	0.58	0.66	4.40 (4.21 ± 0.18)
PPSiDT2FBT	1:2	X	10.2	9.96	0.62	0.61	3.85 (3.63 ± 0.21)
		O	12.59	12.06	0.66	0.68	5.65 (5.49 ± 0.16)

a) The average values and standard deviations of the PCEs based on the 10 devices. Thickness of active layers was determined to be 160–180 nm.



### 9.3.3 Morphology and Microstructure Analyses

To study the morphological difference of three blend films, the surface morphology was investigated via AFM. As shown in **Figure 9.5**, thin films processed without DPE show high roughness and large domains resulted from agglomerated polymers, with root mean square (RMS) roughness of 14.49, 5.12 and 4.25 nm for PPSiDTBT, PPSiDTFBT and PPSiDT2FBT blends, respectively. Undesired topographical morphology explains partially poor exciton separation and charge extraction with the resulting low PCE values of 1.78 %–3.85 % without DPE. However, the smoother surface morphologies with RMS roughness of 2.52–3.23 nm were observed for blend films with DPE additive.

To investigate the detailed interchain packing structures of polymers, GIWAXS was measured for pristine polymer films and blend films (**Figure 9.6**). The packing parameters are summarized in **Table 9.4**. Neat polymer thin films exhibit multi-diffractions from interlamellar stacking along both the *xy* and *z* directions, indicating bimodal-texture packing (edge-on and face-on orientation) with 3D charge hopping and/or transport. All neat polymer films showed the multi-scattering peaks up to (300) in the out-of-plane direction with 27.3–28.6 Å interlamellar d-spacing. In the case of in-plane direction, with increasing the number of fluorine substituents on BT, the interlamellar scattering peaks became clear, showing up to (300) peak for PPSiDT2FBT with the enhanced intermolecular interaction via noncovalent F···S and F···H coulombic interactions. In addition, a strong (010) peak was observed for all pristine polymer films, suggesting a dominant face-on  $\pi$ - $\pi$  stacking. Interestingly, difluorination onto a polymer backbone clearly induced a face-on orientation with much stronger (010) peak in the *z* direction, compared to unsubstituted and monofluorinated polymers. The hump shape (100) peak for PPSiDTBT and PPSiDTFBT was also separated into two peaks in the out-of-plane and in-plane directions for PPSiDT2FBT, forming a bimodal interchain organization. Furthermore, the shorter  $\pi$ - $\pi$  stacking distance was measured to be 3.57 Å of PPSiDT2FBT film compared to 3.61 Å of PPSiDTBT, supporting the enhanced intermolecular coulombic dipole-dipole interactions with fluorine substitution. After blending with PC71BM with DPE, suppressed crystalline scatterings were observed for all polymers, but the (010) peak in the out-of-plane direction became stronger with fluorine substitution. With increment of fluorine functionalization along the polymer backbone, the intermolecular packing behavior could be modulated with preferential face-on orientation, which is consistent with the enhanced charge carrier transport and the higher  $J_{sc}$  for PPSiDT2FBT compared to other two polymers.

To get a clear insight into the detailed packing patterns, the lamellar scattering and  $\pi$ - $\pi$  stacking peaks were analyzed in detail for pristine polymer films and blend films and the corresponding coherence length was also calculated from the full width at half maximum of each scattering peak (**Table 9.4**). In neat film, the same (100) lamellar spacing (31.4 Å) was measured for all three polymers in the *xy* direction. However, the larger lamellar coherence length of 80.7 Å was calculated for PPSiDT2FBT compared to 68.3 Å for PPSiDTBT and 59.5 Å for PPSiDTFBT. The face-on  $\pi$ - $\pi$  stacking (010) spacing of 3.61, 3.59 and 3.57 Å with the coherence length of 30.8, 33.6 and 37.3 Å were measured for

PPsiDTBT, PPsiDTFBT and PPsiDT2FBT, respectively. With regard to the (100) scattering in the out-of-plane direction, the increased lamellar spacing from 27.32 Å of PPsiDTBT to 28.56 Å of PPsiDT2FBT with decreased coherence length from 63.1 Å of PPsiDTBT to 53.9 Å of PPsiDT2FBT were observed, indicating the more preferential face-on orientation for PPsiDT2FBT relative to other polymers. In order to compare the relative interchain orientation of three polymers, the ratio of coherence length of the lamellar (100) reflections in the in-plane and out-of-plane directions ( $R=C_{xy}/C_z$ ) were also calculated for both neat and blend films. PPsiDTBT and PPsiDTFBT showed the  $C_{xy}/C_z=1.08$  and 1.05 for neat films and 1.99 and 1.97 for blend films. In the case of PPsiDT2FBT, the stronger face-on tendency was measured with  $C_{xy}/C_z=1.50$  for neat and 2.46 for blend films, compared to those of other two polymers. The GIWAXS morphological data show a good agreement with the measured photovoltaic device characteristics.

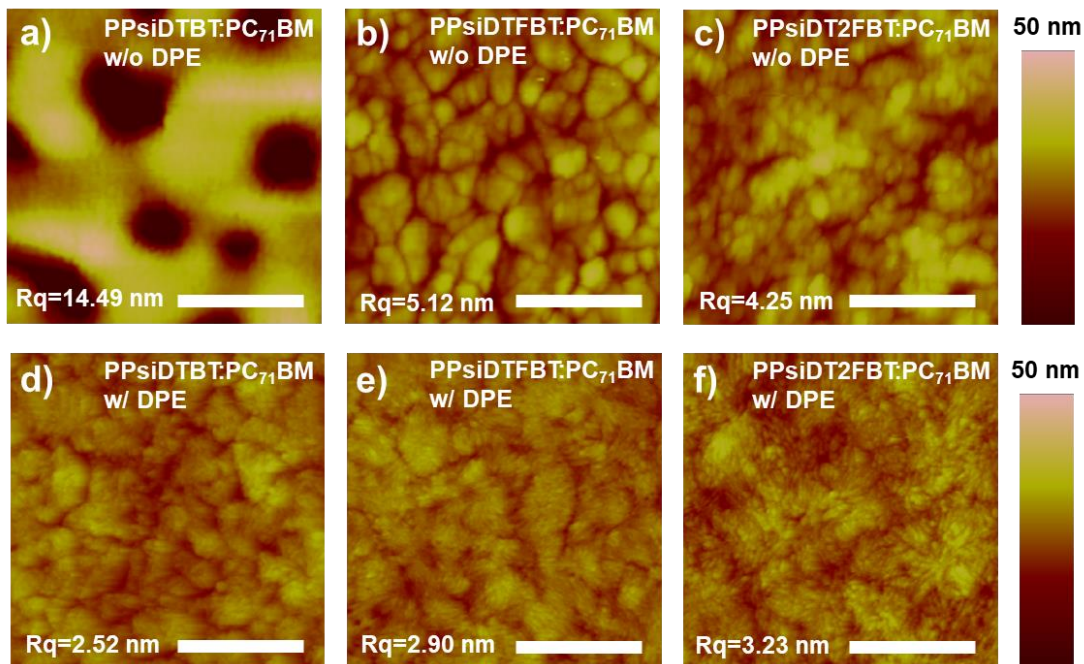


**Figure 9. 3** Topographic morphology images ( $2.5 \mu\text{m} \times 2.5 \mu\text{m}$ ) of polymer:PC<sub>71</sub>BM blends (a–c) without and (d–f) with 3 vol% DPE. (a, d) PPsiDTBT, (b, e) PPsiDTFBT, (c, f) PPsiDT2FBT BHJ films deposited on ITO/PEDOT:PSS under the same condition for the optimized devices. RMS roughness values are at the left-bottom corner of each figure (color online).

**Table 9. 4** Crystallographic parameters calculated from GIWAXS profiles of three polymers

Polymer	Films	Crystallographic parameters						
		Axis	$\pi$ - $\pi$ stack [ $\text{\AA}^{-1}$ ]	d- spacing [ $\text{\AA}$ ]	Coherence length [ $\text{\AA}$ ]	Lamella stack [ $\text{\AA}^{-1}$ ]	d- spacing [ $\text{\AA}$ ]	Coherence length [ $\text{\AA}$ ]
PPsiDTBT	Neat	$q_{xy}$	-	-	-	0.20	31.42	68.3
		$q_z$	1.74	3.61	30.8	0.23	27.32	63.1
	:PC <sub>71</sub> BM w/ DPE	$q_{xy}$	-	-	-	0.20	31.42	197.1
		$q_z$	-	-	-	0.23	27.32	99.2
PPsiDTFBT	Neat	$q_{xy}$	1.75	3.59	74.8	0.20	31.42	59.5
		$q_z$	1.75	3.59	33.6	0.22	28.56	56.6
	:PC <sub>71</sub> BM w/ DPE	$q_{xy}$	-	-	-	0.20	31.42	194.4
		$q_z$	1.75	3.59	41.7	0.22	28.56	98.5
PPsiDT2FBT	Neat	$q_{xy}$	1.76	3.57	78.6	0.20	31.42	80.7
		$q_z$	1.76	3.57	37.3	0.22	28.56	53.9
	:PC <sub>71</sub> BM w/ DPE	$q_{xy}$	-	-	-	0.20	31.42	193.4
		$q_z$	1.77	3.55	47.2	0.22	28.56	78.6

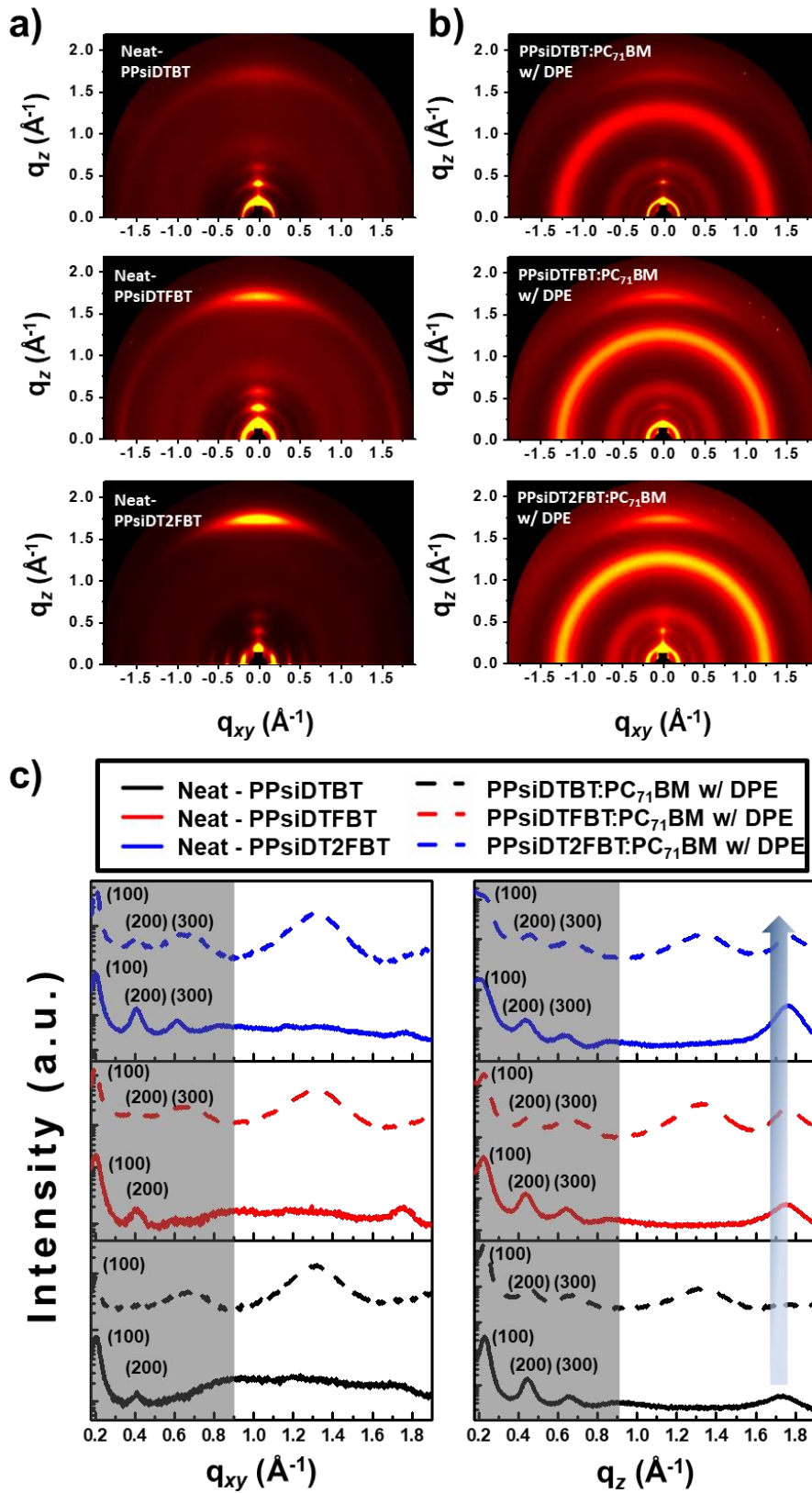
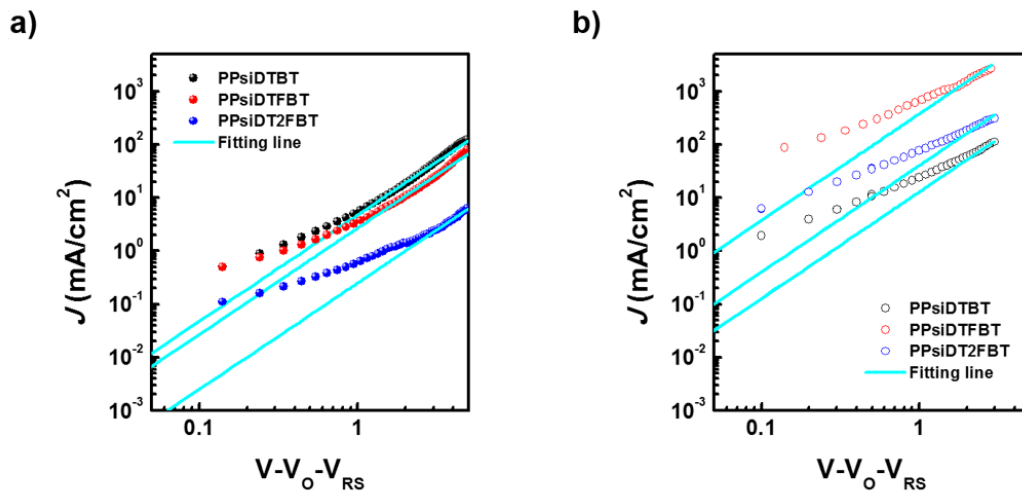


Figure 9. 4 GIWAXS images of (a) neat polymer films and (b) blends of polymer:PC<sub>71</sub>BM with DPE; (c) in-plane and out-of-plane line cuts of the above patterns (color online)

### 9.3.4 Charge Dynamics and Recombination

In addition, carrier mobility in a vertical direction was investigated by the space-charge limited current (SCLC) technique. Hole-only (ITO/PEDOT:PSS/polymer:PC<sub>71</sub>BM/Au) and electron-only diodes (FTO/polymer:PC<sub>71</sub>BM/Al) were fabricated under the same fabrication condition for the optimal devices with DPE additive. The SCLC plots and extracted charge carrier mobilities are displayed in **Figure 9.7** and **Table 9.5**. The measured hole (and electron) mobilities are  $2.5 \times 10^{-4}$  ( $4.3 \times 10^{-5}$ ),  $2.7 \times 10^{-4}$  ( $6.5 \times 10^{-4}$ ) and  $1.1 \times 10^{-4}$  ( $1.8 \times 10^{-4}$ )  $\text{cm}^2\text{Vs}^{-1}$  for PPSiDTBT:PC<sub>71</sub>BM, PPSiDTFBT:PC<sub>71</sub>BM and PPSiDT2FBT:PC<sub>71</sub>BM, respectively. The most well balanced electron/hole mobility ratio was measured to be  $\mu_{\text{electron}}/\mu_{\text{hole}}=1.64$  for PPSiDT2FBT:PC<sub>71</sub>BM relative to PPSiDTBT: PC<sub>71</sub>BM (0.17) and PPSiDTFBT:PC<sub>71</sub>BM (2.24).



**Figure 9. 5** Double-logarithmic plot from dark  $J$ - $V$  characteristics of (a) hole-only devices and (b) electron-only devices.

**Table 9. 5** Charge mobilities calculated from SCLC modeling devices

Polymer	Hole mobility [ $\text{cm}^2\text{Vs}^{-1}$ ]	Electron mobility [ $\text{cm}^2\text{Vs}^{-1}$ ]	$\mu_e/\mu_{\text{hole}}$
PPSiDTBT	$2.5 \times 10^{-4}$	$4.3 \times 10^{-5}$	0.17
PPSiDTFBT	$2.7 \times 10^{-4}$	$6.5 \times 10^{-4}$	2.24
PPSiDT2FBT	$2.3 \times 10^{-5}$	$8.6 \times 10^{-6}$	0.37

Furthermore, we investigated the light intensity dependence of  $J_{sc}$  and  $V_{oc}$  to investigate the charge recombination and extraction processes for three different PSC devices. The  $J_{sc}$  vs. light intensity curve can be fitted according to a power-law **Equation. 9.1**, where  $I$  is the light intensity and  $\alpha$  indicates a slope of a logarithmic plot of  $J_{sc}$  versus light intensity.

$$J_{sc} \propto I^\alpha \quad (\text{Eq. 9.1})$$

As the value  $\alpha$  is close to unity, the bimolecular recombination becomes negligible during a charge sweep out process. As shown in **Figure 9.8**, all devices based on three polymers showed the similar  $\alpha$  values of 0.98, which indicates that the devices have no significant difference in bimolecular recombination in the photoactive layer. In contrast, the stronger dependence of  $V_{oc}$  on light intensity was measured with different slopes larger than  $kT/q$  ( $k$  is the Boltzman constant,  $T$  is the absolute temperature and  $q$  is the electron charge):  $3.22 kT/q$  for PPSiDTBT:PC<sub>71</sub>BM,  $2.76 kT/q$  for PPSiDTFBT:PC<sub>71</sub>BM and  $2.29 kT/q$  for PPSiDT2FBT:PC<sub>71</sub>BM, respectively. Since the trap-assisted recombination significantly competes with bimolecular recombination as a loss mechanism of PSCs, these results indicate that the trap-assisted recombination is clearly dominant in the loss of  $J_{sc}$  and FF in PPSiDTBT:PC<sub>71</sub>BM compared to PPSiDTFBT:PC<sub>71</sub>BM and PPSiDT2FBT:PC<sub>71</sub>BM. We think the higher trap-assisted recombination for PPSiDTBT:PC<sub>71</sub>BM might be ascribed to its BHJ morphology (see AFM and GIWAXS images) and unbalanced electron/hole SCLC mobilities ( $\mu_{\text{electron}}/\mu_{\text{hole}}=0.17$ ). The larger phase separation and weaker face-on orientation (compared to PPSiDT2FBT:PC<sub>71</sub>BM) may generate more charge traps in a vertical direction and hinder the carrier transport and extraction in the PSC device.

To understand the charge generation, transport and extraction properties, the net photocurrent ( $J_{ph}$ ) for each device was analyzed as a function of effective applied bias ( $V_{\text{eff}}$ ), where  $J_{ph}$  is the difference of the current density under illumination ( $J_L$ ) and dark ( $J_D$ ) condition ( $J_{ph} = J_L - J_D$ ) and  $V_{\text{eff}}$  is differential voltage between the voltage at  $J_{ph} = 0$  ( $V_o$ ) and applied voltage ( $V$ ) ( $V_{\text{eff}} = V_o - V$ ). Under high reverse-bias over  $V_{\text{eff}} = 0.8$  V, photocurrent shows saturation, indicating efficient sweep out of charge carriers with negligible bimolecular recombination. As shown in **Figure 9.8 (c)**, the PPSiDT2FBT:PC<sub>71</sub>BM device exhibits the significantly higher  $J_{ph}$  compared to other two PSCs. At the maximal power output condition ( $V_{\text{eff}} = 0.2$  V),  $J_{ph}$  was estimated to be 72%, 67% and 64% of the saturated current density,  $J_{\text{sat}}$  ( $J_{ph}$  at  $V_{\text{eff}} > 1$  V) for PPSiDT2FBT, PPSiDTFBT and PPSiDTBT devices, respectively. The higher ratio of  $J_{ph}/J_{\text{sat}}$  of PPSiDT2FBT:PC<sub>71</sub>BM suggests the substantially higher charge extraction and collection efficiency with smaller charge recombination, showing a good agreement with the SCLC charge mobility and  $J$ - $V$  characteristics.

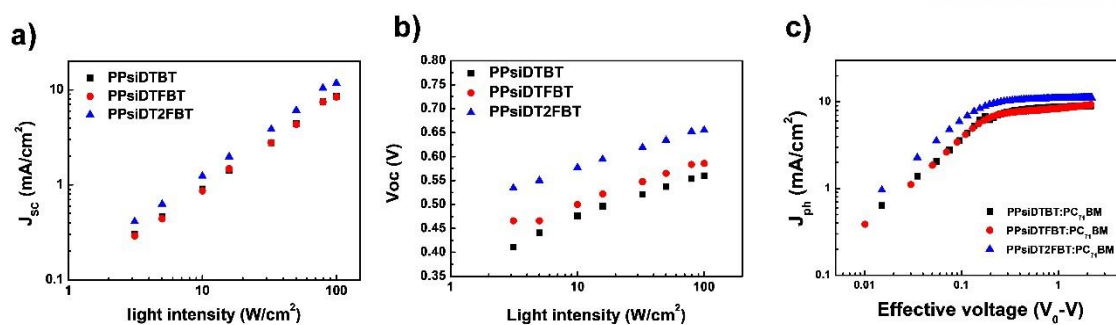


**Figure 9. 6** Light intensity dependence of (a)  $J_{sc}$  and (b)  $V_{oc}$ ; (c) photocurrent versus effective voltage (color online)

## 9.4 Conclusion

In conclusion, we have synthesized three semi-crystalline photovoltaic polymers by incorporating intrachain noncovalent coulombic interactions and siloxane-hybrid terminated side-chains. Different number of fluorine substituents was introduced to modulate the frontier energy levels and intra and interchain coulombic interaction. By attaching the siloxane-terminated side-chains with a branch point away from the polymer backbone, the closer  $\pi$ - $\pi$  stacking between adjacent polymer chains has been pointed out with efficient charge transport. The fluorination significantly affected the HOMO level of polymers, resulting in the higher  $V_{oc}$  (0.66 V) of PPSiDT2FBT:PC<sub>71</sub>BM, relative to that (0.55 V) of PPSiDTBT:PC<sub>71</sub>BM. The resulting PCE was measured to be 3.16 %, 4.4 % and 5.65 % for PPSiDTBT, PPSiDTFBT and PPSiDT2FBT devices, respectively. By investigating blend film morphology by AFM and GIWAXS, strong intermolecular agglomeration was measured due to siloxane side-chains with less steric hindrance. Interestingly, the face-on orientation of polymers was enhanced with increasing the number of fluorine substituents. We further investigated charge generation and recombination characteristics for three blend systems by measuring light intensity dependent  $J_{sc}$  and  $V_{oc}$  and photocurrent generation. Langevin bimolecular charge recombination was similar for three blends but the trap-assisted recombination was proved to be a dominant loss mechanism for poor PCE in PPSiDTBT:PC<sub>71</sub>BM. The results provide a new insight into the molecular design of semiconducting polymers (not only a conjugated backbone but also a solubilizing side-chain) by carefully considering the intermolecular agglomeration for OPV applications.

## Chapter 10. Hot Slot Die Coating for Additive-Free Fabrication of High-Performance Roll-to-Roll Processed Polymer Solar Cells

### 10.1 Research Background

Over the past few decades, bulk-heterojunction (BHJ) polymer solar cells (PSCs) have attracted considerable attention as a next generation energy source owing to their advantages such as flexibility, light weight and potential for high-throughput manufacturing with low cost. <sup>[3, 5]</sup> Recently, a number of approaches for PSC development have raised the record performance to over a 17.3% power conversion efficiency (PCE) in laboratory scale devices fabricated by spin coating. <sup>[93]</sup> Improvements in performance through new organic materials design<sup>[94]</sup>, morphology control<sup>[95, 96]</sup> and device engineering<sup>[22, 97]</sup> have yielded PCEs which are thought to be commercially competitive and large area devices have been demonstrated by roll-to-roll (R2R) processing. However, PCE losses arising from the low conductivity of the ITO electrode, difficulties in finding suitable photoactive and charge transport layer materials (which should be solution processible) and BHJ morphological changes, etc. during the transition from laboratory processes to industrial scale manufacturing for module systems have been a major hurdle for the R2R-based mass production of PSCs.<sup>[98, 99]</sup> From this perspective, the key challenge to further progress towards commercialization is finding solutions to overcome the discrepancy between research cells and large-area R2R produced ones.

These discrepancies arise from intrinsic differences between lab-scale and industrial-scale processes and the demanding processing conditions required for R2R processing. For R2Rbased mass production of PSCs, first, active materials need to be robust enough to keep performance under harsh drying environments. Although mild drying under inert atmospheres is technically possible, it makes PSCs much less commercially competitive. Secondly, it is challenging to produce defect-free, large area films by industrial processes when the target thickness of photoactive films is very thin. Therefore, materials should perform well using film thicknesses > 200–300 nm while tolerating variations in film thickness. Thirdly, only relatively simple processing treatments are feasible in R2R processing. Although solvent additives<sup>[100]</sup> and solvent vapor annealing<sup>[101]</sup> are very effective techniques to modulate film morphology resulting in improved device performance in the lab, these post treatments are not practical in R2R processes. Therefore, scalable materials must be able to achieve optimal film morphologies using procedures which can be implemented on R2R equipment. Fourth, commercially viable devices must have good long-term and thermal stability. Research in this area has so far included approaches such as inverted device structures, encapsulation techniques and so on. Although many reports have shown that solvent additives improve the PCE by not only controlling nano- or/and mesoscale morphology<sup>[96]</sup>, but



also enhancement of molecular crystallinity,<sup>[102]</sup> additive processing leads to deteriorated stability in PSCs.<sup>[103]</sup> It has been demonstrated that the stability of PSCs processed with additives can be recovered somewhat using vacuum drying to completely remove additive residues<sup>[104]</sup>, however, this step is incompatible with R2R processing. For these reasons, active solutions without additives of excessively high boiling points are desirable. Lastly, the development of scalable processing techniques such as doctor blade coating and slot die coating are necessary. Recently, using either hot casting or hot substrates for active film formation<sup>[42, 105]</sup>, enhanced device performance has been reported. Further, some groups have reported applying hot solution casting to the doctor blading process.<sup>[106]</sup> Since the premeasured slot die coating process typically works like the doctor blading method,<sup>[4]</sup> slot die processes have the potential to utilize hot solution strategies by supplying fresh hot active ink. In this area, modified 3D printers for automated slot die coating have been introduced by Vak et al.<sup>[99, 107]</sup> 3D printers allow accurate control of the x-, y-, z position of the head via digital coding with a personal computer, which allows convenient fabrication of PSCs with uniform film formation, patterning and high device reproducibility.

In this work, we successfully investigate not only the combination of thermal effects of the slot head (solution) and stage (substrate) by remodelling a 3D printer for efficient slot die processed PSCs, but also PSC fabrication in air using a suitable polymer having high environmental stability and a large thickness tolerance. Furthermore, we use a single solvent and inverted architecture to improve the stability of devices. Notably, we provide an in-depth analysis of the changes in morphology, molecular orientation and charge recombination of active films based on head and stage temperatures. Finally, optimal conditions identified using 3D printer-based devices are applied to R2R equipment with flexible substrates, which yield a high PSC performance of 7.06% comparable in efficiency to the ITO glass-based devices processed with a 3D printer. This work demonstrates that the combination of solution and substrate thermal processing by hot slot-die coating may suggest a useful method to test the lab-to-fab scale-up for optimization of mass production of PSCs.

## 10.2 Experimental

### 10.2.1 Fabrication of Inverted Photovoltaic Cells (The 3D Printing Slot Die Method and Roll-to-Roll Process)

Polymer solar cells were fabricated with an inverted structure (ITO/ZnO/polymer:PC<sub>71</sub>BM/MoO<sub>3</sub>/Ag). For rigid substrate-based polymer solar cells, patterned ITO glass substrates were cleaned by ultrasonic treatment in detergent, distilled water, acetone and isopropyl alcohol (IPA), then dried and treated with UV-ozone for 15 min to remove residues. Zinc oxide nanoparticles dissolved in methanol were deposited by spin coating at 5000 rpm for 30s onto the cleaned ITO substrates and dried for 10 min at 130 °C in air. Then, a mixed solution of PPDT2FBT:PC<sub>71</sub>BM in *o*-DCB was slot die-coated on top of the ZnO NP film in air using the 3D printer machine. The gap between the substrate and head was 100

mm. The optimal coating speed was  $11 \text{ mm s}^{-1}$  and the concentration of the PPDT2FBT:PC<sub>71</sub>BM blend solution was  $14 \text{ mg ml}^{-1}$ . The volume of the slot die coating was  $4 \text{ ml cm}^{-2}$ . For fabrication of devices using the roll-to-roll process, ITO patterned PET substrates (OC50: resistance  $40\text{--}60 \text{ } \Omega \text{ sq}^{-1}$ , transmittance 80%) were used after cleaning by isopropyl alcohol. The ZnO solution was slot die coated at a  $0.2 \text{ m min}^{-1}$  coating speed (with a  $10 \text{ ml min}^{-1}$  volume) and thermally annealed at  $130 \text{ }^\circ\text{C}$ . Then, the PPDT2FBT:PC<sub>71</sub>BM active layer was coated using variable head and substrate temperatures. The coating speed and volume for the active layer in the roll-to-roll process were  $0.2 \text{ m min}^{-1}$  and  $50 \text{ ml min}^{-1}$ , respectively. The gap between the plastic substrate and head was 100 mm. To complete inverted PSC fabrication, a 10 nm MoO<sub>3</sub> ( $\sim 0.5 \text{ } \text{Ås}^{-1}$ ) layer and a 100 nm Ag ( $\sim 1.0 \text{ } \text{Ås}^{-1}$ ) electrode were thermally evaporated at  $< 1.0 \times 10^{-6}$  Torr using a shadow mask. For deposition of solution-processable PEDOT:PSS materials on the active layer instead of the evaporated MoO<sub>3</sub>, blends of AI4083 (Heraeus Clevios<sup>TM</sup> P VP):IPA, PH(Heraeus Clevios<sup>TM</sup> P VP):IPA and neutral-PEDOT:PSS (Sigma-Aldrich):IPA were used. The active area of all PSCs was  $10 \text{ mm}^2$ . The  $J\text{--}V$  characteristics of the devices were measured using a Keithley 2400-LV source measure unit under AM 1.5G solar irradiation.

### 10.2.2 Characterization

An Agilent 5500 scanning probe microscope (SPM) running with a Nanoscope V controller was used to obtain AFM images of polymer thin films. AFM images were recorded in high resolution tapping mode under ambient conditions. Premium silicon cantilevers (TESP-V2) were used with a rotated tip to provide a more symmetric representation of features over 200 nm. Field emission-transmission electron microscopy (FE-TEM) (model: Tecnai G2 F20 X-Twin) was carried out using 200 kV acceleration voltage. Samples for TEM were prepared on a Cu mesh grid. Grazing-incidence wide-angle X-ray scattering (GIWAXS) measurements were conducted at the PLS-II 9A U-SAXS beamline of the Pohang Accelerator Laboratory in Korea. X-rays coming from the in-vacuum undulator (IVU) were monochromated (wavelength  $\lambda = 1.10994 \text{ } \text{Å}$ ) using a double crystal monochromator and focused both horizontally and vertically ( $450 \text{ (H)} \times 60 \text{ (V)} \text{ mm}^2$  in FWHM @ the sample position) using K-B type mirrors. The GIWAXS sample stage was equipped with a 7-axis motorized stage for the fine alignment of the sample, and the incidence angle of the X-ray beam was set to be  $0.12^\circ$  to  $0.14^\circ$  for polymer films. GIWAXS patterns were recorded with a 2D CCD detector (Rayonix SX165) and the X-ray irradiation time was 6–9 s, dependent on the saturation level of the detector. Diffraction angles were calibrated using a sucrose standard (monoclinic, P21,  $a = 10.8631 \text{ } \text{Å}$ ,  $b = 8.7044 \text{ } \text{Å}$ ,  $c = 7.7624 \text{ } \text{Å}$ ,  $\beta = 102.938^\circ$ ) and the sample-to-detector distance was  $\sim 231 \text{ mm}$ .

## 10.3 Results and Discussion

### 10.3.1 Polymer Solar Cells Fabrication

Polymer solar cell fabrication and slot die coating to improve the previously reported printing technique

of 3D printer-based slot die coating, a 3D printer was modified to allow control of the temperature of the slot head as well as the sample stage by recoding the control software. This set up led to not only high qualitative reproducibility of PSCs but also accurate analysis of thermal effects of the heated head and substrate. PSCs were fabricated on ITO coated glass substrates in air using the dual thermal treatment process. PSCs were prepared with an inverted device configuration consisting of indium tin oxide (ITO)/zinc oxide nanoparticles (ZnO NPs)/poly[(2,5-bis(2-hexyldecyloxy)phenylene)-alt-(5,6-difluoro-4,7-di(thiophen-2-yl)-benzo[c][1,2,5]thiadiazole)] (PPDT2FBT):[6,6]-phenyl-C71-butyric acid ester (PC<sub>71</sub>BM)/MoO<sub>3</sub>/Ag as shown in **Figure 10.3 (a)**, wherein active materials were dissolved in only *o*-dichlorobenzene (*o*-DCB) without processing additives. Detailed fabrication methods are described in the Experimental section. PPDT2FBT (M<sub>n</sub> = 40 KDa) has been reported to yield high PCEs of up to 9.4% using the spin coating method in an inert atmosphere with optimized formulation with a diphenyl ether (DPE) additive in the host solvent of chlorobenzene. Without processing additives, the PPDT2FBT PSC also shows a significantly high photovoltaic performance (PCE = 7.26%) with only thermal annealing at 130 °C using *o*-DCB as a solvent. These PSCs show outstanding thickness tolerance for performance, and thus PPDT2FBT was chosen as a suitable material for this study. Because of these superior merits of the polymer, we were able to focus on optimization of active films with respect to the temperature combination without significant influence of thickness on device performance. Using the 3D printer-based slot die coating method, inverted PSCs processed using a mixed solvent of chlorobenzene and DPE additive showed a PCE of 7.4%, which was higher than that observed using a single solvent of *o*-DCB when devices were processed at a substrate temperature of 80 °C (see **Figure 10.1** and **Table 10.1**), however, subsequent PSCs were fabricated using a single solvent (*o*-DCB) in order to focus on optimization of thermal processing conditions and avoid long-term stability issues associated with solvent additives (see **Figure 10.2**).

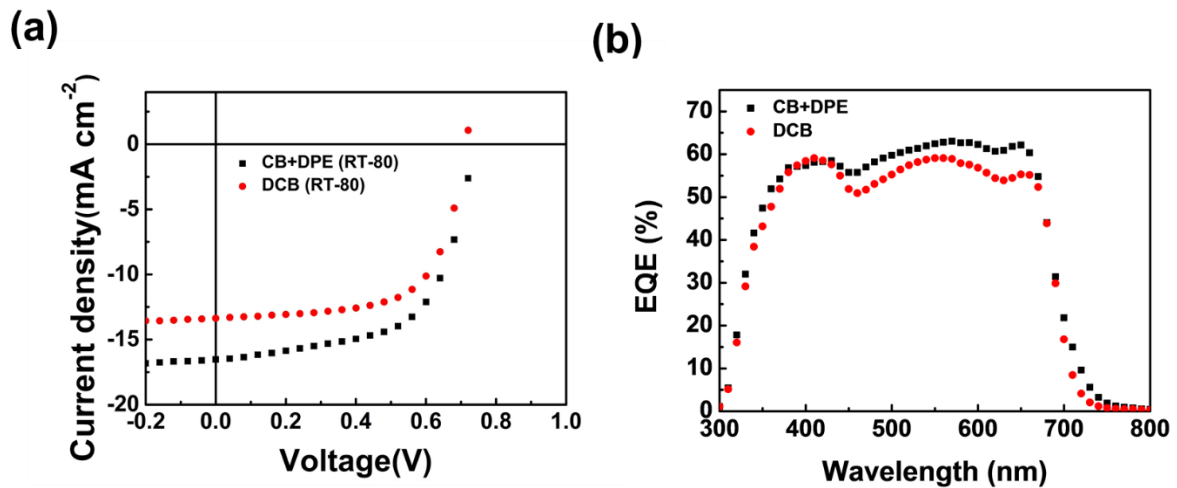


**Figure 10. 1** *J-V* characteristics and EQE spectra of PPDT2FBT:PC<sub>71</sub>BM-based inverted PSCs with different solvents at Head:25 °C-Substrate: 80 °C (H25-S80) condition

**Table 10. 1** Detailed photovoltaic parameters at variable processing temperatures

Solvent	Temperature of substrates	$J_{sc}$ (mA/cm <sup>2</sup> )	$V_{oc}$ (V)	FF	PCE (%)
CB+DPE	25	12.8	0.69	0.34	2.99
	40	16.4	0.70	0.47	6.12
	60	16.8	0.73	0.52	6.33
	80	16.5	0.74	0.61	7.43
	100	15.8	0.73	0.58	6.13
DCB	25	9.83	0.66	0.54	3.55
	40	11.7	0.71	0.54	4.49
	60	12.2	0.72	0.65	5.65
	80	12.6	0.71	0.65	5.89
	100	7.29	0.73	0.51	2.72

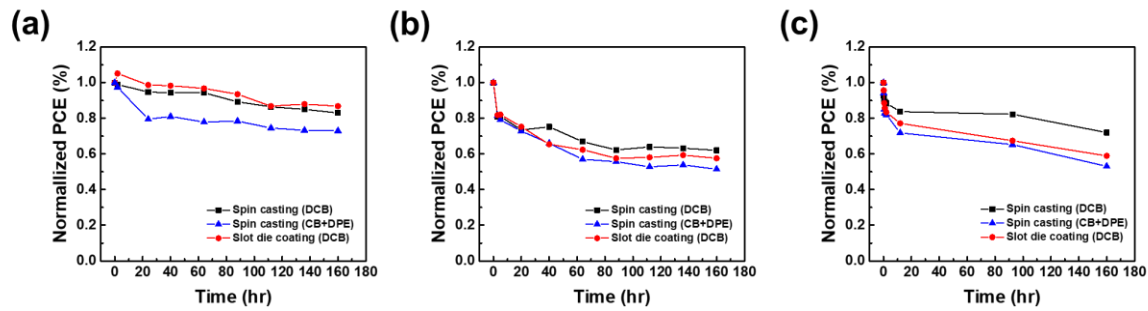


**Figure 10.2** (a) long-term stabilities in air atmosphere (b) thermal stabilities at 120 °C in N<sub>2</sub> filled glove box and (c) photo stabilities under AM 1.5G illumination in air condition. photoactive layer of PSCs spin-coated with and without additives, and slot die coated for comparisons of devices durability. The devices used for stability testing in air were encapsulated in glass.

Active layers were deposited using a controlled temperature matrix of solution (slot-head, H) and substrate (stage, S) temperatures in a range of 25 °C to 100 °C as shown in **Figure 10.3 (b)**. The PCE variation and detailed photovoltaic parameters of all PSCs processed using various processing temperature combinations are shown in **Figure 10.3 (c)** and **Table 10.2**. With the increase of the substrate temperature up to 100 °C (using fixed head temperatures), PSCs showed a dramatic improvement in performance, from a 1.95–3.55% PCE using 25 °C substrates up to a 4.75–7.61% PCE for 80 °C substrates, stemming from significant increases in all photovoltaic parameters. Increasing the temperature of the slot head also had positive effects on the performance of PSCs, showing slightly improved open-circuit voltages ( $V_{oc}$ s) and fill factors relative to heated substrates alone. Processing at over 100 °C deteriorated the performance with drastically decreased  $J_{sc}$  values. Additionally, high temperatures rapidly dried the active solution before completely wetting the substrates, which led to the excessive crystallinity of the polymer and clumpy film formation including plastered and early drying materials.

To identify clear trends in photovoltaic parameters as a function of temperature combinations, the results using a fixed solution temperature of 80 °C or a fixed substrate temperature of 80 °C have been arranged in **Figure 10.3 (d-e)**, clearly illustrating the results described above. Furthermore, data of four representative PSCs processed with temperature combinations (H25–S25, H25–S80, H80–S25, and H80–S80) are summarized in **Table 10.3** for clear comparison. H and S in front of each number refer to slot head and substrate, respectively, while the number indicates the temperature (°C). The thicknesses of the four films were 280, 320, 140 and 250 nm for conditions of H25–S25, H25–S80, H80–S25 and H80–S80, respectively. Optimal PSC performance was observed at H80–S80 and showed a 7.61% PCE with a  $J_{sc}$  of 14.80 mA cm<sup>-2</sup>,  $V_{oc}$  of 0.78 V and FF of 0.66. The photovoltaic characteristics at H80–S80 with varying the active layer thickness (by controlling the coating speed) are also compared in **Table 10.4**. These results are even higher than the performance of PSCs processed by spin coating

under an inert atmosphere. In addition, hot processing with 80 °C substrates significantly increased the shunt resistance (284.53–398.94 kΩ cm<sup>2</sup>) and decreased the series resistance (3.76–9.25 Ω cm<sup>2</sup>), leading to significant enhancements in  $V_{oc}$  and FF (dark  $J$ - $V$  curves are shown in **Figure 10.4**). Additionally, these increased  $V_{oc}$ s with the increment of substrate temperature originate from reduced charge recombination and increased exciton dissociation in the donor/acceptor blend as well as the high crystallinity of the blend films with reduced defect density, which will be discussed in the following analysis section. These results indicate the optimization of a thermal matrix of head and substrate temperatures during film formation using a modified 3D printer-based slot die method has high potential for comparable PSC performance and constitutes a nice strategy for PSC fabrication.

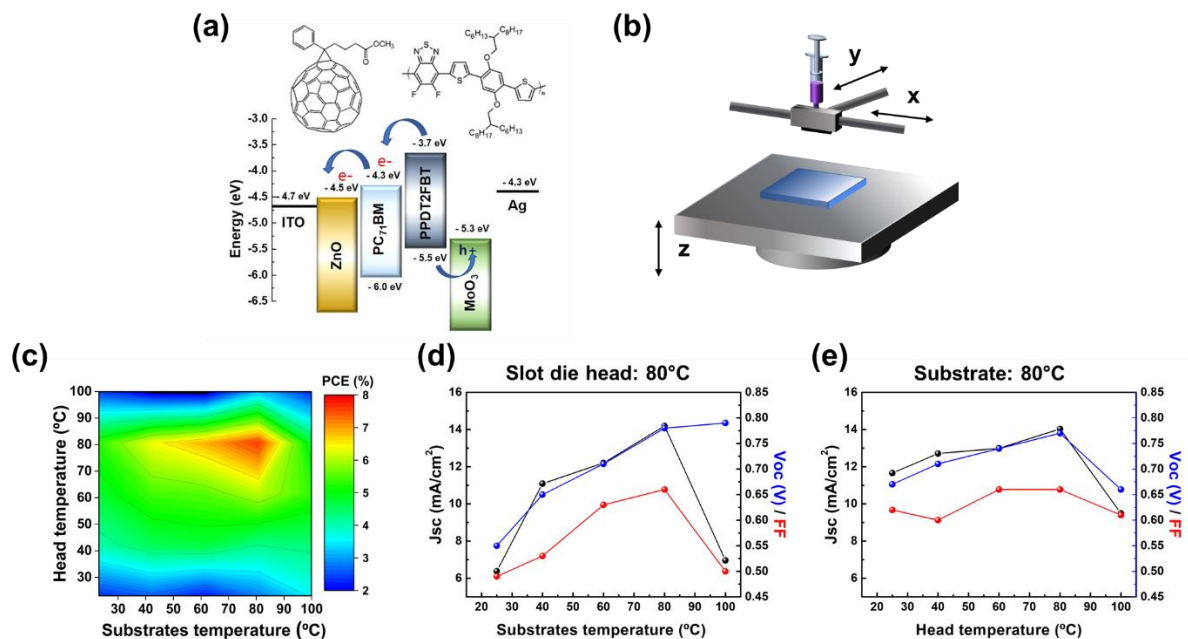


**Figure 10. 3** (a) Slot-die process using with 3D printer for PSCs fabrication and (b) The performance of inverted PP2FBT:PC<sub>71</sub>BM-based PSCs depending on both temperature, changes of photovoltaic parameters (c) on substrate (or/and stage) temperature in case of fixed head T at 80 °C and (d) on slot-die head temperature in fixed substrate T at 80 °C

**Table 10. 2** Summary of optimal photovoltaic parameters of PSCs processed using various processing temperatures

Head Temperature (°C)	Temperature of substrates (°C)	$J_{sc}$ (mA cm <sup>-2</sup> )	$V_{oc}$ (V)	FF	Best PCE (%)
25	25	7.29	0.62	0.52	2.35
	40	11.1	0.66	0.56	4.06
	60	11.8	0.68	0.60	4.79
	80	12.2	0.70	0.62	5.29
	100	4.77	0.70	0.61	2.41
40	25	7.53	0.61	0.57	2.62
	40	11.2	0.67	0.61	4.57
	60	12.8	0.71	0.60	5.42
	80	13.2	0.74	0.63	6.40
	100	4.20	0.71	0.62	1.84
60	25	6.58	0.62	0.53	2.18
	40	11.4	0.69	0.60	4.72
	60	11.7	0.72	0.65	5.52
	80	13.5	0.75	0.68	6.89
	100	4.98	0.68	0.53	1.76
80	25	6.91	0.70	0.58	2.80
	40	11.6	0.68	0.54	4.26
	60	12.6	0.74	0.65	6.06
	80	14.80	0.78	0.66	7.61
	100	7.50	0.81	0.57	3.16
100	25	9.37	0.69	0.55	3.55
	40	10.9	0.70	0.58	4.38
	60	12.1	0.72	0.61	5.32
	80	10.7	0.70	0.63	4.75
	100	4.95	0.73	0.58	2.10

**Table 10. 3** Photovoltaic parameters of representative PSCs

Head Temperature (°C)	Temperature of substrates (°C)	Best PCE (avg. PCE) (%)	$J_{sc}$ (mA cm <sup>-2</sup> )	$J_{sc}$ (mA cm <sup>-2</sup> )	$V_{oc}$ (V)	FF	$R_{shunt}$ (kΩcm <sup>2</sup> )	$R_s$ (Ωcm <sup>2</sup> )
25	25	2.35 (1.55)	7.29	7.04	0.62	0.52	0.57	31.01
	80	5.29 (4.67)	12.2	11.79	0.70	0.62	284.53	9.25
80	25	2.80 (1.78)	6.91	7.41	0.70	0.58	3.55	22.34
	80	7.61 (6.72)	14.80	14.38	0.78	0.66	398.94	3.76

**Table 10. 4** PSCs performance with various thickness in H80-S80 process

Processing condition	Average thickness of films (nm)	$J_{sc}$ (mA cm <sup>-2</sup> )	$V_{oc}$ (V)	FF	PCE (%)
H80-S80	120	13.56	0.78	0.67	7.11
	250	14.92	0.78	0.64	7.42
	500	13.44	0.76	0.63	6.47
	1100	12.31	0.75	0.49	4.54

\*Using a 14 mg/ml PPDT2FBT:PC<sub>71</sub>BM concentration solution, the coating speeds at 3, 11 and 40 mm/s yielded the film thickness of 120, 250 and 500 nm, respectively. The slot die coating at 40 mm /s with 20 mg/ml blend solution yielded ~1100 nm thick films.



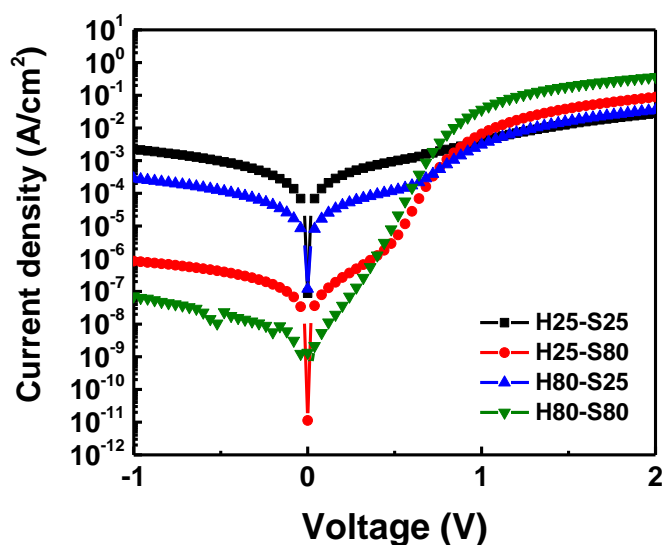


**Figure 10. 4** Dark  $J$ - $V$  characteristics of devices processed at various temperature combination conditions.

### 10.3.2 Morphology and Crystallinity Analyses

Nanoscale, phase-separated morphologies in BHJ devices play a critical role in determining the photovoltaic performance, since bi-continuous pathways for photo-generated charges lead to efficient charge dissociation and extraction. The morphologies and internal composite structure of four representative films (H25–S25, H25–S80, H80–S25, and H80–S80) were characterized using tapping mode atomic force microscopy (AFM) and field emission transmission electron microscopy (FE-TEM) to investigate changes in surface and BHJ morphologies due to variations in the processing temperature. TEM images indicate that the brighter regions represent the PPDT2FBT polymer phase while darker areas represent the PC<sub>71</sub>BM phase (due to greater electron scattering by PC<sub>71</sub>BM). As shown in **Figure 10.5 (a–d)**, the blend films processed at room temperature (H25–S25) exhibited a blurred composite phase. Although the interfacial area of PPDT2FBT and PC<sub>71</sub>BM may be large, this type of morphology results in impeded charge transport due to poorly formed domains in blend films. In the films fabricated with the hot slot die head (H80–S25), clearer PC<sub>71</sub>BM and PPDT2FBT phases were observed relative to the ones at H25–S25, since a hot slot head and PPDT2FBT:PC<sub>71</sub>BM ink not only increase the solubility of photoactive materials, but also lead to semi-crystalline film morphology during film formation. Interestingly, the use of a hot substrate clearly shows a brighter polymer phase in TEM images. Using a hot substrate (H25–S80) led to more aggregated PC<sub>71</sub>BM and PPDT2FBT phases and larger phase separation (compared to that at H80–S25). Notably, films processed using a hot head and hot substrate (H80–S80) showed a clearly discernible composite phase structure, as well as homogeneous fibril-like features in the polymer phase, resulting from the combination of the effects of hot ink and hot substrates as mentioned above. The fibril-like nanostructures lead to efficient charge

transport pathways for charge extraction, which is the main reason for the significantly enhanced PSC performance with the largest shunt resistance among the four different temperature combinations.

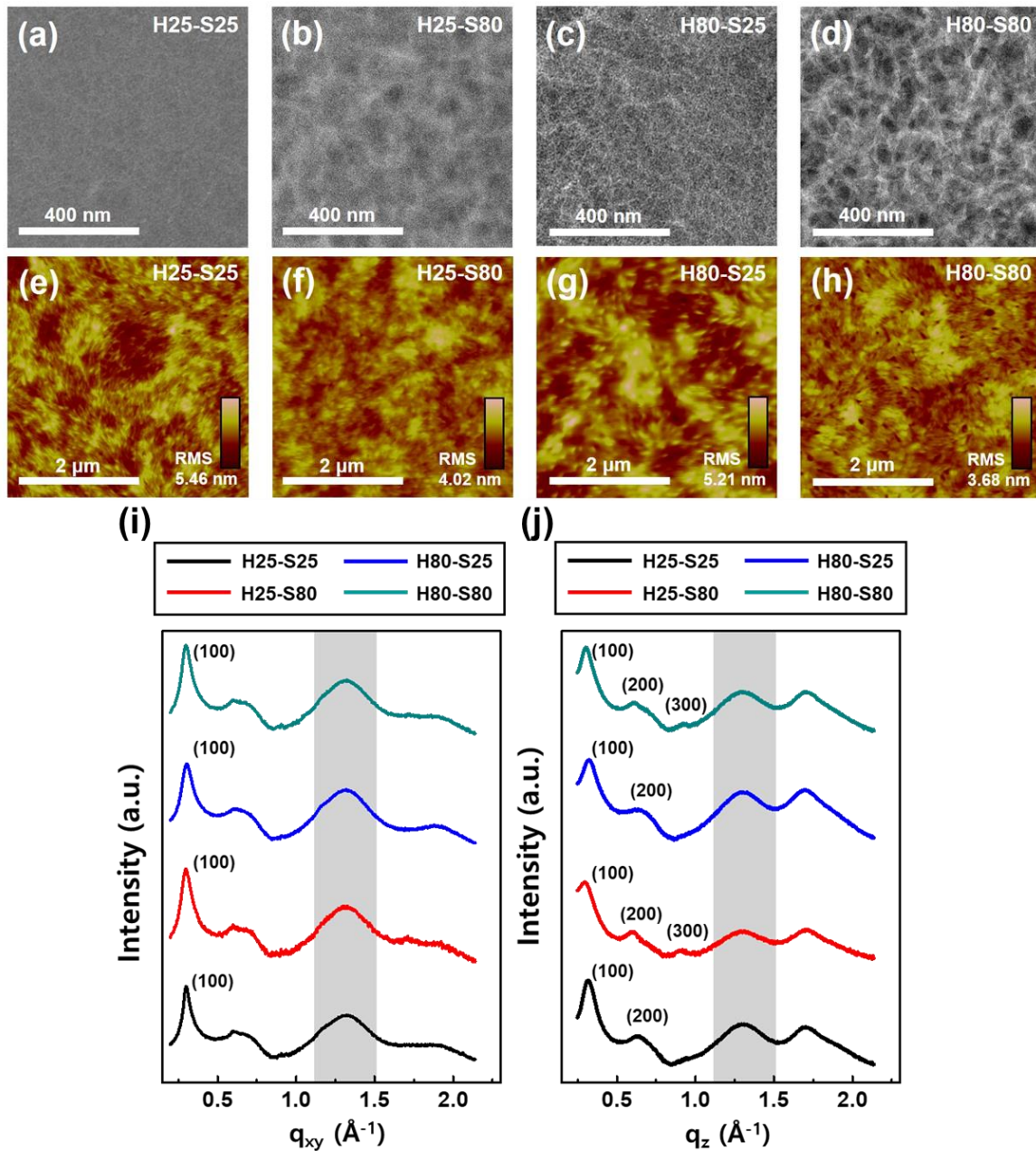


**Figure 10.5** . (a–d) FE-TEM and (e–h) AFM topography images of active layers processed with the dual temperature treatment (H25–S25, H25–S80, H80–S25 and H80–S80). The RMS scale is 40 nm. (i and j) GIWAXS line-cut profiles of the  $q_{xy}$  and the  $q_z$  axis for the four films.

**Figure 10.5 (e–h)** show the AFM surface morphologies of active thin films deposited under four representative conditions. The ambient temperature blend film (H25–S25) showed the highest surface roughness of 5.46 nm. Hot slot head and/or hot substrate processing both contributed to reduced surface roughness, showing surface roughnesses of 4.02, 5.21 and 3.68 nm for films H25–S80, H80–S25 and H80–S80, respectively. In addition, hot substrate processing loosened domain coarsening with smoother surface roughness. The film at H80–S80 showed a finely distributed bicontinuous morphology and the lowest RMS roughness, together with a small series resistance, providing additional evidence for performance enhancement in the corresponding devices.

Furthermore, to investigate changes in molecular packing and orientation in the films, grazing incidence wide-angle X-ray scattering (GIWAXS) measurements were carried out. Line-cuts are displayed in **Figure 10.5 (i–j)**. A broad scattering at around  $1.30 \text{ \AA}^{-1}$  in **Figure 10.6** corresponds to the PC<sub>71</sub>BM aggregates. The crystallographic parameters calculated from GIWAXS profiles are summarized in **Table 10.5**. The films processed on hot substrates exhibited pronounced lamellar diffractions up to (300) peaks in the out-of-plane ( $q_z$ ) direction, correlating to well-ordered PPDT2FBT polymer chains and a higher degree of crystallinity. The photovoltaic performance, blend film morphology and crystalline structures with fast drying and slow drying of wet films were compared by changing the cooling rate. More ordered polymer packing structures as well as increased crystallite size were observed with slow cooling procedures (see the results in **Table 10.6** and **Figure 10.7**). This result can be understood in terms of a pronounced thermal annealing effect by slow cooling. The high head temperature increases the solubility with well dissolved photoactive materials and the hot substrate treatment induces well-ordered polymers via the thermal annealing effect. Consequently, the processing using 80 °C for both the head and stage temperatures resulted in highly ordered molecular packing, resulting in efficient charge transport and performance enhancement.

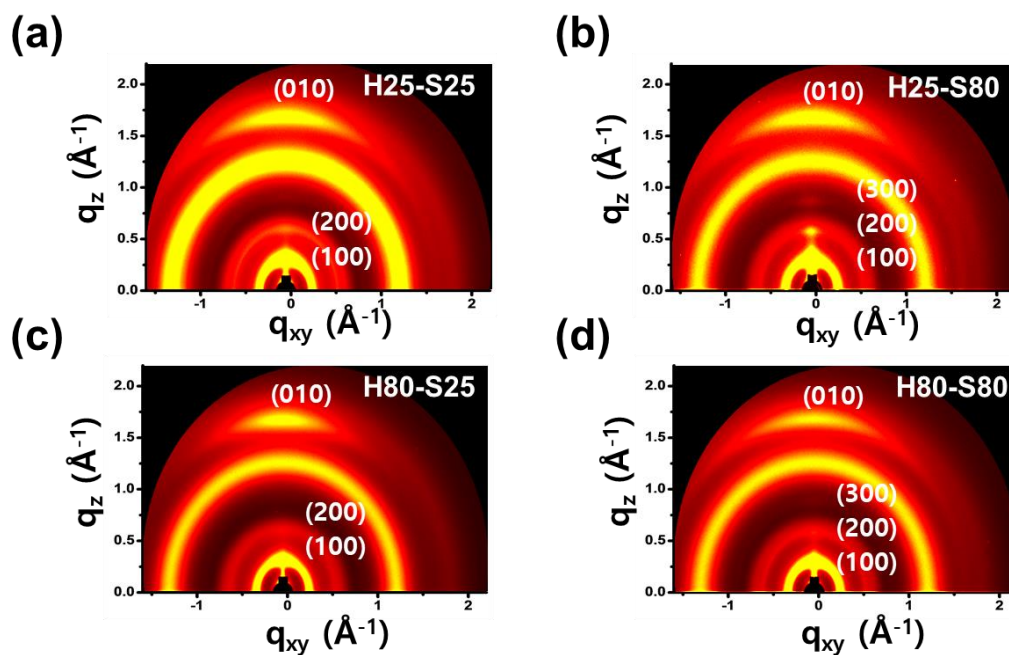


**Figure 10. 6** Two-dimensional GIWAXS data for films processed at (a) H25-S25, (b) H25-S80, (c) H80-S25 and (d) H80-S80 conditions, respectively

**Table 10. 5** Crystallographic parameters from GIWAXS data

Condition	Crystallographic parameters					
	Axis	$\pi$ - $\pi$ stack [ $\text{\AA}^{-1}$ ]	d-spacing [ $\text{\AA}$ ]	Coherence length [ $\text{\AA}$ ]	Lamella stack [ $\text{\AA}^{-1}$ ]	d-spacing [ $\text{\AA}$ ]
H25-S25	$q_{xy}$	-	-	-	0.30	20.94
	$q_z$	1.70	3.70	38.1	0.32	19.63
H25-S80	$q_{xy}$	-	-	-	0.29	21.67
	$q_z$	1.70	3.70	41.7	0.30	20.94
H80-S25	$q_{xy}$	1.90	3.31	45.9	0.31	20.27
	$q_z$	1.70	3.70	38.6	0.30	20.94
H80-S80	$q_{xy}$	-	-	-	0.31	20.27
	$q_z$	1.70	3.70	44	0.31	20.27

**Table 10. 6** PSC performances for comparison of fast cooling and slow cooling after slot die coating

Slot die coating condition	Cooling condition	Drying time (seconds)	$J_{sc}$ ( $\text{mA cm}^{-2}$ )	$V_{oc}$ (V)	FF	PCE (%)
H80-S60	Slow <sup>a)</sup>	30	9.28	0.75	0.69	4.80
	Fast <sup>b)</sup>	240	7.31	0.72	0.61	3.20
H80-S80	Slow <sup>a)</sup>	5	11.73	0.82	0.69	6.63
	Fast <sup>b)</sup>	23	12.36	0.80	0.62	6.13

a) The substrates after slot die coating were maintained at processing temperature until complete drying.

b) The substrates were cooled to 20 °C right after coating.

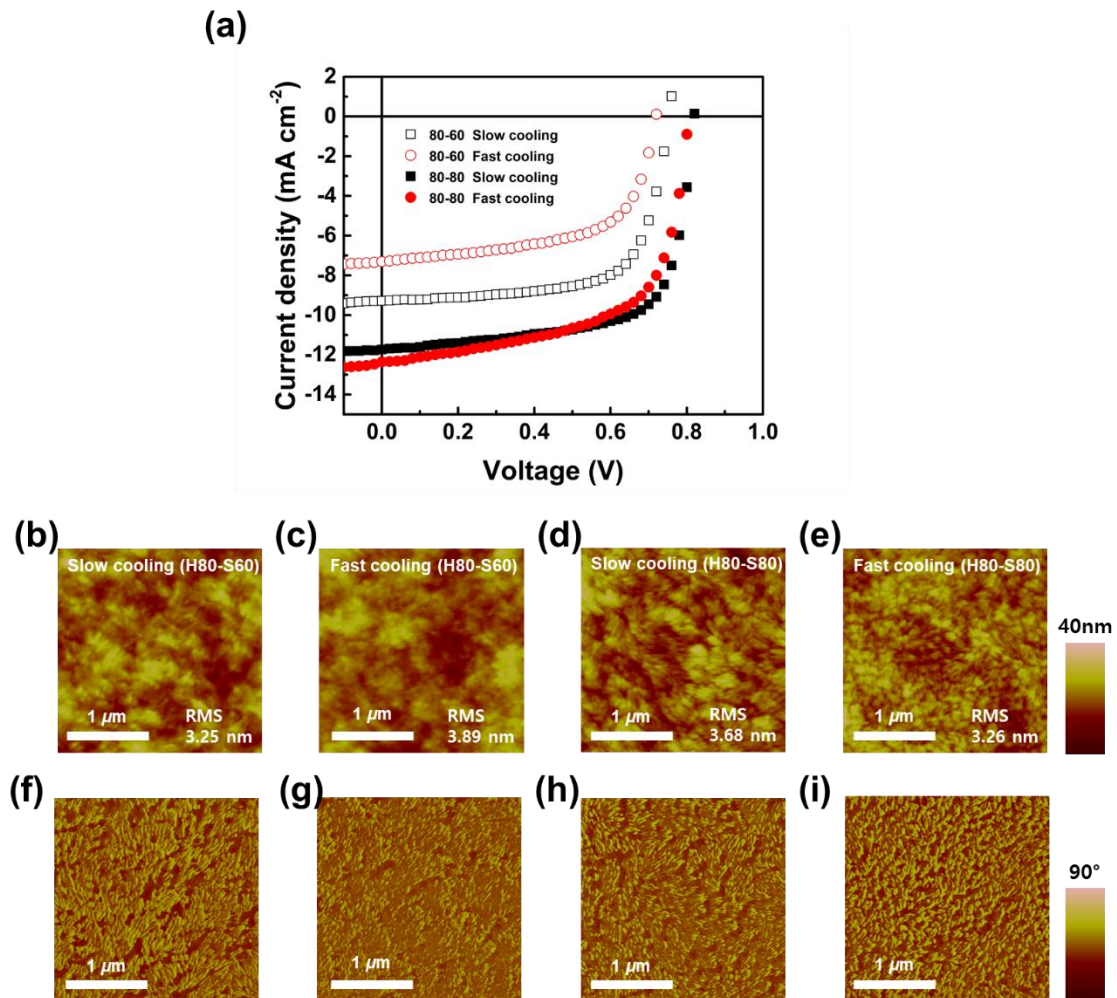


**Figure 10. 7** (a)  $J$ - $V$  curve of fast and slowly dried PSCs and AFM topography (b-e) and corresponding phase images (f-i) for comparison of film morphologies dried by fast and slow cooling after slot die coating at H80-S60 and H80-S80

### 10.3.3 Charge Transport and Recombination in PSCs

To further understand how differences in PSC performance depend on processing temperatures, the recombination kinetics and charge extraction probability were investigated by analysis of the light intensity-dependence of the  $J$ - $V$  characteristics and the dependence of photocurrent ( $J_{ph}$ ) on effective voltage ( $V_{eff}$ ). Four devices were studied under a range of illumination from  $10 \text{ mW cm}^{-2}$  to  $100 \text{ mW cm}^{-2}$  to identify the dominant recombination mechanisms in devices. **Figure 10.8 (a)** shows a semi-logarithmic plot of  $V_{oc}$  versus light intensity; the slope of the  $V_{oc}$  versus light intensity plot provides information on the charge recombination. Devices processed with room temperature substrates showed a strong dependence of  $V_{oc}$  on the light intensity with a slope of over  $2\text{kT}/q$ , indicating that monomolecular Shockley-Read-Hall (SRH) recombination is predominant at the open-circuit condition due to incomplete phase separation and trap-based recombination. In contrast, processing using hot substrates significantly decreased the trap assisted recombination, evident as reduced slopes of  $1.81\text{kT}/q$  (H25-S80) and  $1.70\text{kT}/q$  (H80-S80), respectively.

Photocurrent ( $J_{ph} = J_{illumination} - J_{dark}$ ) is plotted as a function of effective voltage ( $V_{eff} = V_o - V_{app}$ , where,  $V_{app}$  is the applied voltage and  $V_o$  is the voltage at which  $J_{ph} = 0$ ) in **Figure 10.8 (b)**. The charge collection/extraction probability was calculated using the ratio of photocurrent ( $J_{ph}$ ) and saturated photocurrent ( $J_{sat}$ ) at the maximum power output condition ( $V_{eff} = 0.2$ ). The charge extraction probabilities at  $V_{eff} = 0.2$  were 51.1% (H25-S25), 79.2% (H25-S80), 58.3% (H80-S25) and 80.5% (H80-S80), respectively, which indicate that the H80-S80 processing reduced space charge build-up, with superior transport balance arising from minimized charge recombination. The trend of charge collection probability was consistent with the  $V_{oc}$  dependence on light intensity, indicating that good phase separation by dual temperature controlling has significant effects on recombination kinetics and charge dynamics.

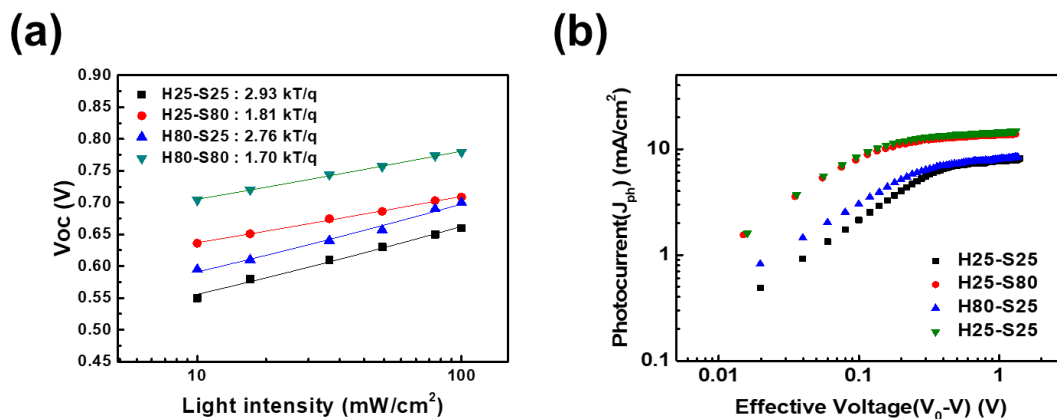


**Figure 10. 8** (a) Light intensity dependence of  $V_{oc}$  and (b) photocurrent versus effective voltage

### 10.3.4 Flexible PSCs Processed Using Roll-to-Roll Equipment

In the final goal of this work, PSCs based on flexible ITO substrates were processed using the 3D printer modified slot die and a R2R system in an atmosphere of air. Except for the final electrodes, other layers including the ZnO NPs and PPDT2FBT:PC<sub>71</sub>BM blend layer were coated by the slot die and R2R method. R2R process conditions for each layer were set up following optimal conditions identified in PSCs fabricated by 3D printer-based slot die coating. H80–S80 conditions were used for PPDT2FBT:PC<sub>71</sub>BM processing, where the film passed over a hot plate after slot die coating of the ZnO NP layer as shown in **Figure 10.9 (a)**. The best PSC performance based on flexible poly(ethylene terephthalate) (PET) substrates and R2R slot die processing was a 7.06% PCE, with a  $J_{SC}$  of 15.6 mA cm<sup>-2</sup>,  $V_{OC}$  of 0.74 V and FF of 0.61 (the thickness of the film was around 500 nm), while the PSCs on rigid glass substrates using 3D printer processing showed a 7.61% PCE (a  $J_{SC}$  of 14.8 mA cm<sup>-2</sup>,  $V_{OC}$  of 0.78 V and FF of 0.66). The  $V_{oc}$  and FF of R2R processed PSCs were decreased, due to lower shunt resistance which is typical for PET substrates and current leakage of the fragile ITO layer during processing. However, the  $J_{sc}$  of R2R devices was still similar to the value of PSCs on ITO glass substrates. **Figure 10.9 (b)** shows  $J$ – $V$  characteristics of the best performing PSCs on both PET and glass substrates. Both PSCs showed similar performance with PCEs over 7%, owing to the use of the same optimized processing conditions identified *via* the thermal matrix of slot head and substrate temperatures as well as the low sensitivity of device performance to thickness variations of PPDT2FBT. Furthermore, PSCs were fabricated on glass substrates *via* the slot die solution process except the anode (Ag). The ZnO NPs, PPDT2FBT:PC<sub>71</sub>BM blend and PEDOT:PSS layers were coated by the slot die method, resulting in a PCE of 4.94% with a  $J_{sc}$  of 10.29 mA cm<sup>-2</sup>,  $V_{oc}$  of 0.80 V and FF of 0.60 (**Figure 10.10** and **Table 10.7**). All solution-processed PSCs are still a great challenge in this research field. Consequently, we successfully demonstrated that thermal matrix optimization of R2R processing via dual thermal treatments constitutes a practical methodology which allows a similar performance of flexible devices to ITO glass-based PSCs without supplementary treatments such as additives or post-thermal annealing.

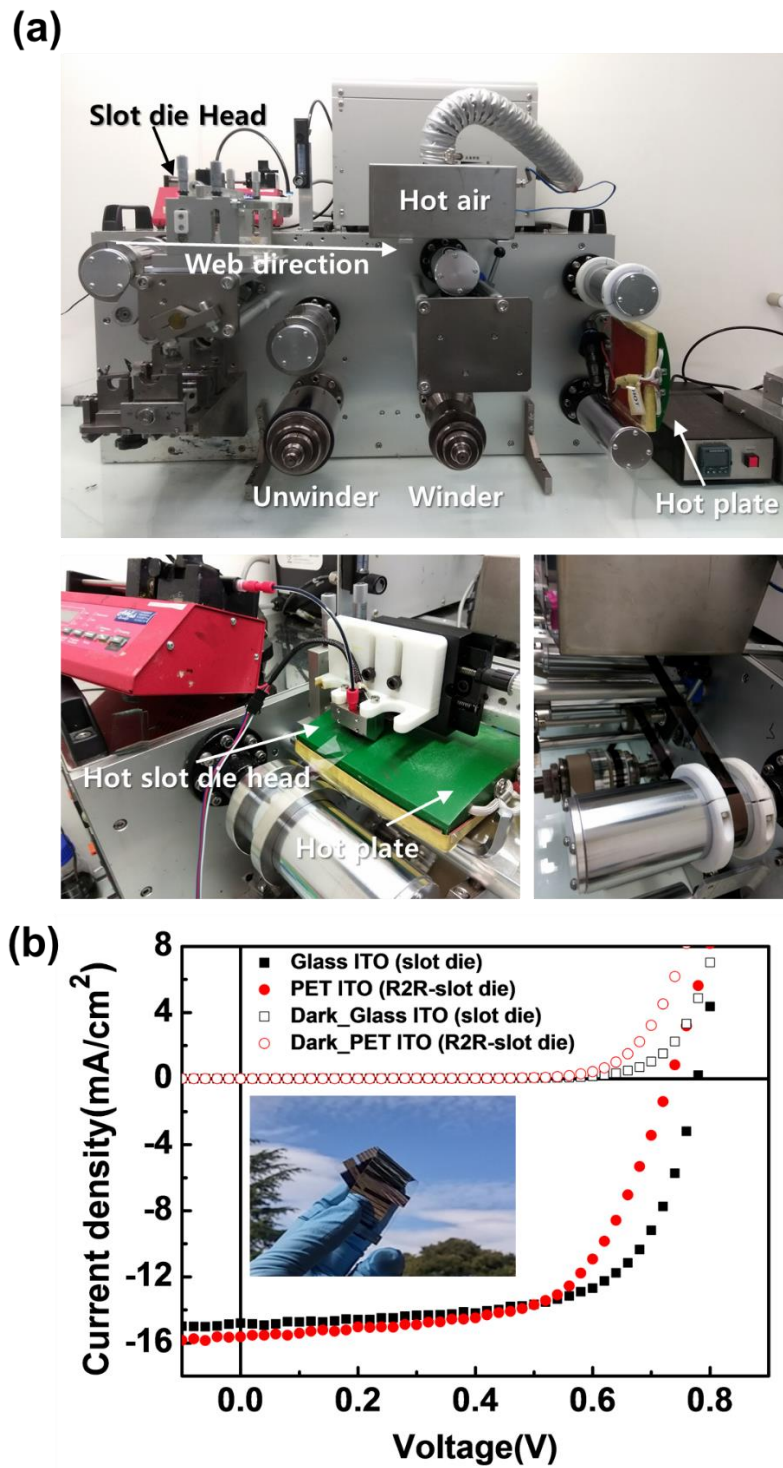


**Figure 10. 9** (a) Pictures of 3D printer-based R2R equipment and (b)  $J$ - $V$  characteristics of slot die processed polymer solar cells on ITO coated glass and flexible PET substrates



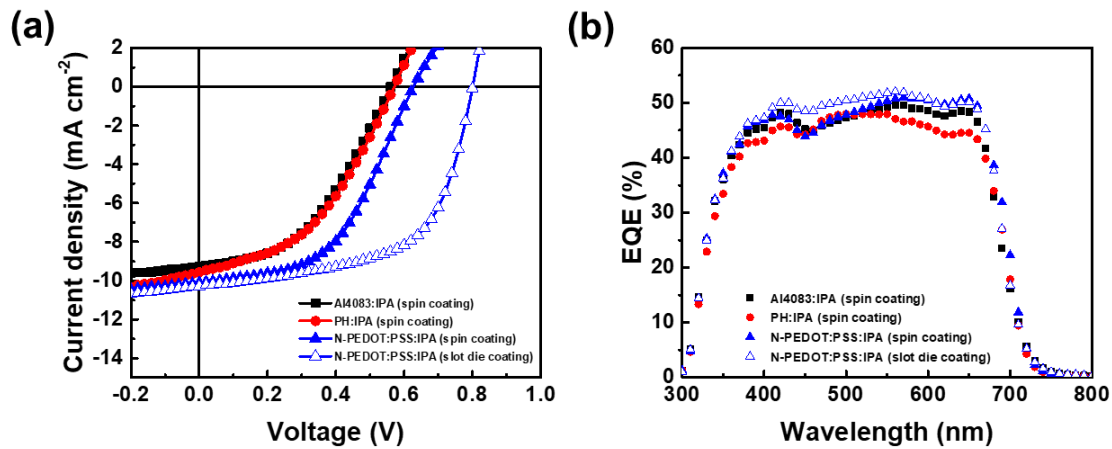


**Figure 10. 10** *J-V* characteristics and EQE results of PSCs fabricated by slot die-based all solution process except electrodes

**Table 10. 7** Photovoltaic parameters of devices fabricated by slot die-based all solution process including ETL, active layer and HTL

Slot die coating condition	HTL	Coating method	$J_{sc}$ (mA cm <sup>-2</sup> )	$Cal.J_{sc}$ (mA cm <sup>-2</sup> )	$V_{oc}$ (V)	FF	PCE (%)
H80-S80	AI4083:IPA (1:3)	Spin	9.27	9.41	0.56	0.45	2.31
	PH:IPA (1:3)	Spin	9.79	9.09	0.59	0.44	2.53
	N-PEDOT:PSS : IPA (1:3)	Spin	10.37	9.76	0.64	0.48	3.18
	N-PEDOT:PSS : IPA (1:3)	Slot die	10.29	9.93	0.80	0.60	4.94

## 10.4 Conclusion

The highlight of this study is the first systematic study on the temperature combination of solution and substrate for film processing by remodeling a 3D printer-based slot die process. This methodology results in comparable PSC performance to devices prepared by the spin casting method. This slot die coating approach suggests a vital strategy for PSC fabrication to overcome the difficulties of lab-to-fab scale up when PSC materials are adapted to R2R equipment. Inverted geometry PSCs using a PPDT2FBT:PC<sub>71</sub>BM blend dissolved in *o*-DCB (without additives) were selected to overcome the current problems of PSCs such as stability, reproducibility and sensitivity to film thickness. We thoroughly investigated the morphologies, changes in molecular ordering of active films, charge recombination and the resulting photovoltaic properties as functions of processing temperatures of both slot head and substrate. Finally, roll to roll processing equipment with flexible substrates was used to fabricate PSCs at optimal conditions identified using 3D printer-based slot die processing. An optimal performance of a 7.06% PCE was achieved, which is comparable to the performance of spin-cast PSCs and 3D printer-based slot die coated PSCs on ITO covered glass. This work may suggest a simple and useful way to test the feasibility of lab-scale PSC devices for R2R-based mass production, including in-depth analysis of not only active material requirements such as thickness tolerance and air stability but also development of a new methodological approach based on temperature controllable slot die coating as a useful mid step in the lab-to-fab transition.

## Chapter 11. Summary

Organic solar cells (OSCs) have attracted as one of energy source in next generation because of their advantages such as light weight, flexibility and easy fabrication and so on. The organic solar cells are certainly required the light for working, since OSCs is a device for energy conversion system from light to electricity. Therefore, we have mainly studied the organic solar cells incorporating light manipulation, which can offer ways to enhance the OSCs performance and research of optics into optoelectronics. We believe that this study applying nanophotonic to organic solar cells leads commercialization of OSCs as well as provide the strategy of light engineering for others optoelectronics. The main research is as follows.

Firstly, the localized surface plasmon resonance (LSPR) phenomenon from arrayed silver (Ag) nanoparticles were studied. According to Mie's theory for spherical nanoparticle, the plasmon resonance were depending on surrounding's optical property. In this work, arrayed Ag nanoparticles fabricated by block copolymer micell lithography (BCML) were embedded in two different ETL having different refractive indices. TiO<sub>2</sub> nanoparticles of higher refractive index introducing Ag nano particle showed higher OSCs performance with significant enhanced  $J_{sc}$  values by 11% enhancement, compared to control device than ZnO ETL case, due to higher far-field scattering of Ag nanoparticles in plasmon phenomenon.

Secondly, in order to reduce incident light loss, we demonstrated hetero polymer tandem solar cells (PTSCs). Here, we had calculated the optimal thickness of each photoactive layers and took account the limited factors of tandem structure as well as the issues to consider in the PTSCs fabrication process. Two new designed polymers of wide band gap were used in bottom cells and PTB7-Th:PC<sub>71</sub>BM blends was used in top cells, consequently, the 11.42 % of PCE were obtained.

Thirdly, semitransparent organic solar cells were implemented by using dielectric-metal-dielectric (DMD) transparent electrode. Sb<sub>2</sub>O<sub>3</sub> and silver were used as a dielectric and a metal films, respectively, in this work. We analyzed the influence of each layers: bottom Sb<sub>2</sub>O<sub>3</sub> layer, Ag thin film, top Sb<sub>2</sub>O<sub>3</sub> layer. 2 nm thin Sb<sub>2</sub>O<sub>3</sub> layer has effect on uniformly deposited Ag thin films, The Ag thin films showed the relationship of sheet resistance and transmittance, and top Sb<sub>2</sub>O<sub>3</sub> layer contributes to shifting maximum transmittance peaks. Finally, we successfully demonstrated colorful semitransparent OSCs with using colorful active blends.

Fourth, as other way for colorful semitransparent OSCs, color filter composing of two metallic mirrors and transparent dielectric medium were investigated for implement selective colors saturation. We also used Sb<sub>2</sub>O<sub>3</sub> dielectric for a cavity layer. By using PTB7-Th:PC<sub>71</sub>BM blends able to absorb all visible range, the colored organic solar cells dependent on only color filter were successfully fabricated showing higher performance at blue color filter. Furthermore, the colorful semitransparent OSCs based on DMD electrode and color filter also showed the higher performance at blue color filter.

I believe that these light engineering for OSCs will provide breakthroughs for innovative OSCs as well

as novel strategy for OSCs marketing

In addition, as sub-research, I also have been researched morphologies and molecular packing structures not only of photoactive films with various conjugated donor polymers but also of processing methods. New designed donor polymers were modified side chains on the backbones including various type of side chain, controlled side chain length, introducing fluorine units and hydrophilic side chain, and so on. The Morphology and structural packing have been depending on chemical structure of conjugated polymers and processing methods including thermal-, additives-, solvent treatment and so on. Finally, i propose the potential of flexible OSCs fabricated by a roll-to-roll (R2R) process without performance loss, by using dual thermal treatment of slot die coating for optimizing morphology and molecular orientation.

In conclusion, these studies about light manipulation for OSCs with trying film optimization via modified side chain and processing methodology may be helpful to lead aesthetic OSCs commercial market.

## Reference

1. Yan, J.; Saunders, B. R., Third-Generation Solar Cells: A Review and Comparison of Polymer:Fullerene, Hybrid Polymer and Perovskite Solar Cells. *RSC Advances* **2014**, *4*, 43286-43314.
2. Abdulrazzaq, O. A.; Saini, V.; Bourdo, S.; Dervishi, E.; Biris, A. S., Organic Solar Cells: A Review of Materials, Limitations, and Possibilities for Improvement. *Particulate Science and Technology* **2013**, *31*, 427-442.
3. Lu, L.; Zheng, T.; Wu, Q.; Schneider, A. M.; Zhao, D.; Yu, L., Recent Advances in Bulk Heterojunction Polymer Solar Cells. *Chemical Reviews* **2015**, *115*, 12666-12731.
4. Krebs, F. C., Fabrication and Processing of Polymer Solar Cells: A Review of Printing and Coating Techniques. *Solar Energy Materials and Solar Cells* **2009**, *93*, 394-412.
5. Li, G.; Zhu, R.; Yang, Y., Polymer Solar Cells. *Nat Photon* **2012**, *6*, 153-161.
6. Søndergaard, R.; Hösel, M.; Angmo, D.; Larsen-Olsen, T. T.; Krebs, F. C., Roll-to-Roll Fabrication of Polymer Solar Cells. *Materials Today* **2012**, *15*, 36-49.
7. Forberich, K.; Guo, F.; Bronnbauer, C.; Brabec, C. J., Efficiency Limits and Color of Semitransparent Organic Solar Cells for Application in Building-Integrated Photovoltaics. *Energy Technology* **2015**, *3*, 1051-1058.
8. Jelle, B. P.; Breivik, C., The Path to the Building Integrated Photovoltaics of Tomorrow. *Energy Procedia* **2012**, *20*, 78-87.
9. Sariciftci, N. S.; Smilowitz, L.; Heeger, A. J.; Wudl, F., Photoinduced Electron Transfer from a Conducting Polymer to Buckminsterfullerene. *Science* **1992**, *258*, 1474-1476.
10. Brabec, C. J.; Cravino, A.; Meissner, D.; Sariciftci, N. S.; Fromherz, T.; Rispen, M. T.; Sanchez, L.; Hummelen, J. C., Origin of the Open Circuit Voltage of Plastic Solar Cells. *Advanced Functional Materials* **2001**, *11*, 374-380.
11. Heremans, P.; Cheyns, D.; Rand, B. P., Strategies for Increasing the Efficiency of Heterojunction Organic Solar Cells: Material Selection and Device Architecture. *Accounts of Chemical Research* **2009**, *42*, 1740-1747.
12. Facchetti, A., Polymer Donor–Polymer Acceptor (All-Polymer) Solar Cells. *Materials Today* **2013**, *16*, 123-132.
13. Kurpiers, J., et al., Probing the Pathways of Free Charge Generation in Organic Bulk Heterojunction Solar Cells. *Nature Communications* **2018**, *9*, 2038.
14. Schilinsky, P.; Waldauf, C.; Hauch, J.; Brabec, C. J., Simulation of Light Intensity Dependent Current Characteristics of Polymer Solar Cells. *Journal of Applied Physics* **2004**, *95*, 2816-2819.
15. Waldauf, C.; Scharber, M. C.; Schilinsky, P.; Hauch, J. A.; Brabec, C. J., Physics of Organic Bulk Heterojunction Devices for Photovoltaic Applications. *Journal of Applied Physics* **2006**, *99*, 104503.

16. Su, Y.-W.; Lan, S.-C.; Wei, K.-H., Organic Photovoltaics. *Materials Today* **2012**, *15*, 554-562.
17. Hedley, G. J.; Ruseckas, A.; Samuel, I. D. W., Light Harvesting for Organic Photovoltaics. *Chemical Reviews* **2017**, *117*, 796-837.
18. Tadatsugu, M., Transparent Conducting Oxide Semiconductors for Transparent Electrodes. *Semiconductor Science and Technology* **2005**, *20*, S35.
19. Qi, B.; Zhang, Z.-G.; Wang, J., Uncovering the Role of Cathode Buffer Layer in Organic Solar Cells. *Scientific Reports* **2015**, *5*, 7803.
20. Po, R.; Carbonera, C.; Bernardi, A.; Camaioni, N., The Role of Buffer Layers in Polymer Solar Cells. *Energy & Environmental Science* **2011**, *4*, 285-310.
21. Choi, J. K.; Jin, M. L.; An, C. J.; Kim, D. W.; Jung, H.-T., High-Performance of Pedot/Pss Free Organic Solar Cells on an Air-Plasma-Treated Ito Substrate. *ACS Applied Materials & Interfaces* **2014**, *6*, 11047-11053.
22. Alemu Mengistie, D.; Wang, P.-C.; Chu, C.-W., Effect of Molecular Weight of Additives on the Conductivity of Pedot:Pss and Efficiency for Ito-Free Organic Solar Cells. *Journal of Materials Chemistry A* **2013**, *1*, 9907-9915.
23. Wang, L.; Liu, H.; Konik, R.; A Misewich, J.; S Wong, S., *Cheminform Abstract: Carbon Nanotube-Based Heterostructures for Solar Energy Applications*, 2013; Vol. 42.
24. He, M.; Qiu, F.; Lin, Z., Conjugated Rod–Coil and Rod–Rod Block Copolymers for Photovoltaic Applications. *Journal of Materials Chemistry* **2011**, *21*, 17039-17048.
25. Li, K.; Li, Z.; Feng, K.; Xu, X.; Wang, L.; Peng, Q., Development of Large Band-Gap Conjugated Copolymers for Efficient Regular Single and Tandem Organic Solar Cells. *Journal of the American Chemical Society* **2013**, *135*, 13549-13557.
26. Kim, J. Y.; Lee, K.; Coates, N. E.; Moses, D.; Nguyen, T.-Q.; Dante, M.; Heeger, A. J., Efficient Tandem Polymer Solar Cells Fabricated by All-Solution Processing. *Science* **2007**, *317*, 222-225.
27. Ameri, T.; Dennler, G.; Lungenschmied, C.; Brabec, C. J., Organic Tandem Solar Cells: A Review. *Energy & Environmental Science* **2009**, *2*, 347-363.
28. A Willets, K.; P Van Duyne, R., *Localized Surface Plasmon Resonance Spectroscopy and Sensing*, 2007; Vol. 58, p 267-97.
29. Barnes, W. L.; Dereux, A.; Ebbesen, T. W., Surface Plasmon Subwavelength Optics. *Nature* **2003**, *424*, 824.
30. Baek, S.-W.; Park, G.; Noh, J.; Cho, C.; Lee, C.-H.; Seo, M.-K.; Song, H.; Lee, J.-Y., Au@Ag Core–Shell Nanocubes for Efficient Plasmonic Light Scattering Effect in Low Bandgap Organic Solar Cells. *ACS Nano* **2014**, *8*, 3302-3312.
31. Zilberberg, K.; Riedl, T., Metal-Nanostructures – a Modern and Powerful Platform to Create Transparent Electrodes for Thin-Film Photovoltaics. *Journal of Materials Chemistry A* **2016**, *4*, 14481-14508.

32. Kim, S.; Cho, H. W.; Hong, K.; Son, J. H.; Kim, K.; Koo, B.; Kim, S.; Lee, J.-L., Design of Red, Green, Blue Transparent Electrodes for Flexible Optical Devices. *Optics Express* **2014**, *22*, A1257-A1269.
33. Linic, S.; Christopher, P.; Ingram, D. B., Plasmonic-Metal Nanostructures for Efficient Conversion of Solar to Chemical Energy. *Nat Mater* **2011**, *10*, 911-921.
34. Atwater, H. A.; Polman, A., Plasmonics for Improved Photovoltaic Devices. *Nat Mater* **2010**, *9*, 205-213.
35. Lu, L.; Luo, Z.; Xu, T.; Yu, L., Cooperative Plasmonic Effect of Ag and Au Nanoparticles on Enhancing Performance of Polymer Solar Cells. *Nano Letters* **2013**, *13*, 59-64.
36. Kim, S.-S.; Na, S.-I.; Jo, J.; Kim, D.-Y.; Nah, Y.-C., Plasmon Enhanced Performance of Organic Solar Cells Using Electrodeposited Ag Nanoparticles. *Applied Physics Letters* **2008**, *93*, 073307.
37. Mahmoud, M. A.; Chamanzar, M.; Adibi, A.; El-Sayed, M. A., Effect of the Dielectric Constant of the Surrounding Medium and the Substrate on the Surface Plasmon Resonance Spectrum and Sensitivity Factors of Highly Symmetric Systems: Silver Nanocubes. *Journal of the American Chemical Society* **2012**, *134*, 6434-6442.
38. Cho, H.; Choi, S.; Kim, J. Y.; Park, S., Fabrication of Gold Dot, Ring, and Corpuscle Arrays from Block Copolymer Templates Via a Simple Modification of Surface Energy. *Nanoscale* **2011**, *3*, 5007-5012.
39. Heo, M.; Cho, H.; Jung, J.-W.; Jeong, J.-R.; Park, S.; Kim, J. Y., High-Performance Organic Optoelectronic Devices Enhanced by Surface Plasmon Resonance. *Advanced Materials* **2011**, *23*, 5689-5693.
40. Beek, W. J. E.; Wienk, M. M.; Kemerink, M.; Yang, X.; Janssen, R. A. J., Hybrid Zinc Oxide Conjugated Polymer Bulk Heterojunction Solar Cells. *The Journal of Physical Chemistry B* **2005**, *109*, 9505-9516.
41. Wang, J.; Polleux, J.; Lim, J.; Dunn, B., Pseudocapacitive Contributions to Electrochemical Energy Storage in Tio<sub>2</sub> (Anatase) Nanoparticles. *The Journal of Physical Chemistry C* **2007**, *111*, 14925-14931.
42. Draine, B. T., The Discrete-Dipole Approximation and Its Application to Interstellar Graphite Grains. *Astrophys J* **1988**, *333*, 848-872.
43. Seo, E.; Ko, S.-J.; Min, S. H.; Kim, J. Y.; Kim, B.-S., Plasmonic Transition Via Interparticle Coupling of Au@Ag Core-Shell Nanostructures Sheathed in Double Hydrophilic Block Copolymer for High-Performance Polymer Solar Cell. *Chemistry of Materials* **2015**, *27*, 4789-4798.
44. Pillai, S.; Catchpole, K. R.; Trupke, T.; Green, M. A., Surface Plasmon Enhanced Silicon Solar Cells. *Journal of Applied Physics* **2007**, *101*, 093105.
45. Xu, W.; Min, X.; Chen, X.; Zhu, Y.; Zhou, P.; Cui, S.; Xu, S.; Tao, L.; Song, H., Ag-Sio<sub>2</sub>-

Er<sub>2</sub>O<sub>3</sub> Nanocomposites: Highly Effective Upconversion Luminescence at High Power Excitation and High Temperature. *Scientific Reports* **2014**, *4*, 5087.

46. Wu, B.; Wu, X.; Guan, C.; Fai Tai, K.; Yeow, E. K. L.; Jin Fan, H.; Mathews, N.; Sum, T. C., Uncovering Loss Mechanisms in Silver Nanoparticle-Blended Plasmonic Organic Solar Cells. **2013**, *4*, 2004.

47. Boix, P. P.; Ajuria, J.; Etxebarria, I.; Pacios, R.; Garcia-Belmonte, G.; Bisquert, J., Role of ZnO Electron-Selective Layers in Regular and Inverted Bulk Heterojunction Solar Cells. *The Journal of Physical Chemistry Letters* **2011**, *2*, 407-411.

48. Kim, J. Y.; Kim, S. H.; Lee, H. H.; Lee, K.; Ma, W.; Gong, X.; Heeger, A. J., New Architecture for High-Efficiency Polymer Photovoltaic Cells Using Solution-Based Titanium Oxide as an Optical Spacer. *Advanced Materials* **2006**, *18*, 572-576.

49. Fung, D. D. S.; Qiao, L.; Choy, W. C. H.; Wang, C.; Sha, W. E. I.; Xie, F.; He, S., Optical and Electrical Properties of Efficiency Enhanced Polymer Solar Cells with Au Nanoparticles in a Pedot-Pss Layer. *Journal of Materials Chemistry* **2011**, *21*, 16349-16356.

50. Khaleque, T.; Magnusson, R., Light Management through Guided-Mode Resonances in Thin-Film Silicon Solar Cells. *NANOP* **2014**, *8*, 083995-083995.

51. Lee, Y.-C.; Huang, C.-F.; Chang, J.-Y.; Wu, M.-L., Enhanced Light Trapping Based on Guided Mode Resonance Effect for Thin-Film Silicon Solar Cells with Two Filling-Factor Gratings. *Optics Express* **2008**, *16*, 7969-7975.

52. You, J.; Dou, L.; Hong, Z.; Li, G.; Yang, Y., Recent Trends in Polymer Tandem Solar Cells Research. *Progress in Polymer Science* **2013**, *38*, 1909-1928.

53. Ameri, T.; Li, N.; Brabec, C. J., Highly Efficient Organic Tandem Solar Cells: A Follow up Review. *Energy & Environmental Science* **2013**, *6*, 2390-2413.

54. Li, S.; Ye, L.; Zhao, W.; Zhang, S.; Mukherjee, S.; Ade, H.; Hou, J., Energy-Level Modulation of Small-Molecule Electron Acceptors to Achieve over 12% Efficiency in Polymer Solar Cells. *Advanced Materials* **2016**, *28*, 9423-9429.

55. Oh, J.; Kranthiraja, K.; Lee, C.; Gunasekar, K.; Kim, S.; Ma, B.; Kim, B. J.; Jin, S.-H., Side-Chain Fluorination: An Effective Approach to Achieving High-Performance All-Polymer Solar Cells with Efficiency Exceeding 7%. *Advanced Materials* **2016**, *28*, 10016-10023.

56. Zhao, J.; Li, Y.; Yang, G.; Jiang, K.; Lin, H.; Ade, H.; Ma, W.; Yan, H., Efficient Organic Solar Cells Processed from Hydrocarbon Solvents. *Nature Energy* **2016**, *1*, 15027.

57. Zheng, Z.; Zhang, S.; Zhang, M.; Zhao, K.; Ye, L.; Chen, Y.; Yang, B.; Hou, J., Highly Efficient Tandem Polymer Solar Cells with a Photovoltaic Response in the Visible Light Range. *Advanced Materials* **2015**, *27*, 1189-1194.

58. Ma, Y.; Chen, S.-C.; Wang, Z.; Ma, W.; Wang, J.; Yin, Z.; Tang, C.; Cai, D.; Zheng, Q., Indacenodithiophene-Based Wide Bandgap Copolymers for High Performance Single-Junction and



Tandem Polymer Solar Cells. *Nano Energy* **2017**, *33*, 313-324.

59. Zhou, H.; Zhang, Y.; Mai, C.-K.; Collins, S. D.; Bazan, G. C.; Nguyen, T.-Q.; Heeger, A. J., Polymer Homo-Tandem Solar Cells with Best Efficiency of 11.3%. *Advanced Materials* **2015**, *27*, 1767-1773.
60. Yusoff, A. R. b. M.; Kim, D.; Kim, H. P.; Shneider, F. K.; da Silva, W. J.; Jang, J., A High Efficiency Solution Processed Polymer Inverted Triple-Junction Solar Cell Exhibiting a Power Conversion Efficiency of 11.83%. *Energy & Environmental Science* **2015**, *8*, 303-316.
61. Kim, J.-H.; Park, J. B.; Xu, F.; Kim, D.; Kwak, J.; Grimsdale, A. C.; Hwang, D.-H., Effect of [Small Pi]-Conjugated Bridges of Tpd-Based Medium Bandgap Conjugated Copolymers for Efficient Tandem Organic Photovoltaic Cells. *Energy & Environmental Science* **2014**, *7*, 4118-4131.
62. Zhang, Q.; Wan, X.; Liu, F.; Kan, B.; Li, M.; Feng, H.; Zhang, H.; Russell, T. P.; Chen, Y., Evaluation of Small Molecules as Front Cell Donor Materials for High-Efficiency Tandem Solar Cells. *Advanced Materials* **2016**, *28*, 7008-7012.
63. Li, M., et al., Solution-Processed Organic Tandem Solar Cells with Power Conversion Efficiencies >12%. *Nat Photon* **2017**, *11*, 85-90.
64. You, J.; Chen, C.-C.; Hong, Z.; Yoshimura, K.; Ohya, K.; Xu, R.; Ye, S.; Gao, J.; Li, G.; Yang, Y., 10.2% Power Conversion Efficiency Polymer Tandem Solar Cells Consisting of Two Identical Sub-Cells. *Advanced Materials* **2013**, *25*, 3973-3978.
65. Zhang, S.; Qin, Y.; Uddin, M. A.; Jang, B.; Zhao, W.; Liu, D.; Woo, H. Y.; Hou, J., A Fluorinated Polythiophene Derivative with Stabilized Backbone Conformation for Highly Efficient Fullerene and Non-Fullerene Polymer Solar Cells. *Macromolecules* **2016**, *49*, 2993-3000.
66. Kim, J.-H.; Shin, S. A.; Park, J. B.; Song, C. E.; Shin, W. S.; Yang, H.; Li, Y.; Hwang, D.-H., Fluorinated Benzoselenadiazole-Based Low-Band-Gap Polymers for High Efficiency Inverted Single and Tandem Organic Photovoltaic Cells. *Macromolecules* **2014**, *47*, 1613-1622.
67. Duan, C.; Furlan, A.; van Franeker, J. J.; Willems, R. E. M.; Wienk, M. M.; Janssen, R. A. J., Wide-Bandgap Benzodithiophene–Benzothiadiazole Copolymers for Highly Efficient Multijunction Polymer Solar Cells. *Advanced Materials* **2015**, *27*, 4461-4468.
68. Kim, J.-H.; Song, C. E.; Kim, B.; Kang, I.-N.; Shin, W. S.; Hwang, D.-H., Thieno[3,2-B]Thiophene-Substituted Benzo[1,2-B:4,5-B']Dithiophene as a Promising Building Block for Low Bandgap Semiconducting Polymers for High-Performance Single and Tandem Organic Photovoltaic Cells. *Chemistry of Materials* **2014**, *26*, 1234-1242.
69. Kim, J.-H.; Song, C. E.; Kim, H. U.; Grimsdale, A. C.; Moon, S.-J.; Shin, W. S.; Choi, S. K.; Hwang, D.-H., High Open Circuit Voltage Solution-Processed Tandem Organic Photovoltaic Cells Employing a Bottom Cell Using a New Medium Band Gap Semiconducting Polymer. *Chemistry of Materials* **2013**, *25*, 2722-2732.
70. Chen, C.-C.; Dou, L.; Gao, J.; Chang, W.-H.; Li, G.; Yang, Y., High-Performance Semi-

- Transparent Polymer Solar Cells Possessing Tandem Structures. *Energy & Environmental Science* **2013**, *6*, 2714-2720.
71. Zuo, L.; Chang, C.-Y.; Chueh, C.-C.; Zhang, S.; Li, H.; Jen, A. K. Y.; Chen, H., Design of a Versatile Interconnecting Layer for Highly Efficient Series-Connected Polymer Tandem Solar Cells. *Energy & Environmental Science* **2015**, *8*, 1712-1718.
72. Kouijzer, S.; Esiner, S.; Frijters, C. H.; Turbiez, M.; Wienk, M. M.; Janssen, R. A. J., Efficient Inverted Tandem Polymer Solar Cells with a Solution-Processed Recombination Layer. *Advanced Energy Materials* **2012**, *2*, 945-949.
73. Sun, Q.; Zhang, F.; Wang, J.; An, Q.; Zhao, C.; Li, L.; Teng, F.; Hu, B., A Two-Step Strategy to Clarify the Roles of a Solution Processed Pfn Interfacial Layer in Highly Efficient Polymer Solar Cells. *Journal of Materials Chemistry A* **2015**, *3*, 18432-18441.
74. Chen, C.-C.; Chang, W.-H.; Yoshimura, K.; Ohya, K.; You, J.; Gao, J.; Hong, Z.; Yang, Y., An Efficient Triple-Junction Polymer Solar Cell Having a Power Conversion Efficiency Exceeding 11%. *Advanced Materials* **2014**, *26*, 5670-5677.
75. Zhou, J.; Anjum, D. H.; Chen, L.; Xu, X.; Ventura, I. A.; Jiang, L.; Lubineau, G., The Temperature-Dependent Microstructure of Pedot/Pss Films: Insights from Morphological, Mechanical and Electrical Analyses. *Journal of Materials Chemistry C* **2014**, *2*, 9903-9910.
76. Burdick, J.; Glatfelter, T., Spectral Response and I–V Measurements of Tandem Amorphous-Silicon Alloy Solar Cells. *Solar Cells* **1986**, *18*, 301-314.
77. Rand, B. P.; Peumans, P.; Forrest, S. R., Long-Range Absorption Enhancement in Organic Tandem Thin-Film Solar Cells Containing Silver Nanoclusters. *Journal of Applied Physics* **2004**, *96*, 7519-7526.
78. Yao, H.; Yu, R.; Shin, T. J.; Zhang, H.; Zhang, S.; Jang, B.; Uddin, M. A.; Woo, H. Y.; Hou, J., A Wide Bandgap Polymer with Strong  $\pi$ – $\pi$  Interaction for Efficient Fullerene-Free Polymer Solar Cells. *Advanced Energy Materials* **2016**, *6*, 1600742-n/a.
79. Ma, Y.; Kang, Z.; Zheng, Q., Recent Advances in Wide Bandgap Semiconducting Polymers for Polymer Solar Cells. *Journal of Materials Chemistry A* **2017**, *5*, 1860-1872.
80. Zheng, Z.; Zhang, S.; Zhang, J.; Qin, Y.; Li, W.; Yu, R.; Wei, Z.; Hou, J., Over 11% Efficiency in Tandem Polymer Solar Cells Featured by a Low-Band-Gap Polymer with Fine-Tuned Properties. *Advanced Materials* **2016**, *28*, 5133-5138.
81. Martinez-Otero, A.; Liu, Q.; Mantilla-Perez, P.; Bajo, M. M.; Martorell, J., An Extremely Thin and Robust Interconnecting Layer Providing 76% Fill Factor in a Tandem Polymer Solar Cell Architecture. *Journal of Materials Chemistry A* **2015**, *3*, 10681-10686.
82. Kang, H.; Kee, S.; Yu, K.; Lee, J.; Kim, G.; Kim, J.; Kim, J.-R.; Kong, J.; Lee, K., Simplified Tandem Polymer Solar Cells with an Ideal Self-Organized Recombination Layer. *Advanced Materials* **2015**, *27*, 1408-1413.

83. Lu, S.; Liu, K.; Chi, D.; Yue, S.; Li, Y.; Kou, Y.; Lin, X.; Wang, Z.; Qu, S.; Wang, Z., Constructing Bulk Heterojunction with Componential Gradient for Enhancing the Efficiency of Polymer Solar Cells. *Journal of Power Sources* **2015**, *300*, 238-244.
84. Sun, J.; Jasieniak, J. J., Semi-Transparent Solar Cells. *Journal of Physics D: Applied Physics* **2017**, *50*, 093001.
85. Cho, H.; Yun, C.; Yoo, S., Multilayer Transparent Electrode for Organic Light-Emitting Diodes: Tuning Its Optical Characteristics. *Optics Express* **2010**, *18*, 3404-3414.
86. Zhang, S.; Qin, Y.; Zhu, J.; Hou, J., Over 14% Efficiency in Polymer Solar Cells Enabled by a Chlorinated Polymer Donor. *Advanced Materials* **2018**, *30*, 1800868.
87. Meng, L., et al., Organic and Solution-Processed Tandem Solar Cells with 17.3% Efficiency. *Science* **2018**.
88. Kim, H.; Lee, K.-T.; Zhao, C.; Guo, L. J.; Kanicki, J., Top Illuminated Organic Photodetectors with Dielectric/Metal/Dielectric Transparent Anode. *Organic Electronics* **2015**, *20*, 103-111.
89. Bauch, M.; Dimopoulos, T., Design of Ultrathin Metal-Based Transparent Electrodes Including the Impact of Interface Roughness. *Materials & Design* **2016**, *104*, 37-42.
90. Liu, X.; Cai, X.; Qiao, J.; Mao, J.; Jiang, N., The Design of ZnS/Ag/ZnS Transparent Conductive Multilayer Films. *Thin Solid Films* **2003**, *441*, 200-206.
91. Lim, D. C.; Jeong, J. H.; Hong, K.; Nho, S.; Lee, J.-Y.; Hoang, Q. V.; Lee, S. K.; Pyo, K.; Lee, D.; Cho, S., Semi-Transparent Plastic Solar Cell Based on Oxide-Metal-Oxide Multilayer Electrodes. *Progress in Photovoltaics: Research and Applications* **2018**, *26*, 188-195.
92. Lin, X.; Luo, H.; Jia, X.; Wang, J.; Zhou, J.; Jiang, Z.; Pan, L.; Huang, S.; Chen, X., Efficient and Ultraviolet Durable Inverted Polymer Solar Cells Using Thermal Stable Gzo-Agti-Gzo Multilayers as a Transparent Electrode. *Organic Electronics* **2016**, *39*, 177-183.
93. Yun, J., Ultrathin Metal Films for Transparent Electrodes of Flexible Optoelectronic Devices. *Advanced Functional Materials* **2017**, *27*, 1606641.
94. Han, J. H.; Kim, D.-Y.; Kim, D.; Choi, K. C., Highly Conductive and Flexible Color Filter Electrode Using Multilayer Film Structure. *Scientific Reports* **2016**, *6*, 29341.
95. Ji, C.; Lee, K.-T.; Xu, T.; Zhou, J.; Park, H. J.; Guo, L. J., Engineering Light at the Nanoscale: Structural Color Filters and Broadband Perfect Absorbers. *Advanced Optical Materials* **2017**, *5*, 1700368.
96. Xu, G., et al., High-Performance Colorful Semitransparent Polymer Solar Cells with Ultrathin Hybrid-Metal Electrodes and Fine-Tuned Dielectric Mirrors. *Advanced Functional Materials* **2017**, *27*, 1605908.
97. Larouche, S.; Martinu, L., Openfilters: Open-Source Software for the Design, Optimization, and Synthesis of Optical Filters. *Appl. Opt.* **2008**, *47*, C219-C230.
98. Xu, Z.; Chen, L. M.; Yang, G.; Huang, C. H.; Hou, J.; Wu, Y.; Li, G.; Hsu, C. S.; Yang, Y.,

Vertical Phase Separation in Poly (3-Hexylthiophene): Fullerene Derivative Blends and Its Advantage for Inverted Structure Solar Cells. *Adv. Funct. Mater.* **2009**, *19*, 1227-1234.

99. Campoy-Quiles, M.; Ferenczi, T.; Agostinelli, T.; Etchegoin, P. G.; Kim, Y.; Anthopoulos, T. D.; Stavrinou, P. N.; Bradley, D. D.; Nelson, J., Morphology Evolution Via Self-Organization and Lateral and Vertical Diffusion in Polymer: Fullerene Solar Cell Blends. *Nat. Mater.* **2008**, *7*, 158-164.

100. Meyer, J.; Khalandovsky, R.; Görrn, P.; Kahn, A., Moo<sub>3</sub> Films Spin-Coated from a Nanoparticle Suspension for Efficient Hole-Injection in Organic Electronics. *Adv. Mater.* **2011**, *23*, 70-73.

101. Murase, S.; Yang, Y., Solution Processed Moo<sub>3</sub> Interfacial Layer for Organic Photovoltaics Prepared by a Facile Synthesis Method. *Adv. Mater.* **2012**, *24*, 2459-2462.

102. Xie, F.; Choy, W. C.; Wang, C.; Li, X.; Zhang, S.; Hou, J., Low-Temperature Solution-Processed Hydrogen Molybdenum and Vanadium Bronzes for an Efficient Hole-Transport Layer in Organic Electronics. *Adv. Mater.* **2013**, *25*, 2051-2055.

103. Irwin, M. D.; Servaites, J. D.; Buchholz, D. B.; Leever, B. J.; Liu, J.; Emery, J. D.; Zhang, M.; Song, J.-H.; Durstock, M. F.; Freeman, A. J., Structural and Electrical Functionality of Nio Interfacial Films in Bulk Heterojunction Organic Solar Cells. *Chem. Mater.* **2011**, *23*, 2218-2226.

104. Steirer, K. X.; Ndione, P. F.; Widjonarko, N. E.; Lloyd, M. T.; Meyer, J.; Ratcliff, E. L.; Kahn, A.; Armstrong, N. R.; Curtis, C. J.; Ginley, D. S., Enhanced Efficiency in Plastic Solar Cells Via Energy Matched Solution Processed Niox Interlayers. *Adv. Energy Mater.* **2011**, *1*, 813-820.

105. Stubhan, T.; Li, N.; Luechinger, N. A.; Halim, S. C.; Matt, G. J.; Brabec, C. J., High Fill Factor Polymer Solar Cells Incorporating a Low Temperature Solution Processed Wo<sub>3</sub> Hole Extraction Layer. *Adv. Energy Mater.* **2012**, *2*, 1433-1438.

106. Terán-Escobar, G.; Pampel, J.; Caicedo, J. M.; Lira-Cantú, M., Low-Temperature, Solution-Processed, Layered V<sub>2</sub>O<sub>5</sub> Hydrate as the Hole-Transport Layer for Stable Organic Solar Cells. *Energy Environ. Sci.* **2013**, *6*, 3088-3098.

107. Stubhan, T.; Ameri, T.; Salinas, M.; Krantz, J.; Machui, F.; Halik, M.; Brabec, C. J., High Shunt Resistance in Polymer Solar Cells Comprising a Moo<sub>3</sub> Hole Extraction Layer Processed from Nanoparticle Suspension. *Appl. Phys. Lett.* **2011**, *98*, 253308-253308-3.

108. Li, G.; Chu, C.-W.; Shrotriya, V.; Huang, J.; Yang, Y., Efficient Inverted Polymer Solar Cells. *Appl. Phys. Lett.* **2006**, *88*, 253503-253503-3.

109. Sun, Y.; Seo, J. H.; Takacs, C. J.; Seifert, J.; Heeger, A. J., Inverted Polymer Solar Cells Integrated with a Low-Temperature-Annealed Sol-Gel-Derived Zno Film as an Electron Transport Layer. *Adv. Mater.* **2011**, *23*, 1679-1683.

110. Chen, Z.; Zhang, H.; Yu, W.; Li, Z.; Hou, J.; Wei, H.; Yang, B., Inverted Hybrid Solar Cells from Aqueous Materials with a Pce of 3.61%. *Adv. Energy Mater.* **2013**, *3*, 433-437.

111. Cho, N.; Schlenker, C. W.; Knesting, K. M.; Koelsch, P.; Yip, H. L.; Ginger, D. S.; Jen, A. K.-

- Y., High-Dielectric Constant Side-Chain Polymers Show Reduced Non-Geminate Recombination in Heterojunction Solar Cells. *Adv. Energy Mater.* **2014**, *4*, DOI: 10.1002/aenm.201301857.
112. Hoven, C. V.; Yang, R.; Garcia, A.; Crockett, V.; Heeger, A. J.; Bazan, G. C.; Nguyen, T.-Q., Electron Injection into Organic Semiconductor Devices from High Work Function Cathodes. *Proc. Natl. Acad. Sci. U.S.A.* **2008**, *105*, 12730-12735.
113. Darling, S. B.; You, F., The Case for Organic Photovoltaics. *RSC Advances* **2013**, *3*, 17633-17648.
114. Li, G.; Zhu, R.; Yang, Y., Polymer Solar Cells. *Nature Photonics* **2012**, *6*, 153.
115. Park, S. S.; Hendon, C. H.; Fielding, A. J.; Walsh, A.; O’Keeffe, M.; Dincă, M., The Organic Secondary Building Unit: Strong Intermolecular  $\pi$  Interactions Define Topology in Mit-25, a Mesoporous Mof with Proton-Replete Channels. *Journal of the American Chemical Society* **2017**, *139*, 3619-3622.
116. Hou, J.; Chen, H.-Y.; Zhang, S.; Chen, R. I.; Yang, Y.; Wu, Y.; Li, G., Synthesis of a Low Band Gap Polymer and Its Application in Highly Efficient Polymer Solar Cells. *Journal of the American Chemical Society* **2009**, *131*, 15586-15587.
117. Yuan, J.; Zhai, Z.; Dong, H.; Li, J.; Jiang, Z.; Li, Y.; Ma, W., Efficient Polymer Solar Cells with a High Open Circuit Voltage of 1 Volt. *Advanced Functional Materials* **2012**, *23*, 885-892.
118. Zhou, H.; Yang, L.; Stuart, A. C.; Price, S. C.; Liu, S.; You, W., Development of Fluorinated Benzothiadiazole as a Structural Unit for a Polymer Solar Cell of 7 % Efficiency. *Angewandte Chemie International Edition* **2011**, *50*, 2995-2998.
119. Dang, D.; Chen, W.; Himmelberger, S.; Tao, Q.; Lundin, A.; Yang, R.; Zhu, W.; Salleo, A.; Müller, C.; Wang, E., Enhanced Photovoltaic Performance of Indacenodithiophene-Quinoxaline Copolymers by Side-Chain Modulation. *Advanced Energy Materials* **2014**, *4*, 1400680.
120. Yum, S., et al., Benzotriazole-Containing Planar Conjugated Polymers with Noncovalent Conformational Locks for Thermally Stable and Efficient Polymer Field-Effect Transistors. *Chemistry of Materials* **2014**, *26*, 2147-2154.
121. Yu, G.; Gao, J.; Hummelen, J.; Wudl, F.; Heeger, A., Polymer Photovoltaic Cells: Enhanced Efficiencies Via a Network of Internal Donor-Acceptor Heterojunctions. *Science* **1995**, *270*, 1789-1790.
122. Wienk, M. M.; Kroon, J. M.; Verhees, W. J.; Knol, J.; Hummelen, J. C.; van Hal, P. A.; Janssen, R. A., Efficient Methano [70] Fullerene/Mdmo-Ppv Bulk Heterojunction Photovoltaic Cells. *Angew. Chem., Int. Ed.* **2003**, *115*, 3493-3497.
123. Li, G.; Zhu, R.; Yang, Y., Polymer Solar Cells. *Nat. Photonics* **2012**, *6*, 153-161.
124. Günes, S.; Neugebauer, H.; Sariciftci, N. S., Conjugated Polymer-Based Organic Solar Cells. *Chem. Rev.* **2007**, *107*, 1324-1338.
125. Huo, L.; Zhang, S.; Guo, X.; Xu, F.; Li, Y.; Hou, J., Replacing Alkoxy Groups with Alkylthienyl Groups: A Feasible Approach to Improve the Properties of Photovoltaic Polymers. *Angew.*

*Chem., Int. Ed.* **2011**, *123*, 9871-9876.

126. Takimiya, K.; Osaka, I.; Nakano, M., II-Building Blocks for Organic Electronics: Reevaluation of “Inductive” and “Resonance” Effects of II-Electron Deficient Units. *Chem. Mater.* **2013**.

127. Huang, Y.; Liu, F.; Guo, X.; Zhang, W.; Gu, Y.; Zhang, J.; Han, C. C.; Russell, T. P.; Hou, J., Manipulating Backbone Structure to Enhance Low Band Gap Polymer Photovoltaic Performance. *Adv. Energy Mater.* **2013**, *3*, 930-937.

128. Dutta, G. K.; Kim, T.; Choi, H.; Lee, J.; Kim, D. S.; Kim, J. Y.; Yang, C., Synthesis of Fluorinated Analogues of a Practical Polymer Tq for Improved Open-Circuit Voltages in Polymer Solar Cells. *Polym. Chem.* **2014**.

129. Kim, B.; Yeom, H. R.; Yun, M. H.; Kim, J. Y.; Yang, C., A Selenophene Analogue of Pcdtbt: Selective Fine-Tuning of Lumo to Lower of the Bandgap for Efficient Polymer Solar Cells. *Macromolecules* **2012**, *45*, 8658-8664.

130. Uy, R. L.; Yan, L.; Li, W.; You, W., Tuning Fluorinated Benzotriazole Polymers through Alkylthio Substitution and Selenophene Incorporation for Bulk Heterojunction Solar Cells. *Macromolecules* **2014**.

131. Hou, J.; Huo, L.; He, C.; Yang, C.; Li, Y., Synthesis and Absorption Spectra of Poly (3-(Phenylenevinyl) Thiophene) S with Conjugated Side Chains. *Macromolecules* **2006**, *39*, 594-603.

132. Hou, J.; Tan, Z. a.; Yan, Y.; He, Y.; Yang, C.; Li, Y., Synthesis and Photovoltaic Properties of Two-Dimensional Conjugated Polythiophenes with Bi (Thienylenevinylene) Side Chains. *J. Am. Chem. Soc.* **2006**, *128*, 4911-4916.

133. Wang, M.; Hu, X.; Liu, P.; Li, W.; Gong, X.; Huang, F.; Cao, Y., Donor–Acceptor Conjugated Polymer Based on Naphtho [1, 2-C: 5, 6-C] Bis [1, 2, 5] Thiadiazole for High-Performance Polymer Solar Cells. *J. Am. Chem. Soc.* **2011**, *133*, 9638-9641.

134. He, Z.; Zhong, C.; Su, S.; Xu, M.; Wu, H.; Cao, Y., Enhanced Power-Conversion Efficiency in Polymer Solar Cells Using an Inverted Device Structure. *Nat. Photonics* **2012**, *6*, 591-595.

135. Cheng, Y.-J.; Yang, S.-H.; Hsu, C.-S., Synthesis of Conjugated Polymers for Organic Solar Cell Applications. *Chem. Rev.* **2009**, *109*, 5868-5923.

136. Zhou, H.; Yang, L.; You, W., Rational Design of High Performance Conjugated Polymers for Organic Solar Cells. *Macromolecules* **2012**, *45*, 607-632.

137. He, Z.; Zhong, C.; Su, S.; Xu, M.; Wu, H.; Cao, Y., Enhanced Power-Conversion Efficiency in Polymer Solar Cells Using an Inverted Device Structure. *Nature Photonics* **2012**, *6*, 591.

138. Li, Y., Molecular Design of Photovoltaic Materials for Polymer Solar Cells: Toward Suitable Electronic Energy Levels and Broad Absorption. *Accounts of Chemical Research* **2012**, *45*, 723-733.

139. Ren, Y.; Hailey, A. K.; Hiszpanski, A. M.; Loo, Y.-L., Isoindigo-Containing Molecular Semiconductors: Effect of Backbone Extension on Molecular Organization and Organic Solar Cell Performance. *Chemistry of Materials* **2014**, *26*, 6570-6577.

140. Osaka, I.; Zhang, R.; Sauvé, G.; Smilgies, D.-M.; Kowalewski, T.; McCullough, R. D., High-Lamellar Ordering and Amorphous-Like  $\pi$ -Network in Short-Chain Thiazolothiazole–Thiophene Copolymers Lead to High Mobilities. *Journal of the American Chemical Society* **2009**, *131*, 2521-2529.
141. Sung, A.; Ling, M. M.; Tang, M. L.; Bao, Z.; Locklin, J., Correlating Molecular Structure to Field-Effect Mobility: The Investigation of Side-Chain Functionality in Phenylene–Thiophene Oligomers and Their Application in Field Effect Transistors. *Chemistry of Materials* **2007**, *19*, 2342-2351.
142. Back, J. Y.; Yu, H.; Song, I.; Kang, I.; Ahn, H.; Shin, T. J.; Kwon, S.-K.; Oh, J. H.; Kim, Y.-H., Investigation of Structure–Property Relationships in Diketopyrrolopyrrole-Based Polymer Semiconductors Via Side-Chain Engineering. *Chemistry of Materials* **2015**, *27*, 1732-1739.
143. Akkerman, H. B., et al., Effects of Odd–Even Side Chain Length of Alkyl-Substituted Diphenylbithiophenes on First Monolayer Thin Film Packing Structure. *Journal of the American Chemical Society* **2013**, *135*, 11006-11014.
144. Mei, J.; Kim, D. H.; Ayzner, A. L.; Toney, M. F.; Bao, Z., Siloxane-Terminated Solubilizing Side Chains: Bringing Conjugated Polymer Backbones Closer and Boosting Hole Mobilities in Thin-Film Transistors. *Journal of the American Chemical Society* **2011**, *133*, 20130-20133.
145. Mark, J. E., Some Interesting Things About Polysiloxanes. *Accounts of Chemical Research* **2004**, *37*, 946-953.
146. Lee, J.; Han, A. R.; Kim, J.; Kim, Y.; Oh, J. H.; Yang, C., Solution-Processable Ambipolar Diketopyrrolopyrrole–Selenophene Polymer with Unprecedentedly High Hole and Electron Mobilities. *Journal of the American Chemical Society* **2012**, *134*, 20713-20721.
147. Scharber, M. C.; Mühlbacher, D.; Koppe, M.; Denk, P.; Waldauf, C.; Heeger, A. J.; Brabec, C. J., Design Rules for Donors in Bulk-Heterojunction Solar Cells—Towards 10 % Energy-Conversion Efficiency. *Advanced Materials* **2006**, *18*, 789-794.
148. Gasparini, N.; Lucera, L.; Salvador, M.; Prosa, M.; Spyropoulos, G. D.; Kubis, P.; Egelhaaf, H.-J.; Brabec, C. J.; Ameri, T., High-Performance Ternary Organic Solar Cells with Thick Active Layer Exceeding 11% Efficiency. *Energy & Environmental Science* **2017**, *10*, 885-892.
149. Lee, J.; Sin, D. H.; Moon, B.; Shin, J.; Kim, H. G.; Kim, M.; Cho, K., Highly Crystalline Low-Bandgap Polymer Nanowires Towards High-Performance Thick-Film Organic Solar Cells Exceeding 10% Power Conversion Efficiency. *Energy & Environmental Science* **2017**, *10*, 247-257.
150. Song, S.; Kranthiraja, K.; Heo, J.; Kim, T.; Walker, B.; Jin, S.-H.; Kim, J. Y., Efficiency Exceeding 11% in Tandem Polymer Solar Cells Employing High Open-Circuit Voltage Wide-Bandgap  $\pi$ -Conjugated Polymers. *Advanced Energy Materials* **2017**, 1700782.
151. Qin, Y.; Uddin, M. A.; Chen, Y.; Jang, B.; Zhao, K.; Zheng, Z.; Yu, R.; Shin, T. J.; Woo, H. Y.; Hou, J., Highly Efficient Fullerene-Free Polymer Solar Cells Fabricated with Polythiophene Derivative. *Advanced Materials* **2016**, *28*, 9416-9422.

152. Ma, W., et al., Influence of Processing Parameters and Molecular Weight on the Morphology and Properties of High-Performance Pffbt4t-2od:Pc71bm Organic Solar Cells. *Advanced Energy Materials* **2015**, *5*, 1501400.
153. Nguyen, T. L., et al., Semi-Crystalline Photovoltaic Polymers with Efficiency Exceeding 9% in a 300 nm Thick Conventional Single-Cell Device. *Energy & Environmental Science* **2014**, *7*, 3040-3051.
154. Nguyen, T. L.; Song, S.; Ko, S.-J.; Choi, H.; Jeong, J.-E.; Kim, T.; Hwang, S.; Kim, J. Y.; Woo, H. Y., Benzodithiophene-Thiophene-Based Photovoltaic Polymers with Different Side-Chains. *Journal of Polymer Science Part A: Polymer Chemistry* **2015**, *53*, 854-862.
155. Peet, J.; Kim, J. Y.; Coates, N. E.; Ma, W. L.; Moses, D.; Heeger, A. J.; Bazan, G. C., Efficiency Enhancement in Low-Bandgap Polymer Solar Cells by Processing with Alkane Dithiols. *Nat Mater* **2007**, *6*, 497-500.
156. He, Z.; Zhong, C.; Su, S.; Xu, M.; Wu, H.; Cao, Y., Enhanced Power-Conversion Efficiency in Polymer Solar Cells Using an Inverted Device Structure. *Nat Photon* **2012**, *6*, 591-595.
157. Koidis, C.; Logothetidis, S.; Kassavetis, S.; Kapnopoulos, C.; Karagiannidis, P. G.; Georgiou, D.; Laskarakis, A., Effect of Process Parameters on the Morphology and Nanostructure of Roll-to-Roll Printed P3ht:Pcbm Thin Films for Organic Photovoltaics. *Solar Energy Materials and Solar Cells* **2013**, *112*, 36-46.
158. Vak, D.; Hwang, K.; Faulks, A.; Jung, Y.-S.; Clark, N.; Kim, D.-Y.; Wilson, G. J.; Watkins, S. E., 3d Printer Based Slot-Die Coater as a Lab-to-Fab Translation Tool for Solution-Processed Solar Cells. *Advanced Energy Materials* **2015**, *5*, 1401539.
159. Po, R.; Bernardi, A.; Calabrese, A.; Carbonera, C.; Corso, G.; Pellegrino, A., From Lab to Fab: How Must the Polymer Solar Cell Materials Design Change? - an Industrial Perspective. *Energy & Environmental Science* **2014**, *10*, 925-943.
160. Bundgaard, E., et al., Matrix Organization and Merit Factor Evaluation as a Method to Address the Challenge of Finding a Polymer Material for Roll Coated Polymer Solar Cells. *Advanced Energy Materials* **2015**, *5*, 1402186.
161. Krebs, F. C.; Tromholt, T.; Jorgensen, M., Upscaling of Polymer Solar Cell Fabrication Using Full Roll-to-Roll Processing. *Nanoscale* **2010**, *2*, 873-886.
162. Verploegen, E.; Mondal, R.; Bettinger, C. J.; Sok, S.; Toney, M. F.; Bao, Z., Effects of Thermal Annealing Upon the Morphology of Polymer-Fullerene Blends. *Advanced Functional Materials* **2010**, *20*, 3519-3529.
163. Kang, H.; An, S. Y.; Walker, B.; Song, S.; Kim, T.; Kim, J. Y.; Yang, C., Thienoisindigo (Tiig)-Based Small Molecules for the Understanding of Structure-Property-Device Performance Correlations. *Journal of Materials Chemistry A* **2015**, *3*, 9899-9908.
164. Li, G.; Yao, Y.; Yang, H.; Shrotriya, V.; Yang, G.; Yang, Y., "Solvent Annealing" Effect in



Polymer Solar Cells Based on Poly(3-Hexylthiophene) and Methanofullerenes. *Advanced Functional Materials* **2007**, *17*, 1636-1644.

165. Kim, W.; Kim, J. K.; Kim, E.; Ahn, T. K.; Wang, D. H.; Park, J. H., Conflicted Effects of a Solvent Additive on Ptb7:Pc71bm Bulk Heterojunction Solar Cells. *The Journal of Physical Chemistry C* **2015**, *119*, 5954-5961.

166. Kim, G.; Song, S.; Lee, J.; Kim, T.; Lee, T. H.; Walker, B.; Kim, J. Y.; Yang, C., Control of Charge Dynamics Via Use of Nonionic Phosphonate Chains and Their Effectiveness for Inverted Structure Solar Cells. *Advanced Energy Materials* **2015**, *5*, 1500844.

167. Zheng, Y.; Li, S.; Zheng, D.; Yu, J., Effects of Different Polar Solvents for Solvent Vapor Annealing Treatment on the Performance of Polymer Solar Cells. *Organic Electronics* **2014**, *15*, 2647-2653.

168. Ye, L.; Jing, Y.; Guo, X.; Sun, H.; Zhang, S.; Zhang, M.; Huo, L.; Hou, J., Remove the Residual Additives toward Enhanced Efficiency with Higher Reproducibility in Polymer Solar Cells. *The Journal of Physical Chemistry C* **2013**, *117*, 14920-14928.

169. Liu, Y.; Zhao, J.; Li, Z.; Mu, C.; Ma, W.; Hu, H.; Jiang, K.; Lin, H.; Ade, H.; Yan, H., Aggregation and Morphology Control Enables Multiple Cases of High-Efficiency Polymer Solar Cells. *Nature Communications* **2014**, *5*, 5293.

170. Ro, H. W., et al., Morphology Changes Upon Scaling a High-Efficiency, Solution-Processed Solar Cell. *Energy & Environmental Science* **2016**, *9*, 2835-2846.

171. Zhao, K., et al., Highly Efficient Polymer Solar Cells with Printed Photoactive Layer: Rational Process Transfer from Spin-Coating. *Journal of Materials Chemistry A* **2016**, *4*, 16036-16046.

172. Lin, Y.; Cai, C.; Zhang, Y.; Zheng, W.; Yang, J.; Wang, E.; Hou, L., Study of Ito-Free Roll-to-Roll Compatible Polymer Solar Cells Using the One-Step Doctor Blading Technique. *Journal of Materials Chemistry A* **2017**, *5*, 4093-4102.

173. Hwang, K.; Jung, Y.-S.; Heo, Y.-J.; Scholes, F. H.; Watkins, S. E.; Subbiah, J.; Jones, D. J.; Kim, D.-Y.; Vak, D., Toward Large Scale Roll-to-Roll Production of Fully Printed Perovskite Solar Cells. *Advanced Materials* **2015**, *27*, 1241-1247.

## Acknowledgement

20대의 시간을 꾸며온 대학원 생활의 마침표를 찍기에 앞서 사랑하는 이들과 만났던 인연들에 감사의 인사를 드립니다.

우선 언제나 제 선택과 결정에 믿음을 주시고 아낌없이 응원을 해 주신 우리 아버지, 어머니 그리고 우리 가족에게 감사드립니다. 자주 찾아 뵙지 못한 죄송함과 더불어 여전히 지지해 주시는 부모님께 이 서면을 통해 감사함을 전합니다.

오래된 인연으로, 대학원 7년의 시간까지 늘 가까이서 응원을 해주고 버팀목이 되어준 그 이에게도 감사함을 전합니다.

“너는 꼭 대학원에 가서 연구해야 해, 네 적성에 딱 맞을 것 같은데.”라고 늘 말씀해 주시며 대학원의 길을 인도해주신 학부 시절 지도 교수였던 김석순 교수님께 감사드립니다. 그렇게 대학원 길에 들어서면서 만나 뵙게 된 우리 지도 교수님, 김진영 교수님. 제 열정을 품어 주시고 연구를 맘껏 할 수 있도록 아낌없는 격려와 기회를 적극적으로 주심에 진심으로 감사드립니다. 교수님 밑에서 지도를 받으며 박사로서, 연구자로서, 한 사람으로서 갖추어야 할 소양과 자세를 배우며 성장할 수 있었습니다. “대학원은 버티는 것이다”라는 말씀에 이 자리까지 올 수 있었던 끈기를, “안 해 볼 이유는 없지”라는 말씀에 디테일의 중요함과 시도를 두려워하지 않은 용기를 배웠습니다. 또, 교수님의 다방면 연구 열정에 저 또한 연구의 폭을 넓힐 수 있었습니다. 여전히 부족함이 많지만, 이를 토대로 어디서든 무엇이든 할 수 있는 마음가짐을 가지게 되었습니다. 저의 20대 성장의 귀중한 분이 되어 주심에 다시 한번 감사드립니다.

공동연구를 통해 연구에 대한 넓은 접근법을 가르쳐주신 우한영 교수님과 “당돌이”라고 부르시며 연구의 관점의 중요성을 알려주신 양창덕 교수님께도 감사드립니다. 따뜻한 조언과 함께 다정히 챙겨주신 권태혁 교수님, 긍정적이고 늘 유쾌하신 송명훈 교수님, 행동 중심의 열정을 보여주신 박두진 박사님, 연구에 유머러스와 여유를 겸비한 나석인 교수님, 여성 공학자로서 많은 조언을 주신 서정화 교수님과 김석순 교수님께도 감사를 전합니다. 교수님들의 가르침과 연구자의 삶을 보며 많이 배우게 되었습니다.

그리고 사랑하는 우리 NGEL 식구들에게도 감사함을 전합니다. 너무나도 좋은 사람들을 만난 것이 행운일 정도로 대학원 생활의 큰 즐거움이 되었습니다. 짧은 시간임에도 오래된 인연처럼 살갑게 대해주신 송수희 박사님, 항상 다정한 태효오빠, 인정도 장난도 많은 재기 오빠와 학범 오빠, 언제나 당차고 야무진 정우, 외유내강의 송이와 택호, 책임감 있는 다정한 영진이, 절제와 의리가 있는 강택이, 꾸준함의 힘을 가진 나경이, 언제나 밝고 유쾌한 재원이, NGEL의 유능한 맥가이버 형수, 솔직함의

귀여움을 가진 혜원이, 야무짐과 허당 사이의 귀여운 윤섭이, 뜰망한 눈을 가진 열정의 우리 지우, 수줍은 막내 종득이, NGEL의 착한 새싹들까지, 모두 고마워요. NGEL의 값진 인연으로써 대학원 생활의 활력소이자 이제는 선후배 관계를 뛰어넘어 친구가 된 실험실 큰언니인 명희 언니와 작은언니인 혜림 언니에게도 감사함을 전합니다. 그리고 이제는 사회에서 독립된 연구자의 길을 가고 있는 선배들에게도 전합니다. “요정님”이라고 부르신 창의적 사고의 Bright walker 교수님, 마무리의 중요성, 시간관리의 중요성, 성실함의 힘을 보여준 김기환 박사님, 최효성 교수님, 고서진 박사님께셔도 많이 배웠습니다. 감사합니다.

이 밖에도 목장 식구들을 비롯하여 무수히 만났던 인연들에도 감사드립니다.

딸, 동생, 누나, 이모, 여자친구, 선배, 후배, 제자 등 제가 가지고 있는 역할에 “박사. 연구자”의 역할이 추가됩니다. 주어진 환경과 각 역할에 최선을 다하는 사람이 되어 모두를 위한, 세상에 도움이 되는 사람이 되겠습니다.

송 세영 드림